



**Università
degli Studi
di Ferrara**

Doctoral Course in Physics

Cycle XXXVI

**The power of time evolution: properties
of GRB sources inferred from temporal
studies and simulations**

Candidate: Anna Elisa Camisasca

Supervisor: Prof. Cristiano Guidorzi

Università degli Studi di Ferrara
Dipartimento di Fisica e Scienze della Terra
October, 2023

Table of Contents

1	GRB main properties and key aspects	1
1.1	GRBs first discovery	1
1.2	Duration and temporal profile	2
1.3	Isotropic distribution	4
1.4	Released energy	5
1.5	Energy spectra	6
1.6	Spectral-duration distribution	7
1.7	Achromatic (jet) break	8
1.8	Fireball Shock model	9
1.9	Compactness problem	10
1.10	Jets	13
1.10.1	Beaming theory	13
1.10.2	Jet properties	13
1.11	Central engines	14
1.11.1	Black hole central engines	14
1.11.2	Magnetar central engines	15
1.12	Progenitors	15
1.12.1	Long GRBs	15
1.12.2	Short GRBs	16
1.13	Kilonovae	19
1.13.1	Properties	19
1.13.2	Main equations	21
1.13.3	Observations	23
1.13.4	Kilonovae polarization	26
2	Prompt emission detection	29
2.1	THESEUS	29
2.1.1	IRT	30
2.1.2	SXI	31
2.1.3	XGIS	32
2.2	MEPSA	33
2.3	Our simulations and results	34
3	Prompt emission and minimum variability timescale	37
3.1	Minimum variability timescale	37
3.2	Our study and results	38

TABLE OF CONTENTS

4	Kilonovae detection	41
4.1	Liverpool Telescope	41
4.1.1	IO:O	42
4.1.2	MOPTOP	42
4.2	POSSIS	42
4.3	Our simulations and results	43
4.3.1	Light curve analysis	43
4.3.2	Polarization analysis	47
5	Appendix A	75
6	Appendix B	103
7	Appendix C	123

Acknowledgments

These past three years have been a time of both professional and personal growth. I express my gratitude to all those who contributed to this journey, and to everyone who shared moments of joy with me. It was truly beautiful.

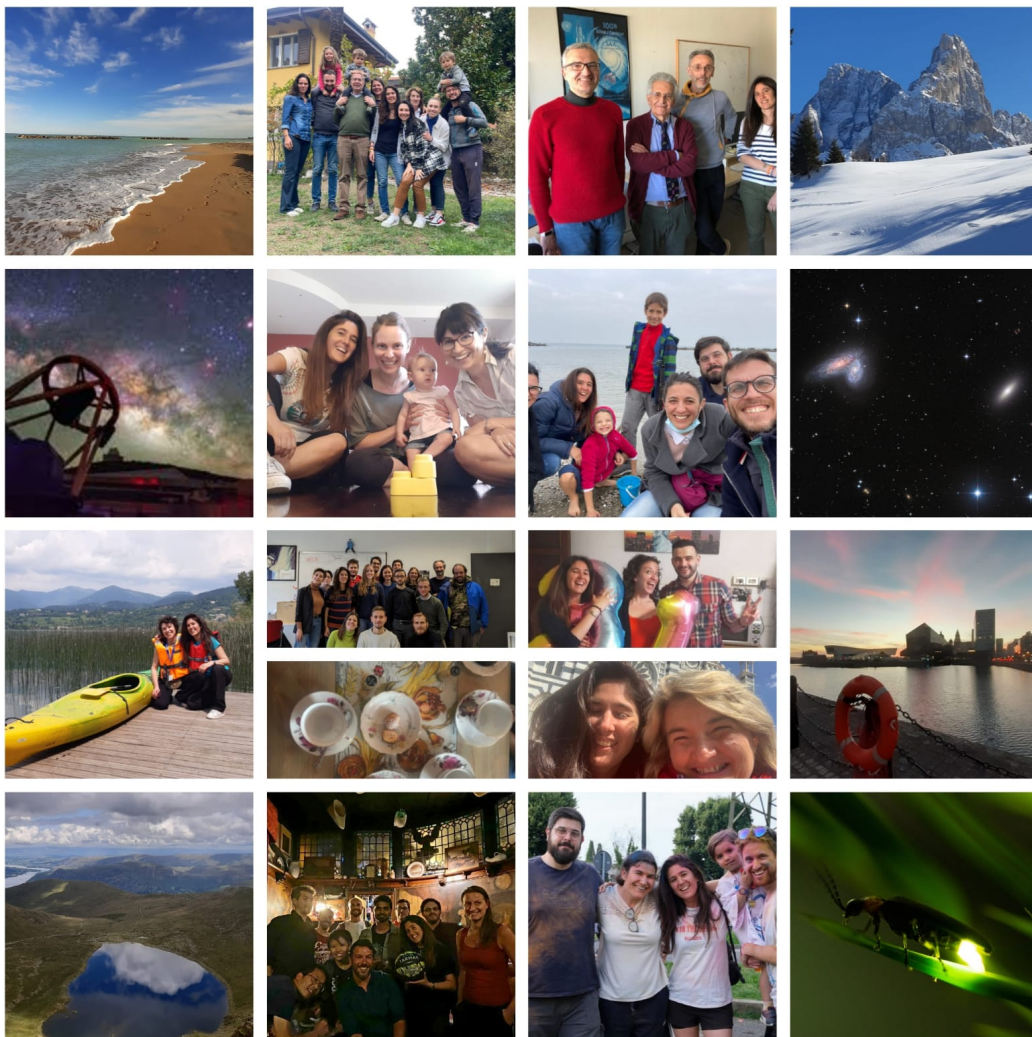
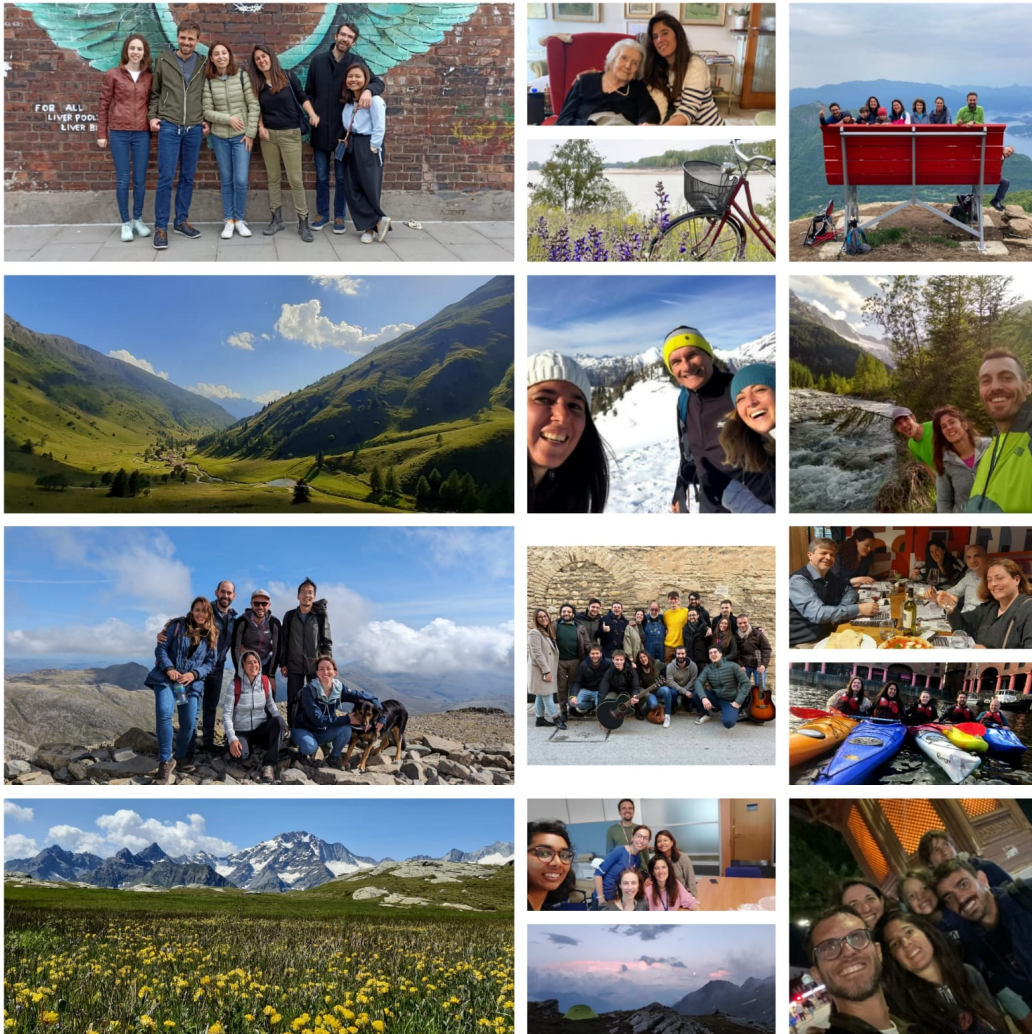


TABLE OF CONTENTS



Abstract

Since their discovery, there has been notable advancement in our ability to *identify*, *observe*, and *comprehend* the physics behind gamma-ray bursts (GRBs). The introduction of new detectors and both space-based and ground-based telescopes has greatly improved our ability to detect and collect more detailed data on GRBs: missions such as the Compton Gamma-Ray Observatory, BeppoSAX, the Neil Gehrels Swift Observatory, and the Fermi Gamma-ray Space Telescope have significantly contributed to GRB observations. Multi-messenger observations, including radio, infrared, optical, all the way up to GeV and TeV, along with gravitational waves measurements, provide us with an increasingly more comprehensive understanding of GRBs. This has led to a deeper insight into their physics and origins, such as the understanding of a close connection between short GRBs, kilonovae, and compact object mergers. Moreover, studies of the polarization of GRB radiation are providing valuable insights into the geometry and nature of the physical processes involved: polarization can help reveal details about the source and emission region. However, there are still many open questions: i.e., how can we improve our detection capabilities for both GRBs and kilonovae? Can the study of the prompt emission, so potentially rich in information as it is emitted in close proximity to the source and linked to the composition of the outflow, provide us with information about the nature of the progenitor?

In my Ph.D. research, I focused my activity on optimizing the *identification* of GRBs with THESEUS satellite, on the *comprehension* of GRBs imprint of the inner engine activity and jet properties from the study of the minimum variability timescale (MVT), and on finding the most suitable strategies for kilonovae *observation* with medium-size telescope:

- 1) THESEUS (Transient High Energy Sky and Early Universe Surveyor) is a proposed space mission devoted to the study of GRBs; it is one of the three mission concepts selected by ESA for a Phase-A study as M7 candidates. My aim was to test the efficiency of different algorithms, in particular MEPSA (Guidorzi, 2015), that could be implemented aboard of THESEUS in detecting GRB events. To this goal, I carried out GRB light curve simulations assuming a grid of parameter values (peak energy, fluence, directions; see Chapter 2).
- 2) GRBs light curves often exhibit fluctuations or variations in their intensity over different timescales. The MVT is the smallest time interval at which these fluctuations, which must significantly exceed the Poisson counting noise, can be reliably measured and quantified. MVT can offer clues about the central engine responsible for generating these bursts: we can infer the physical mechanisms and the size of the region where the energy release occurs. Also,

it is linked to the physical conditions and processes within the GRB's emission region. My aim was to characterize the MVT for a sample of GRBs in the keV–MeV energy range and test correlations with other key observables, such as the peak luminosity, the Lorentz factor, and the jet opening angle.

In my work I considered Swift GRBs (from 2005 to July 2022) and Insight Hard Modulation X-ray Telescope (Insight-HXMT) GRBs (from June 2017 to July 2021) (Chapter 3).

- 3) During my academic path, I had the opportunity to collaborate closely with the staff of the Astrophysics Research Institute of the John Moores University of Liverpool, where I focused my study on the performance optimization of the Liverpool Telescope with IO:O (an optical camera) and MOPTOP (Multicolor Optimized Optical Polarimeter) instruments. My research aimed to enhance their observational capabilities in studying kilonovae (KNe). I made extensive use of simulated multifilter lightcurves of KNe obtained with the POLarization Spectral Synthesis In Supernovae (POSSIS; Bulla, 2019) code. By adding the appropriate photon counting noise to the synthetic light curves, I studied which temporal observation sequences and filters could provide better results for constraining the properties of kilonovae. A similar work is being developed with polarization curves as seen by MOPTOP and the Liverpool Telescope (Chapter 4).

Introduction

Gamma-ray bursts (GRBs) are flares of gamma rays that can endure from a fraction of a second (short GRBs, S-GRBs) to several minutes (long GRBs, L-GRBs). Remarkably, GRBs are really energetic sources, the most powerful explosions in the Universe: they briefly outshine all other objects in the sky and emit as much energy in a few seconds as the Sun in its entire lifetime.¹ This property allows to explore the early Universe (up to when it was only a few hundred million years old). Long GRB are related to the collapse of some kind of massive stars (it is supposed they have a high-speed rotating core, for example). It means that long GRBs are formed only from an exclusive type of star, so their study enables unique constraints on stellar evolution. Short GRBs are instead the result of a merger of two compact objects (either two neutron stars or a neutron star and a black hole) and also provide essential constraints on the evolution of binary stars, as well as being powerful sources of gravitational waves. The GRB itself (long or short) is created by the ultrarelativistic motion of material and its interaction with both itself and the ambient medium.

The proton acceleration in the GRB jets should produce a shower of neutrinos, which should reach Earth without deviation due to their neutral charge. However, while large neutrino detectors, such as IceCube, have now reached the necessary sensitivity to observe GRB neutrinos, none has yet been found (Abbasi et al. 2022). These properties suggest that GRBs provide direct information across a broad range of astronomical disciplines: cosmology, stellar and binary evolution, the interstellar and intergalactic medium, relativistic astrophysics; GRBs can also be studied through a multimessenger approach. The connections they provide across so different fields make them so interesting and challenging.

The subject therefore lends itself well to being treated both at a popular level, due to the fascinating challenges it hides and the deep effects on the knowledge of the universe, and at a didactic level, touching on topics typical of the last year of Italian upper secondary school (study of function, relativity, black body spectra, ...). I therefore decided to set up the first part of the work (Chapters 1) with a flavour and a succession of topics that can be reused in the case of a didactic path at a secondary school, or for the creation of a popular science book, always starting from observations, images, graphs, plots, the real data. However, the discussion does not exactly coincide with what can be achieved at school or in a popular book, in order to maintain the appropriate level for a doctoral thesis presentation.

The heart of the work are Chapters 2, 3 and 4: alongside simulations aimed at testing the efficiency of different algorithms in detecting GRBs with THESEUS satellite and simulations of kilonovae light curves to improve the performances of

¹Observations of the brightest-of-all-time GRB 221009A revealed an isotropic-equivalent energy E_{iso} of $\sim 1.5 \times 10^{55}$ erg, which is about eight times of the total rest-mass energy of the Sun (An et al. 2023).

the Liverpool telescope, I analyzed the minimum variability timescale of thousands of GRBs and tested the correlations with other key observables, such as the peak luminosity, the Lorentz factor, and the jet opening angle.

Chapter 1

GRB main properties and key aspects

Over the past 50 years since their discovery was published (Klebesadel et al., 1973), Gamma-Ray Bursts (GRBs) have evolved from a serendipitous finding to a captivating tool for exploring the universe. This initial chapter, while not exhaustive, aims to present some observational data derived from GRB studies. The goal is to elucidate how these data have led to hypotheses regarding the nature of their central engine, the properties of the jet, and the apparent subdivision of GRBs in two families (long and short). In the opening sections we wrote in italics the key observations that provide readers with the essential concepts to facilitate their understanding of the subsequent analysis.

1.1 GRBs first discovery

The history of the discovery of GRBs is intertwined with one of the most dramatic periods of the 20th century: the Cold War. In the early 1960s, as efforts were made to contain nuclear rearmament, both Russians and Americans signed an initial treaty to limit unconventional weapons testing. The agreement, known as *the Treaty Banning Nuclear Weapon Tests In The Atmosphere, In Outer Space And Under Water*, prohibited nuclear explosions in the atmosphere, outer space, and beneath the oceans. However, it was a partial treaty that did not prevent testing underground. Just three days after the treaty was signed, the USA

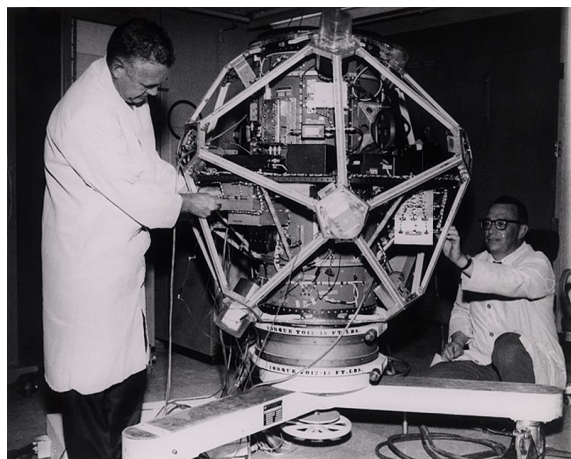


Figure 1.1: One of the eight Vela satellites during its construction.

launched the first two Vela satellites into orbit. These satellites, named from the Spanish word *velar*, meaning *to watch*, were designed to detect nuclear explosions in space: the Americans feared that the Russians might be capable of reaching the moon and detonating atomic bombs on its far side. In such a scenario, in addition

THE ASTROPHYSICAL JOURNAL, **182**:L85–L88, 1973 June 1
© 1973. The American Astronomical Society. All rights reserved. Printed in U.S.A.

OBSERVATIONS OF GAMMA-RAY BURSTS OF COSMIC ORIGIN

RAY W. KLEBESADEL, IAN B. STRONG, AND ROY A. OLSON

University of California, Los Alamos Scientific Laboratory, Los Alamos, New Mexico
Received 1973 March 16; revised 1973 April 2

ABSTRACT

Sixteen short bursts of photons in the energy range 0.2–1.5 MeV have been observed between 1969 July and 1972 July using widely separated spacecraft. Burst durations ranged from less than 0.1 s to ~ 30 s, and time-integrated flux densities from $\sim 10^{-5}$ ergs cm^{-2} to $\sim 2 \times 10^{-4}$ ergs cm^{-2} in the energy range given. Significant time structure within bursts was observed. Directional information eliminates the Earth and Sun as sources.

Figure 1.2: Title and abstract from the first article about GRBs (Klebesadel et al., 1973)

to X-rays emitted directly from the nuclear explosion, the radioactive decay of lunar dust was expected to produce gamma rays.

From 1963 to 1967, four pairs of Vela satellites were launched, with the last pair capable of identifying nuclear explosions in the atmosphere (Fig. 1.1). On July 2, 1967, Vela 3 and Vela 4 recorded a brief but intense emission in gamma rays — a rapid burst, a flash. By recording the arrival time of photons, it was immediately possible to indicate the direction of the gamma-ray bursts. The measurements were rough but sufficient to exclude that the gamma-ray burst had originated from Earth, the Moon, or the Solar System. The news was kept secret until 1973, when the number of observed gamma-ray bursts was about a dozen, and the discovery of gamma-ray bursts (GRBs) was finally made public (Klebesadel et al., 1973, see Fig. 1.1).

1.2 Duration and temporal profile

A GRB is a burst of gamma rays that can last from a fraction of a second up to several minutes. Quantitatively, the duration of a burst is defined by the so-called T_{90} : the time interval between the instants when 5% and 95% of the total fluence is registered by the detector. T_{90} is used to limit the uncertainty on the entire duration, as the start and the end of a GRB cannot be determined precisely due to the background fluctuations. For a given GRB, T_{90} depends on the energy band and sensitivity of the detector. Figure 1.3 shows *the T_{90} distribution* as observed by BATSE: it *includes at least two log-normal components* with a separation line around 2 seconds in the observer frame in the BATSE energy band (25 - 350 keV) (Kouveliotou et al. 2013): a long-duration class (L-GRBs) with $T_{90} > 2\text{s}$ and distribution peaking at 20-30 s, and a short-duration one (S-GRBs) with $T_{90} < 2\text{s}$ peaking at 0.2-0.3 s. It was also suggested that the T_{90} distribution may include a third, intermediate-duration group and that the dividing value between the two

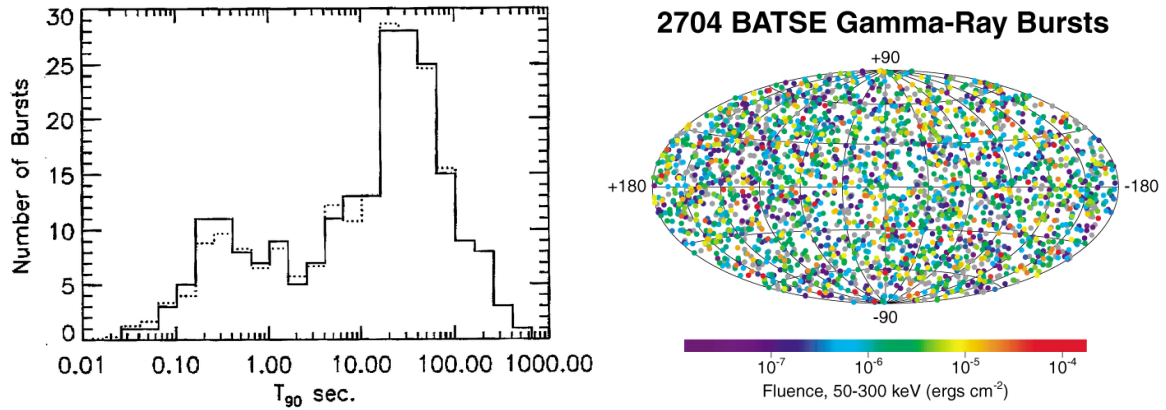


Figure 1.3: left panel: duration distribution of short-long GRBs as observed by BATSE (Kouveliotou et al. 1993); right panel: distribution of BATSE GRBs on the sky, color coded by the measured fluence of the burst (Briggs et al. 1996).

populations depends on the detector in use (e.g. Horváth et al. 2010, Bromberg et al. 2013).

Sometimes the event is a single burst, usually described as a fast rise exponential decay (FRED) (Norris et al. 1996):

$$N(t) = \begin{cases} Ae^{-\left(\frac{|t-t_0|}{\tau_r}\right)^p} & t < t_0 \\ Ae^{-\left(\frac{|t-t_0|}{\tau_d}\right)^p} & t \geq t_0 \end{cases} \quad (1.1)$$

where $N(t)$ is the number of counts/s detected, t_0 is the peak time, A the peak rate, τ_r , τ_d are the rise ($t < t_0$) and decay ($t > t_0$) time constants, respectively, p is a measure of peak sharpness. More often, GRBs show different rises and decays and there are quiescent episodes during a burst. The distribution of the separation times between pulses seems to satisfy a lognormal distribution (e.g. McBreen et al. 1994, Nakar et al. 2002), even if it is not possible to reject an exponential case, so a memoryless process (Guidorzi et al. 2015, Baldeschi and Guidorzi 2015).

The duration of a single peak can be so short to last few milliseconds. This places stringent limits on the size of the GRB source, since signal crossing the region cannot travel faster than light: for a duration ΔT of 1 ms, for example, we can find $c\Delta T = 300\text{km}$. We will focus on this subject in the next Chapter.

Moreover, lightcurves (LCs) vary with energy band:

- a. in the keV - MeV regime, for many L-GRBs, we can observe that pulses with a lower energy systematically lagged behind those with a high energy (Norris et al. 2005); S-GRBs do not show significant spectral lags (Norris and Bonnell 2006).
- b. pulses tend to be narrower in harder bands, and the width w of individual pulses can be described as a function of energy E : $w(E) \propto E^{-\alpha}$ with $\alpha \sim 0.35$ – 0.45 (Fenimore et al. 1995, Norris et al. 1996, 2005).

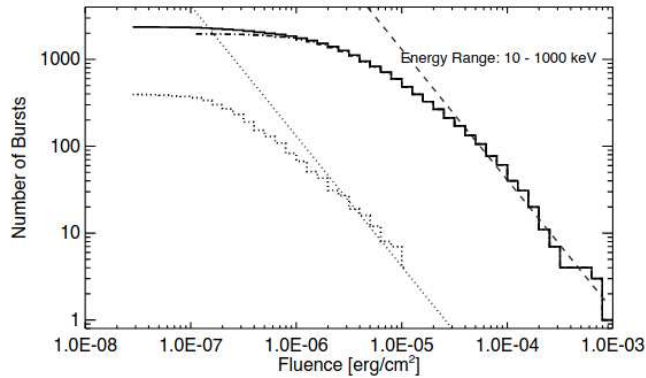


Figure 1.4: Integral distribution of GRB fluence in 10-1000 keV energy ranges from FERMI GBM gamma-ray burst catalog. Distributions are shown for the total sample (solid), short GRBs (dots) and long GRBs (dash-dotted), using $T_{90} = 2$ s as the distinguishing criterion. In each plot a power law with a slope of $-3/2$ (dashed) is drawn to guide the eye.

T_{90} distribution shown in Fig. 1.3, left panel, regards a time measurement defined in the observer frame, not in the rest frame of the burst, where it should last $T_{90}/(1+z)$. Actually, there are two main effects that contribute to mask the impact of cosmic dilation: (i) for a given observer energy passband, further GRBs are observed in a rest-frame harder band, which implies narrower temporal structures, according to the narrowing of pulses with energy, as described in the previous paragraph; (ii) the signal-to-noise ratio (hereafter, S/N) of a LC decreases with increasing z , so only the brightest portion of the LC can be detected (Kocevski and Petrosian 2013). This means that Fig. 1.3, left panel distribution can be mostly considered as a rest frame one.

1.3 Isotropic distribution

The right panel of Figure 1.3 shows the isotropic distribution as found with BATSE (Briggs et al., 1996). This distribution can be understood assuming a GRB cosmological origin, or supposing bursts located at short distances, a few hundred pc, within the thin disk of the Milky Way. If the visibility horizon was of this scale, then we would view an isotropic distribution. GRBs could have a Galactic origin also if we think that neutron stars can receive a natal kick that could move them into a corona around the Galaxy (Levan, 2018). The solution to the debate about Galactic/cosmological origin had an initial direction to a cosmological answer through the study of the integral distribution of GRB fluence, and was finally solved through redshift measurements. In an Euclidean and homogeneous universe, in fact, we expect a number N of GRB with fixed energy E having a fluence higher than a specific value ϕ , proportional to the corresponding accessible volume:

$$N(> \phi) \propto V \propto D^3 \propto \phi^{-3/2}, \quad (1.2)$$

where D is the maximum distance beyond which GRBs with E have a fluence ϕ lower than the instrumental sensitivity. In Equation (1.2) we used the scaling of

fluence E with distance, $\phi \propto D^{-2}$ ($\phi = E/4\pi D^2$). The resulting scaling of $N(> \phi)$ with ϕ is the same for all values of E , so integrating over all possible values of E , the $-3/2$ scaling at large values of ϕ does not change.

Instead we observe, for low fluence values (populated also by high- z GRBs), a deviation of $N(> \phi)$ from $\phi^{-3/2}$ is observed (Fig. 1.4, von Kienlin et al. 2014). A cosmological population can account for this:

- photons in the GRB rest frame are harder than in observer frame, especially at high z ; harder photons are fewer because of the declining photon spectrum of GRBs with energy;
- the number of photons in a fixed time interval decreases with distance due to the cosmic dilation, so the triggering logic cannot be as effective as for nearby sources;
- also the observed GRB rate decreases with cosmic dilation: in fact, the same given number of GRBs is observed within a time interval stretched by a factor $(1 + z)$.

The solution of the mystery about the GRB origin started with the discovery by Italian-Dutch satellite BeppoSAX (Boella et al. 1997) of the X-ray and optical counterpart of the GRB event occurred on 28th February 1997 (GRB970228). A long burst was detected by the gamma ray detectors. At the same time, one of the two X-ray Wide Field Cameras on board of BeppoSAX showed a counting excess and allowed a burst localisation with an error radius of ~ 10 arcmin. The location was followed up by narrow-field instruments onboard BeppoSAX (Costa et al., 1997, Frontera, 2019), and from the William Herschel Telescope on La Palma (van Paradijs et al., 1997). Both X-ray and optical observations were revisited several days later and revealed a fading source: it was the first detection of a GRB afterglow (see Fig. 1.5). This afterglow allowed to pinpoint the source, detect the host galaxy and, after 4 years, it was also possible to measure GRB 970228 redshift ($z = 0.695$, Bloom et al., 2001). Other redshifts were already obtained by the time the redshift of GRB 970228 was found: this allowed to establish that *GRBs are huge explosions in galaxies at cosmological distances*.

1.4 Released energy

It is common practice to use the quantity E_{iso} to measure the gamma-ray released energy of GRBs: it is the energy that a burst would have emitted assuming isotropy. It is calculated as:

$$E_{iso} = \phi_{\gamma} \frac{4\pi d_L^2}{1+z}, \quad (1.3)$$

where ϕ_{γ} is the measured fluence (which depends from the energy range), d_L is the luminosity distance to the burst and z is the redshift. The factor $(1+z)$ is due to the fact that to have fluence we are time integrating on the flux in the observer frame: dividing by $(1+z)$ correctly places it back in the emitting frame, along with the fact that the definition of luminosity distance refers to luminosity, so energy per unit time.

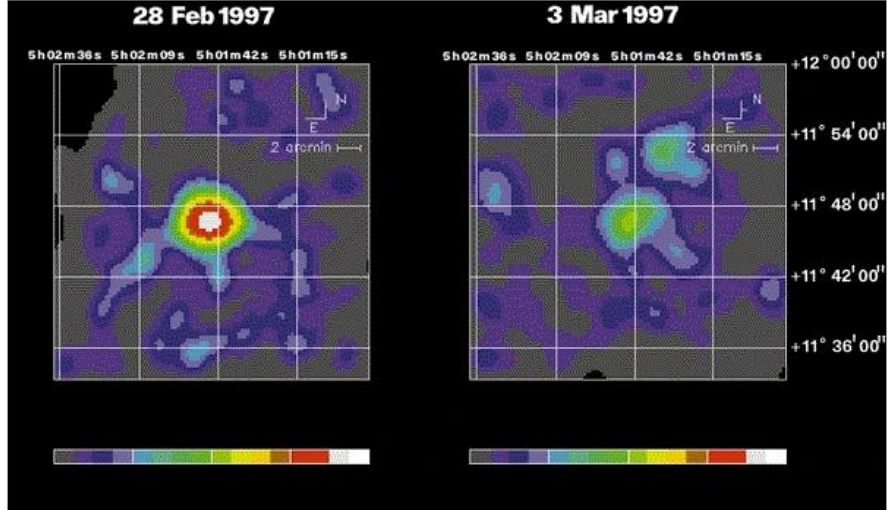


Figure 1.5: BeppoSAX images of the discovery of the X-ray afterglow: the first and second Target of Opportunity observations (TOO1 and TOO2, respectively). White corresponds to 31 counts per pixel², green to 6 counts per pixel² and grey to a background of 0–1 counts per pixel². Taking into account the correction for the number of telescopes (one in TOO1 and three in TOO2) and the vignetting in TOO1 due to off-axis pointing, the source faded by a factor of 20 in three days. The probability that the source detected during the second pointing is coincident by chance with the position of the first is of the order of $1 \cdot 10^{-3}$

At the typical redshift of GRBs, we have $10^{52} < E_{iso}/\text{erg} < 10^{55}$. These *energies are extreme*: with an efficiency factor of $\epsilon \sim 0.1$, they are equivalent of $m = E_{iso}/\epsilon c^2 \sim M_{\odot}$. This is extremely challenging for any models. The solution lies in the beamed nature of GRBs: because of the beaming, GRBs illuminate only a small part of the sky; if θ_j is the half opening angle of the jet in radians, the true energy is then, approximately, $E_{\text{true}} = \frac{\theta_j^2}{2} E_{iso}$. The impact of $\frac{\theta_j^2}{2}$ factor is significant, since $\sim 5^\circ$ jets imply, for example, a change in the total energy by a factor of 250.

1.5 Energy spectra

GRB spectra are characterised by a non thermal shape, that can be fit with a smoothly-joined broken power law known as the “Band-function”:

$$N(E) = \begin{cases} A \left(\frac{E}{100\text{keV}}\right)^{\alpha} e^{-\frac{E}{E_0}}, & E < (\alpha - \beta)E_0 \\ A \left[\frac{(\alpha - \beta)E_0}{100\text{keV}}\right]^{\alpha - \beta} e^{\beta - \alpha} \left(\frac{E}{100\text{keV}}\right)^{\beta}, & E \geq (\alpha - \beta)E_0, \end{cases} \quad (1.4)$$

where A is a constant, $N(E)dE$ is the number of photons with energy between E and $E + dE$, α and β (both negative) are the photon spectral indices below and above the break energy E_0 . The flux density spectrum (F_{ν}) usually used in low-energy (optical, IR, and radio) astronomy corresponds to $EN(E)$, also known as energy spectrum, and the spectral energy distribution corresponds to $E^2N(E)$ or νF_{ν} . The peak of the $E^2N(E)$ spectrum is called “peak energy”, denoted E_p , given

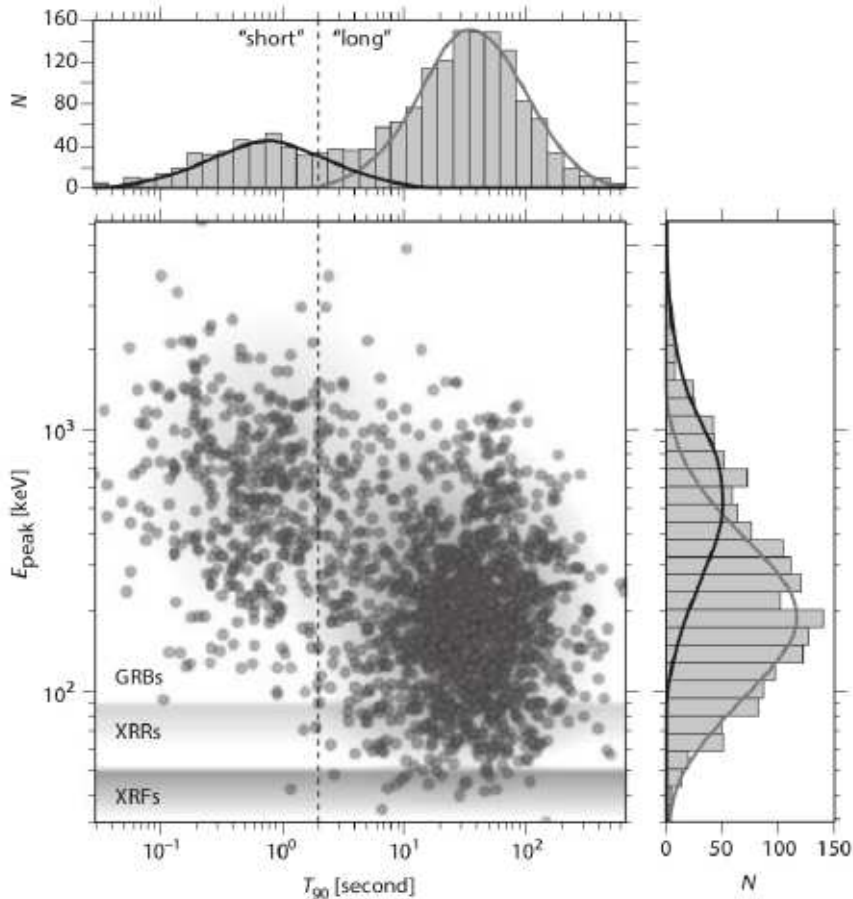


Figure 1.6: The spectral-duration distribution of GRBs, as seen by BATSE; it shows the bimodal GRB distribution in terms of T_{90} and spectral hardness, evaluated through the peak energy. Histograms show the number of events in appropriate duration and energy bin. Two different distributions can be distinguished, even if there is a significant overlap between them. Figure from Bloom, 2011.

by $E_p = (2 + \alpha)E_0$. Typical values are $-1.5 \leq \alpha \leq -0.5$ and $-2.5 \leq \beta < -2$ (e.g. Preece et al. 2000, (Zhang 2011, Nava et al. 2013); typical peak energies E_p range between several keV and a few MeV (e.g. Bošnjak et al. 2014). In a time-resolved analysis, these parameters evolve during the burst.

1.6 Spectral-duration distribution

There is an interesting relation between a GRB hardness and its duration. The hardness is usually defined as a ratio between the total counts in 2 energy ranges; you can also study spectral GRBs properties through the peak energy E_p in $E^2N(E)$ spectrum (Bloom, 2011). In Fig. 1.6 it is quiet clear the evidence of a bimodal distribution in the observer-frame T_{90} /hardness ratio space, where the spectral hardness is evaluated through the peak energy E_p in $E^2N(E)$ spectrum (Bloom, 2011); it show a rough separation between S-GRBs) and L-GRBs. *L-GRBs tend to have a softer spectrum than S-GRBs.*

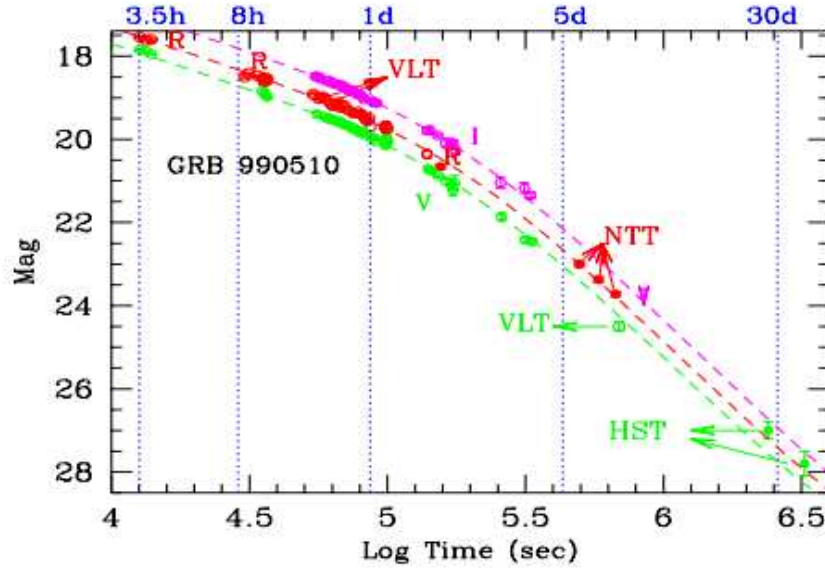


Figure 1.7: Light curves in different optical bands of GRB 990510. Note that the same curve fits the light curve at different frequencies: the break appears achromatic. Figure from Ghisellini, 2001

1.7 Achromatic (jet) break

On 10th May 1999, one of the two Wide Field Cameras (WFCs) aboard BeppoSAX detected and localised the prompt X-ray emission of GRB 990510, whose γ -ray was simultaneously detected by the Gamma-Ray Burst Monitor (GRBM) aboard the same spacecraft.

Extensive follow-up observations were conducted across various wavelengths, which led to the discovery of the X-ray and optical afterglow. During the analysis of the multi-wavelength light curves, *it was observed a simultaneous break in the light curves across different wavelengths*, the so called "achromatic jet break" (Harrison et al., 1999). The achromatic jet break in GRB990510 (see Fig. 1.7) suggests that a common physical process was responsible for the observed change in the emission across all observed wavelengths. An interpretation of this feature, linked with the presence of jet in GRB, is presented in Section 1.10.

1.8 Fireball Shock model

In the previous chapter we described some characteristics emerging from GRB observations that need to be explained by any theoretical model:

- a. burst energies are extremely challenging, and are emitted by a really compact region (see Section 1.2 and Section 1.4);
- b. GRBs show a non thermal spectra (Section 1.5);
- c. GRBs have a cosmological origin (Section 1.3);
- d. GRBs light curves show erratic time variability involving a range of timescales from ~ 10 ms to several seconds (Section 1.2);
- e. GRBs light curves show an achromatic break (Section 1.7);
- f. there exist (at least) two different GRBs families (Section 1.2 and Section 1.6).

These features led to the development of the fireball shock model (e.g., Rees and Meszaros 1994): a plasma that adiabatically would expand and cool, as it converts its internal into bulk kinetic energy. High energy density and a non-thermal spectrum can be understood assuming a relativistic expansion from the source: this reduces the photon energy in the frame by a factor of Γ^{-1} , decreasing the probability of photons producing e^\pm pairs, and thus justifying the presence of a non-thermal spectrum. The relativistic expansion brings to a new determination of the size of the emitting region, as it will be explained in Section 1.9. Driving such a powerful outflow is possible if the initial explosion energy is very high and the outflow has a small baryon load. Since GRB light curves show significant variability, the source should radiate not with constant, but with variable rate. To this aim, we can imagine the Lorentz factor of material emitted at different times during the explosion to vary as well. In this way the ejecta emitted at different times will interact. These shocks can create γ rays, the so called "prompt emission". The interaction of the relativistic flow with the surrounding medium is responsible for the much longer-lived emission, the so called "afterglow". Light curves achromatic break can be explained supposing a collimated expanding plasma (see Section 1.10). Finally, since T_{90} distribution includes at least two log-normal components, we can suppose to have (at least) two different kind of progenitor, as it will be explained in 1.12. See Fig. 1.8 for a fireball model schematic view.

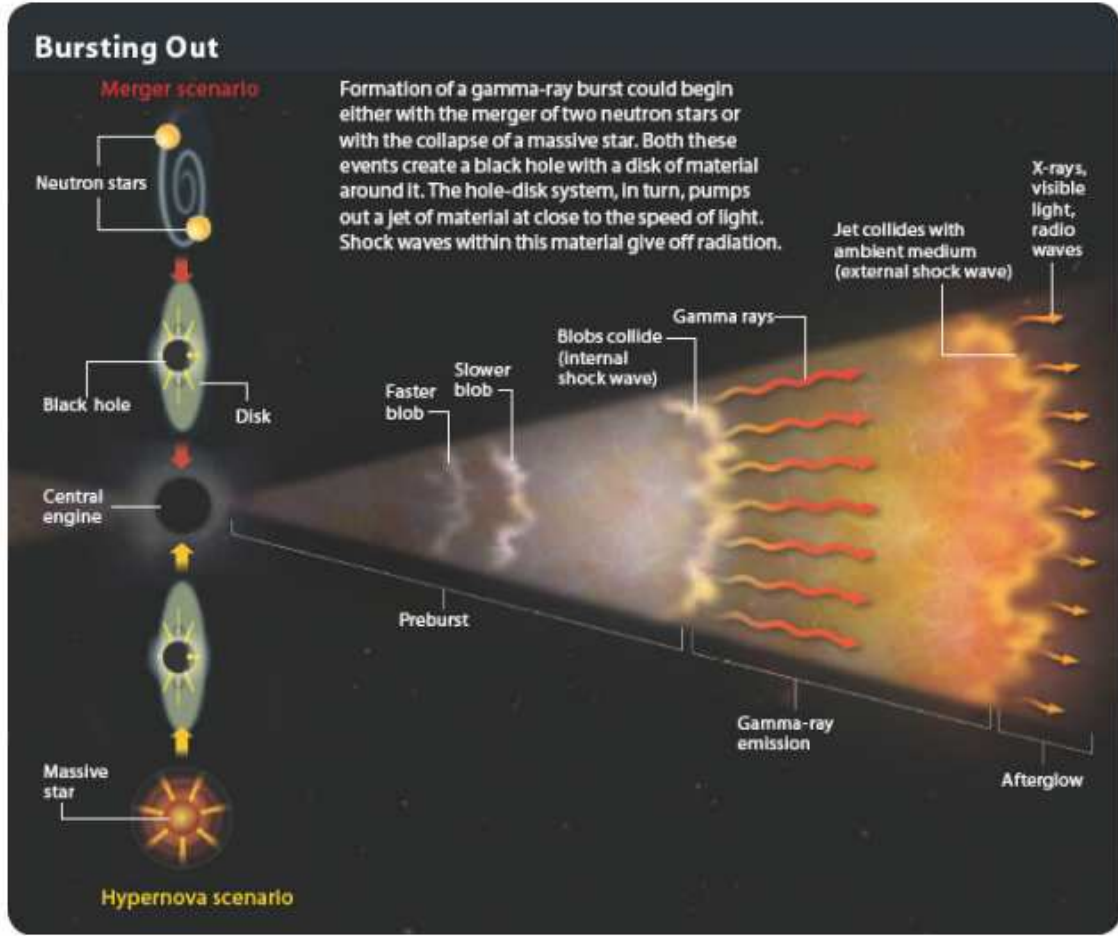


Figure 1.8: Visualization of the fireball model (Gehrels et al., 2004). A merger of compact objects or the explosion of a massive star can give rise to the central engine of a GRB; the release of material from this can occur in the form of shells with different velocities. If a faster shell collides with a slower shell, this generates high-energy emission (prompt GRB); when the ejected material collides with the interstellar medium, the afterglow is instead generated, with emission at various wavelengths, from radio to gamma.

1.9 Compactness problem

As we have previously stated, a small minimum variability timescale would imply an extremely compact emission region, with an high optical depth and strong e^+e^- production, in contradiction with experimental observations showing a non-thermal spectrum with high-energy photons. This apparent inconsistency is known as the “compactness problem” and is solved assuming a relativistic expansion of the source. In the absence of relativistic expansion motion, in fact, the optical depth is:

$$\tau_{\gamma\gamma} = \frac{f_p \sigma_T F D^2}{R_s^2 m_e c^2} = 10^{13} f_p \left(\frac{F}{10^{-7} \text{ erg cm}^{-2}} \right) \left(\frac{D}{3000 \text{ Mpc}} \right)^2 \left(\frac{\Delta T}{10 \text{ ms}} \right)^{-2} \gg 1, \quad (1.5)$$

where:

- f_p is the fraction of photons with energy higher than $m_e c^2$, so able to make

pairs (m_e is the mass of the electron in his rest frame);

- σ_T is Thompson cross section;
- F is the observed fluence;
- D is the luminosity distance;
- R_e is the size of the emitting region.

The fact that $\tau_{\gamma\gamma} \gg 1$ for typical values of F , D , ΔT implies that the source is optically thick, i.e. that photons can hardly escape pair creation. The solution is therefore to assume that the GRBs are produced in a medium that moves with relativistic speed in the direction of the observer with a Lorentz factor Γ .

Consequences of relativistic expansion on f_p

A relativistic outflow implies that photons observed, having energy $E_{obs} = h\nu_{obs}$, where ν_{obs} is the frequency measured in the observer frame, have been Doppler blue-shifted and that their energy at the source is $E_s = h\nu_s \sim h\nu_{obs}/\Gamma$, where ν_s is the frequency measured in the comoving frame of the fluid that emits radiation. Therefore, since at the source the energy of photons is smaller than that observed, also the number of them that can make pairs e^+e^- will be smaller. Consequently, the observed fraction f_p of photons capable to produce pairs is greater than that at the source: specifically, f_p decreases by a factor $\Gamma^{-2(1+\beta)}$ ¹, where β is the high energy Band function parameter we introduced in 1.5.

Consequences of relativistic expansion on R_e

In 1.2 we used the relation $R_e = c\Delta T$ to find the size of the emitting region; we were implicitly assuming that the source was not expanding. If we consider a source expanding relativistically with a Lorentz factor Γ , we will find the relation $R_e = 2\Gamma^2 c\Delta T$. In fact, let us assume a γ -ray emitting shell of radius R_e expanding relativistically and place ourselves in the observer's rest frame. If the observer is

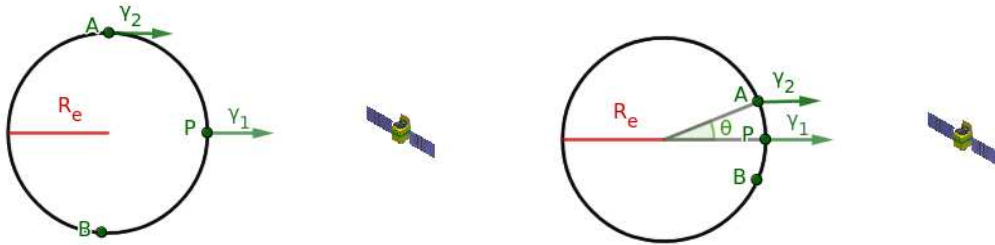


Figure 1.9: Left panel: a shell emitting γ -ray with no expansion. Right panel: the arc \widehat{AB} as seen in the observer rest frame, if the shell is expanding.

¹To find this value, consider the high energy Band function $N(E) = N_0 E^\beta$; the ratio between f_p observed at Earth and f_p at the rest frame is the square of the ratio between $N(E)$ integrated from $\Gamma m_e c^2$ to infinity and from $m_e c^2$ to infinity. In this way one finds $\Gamma^{2(1+\beta)}$; the square is due to the fact that to have pair production two photons are needed.

at a great distance from the shell, we can assume that the photons emitted by its surface in the direction of the observer are parallel one to the other. These photons are all those emitted by the points on the surface of the shell belonging to the arc of the circumference \widehat{AB} facing the observer (see Fig. 1.9). Therefore, the maximum time interval ΔT that separates the arrival of the photons at the observer is the one between the photon γ_1 emitted at the point P and the photon γ_2 emitted at the point A (or B). These points are separated by a distance R_e and therefore $\Delta T = R_e/c$. Now suppose that the surface of the shell is expanding with a relativistic speed and let's move in the observer rest frame: due to the relativistic beaming effect, the observer sees only the photons emitted by the points on the surface belonging to \widehat{AB} , subtended by an angle having half-aperture $\theta \sim 1/\Gamma$. Therefore, in this case, the maximum time interval ΔT that separates the arrival of the photons at the observer is the one between the photon γ_1 emitted at the point P and the photon γ_2 emitted at the point A (or B). These points are separated by a distance $R_e(1 - \cos \theta)$ and therefore it results:

$$\Delta T = \frac{R_e(1 - \cos \theta)}{c} = \frac{R_e[1 - \cos(1/\Gamma)]}{c} \sim \frac{R_e}{2c\Gamma^2}. \quad (1.6)$$

A similar result can be obtained if we consider a point P emitting radiation for a certain time interval and moving towards the observer with a relativistic velocity v (see Fig. 1.10). The first photon emitted by the source is called γ_1 ; then, after P



Figure 1.10: Left panel: Point P of a surface moving towards the observer is emitting γ_1 -ray. Right panel: point P has moved by length R_e towards the observer and is emitting the photon γ_2 .

moved for a distance R_e , it emits γ_2 , the last photon of the event. In the time taken by the source to reach the dimension R_e , i.e. R_e/v , photon γ_1 traveled a distance $R_1 = c(R_e/v)$, while photon γ_2 traveled a distance $R_2 = R_e$ since it is emitted when the source moved by R_e : therefore, the time interval ΔT that separates the arrival of the two photons to the observer is equal to:

$$\Delta T = \frac{R_1 - R_2}{c} = \frac{c(R_e/v) - R_e}{c} = R_e \left(\frac{1}{v} - \frac{1}{c} \right) = \frac{R_e}{v}(1 - \beta) \sim \frac{R_e}{2c\Gamma^2}. \quad (1.7)$$

New optical depth expression

In view of the results obtained in Section 1.9 and Section 1.9, Eq. (1.8) becomes:

$$\tau_{\gamma\gamma} = \frac{10^{13}}{\Gamma^{2-2\beta}} f_p \left(\frac{F}{10^{-7} \text{ erg cm}^{-2}} \right) \left(\frac{D}{3000 \text{ Mpc}} \right)^2 \left(\frac{\Delta T}{10 \text{ ms}} \right)^{-2}; \quad (1.8)$$

considering $\beta \sim 2.5$, we can have $\tau_{\gamma\gamma} \sim 1$ if $\Gamma \sim 100 - 1000$. A proof in favor of the relativistic expansion of the fluid was obtained studying GRB030329: its apparent size increase of ~ 0.3 pc in ~ 50 rest-frame days, suggesting an apparently superluminal expansion speed, that can be understood only invoking a relativistic bulk motion (Taylor et al., 2004).

1.10 Jets

1.10.1 Beaming theory

The hypothesis that the plasma emission is collimated, and therefore that there are jets of material expelled relativistically, arose both to relax the power requirements and to justify the observation of achromatic breaks in the afterglow light curves. To understand this sentence, let us assume that the burst is collimated within a cone of semiaperture θ and that, initially, the bulk Lorentz factor of the fireball is such that $\frac{1}{\Gamma} < \theta$. In this case the observer receive light only from a section of the emitting surface of aperture $1/\Gamma$. This is illustrated in Fig. 1.11.

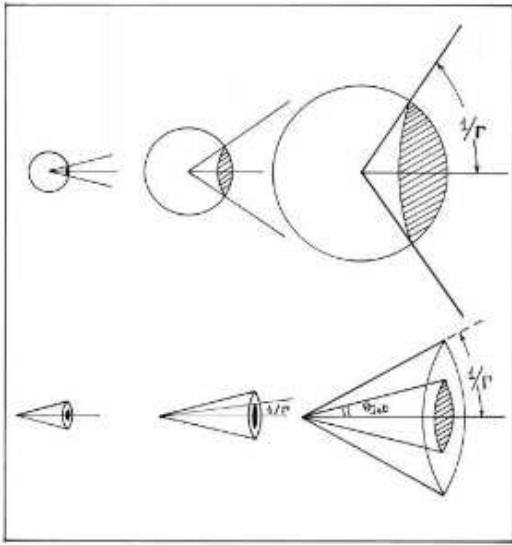


Figure 1.11: Comparison between expansion like a sphere or like a collimated plasma. Figure from Ghisellini, 2001.

Initially, this area increases both because R , the distance from the apex of the cone, increases with time and because Γ decreases. This leads to the estimate of how the received flux varies in time. If the fireball is spherical, this will continue as long as the motion is relativistic. Instead, if the fireball is collimated, there is a time when $1/\Gamma$ becomes comparable to θ . After this time, the observed area will increase only because R increases, while the decrease in velocity, and so in Γ , will not amplify the available surface. Since the rate of increase of the observed emitting area changes, there will be a change in the slope of the light curve: an achromatic break happened (Ghisellini, 2001). The time of the break in the light curve is linked with the degree of collimation, GRB redshift and energy (strong collimation produce an earlier break than mild collimation, Frail et al., 2001); this allow to calculate the jet angle for bursts of known redshifts. Typical collimation angles range from $\sim 4^\circ$ in long GRBs (Frail et al., 2001) to $\sim 16^\circ$ in short GRBs (Fong et al., 2015).

1.10.2 Jet properties

The simplest model of jet is the so called "top-hat" jet, where the energy (and the Lorentz factor) is the same across the jet and drops to zero at sharp edges. Alternatively, the jet can show significant structure: the jet may have a high Lorentz factor when viewed directly on the jet axis, that can decrease rapidly as the viewing angle increases. In particular, mostly two functions were explored initially to describe the jet structure: a power law jet with $dE/d\Omega \propto \theta^{-2}$ (e.g. Lazzati, 2005), supported by numerical simulations (e.g. Morsony et al., 2007) of the jet emerging from its progenitor star envelope, and a Gaussian jet with $dE/d\Omega \propto e^{-(\theta/\theta_c)^2/2}$, where most of the jet energy is contained in two times the core opening angle

θ_c (e.g Rossi et al., 2002, Kumar and Granot, 2003). O’Connor et al., 2023).

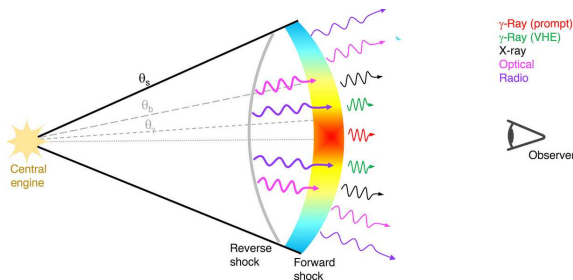


Figure 1.12: Schematic of the structured jet for GRB0606149A. The prompt γ -rays may be radiated from the central narrow core of aperture θ_γ , while the afterglow and very-high energy (VHE) γ -rays could come from a wider angular structure. Figure from O’Connor et al., 2023.

Even more complex structures, such as one composed by a narrow, fast and energetic jet, surrounded by a wider, slower and weaker one, were considered to explain the optical afterglow bumps observed in some GRBs (e.g. Racusin et al., 2008). Also the recent and exceptionally bright GRB 221009A has been interpreted as a two-component jet model (see Fig. 1.12): in this way most of the energy is emitted from the core of the jet, avoiding excessively high GRB energy values (e.g Sato et al., 2023, O’Connor et al., 2023). There is also another possible feature of jets: recent simulations of collapsar (Gottlieb et al., 2022) led us to think about the

presence of oscillating jets; this naturally explain quiescent times in GRB lightcurves: when the jet is not pointing towards us, we have no signal, conversely when it points in our direction, we can see it.

1.11 Central engines

As we learned in Section 1.4, the typical gamma-ray released energy is extreme. These values suggested that the total energy released during the explosion is comparable with the binding energy of a compact object with a stellar mass; since the burst durations are, however, much longer than the free fall time, a viscous process would be needed to account for the observed duration. The most plausible way out is the disk accretion process around a black hole (BH). Alternatively, also the magnetars, being extremely magnetized neutron stars when rotational energy is dissipated on the scale of seconds, may be able to power the GRBs (e.g. Janiuk and Sapountzis, 2018, Zou et al., 2019, Petropoulou et al., 2020, Sharma et al., 2021, Dall’Osso et al., 2023).

1.11.1 Black hole central engines

A black hole central engine can form directly in the core collapse of a massive star, or following the merger of two neutron stars, when the mass of the remnant exceeds the maximum mass of a neutron star (Levan, 2018). Once the BH is formed, the most promising way to extract energy is through the accretion disk. The exact process for energy extraction remains uncertain. One of the possibilities is that GRB is given by neutrino-antineutrino annihilation whose wind originates in the hot disk. Indeed, since the newly formed black hole grows by several solar masses on a time-scale of seconds, the accretion rate is extreme; under these conditions, the accretion disk is a powerful source of neutrinos (Popham et al., 1999, Birkel et al., 2007, Leng and Giannios, 2014). A fraction of these neutrinos annihilate into e^\pm pairs, producing the fireball that powers the GRB. In fact, despite the low interaction rate of neutrinos

to terrestrial detectors, the cross section for weak interactions scales as the square of temperature, so it is possible to have a consistent amount of energy deposited via annihilation (Levan, 2018). Alternatively, the GRB jet (see Section 1.10) may be generated through electromagnetic effect, via the so-called Blandford-Znajec effect (Blandford and Znajec, 1977, Meszaros and Rees, 1997): the interaction of the accretion disk magnetic fields with the BH leads to a slowdown of the BH; the rotational energy of the BH is then converted into jet energy.

1.11.2 Magnetar central engines

An alternative to black hole accretion model is that the GRB energy is provided by a magnetar, a highly magnetic neutron star ($B > 10^{14}\text{G}$) with a very short spin period ($\sim 1\text{ ms}$) (Duncan and Thompson, 1992). Its spin-down and neutrino emission can power a GRB (e.g. Duncan and Thompson, 1992, Usov, 1992, Thompson, 1994, Metzger et al., 2011, Dall’Osso et al., 2023). In fact, let us consider the rotational energy $E_{rot} = \frac{1}{2}I\omega^2$, where ω is the angular frequency and $I = \frac{2}{5}mr^2$ is the moment of inertia for the sphere of mass m and radius r ; assuming that magnetars are born with a period of $\sim 1\text{ ms}$, they lose approximately 10^{52} erg of energy since their formation. If this energy can be extracted rapidly (over a few seconds), then it could power GRBs. The rate of energy loss is given by:

$$\frac{dE_{rot}}{dt} = I\omega \frac{d\omega}{dt} = -\frac{4\pi^2 I}{P^3} \frac{dP}{dt}. \quad (1.9)$$

To maximize the energy deposition rate is necessary a high spin-down rate $\frac{dP}{dt}$ and a small period P (the short period is also required to carry the total energy necessary to power a GRB). Since the dipole field B is proportional to $\sqrt{P \frac{dP}{dt}}$ (e.g. Cordes, 1986), the requirement of spin-down within a few hundred seconds and an initial period of milliseconds also fixes the possible range of magnetic fields, which are typically $B \sim 10^{15}\text{ G}$.

1.12 Progenitors

The discovery of two populations in T_{90} distribution and in the spectral distribution (Section 1.2 and Section 1.6) suggests that there exist (at least) two different GRBs families, with probably different progenitors. We explore the possible progenitors for L-GRBs and S-GRBs.

1.12.1 Long GRBs

Once afterglows were discovered, it was possible to use them to locate bursts on the sky and identify any underlying source. L-GRBs appear to belong to star-forming host galaxies (Levan, 2018); also, low metallicity environments appear to play a role in the formation of L-GRBs (Schneider et al., 2022). Furthermore, L-GRBs seem to be much more concentrated on the brighter regions of their host galaxies (which corresponds to regions with high star formation) (Fruchter et al., 2006, Larsson et al., 2007). Formerly Woosley, 1993 hypothesized that GRBs could be due to star collapsar. The observations of star-forming galaxies led again to wonder if in

particular L-GRBs can be associated with the core collapse of massive stars, and hence with supernovae (SNe), which can only be found where star formation is ongoing. The answer arrived in May 1988, with GRB 980425; observations of the burst few days after the trigger revealed a rising supernova, named SN 1998bw (Galama et al., 1998). This SN showed no signs of either hydrogen or helium emission lines, and had broad spectral lines: it was a so-called SN Ic-BL, with an high expansion velocity (~ 30000 km/s) (Cano et al., 2017). Given this discovery, efforts were put to search for SNe in other GRBs: in the following years, essentially all GRB supernovae found are of Type Ic, and almost all exhibit broad lines (Levan, 2018). The easiest and most popular way to explain the connection between L-GRBs and Type-Ic SNe is the collapsar model, firstly developed by Woosley. The model consisted in the creation of a black hole with a surrounding accretion disk as central engine of the GRB (see Section 1.11). The progenitor is expected to be hydrogen-poor, like a Wolf-Rayet star (Zhang et al., 2004, Langer et al., 2010, Levan, 2018). They are very massive stars ($> 20M_{\odot}$), that lose much of their mass (hydrogen and sometimes helium envelope) to strong stellar winds. They end their lives as compact stars with masses of $\sim 10M_{\odot}$. One way to obtain an estimate of the mass of the progenitor was explored by Fruchter et al. and Larsson et al., who studied the distribution of L-GRBs and core collapse supernovae (cc SN) upon their host galaxies and found L-GRBs are much more concentrated on their host galaxy light than cc SN. This differing distribution reflects different progenitor masses for L-GRBs and cc SN. They found GRBs are likely to arise from stars with initial masses $> 20M_{\odot}$, in agreement with the Wolf-Rayet model hypothesis.

Two GRBs discovered in 2006 with $T_{90} > 2s$ challenged this picture: GRB 060505 and GRB 060614. Despite they are both low-redshift events ($z = 0.089$ and 0.125 , respectively), i.e. sufficient to enable a typical SN Ic-BL identification, there is no sign of any SN emission. This can be understood only either supposing a supernova up to 100 times fainter than SN 198bw (Della Valle et al., 2006, Fynbo et al., 2006, Gal-Yam et al., 2006), or assuming a different progenitor. For example, they may arise from binary mergers, as suggested for S-GRBs (see 1.12.2, "Short GRBs" subsection). In particular, GRB 060614 seems to belong to a different class of GRBs: short bursts with extended emission (SEE-GRBs). The peak luminosity and the spectral lag of its initial spike, in fact, are consistent with that of short GRBs, as shown in Fig. 1.13 (Gehrels et al., 2006), despite it lasts longer than 100 s. Moreover, this burst seems to be associated with a kilonova emission (Yang et al., 2015, Zhu et al., 2022, see 1.12.2, "Short GRBs" and "Kilonovae" subsection).

Finally we emphasize that star-formation galaxies where L-GRBs take place also host significant numbers of young rapidly spinning pulsars that might in principle produce bursts (1.11). It is indeed remarkable that these bursts are now being strongly considered as one of the main potential sources for fast radio bursts (FRBs; Lorimer et al., 2007, Thornton et al., 2013), which may have some connections with GRBs (Metzger et al., 2017, Li et al., 2021).

1.12.2 Short GRBs

Until 2005, only L-GRB afterglows were detected. On 2005 May 9, Swift caught the very faint X-ray afterglow of the short GRB 050509B (Gehrels et al., 2006);

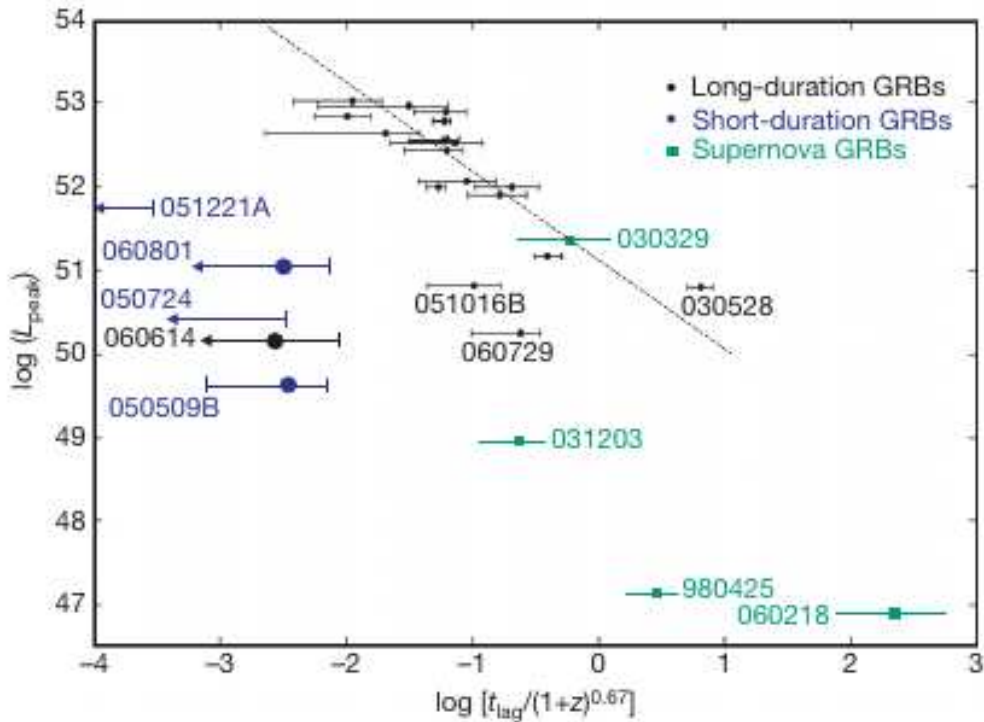


Figure 1.13: Peak luminosity as a function of spectral lag; it shows GRB 060614 in the region of short-duration GRBs. The lags and peak luminosities are corrected to the source frame of the GRB. The lags are defined as the difference in time between light curve structures in the 50–100 keV and 15–25 keV channels. The dashed line shows the lag–luminosity correlation for L-GRBs. Outliers are bursts with unusual properties: GRB 060729, that has an extremely long-lived afterglow and GRB 051016B has extremely soft prompt emission. Figure from Gehrels et al., 2006.

this allowed to localize the burst close to a massive elliptical galaxy with no signs of star formation, at $z = 0.225$ (Bloom et al., 2006). Moreover, deep observations failed to find any evidence of SN related with GRB 050509B (Hjorth et al., 2005). Subsequent observations of S-GRBs and their host galaxies allowed to provide a very different picture from L-GRBs events:

- E_{iso} of S-GRBs is on average 2 orders of magnitude lower than L-GRBs one, with a peak around 10^{51} erg; since the opening angles distribution of S-GRBs is similar to L-GRBs one, typical S-GRBs energy is almost a factor of 100 fainter than that of L-GRBs (Fong et al., 2015);
- S-GRBs have median redshift of $z \sim 0.5$, while for L-GRBs $z \sim 2.4$ (D’Avanzo, 2015, Burrows et al., 2008);
- some S-GRBs (or SEE-GRBs) have host galaxies that are elliptical (like GRB 050509B) or early-type, with little star formation (Gehrels et al., 2005, Barthelmy et al., 2005, others occur in star-forming galaxies (Fox et al., 2005, Fong et al., 2010)

- S-GRBs are well scattered within their host galaxies, often lying off the stellar light, as we can see in Fig. 1.14 (Fong et al., 2013).

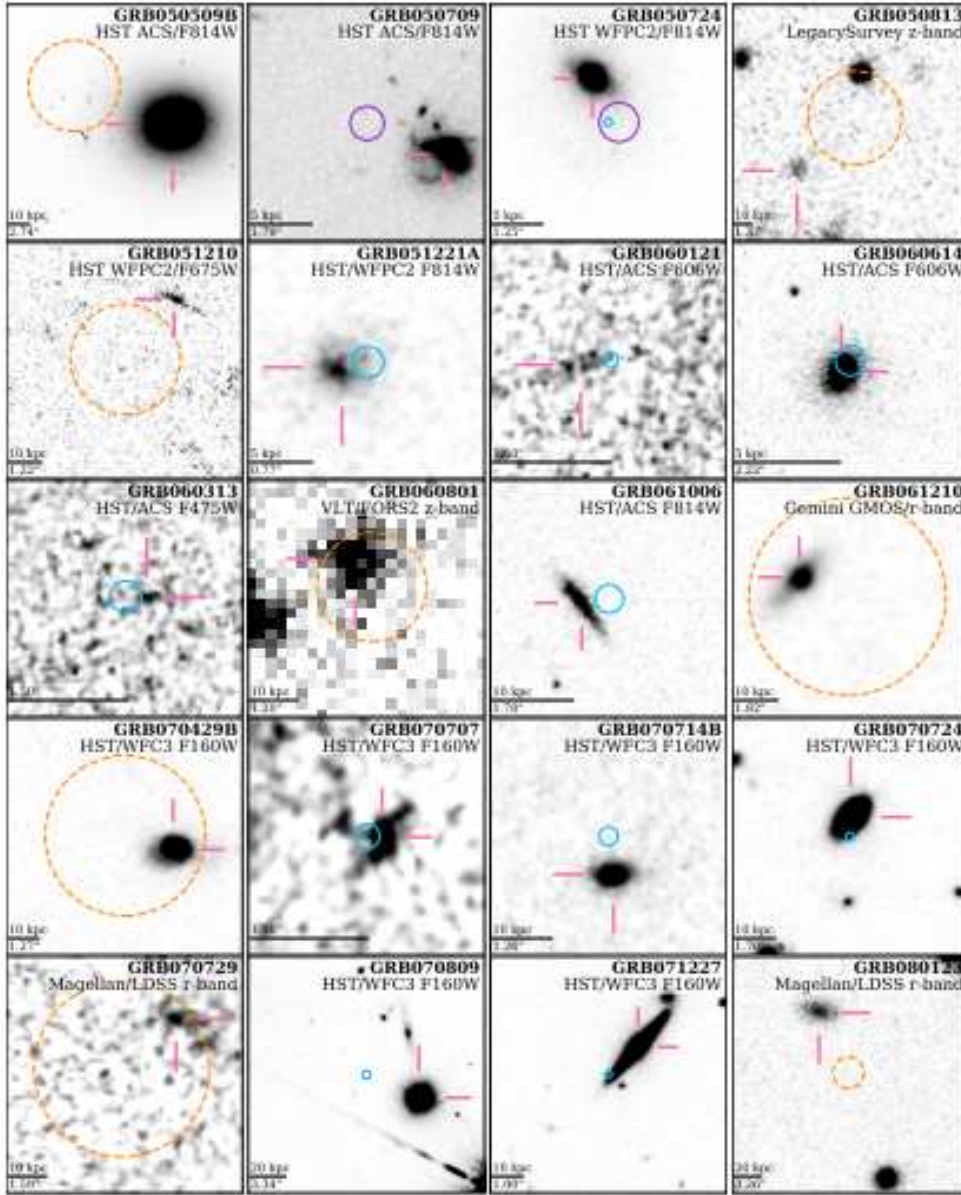


Figure 1.14: Examples of S-GRBs host galaxies and their position relative to the burst. In each panel, the most precise afterglow localization(s) for each burst is/are plotted (XRT 90%: orange dashed, optical 1σ : blue, Chandra or VLA 1σ : purple); the putative host galaxy is denoted by the pink cross-hairs. Figure from Fong et al., 2022.

The most reliable explanation for these features suggests that S-GRBs stem from a binary system comprising either two neutron stars or a neutron star and a black hole (Goodman, 1986, Narayan et al., 1992). In fact:

- according to the internal shock model (e.g. Piran, 2004), the duration of the event is substantially a direct measure of the time interval during which the powering engine is active. Simulations of mergers of two compact objects

showed that the duration of the neutrino-driven wind possibly producing the GRB (Ruffert and Janka, 1999) is less than one second, in accord with S-GRBs. Also, for binary mergers the material the jet must pierce through is less than for a massive star, so shorter duration are rightful.

- As regard the difference in E_{iso} , the longer duration of L-GRBs allows for the buildup of more energy and the production of higher-energy gamma rays. Also, binary systems have less mass and are so generally less energetic compared to the massive stars that are believed to be the progenitors of long GRBs.
- since S-GRBs are less energetic, it is also more challenging to detect them; also, if S-GRBs and L-GRBs have different progenitors, then S-GRBs should be typically localized at lower redshifts with respect to long ones due to the delay time between their formation as binary systems and their merger.
- The merger time from formation of the second object depends on the fourth power of the initial separation between the two objects ($t_{\text{merge}} \propto a^4$, Mandel and de Mink, 2016), so a small difference can dramatically alter the merge time, so we can find S-GRBs arising both from elliptical galaxies and from star-forming system.
- S-GRBs can be found far from their host galaxies, a property which is not observed with long GRBs. This fact can be understood if we think that massive stars have short lifetimes and, therefore, are expected to die close to their birthplace, that is, in dense and dusty environments. On the other hand, compact objects receive kicks (in the range of hundreds of km/s, Arzoumanian et al., 2002) when they are born and are therefore expected to travel far from their birthplaces (Perna and Belczynski, 2002).

One of the strongest evidences of the correlation between S-GRBs and binary mergers is the identification of a kilonova associated with a S-GRB. We discuss this aspect in Section 1.13.

1.13 Kilonovae

1.13.1 Properties

Burbidge et al., 1957 and Cameron, 1957 discovered that approximately 50% of the elements heavier than iron are synthesized through the capture of neutrons onto seed heavy nuclei (like iron) in a dense neutron-rich environment, where the timescale for neutron capture has to be shorter than the β -decay duration. This process is called ‘rapid neutron-capture process’, or r-process. A parameter that influences the realization of r-process is the electron fraction:

$$Y_e = \frac{n_p}{n_p + n_n}, \quad (1.10)$$

where n_p and n_n are the densities of protons and neutrons, respectively. Ordinary stellar material usually has more protons than neutrons ($Y_e \geq 0.5$), while matter with a neutron excess ($Y_e < 0.5$) is typically required for the r-process (Metzger, 2019).

During the merger of two neutron stars or a neutron star with a black hole, mass is lost from the system (ejecta). This material, due to the presence of neutron stars, is generally neutron-rich, so it is a likely place for the creation of neutron-rich elements via the r-process. The subsequent decay of this material produces a thermal transient: a kilonova.

There are different way in which the merger can produce ejecta (e.g. Perego et al., 2014, Shibata and Hotokezaka, 2019, Janiuk and Kaminski, 2014, Metzger, 2019):

- initially, as the neutron stars come together and deform in the merger, some material is expelled in the equatorial plane as tidal tails, the so called dynamical ejecta. Because the typical Y_e value for neutron stars is quite low, 0.05–0.1, also Y_e of the dynamical ejecta would also be low.
- A polar component may also be discharged during this stage. This emission is due to shock heating: as the two compact objects approach each other, intense tidal forces and gravitational interactions cause the material to be compressed heated; the heated material expands and creates an outward-directed flow of ejecta. In such a high temperature environment, the electron-positron pair creation is enhanced; as a result, neutrons easily capture positrons via $n + e^+ \rightarrow p + \bar{\nu}_e$. In this way, the fraction of protons and Y_e are increased ($Y_e \sim 0.3 - 0.4$).
- The excess material that is not expelled during the merger can form an accretion disk around the resulting compact object. The accretion disk is characterized by an internal friction between adjacent layers of the disk material; this causes the disk material to move at different speeds, bringing to a viscous heating. The high temperatures caused by viscous heating can launch outflows and winds from the accretion disk. This component, with a material that is quiet comparable to the dynamic ejecta, has $Y_e \sim 0.1 - 0.3$.
- In the presence of massive neutron star (MNS) as remnant, that is a strong neutrino emitter, the neutrino irradiation to the matter surrounding the MNS could significantly change its composition. This emission, called neutrino-driven wind, can be due also to the accretion disk. The effect is an increase of Y_e : neutrinos can in fact interact with neutrons through: $\nu_e + n \rightarrow p + e^-$. In this way we have $Y_e \sim 0.2 - 0.4$.

Until $Y_e > 0.25$, nucleosynthesis throught is incomplete, we can't have elements heavier than Barium ($Z=56$) and the material is considered as lanthanide-free; if $Y_e \leq 0.25$, we have enough free neutron to have heavier elements, also lanthanide ($57 \leq Z \leq 71$), and the material is called lanthanide-rich. Lanthanide-rich material has a high opacity: these elements have open electron f-shells, which are characterized by a deluge of possible transitions across the optical regions. Optical light in lanthanide-rich ejecta should be essentially extinguished. Rather, we expect to observe a redder transient (Barnes and Kasen, 2013). We present a sketch that summarizes all these properties in Fig. 1.15, where different colors represent the expected wavelengths correlated with different degree of lanthanide richness.

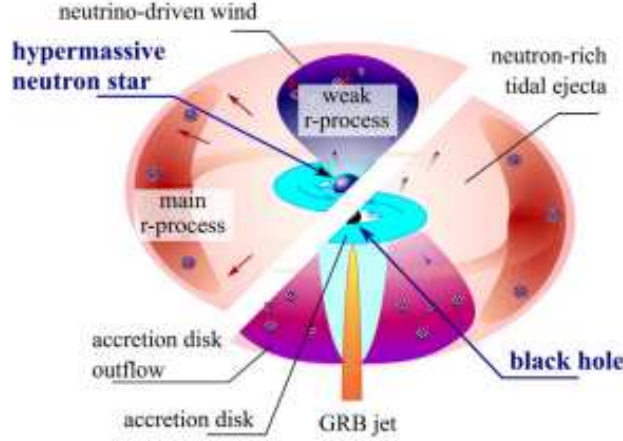


Figure 1.15: A sketch of the merger of two neutron stars, involving either a NS (upper left) or a BH as (lower right) a central object. Different types of ejected matter are represented. Figure from Korobkin et al., 2021.

1.13.2 Main equations

We aim to find the time at which the kilonova emission peaks, and the luminosity value at peak. We consider the merger ejecta of total mass M , which is expanding at a constant mean velocity v , such that its mean radius is $R = vt$ after a time t following the merger. A typical optical depth in the ejecta is $\tau = \rho\kappa R$, where κ is the mass absorption coefficient or opacity (in units of cm^2/g), ρ is the density. Then, the diffusion timescale in the ejecta is:

$$t_{\text{diff}} = \frac{R}{c}\tau = \frac{3M\kappa}{4\pi cR}, \quad (1.11)$$

by adopting $\rho = \frac{M}{\frac{4}{3}\pi R^3}$ (homogeneous ejecta). When the dynamical timescale of the ejecta ($t_{\text{dyn}} = \frac{R}{v} = t$) becomes comparable with the diffusion timescale, photons can escape from the ejecta effectively. From the condition of $t_{\text{dyn}} = t_{\text{diff}}$, the characteristic timescale of the emission can be written as:

$$t_{\text{peak}} = \left(\frac{3\kappa M}{4\pi cv}\right)^{\frac{1}{2}} \sim 2.7 \text{ days} \left(\frac{M}{0.01M_{\odot}}\right)^{\frac{1}{2}} \left(\frac{v}{0.1c}\right)^{-\frac{1}{2}} \left(\frac{\kappa}{1 \text{ cm}^2\text{g}^{-1}}\right)^{\frac{1}{2}}. \quad (1.12)$$

The radioactive decay energy injection rate due to r-process nuclei has a power-law dependence: $\dot{q}(t) \sim 2 \cdot 10^{10} \text{ erg s}^{-1} \text{ g}^{-1} (t/1 \text{ day})^{-1/3}$. By introducing a fraction of energy deposition ϵ , the total energy deposition rate (or the deposition luminosity) is $L = \epsilon M \dot{q}(t)$. In order to find L_{peak} , we calculate $L(t_{\text{peak}})$:

$$\begin{aligned} L_{\text{peak}} &= \epsilon M \dot{q}(t_{\text{peak}}) \\ &\sim 1.3 \cdot 10^{40} \text{ erg s}^{-1} \left(\frac{\epsilon}{0.5}\right)^{\frac{1}{2}} \left(\frac{M}{0.01M_{\odot}}\right)^{0.35} \left(\frac{v}{0.1c}\right)^{0.65} \left(\frac{\kappa}{10 \text{ cm}^2\text{g}^{-1}}\right)^{-0.65}. \end{aligned} \quad (1.13)$$

Typical kilonova peak luminosities are approximately one thousand times brighter than a nova (and 10 or 100 times softer than a SN), this is why the term "kilonova"

was introduced.

Equations 1.12 and 1.13 tell us that both t_{peak} and L_{peak} depend on M , v , κ (Tanaka, 2016, Metzger, 2019). Regarding ejecta mass and velocity, they seem to be strictly related to the merger remnant lifetime, which in turn depends on the binary total mass. As one can see in Fig. 1.16, in fact, if a merger is due to a large total mass binary system², it is supposed to end its life as a BH, with a short lifetime ($\leq 1\text{ms}$, see secondary x-axis for the trend), a low kinetic energy (so a low velocity) and a low mass of the ejecta. Vice versa, a less massive binary merger will end its life as a stable NS, with a virtually infinite lifetime and more massive ejecta. This behavior can be understood by assuming that the longer the collapse time, the larger remnant rotational energy can be transformed in kinetic energy.

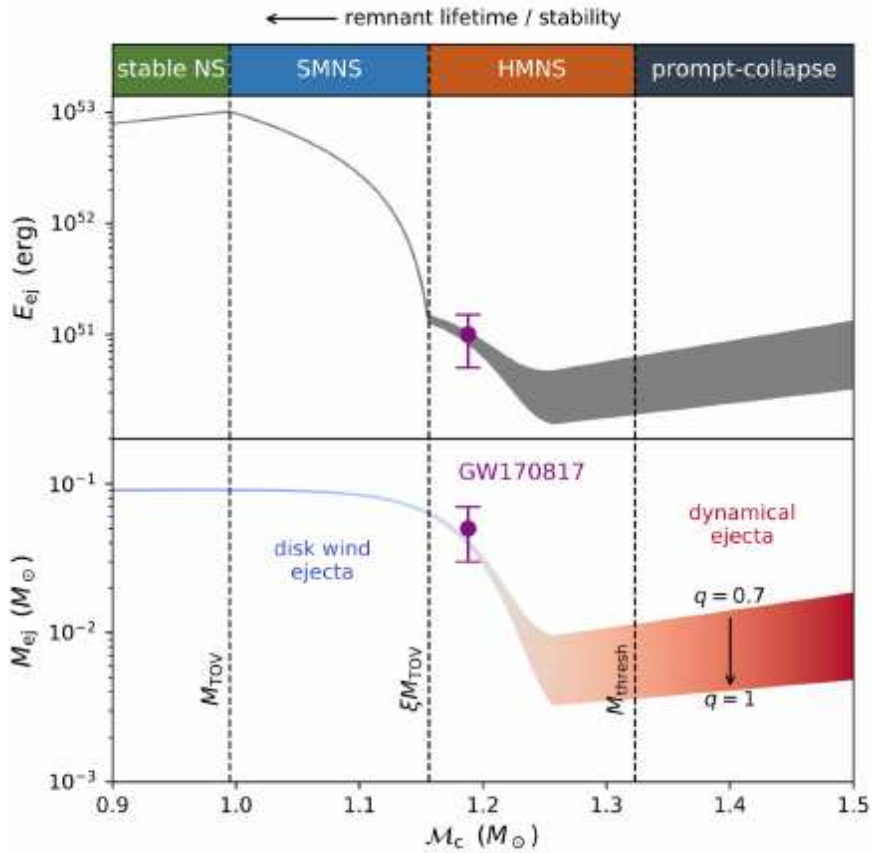


Figure 1.16: Energy and mass of the merger ejecta as a function of the binary chirp mass M_c . Figure from Metzger, 2019.

Figure 1.17 from Tanaka et al., 2020 shows κ as a function of the radiation wavelength for different values of Y_e . As we can see, the opacity decrease with wavelength, so IR photons can more easily escape and contribute to the observed kilonova rather than bluer photons. Also, if we compare κ values referred to lanthanide-rich and poor in the optical band, we have a factor of ~ 50 , which corresponds to a factor of ~ 0.1 in luminosity and a factor of 7 in t_{peak} . The opacity depends not only on

²In Figure 1.16 on the x-axis we have the so called measured chirp mass $M_c = \frac{(M_1 M_2)^{3/5}}{(M_1 + M_2)^{1/5}}$, with M_1 and M_2 masses of the compact objects, considered here as a proxy for the total binary mass.

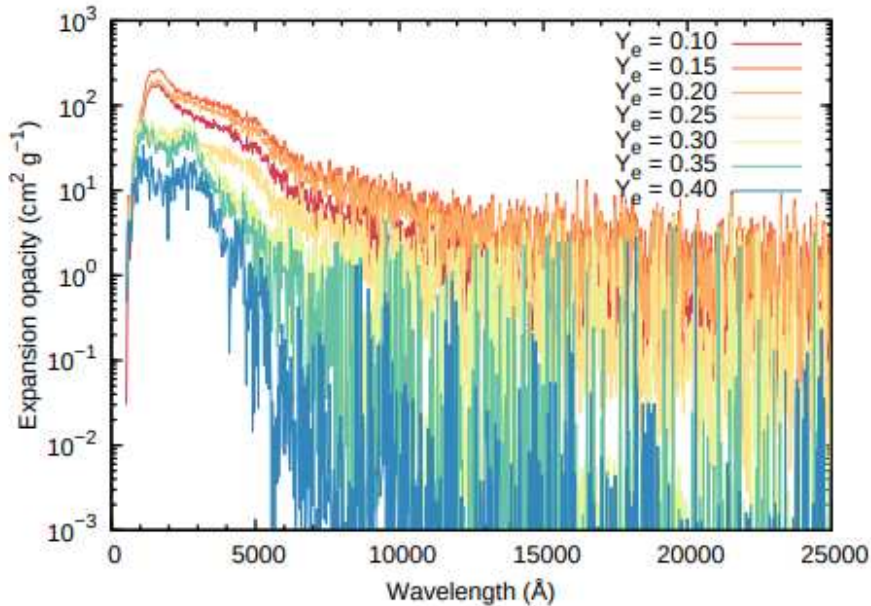


Figure 1.17: Opacity as a function of wavelength for different values of the electron fraction Y_e and for fixed density and temperature. Figure from Tanaka et al., 2020.

elements, but also on the density of the ejecta and on the temperature, so it evolves in time.

1.13.3 Observations

Kilonovae detection is somewhat challenging, due to their faintness. Currently a few events show evidence for kilonova emission. We present the kilonovae that we consider in our study about minimum variability timescale in Chapter 3 and GRB 170817.

GRB 060614

As we remarked in Section 1.12.1, despite its long duration, GRB 060614 peak luminosity and the spectral lag of the initial spike are consistent with that of short GRBs Gehrels et al., 2006, so that it is considered a SEE-GRB. Moderately convincing signatures of kilonovae were uncovered in its light curve, as suggested by Yang et al., 2015, Jin et al., 2015, Tanaka, 2016: in Fig. 1.18, right panel, one can identify a kilonova emerging from GRB 060614 afterglow. Data seem to be reasonably well modeled by a BH-NS merger with a large ejecta mass ($M_{ej} \sim 0.1M_{\odot}$) (Tanaka, 2016).

GRB 070809

GRB 070809 is a S-GRB. The optical component of this burst show a similarity to thermal-like radiation and does not match any afterglow spectrum. It can be interpreted as a blue kilonova, powered by the lanthanide-free material launched during the neutron star merger (Jin et al., 2020).

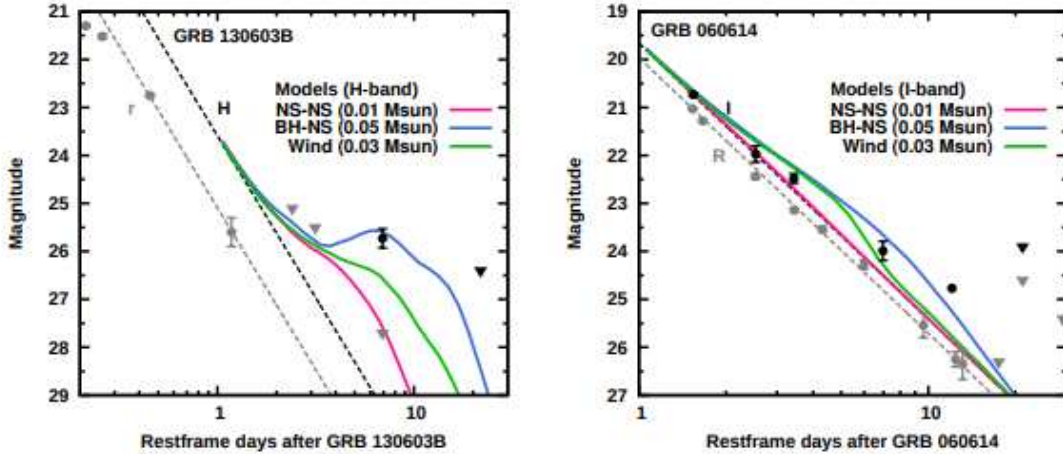


Figure 1.18: Comparison of kilonova models with GRB 130603B (left) and GRB 060614 (right) data. Figure from Tanaka, 2016

GRB 130603B

It was the first event whose light showed clear photometric evidence for a kilonova (the previous kilonovae I described were found only later). GRB 130603B was a short burst at $z = 0.35$ (de Ugarte Postigo et al., 2014). This burst exhibited an optical counterpart that was well monitored from the optical to infrared at early times (Berger et al., 2013, Tanvir et al., 2013). Later observations revealed a color change: ten days after the burst, the source was not detectable in optical light but it was visible in infrared. The infrared light lay above the extrapolation of the afterglow (see Fig. 1.18, left panel) and suggested the presence of a kilonova. The observed brightness of the near-IR excess in GRB 130603B requires a relatively large ejecta mass of $M_{ej} \geq 0.02M_{\odot}$ (Berger et al., 2013, Tanvir et al., 2013).

GRB 160821B

GRB 160821B is a S-GRB. The spectroscopic redshift of the host galaxy is $z = 0.162$, making it one of the lowest redshift S-GRBs identified by Swift. It shows evidence for a late-time excess of optical and near-infrared emission in addition to a complex afterglow: this excess was interpreted as due to a kilonova with dynamical ejecta mass $M_{dyn} = (1.0 \pm 0.6) \cdot 10^{-3}M_{\odot}$ and a post-merger ejecta mass with $M_{pm} = (1.0 \pm 0.6) \cdot 10^{-2}M_{\odot}$ (Lamb et al., 2019).

GRB 170817

On 2017 August 17, Advanced LIGO/Virgo made the first detection (Abbott et al., 2017) of gravitational waves (GWs) from a binary neutron star merger, GW170817; just 1.7 s later there was the detection of a S-GRB by Fermi (Goldstein et al., 2017) and INTEGRAL (Savchenko et al., 2017): GRB 170817A. 11 hr after the GW170817 trigger, an optical counterpart, labelled AT 2017gfo, was discovered in the nearby ($d = 40$ Mpc) galaxy NGC 4993 (Coulter et al., 2017). The ultraviolet, optical, and near-infrared emissions were consistent with being powered by the radioactive decay of nuclei synthesized in the merger ejecta by the r-process (Villar et al., 2017, Watson et al., 2019, Domoto et al., 2021, Kasliwal et al., 2022). This was the first

time one source was detected both in GWs and electromagnetic (EM) radiation, and the first time spectroscopic evidence of a KN was obtained (Chornock et al., 2017, Kasen et al., 2017, Pian et al., 2017, Smartt et al., 2017). One day after the merger, the source was optically bright, but it faded rapidly within days (Arcavi et al., 2017, Cowperthwaite et al., 2017). Meanwhile, the emission in the infrared remained bright for nearly two weeks (Kilpatrick et al., 2017). Kasen et al., 2017 inferred the presence of two distinct components of ejecta, one composed primarily of light (atomic mass number less than 140) and one of heavy (atomic mass number greater than 140) r-process elements. In particular, the observed optical and infrared luminosities implied ejecta masses of $M_{\text{blue}} \sim 0.025M_{\odot}$ and $M_{\text{red}} \sim 0.04M_{\odot}$, respectively, while the spectral analysis indicates velocities of $v_{\text{blue}} \sim 0.3c$ and $v_{\text{red}} \sim 0.1c$.

GRB 211211A

GRB 211211A lasted longer than 50 s and its spectral hardness lies close to the mean of the L-GRB population. The light curve consists of several pulses exhibiting little spectral evolution and lasting for approximately 12 s, followed by a softer emission. While GRB 211211A exhibits similarities to the behavior of previous SEE-GRBs, such as the absence of early spectral changes and subsequent softening, its duration far exceeds those observed in previous cases. It is associated with a kilonova (Troja et al., 2022) sharing luminosity, duration, and color with that of GRB 170817 (Rastinejad et al., 2022). Despite the similarity to the kilonova event GRB 170817A/AT 2017gfo, GRB 211211A long duration led to the possibility that this event may arise from a neutron star-white dwarf (NS-WD) merger (Yang et al., 2022, Zhong et al., 2023).

GRB 230307A

GRB 230307A is a L-GRB ($T_{90} \sim 35s$), with an exceptional fluence (2.951 ± 0.004) $\cdot 10^{-3}$ erg cm^{-2} in the 10-1000 keV band (Dalessi et al., 2023). The measured fluence makes it the second-brightest GRB ever detected Burns et al., 2023. This high luminosity can be due to a highly magnetic progenitor ($\geq 10^{15}$ G), or a rapidly rotating massive neutron star (Dichiara et al., 2023). At 11 days, infrared observations showed a transition from an early blue spectral slope, to a much redder one. This extremely red colour appeared similar to the expectations for a kilonova produced during the merger of a neutron star and another compact object (Levan et al., 2023). Moreover, emission features observed in spectra obtained with JWST are associated with elements obtainable through the r-process, such as, for example, tellurium (Levan et al., 2023, Gillanders et al., 2023). Data fit well with a face-on model with two ejecta components: a dynamical ejecta component with a mass of $0.005M_{\odot}$, an average velocity of $0.25c$ and an average electron fraction $Y_e = 0.15$, and a disk-wind ejecta component with a mass of $0.05M_{\odot}$, an average velocity of $0.1c$ and an average electron fraction $Y_e = 0.3$ (Bulla et al., 2023). Our analysis of the minimum variability time also led us to support the possibility of a merger of compact objects (Camisasca et al., 2023).

1.13.4 Kilonovae polarization

Polarization³ could play a relevant role in the study of KNe properties, especially in understanding the nature and geometry of these astronomical events and their dynamical evolution. The polarization of the KN signal depends on the combination of the polarizing effect due to electron-scattering and the depolarizing effect caused by absorption lines of lanthanide-rich material. For example, assuming a model without jet and schematisable with the presence of a torus of lanthanide-rich material on the merger plane (see Section 1.13.1), linear polarization primarily arises exactly from the asymmetric distribution of lanthanide-rich material in the ejecta: radiation from regions closer to the equatorial plane is typically depolarized by line interactions with lanthanide-rich material, while radiation emerging from higher latitudes is more likely to be polarized by electron-scattering interactions, due to the higher value of Y_e , and lower opacities from lines.

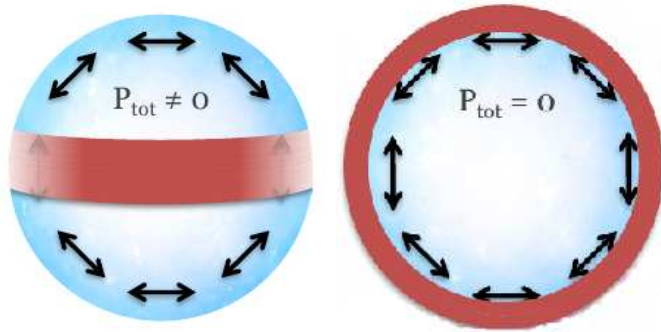


Figure 1.19: Left panel: a KN edge-on view; radiation coming from the equatorial plane is depolarized, due to the absorption in the lanthanide-rich component; radiation crossing lanthanide-poor material is polarized through Thomson electron scattering, mostly in the direction perpendicular to the propagation direction. Q expresses the difference in intensity between the electric field components along the vertical and horizontal direction and U the difference between the component which forms an angle of 45° with the horizontal positive semi-axis and the one which forms an angle of 135° ; it is clear from the picture that for each 45° component there is a 135° one, while it is not the same for vertical and horizontal components. This leads to have $Q \neq 0$ and $U = 0$. Right panel: a KN face-on view; for each vertical component there is an horizontal one, for each 45° there is a 135° one, so both Q and U are null.

reproduce a polarization signal that, after 1.5 days and at $7,000 \text{ \AA}$, peaks at $P = |Q|$

As a consequence, using the standard notation Q and U for the second and third normalized Stokes parameters, in correspondence with an observer placed on the equatorial plane we have $Q \neq 0$ and $U = 0$, so $P = \sqrt{Q^2 + U^2} = |Q|$; for a polar observer, instead, $Q = U = P = 0$ (see Fig. 1.19 for a detailed explanation). The presence of jets and/or a neutrino-driven wind, instead, makes the polarization trend as a function of the angle more complex (see Shrestha et al., 2023) than in a non-jet model.

KN polarization study can bring to a better knowledge of ejected materials and KN geometry. An example resides in simulations of AT 2017gfo by Bulla et al., 2019, realized considering a two-component kilonova. They

³In this part, even if we built this Chapter in such a way that it is easily modifiable for the realization of informative or didactic material, we make the assumption the reader already has a basic knowledge of polarization; in case it is necessary to deepen the subject, for example for an high school audience, we suggest, for an easy introduction about Stokes parameters, the website University of Victoria, Stokes Parameters

$\sim 0.8\%$ for an observer in the equatorial plane and then decreases to smaller and smaller values moving towards the pole. AT 2017gfo intrinsic emission with $P \sim 0.4 - 0.5$ can be understood supposing an observer orientation of the kilonova to within about 65° from the polar direction. This value is less restrictive but consistent with independent estimates from the literature (e.g. Margutti et al., 2017, Pian et al., 2017, Troja et al., 2017, Mandel, 2018).

Chapter 2

Prompt emission detection

The study of prompt emission, whose origin is still much debated, can certainly increase our knowledge about the genesis of GRBs and their properties; moreover, prompt detection is actually the primary way to identify a GRB, although there are possibilities for detecting bursts directly on the ground with the Cherenkov γ -ray detectors, or just detecting the afterglow via wide-field surveys in the x-ray, optical or radio channel. In this chapter I will present the THESEUS mission proposal, designed with the aim of capturing the prompt emission of violent gamma-ray bursts; in particular I will focus on XGIS detectors and I will illustrate my contribution to the characterization of the instrument performance.

2.1 THESEUS

THESEUS (Transient High Energy Sky and Early Universe Surveyor) is a space mission devoted to the study of GRB. It is one of the five mission concepts selected by ESA for a Phase-0 study as M7 candidates; if selected, THESEUS should be launched around 2037. It has been conceived with two main goals:

a. **Exploiting GRBs to investigate the early Universe.**

GRBs are sufficiently luminous to be visible also at high redshift, and they are short-lived, so they have a limited impact on the galaxy and environment around them; this make them good candidate to explore the early Universe. For example, since there is a correlation between L-GRBs and massive stars, studying L-GRBs formation rate at high redshift will make possible to understand star formation rate at high redshift (till the first billion year of the Universe, $z > 6$); also, GRBs discoveries at high z would unveil the bulk of low-luminosity primordial galaxies not accessible by current telescopes.

b. **Providing a great contribution to multi-messenger astrophysics with the observation of the electromagnetic counterparts of gravitational waves and neutrino events.**

THESEUS, for example, would offer substantial and meaningful samples of S-GRBs coincident with gravitational wave observations. This unique

combination would enable us to address essential unresolved inquiries regarding the characteristics of compact binary mergers. We would gain insights into aspects like the effectiveness of forming relativistic jets, the structures of the jets, the properties of electromagnetic emissions from the remnants of mergers, and the significance of NS-NS and NS-BH mergers in the enrichment of r-process elements in the Universe.

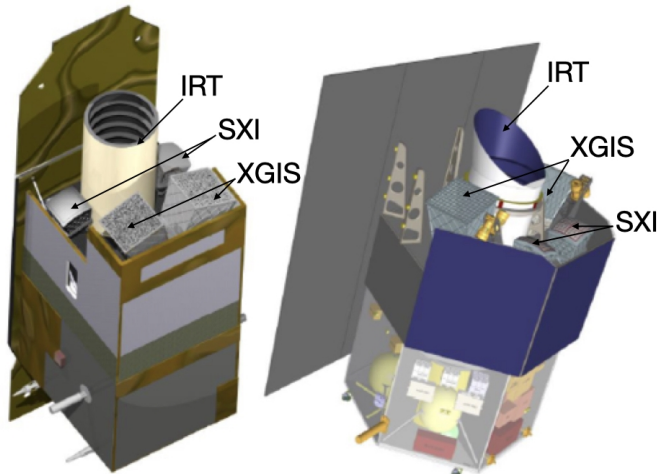


Figure 2.1: Schematic view of the spacecraft design from the industrial study by Airbus Defence and Space (ADS, left) and Thales Alenia Space (TAS, right). Figure from Amati et al., 2021.

To achieve these scientific goals, THESEUS would be equipped with wide-field monitors that operate in the X-ray-to- γ -ray energy range: the Soft X-ray Imager (SXI, 0.3 - 5 keV) and the X and Gamma Imager and Spectrometer (XGIS, 2 keV - 10 MeV). These monitors have the capability to detect and precisely pinpoint GRBs and other transient high-energy sources. Additionally, the wide-field monitors would be supported by a near-infrared telescope (IRT), which would facilitate the characterization of

the identified transients (see Fig. 2.1 for a schematic view of possible THESEUS designs).

The NIR telescope would conduct rapid follow-up observations, thanks to the satellite’s autonomous slewing capabilities. Figure 2.2 shows the predicted improvement in GRB detection at high z thanks to THESEUS (Amati et al., 2021): its performance would be almost two orders of magnitude better with respect to what has been achieved (7 GRBs at $z > 6$) in the last 20 years with past and current GRB detectors (e.g., Swift/BAT, Fermi/GBM, Konus-WIND) combined with intensive follow-up programs with ground small (robotic) and large (e.g., VLT) telescopes (Amati, 2021).

2.1.1 IRT

The IR telescope on board THESEUS has been designed with the main goal of detecting GRB counterparts and measuring their redshift through multiband photometry and moderate resolution spectroscopy. The IRT consists of a 70 cm aperture telescope with an IR camera at its focus, sensitive in the 0.7–1.8 μm range. Five filters (I, Z, Y, J, and H) would be available to acquire images over a field of view (FoV) of 15×15 arcmin², reaching magnitude limits of ~ 21 in 150 s exposures (Mereghetti et al., 2021).

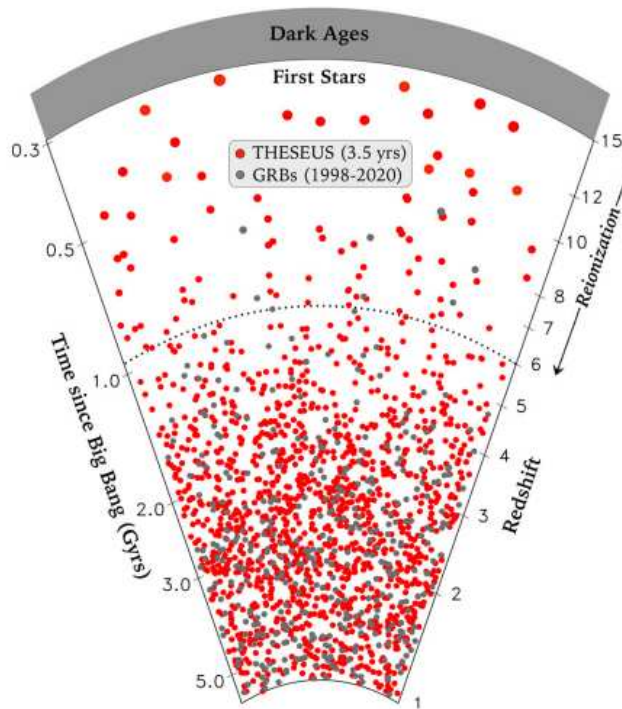


Figure 2.2: THESEUS capability of detecting and identifying high-redshift GRBs, as a function of cosmic age, in 4 years of operations (red dots) compared with what has been achieved in the latest ~ 20 years (gray dots). Figure from Amati et al., 2021.

2.1.2 SXI

The SXI is a focussing X-ray telescope composed of two identical units providing high-sensitivity over a very large field of view thanks to a micro-pore mirror in lobster-eye configuration¹ coupled to wide area detectors (see Fig. 2.3). It would operate in the 0.3–5 keV energy range providing a uniform sensitivity, of the order of few milliCrabs in 1 ks across the whole field of view of $31 \times 61 \text{ deg}^2$. The source location accuracy will be $< 1\text{-}2 \text{ arcmin}$.

One of the main advantages of the lobster-eye optics is that they can focus X-ray photons over a very wide field of view, with uniform efficiency and point spread function, independently of the off-axis angle of the source. The SXI point spread function (PSF) has a characteristic shape consisting of a narrow core produced by the source photons undergoing two reflections in the micro pores (5% of the total) and two cross arms produced by single-reflected photons. The narrow PSF core has a FWHM of 6 arcmin (at 1 keV) across the whole field of view (Mereghetti et al., 2021).

¹The lobster-eye configuration is an optical technique used for focusing high energy rays. It is named after the shape of the eyes of certain lobster species, where a series of micro-pores on the surface of the eye helps to focus light coming from different directions. Similarly, small pores or channels are used to reflect X-rays or γ -rays in the right direction. This configuration allows capturing X-rays coming from various directions and focusing them onto a specific point, providing higher sensitivity and resolution in the acquired images.

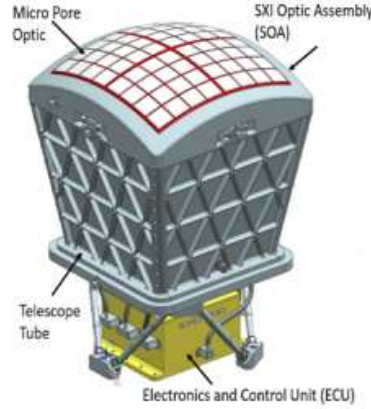


Figure 2.3: SXI module exterior view.

2.1.3 XGIS

XGIS consists of two identical units employing coded masks and position sensitive detection planes, connected through a collimator (see Fig. 2.4).

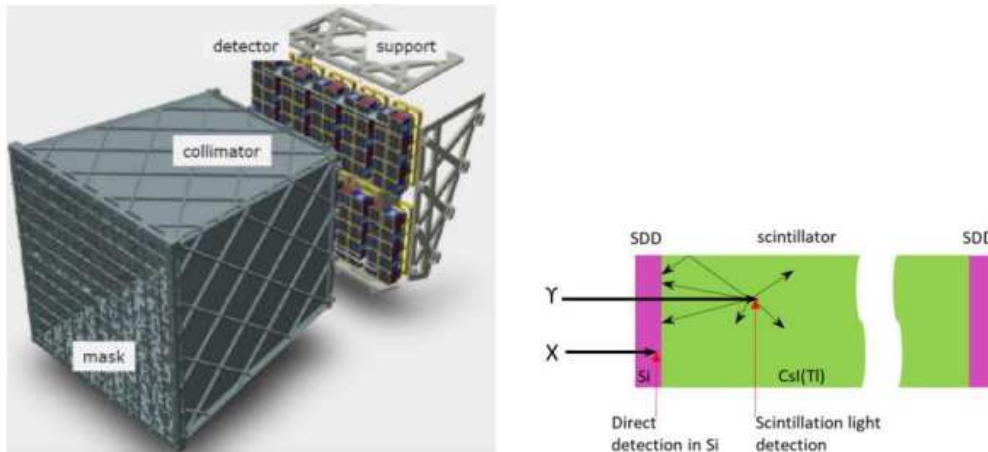


Figure 2.4: Left panel: exploded view of an XGIS camera; right panel: a schematic view of a pixel detector. Figure from Amati et al., 2022.

- The coded mask (1.5 mm thickness) is placed at a distance of 63 cm from the detector; it is made with transparent and high-energies-non-transparent (tungsten) pixel elements; the image reconstruction is based on a correlation procedure between the detected image and a decoding array from the mask pattern. The mask provides imaging capability up to ~ 150 keV over a square field of view of 77×77 deg² for each XGIS unit; the two cameras are misaligned by $\pm 20^\circ$ with respect to SXI and IRT, thus providing a total field FoV of 117×77 deg².
- A collimator mechanically connects the coded mask with the Detector Assembly and is a lateral passive shield for the Imaging System. Above 150 keV, the

mask and the collimator of a XGIS camera become transparent, thus imaging capabilities are lost and FoV is not delimited.

- The XGIS detector plane contains 10×10 Modules arranged side by side. Each Module contains 8×8 pixels (pitch 5 mm). A passive space, one pixel wide, interleaves one Module and the adjacent ones. In this way there are 9 “dead” rows and 9 “dead” columns in the plane. The Module is the basic element of the detector plane; the dedicated electronics can identify, convert in digital word and store all the information of a detected event. Figure 2.4 shows the pixel operation concept. Two Silicon Drift Detector (SDDs) are placed at the two opposite sides of a scintillator CsI(Tl) crystal. Low energy radiation (roughly between 2 and 25–30 keV) is detected in the SDD on the top surface of the Module (the best signal/noise ratio will be achieved with a short shaping time, typically 1 μ s), while harder radiation will reach the scintillator crystal and will be detected in time coincidence in both top and bottom SDD (in this case the signal rise time will be of the order of few μ s, due to the scintillation light characteristic timescale, and the best signal-to-noise ratio will be achieved with a time of the order of 3 μ s).

The inclusion in the THESUS payload of XGIS, a broad FoV detection system with an extended energy band from few keV up to several MeV, is fundamental: it would allow to detect and localize S-GRBs and to determine the hard spectrum of these events, so important in multi-messenger astrophysics. Also, through XGIS it could be possible to provide unique clues to the physics and geometry of the emission of GRBs and other bright X-ray transients through sensitive timing and spectroscopy over an unprecedentedly wide energy band (Amati et al., 2022).

2.2 MEPSA

MEPSA (Multiple Excess Peak Search Algorithm; Guidorzi, 2015) is an algorithm designed to identify peaks in a uniformly sampled time series affected by uncorrelated Gaussian noise. The algorithm has been conceived for the analysis of GRB curves and can therefore be extremely useful in identifying peaks in light curves detected by XGIS. It operates by scanning the time series at various timescales and comparing potential peak candidates with a variable number of adjacent bins. Specifically, MEPSA detects peaks in the input light curves by utilizing a multi-pattern set of excesses, i.e. a set of $N = 39$ patterns. For accurate results, it is necessary to pre-process the series by either subtracting the background or eliminating any potential trends. This ensures that changes in the expected value should only be due to signal and not to background.

For each bin of the light curve, let r_i be the rate in the i -th bin. A given pattern P_k ($k = 1, \dots, N$) consists of a fixed number of adjacent bins around the given i -th bin: around i there are a given $n_{k,l}$ leftward bins (which temporally precede the i -th bin) and $n_{k,r}$ rightward bins (which temporally follow the i -th bin). The pattern assigns each of its bins, except for the i -th bin, a threshold $v_{k,j}$ ($j = 1, \dots, n_{k,l} + n_{k,r}$) in terms of number of σ (where σ is the statistical noise corresponding to that bin). Pattern P_k is then said to be fulfilled by bin i when the following conditions are

simultaneously satisfied:

$$\begin{cases} r_i - r_j \geq v_{k,j-i+n_{k,l}+1} \sigma'_{ij} & (j = i - n_{k,l}, \dots, i - 1) \\ r_i - r_j \geq v_{k,j-i+n_{k,l}+1} \sigma'_{ij} & (j = i + 1, \dots, i + n_{k,r}) \end{cases} \quad (2.1)$$

where $\sigma'_{ij} = (s_i^2 + s_j^2)^{1/2}$. Each pattern has different numbers of leftward and rightward bins, that vary from 1 to 5, and a different threshold values, they vary in a range from 0 to 5. The i -th bin is promoted to peak candidate if at least one of 39 pattern is fulfilled. The complete set of threshold values $v_{k,j}$ currently adopted is reported in Guidorzi, 2015.

2.3 Our simulations and results

Our goal was to evaluate the detection capabilities of XGIS; in particular we tested light curves (LCs) trigger algorithms, especially MEPSA, in detecting synthetic GRBs as seen in a single XGIS unit in THESEUS. Here we report a short summary of the work; for a comprehensive analysis, please refer to Appendix A. This work is also published as a technical notes on the website <https://www.isdc.unige.ch/theseus/> (access restricted to THESEUS team members).

Characteristics of simulated GRBs

We simulated GRB-LCs with one peak; our single-GRB spectrum models are described by the empirical Band function (see Section 1.5). We chose intermediate parameters, so we fixed $\alpha = -1$, $\beta = -2.3$, E_p in the range 2 – 1000 keV. Photon fluence (F) range was 1 – 955 ph/cm² in the energy band 2-2000 keV. Our simulated GRBs could be observed on axis or either 15° or 30° off with respect to the XGIS camera axis.

Procedure

- a. Using Python package *xspec* and XGIS response and ancillary files (version 7), we determine the predicted counts for 8 contiguous energy bands from 2 to 2000 keV. We call "X" the energy bands detected by SDDs (see Section 2.1.3), "S" those detected also through scintillators. If we consider the total band, we call it "XS". Background counts are determined setting a negligible value to the normalization of the GRB spectrum (10^{10}).
- b. To create the simulated LCs, we used the photon counts obtained previously and we assign them a FRED profile with $\tau_r = 0.5$ and $\tau_d = 1.6$ (Section 1.2) for the hardest energy channel (200-2000 keV).
- c. Once we have a LC, we add the background counts and Poissonian noise; then we subtract it the background. Now the LC is ready to be analyzed with MEPSA.
- d. We tested MEPSA with LCs with different E_p , directions, fluences:
 $E_p = 10, 100, 300, 500, 1000$ keV (2 - 5 keV in some cases);
 $\theta = 0^\circ, 15^\circ, 30^\circ$;
 $F = 1, 5, 10, 50, 100$ ph/cm² (up to ph/cm² in some cases).

For each configuration, we carried out 100 simulations of 110 s each, rebinned at 64 ms; we considered both a constant and a variable background.

Results

While comparing different algorithms, we firstly considered/characterized MEPSA. Regarding MEPSA, we obtained the following results:

1. Considering different combinations of values for E_p , fluences, directions, we found that, at low energies, X band alone performs better than using all bands (XS) (see Section 4.1 and 4.2 of technical notes);
2. As to be expected, detection efficiency depends on the GRB direction and is better if the line of sight of the detected GRB is perpendicular to XGIS camera plane (see Section 4.2 of technical notes).
3. For all the values of E_p , all directions, XS band, the detection efficiency $\geq 90\%$ for a peak flux $\geq 0.5 \text{ ph cm}^{-2} \text{ s}^{-1}$ in 50–300 keV (peak flux threshold is also lower for some values of E_p); this value is comparable/better (for some E_p) than Fermi’s Gamma-ray Burst Monitor one (see Section 4.4 in technical notes and von Kienlin et al., 2020), also with a single XGIS unit.
4. As we remarked above, for each configuration we carried out 100 simulations of 110 s each, rebinned at 64 ms; this implies 1.7×10^5 bins per configuration. We found that the rate of false positives is $< 5 \times 10^{-5} \text{ bin}^{-1}$ in all the configurations (Section 4.5 of technical notes).
5. We simulated a background modulation assuming a sinusoidal shape with orbital period of 6000 s, $\pm 10\%$ variable along the orbit (as expected for a quasi-equatorial orbit), random phase. We found that MEPSA performance are essentially unaffected by adding this kind of variable background (see Section 5 of technical notes).

We also compared MEPSA with a significantly simpler algorithm based on considering a peak detected if $\text{SNR} > 7$: as expected, it turns out that MEPSA performs better, especially at low fluence values (see technical notes, Section 4.6).

Further developments

Possible follow-up could include both the implementation of MEPSA and an extension of the analysis here reported. It could be convenient, for example, evaluating whether disabling one of MEPSA patterns would decrease the number of false positives without losing too many true peaks. One could also vary the characteristics of simulated GRBs, such as the duration and the number of peaks. Moreover, one could extend the analysis studying the efficiency of the individual energy bands and assuming to observe a given GRB using both XGIS cameras.

Chapter 3

Prompt emission and minimum variability timescale

3.1 Minimum variability timescale

Light curves often exhibit fluctuations or variations in their intensity over different timescales (see Section 1.2). The minimum variability timescale (MVT) is the smallest time interval at which these fluctuations, which must significantly exceed the Poisson counting noise, can be reliably measured and quantified. The origin of MVT in GRBs is currently still an open issue. This variability can be the result of several different contributions:

- a. it may reflect the time intervals between the emission of successive shells within the internal shock model, as they are modulated by the central engine activity (Kobayashi et al., 1997);
- b. it can be due to viscous and thermal instability occurred in the BH accretion disk (Xie et al., 2017);
- c. it can be correlated with the propagation of the relativistic flow through the stellar envelope (Narayan and Kumar, 2009), which in turn also depends on the jet composition (Gottlieb et al., 2019, 2020b,a, 2021b,a, the jet geometry a possible jet precessing/wobbling trend (Salafia et al., 2016, Gottlieb et al., 2022).

Two empirical correlations associated with MVT and variability has been reported: an anti-correlation between MVT and the bulk Lorentz factor of the GRB, and an anti-correlation between the variability and the isotropic luminosity of the GRB (Sonbas et al., 2015, Wu et al., 2016). It was also noticed that S-GRBs have a variability timescale that is in general significantly shorter than L-GRBs (MacLachlan et al., 2013, Golkhou et al., 2015).

The close connection of MVT with fundamental characteristics of the GRBs (jet opening angle, bulk Lorentz factor, luminosity, size of emitting region) makes the study of MVT necessary to better interpret the nature of these physical phenomena; the different MVT of S-GRBs and L-GRBs suggests that it could be a useful indicator of the progenitor class. In addition, as we remarked in Section 1.9, a measure of MVT can give information on the size of the prompt emission region.

3.2 Our study and results

In our work we analyzed the minimum variability timescale of a set of GRBs in the keV–MeV energy range, where MVT is defined as the full-width half-maximum (FWHM) of the shortest individual pulse that is identified within the light curve. We investigated potential connections between the MVT and other important observables, such as the peak luminosity, Lorentz factor, and jet opening angle. We also inquired whether MVT could be an indicator of GRB progenitor type. Here we report a short summary of the work; for a comprehensive analysis, please refer to Appendix B, where you can find the article: "GRB minimum variability timescale with Insight-HXMT and Swift" and the GCN 33577 "GRB 230307A: short minimum variability timescale compatible with a merger origin".

Data set

We considered GRBs detected both from Swift/BAT and with Insight-HXMT/HE. In particular, our sample included GRBs detected by Swift/BAT in burst mode from January 2005 to July 2022, totalling 1291 bursts. For about one third of Swift sample, the redshift is known spectroscopically. Considering 2 s as the boundary between S-GRBs and L-GRBs, 78 were S-GRBs; in the Swift sample we also had 24 SEE-GRBs. Regarding Insight-HXMT/HE, we considered GRBs detected by Insight-HXMT/HE from June 2017 to June 2021, collecting 212 GRBs, of which 24 S-GRBs, 2 SEE-GRBs. We also added to the sample two recent and exceptionally bright bursts: 221009A (see Section 1.10.2), and 230307A, our analyses of which were reported in the paper and within a dedicated GCN circular (see Section 1.13.3), respectively.

Methods

We used the peak detection algorithm MEPSA (see Section 2.2) to identify the shortest pulse within a GRB time history; we preliminarily calibrated MEPSA to estimate the FWHM duration: we simulated LCs with FWHM values taken from a given lognormal distribution. We used 1600 fast rise and exponential decay (FRED) profiles; simulated LCs at 1 ms were rebinned with rebinning factors = 1, 4, 64, and 1000. These profiles were affected by uncorrelated Gaussian noise. We apply MEPSA to these imulated LC in order to obtain the conversion between MEPSA's timescale and the FRED pulse FWHM. Once MEPSA was calibrated, we applied it to real GRB lighr curves. For each GRB, we started from the 64-ms LC. A detected peak is considered a candidate when it satisfies two conditions, one regarding the signal to noise SNR, with different threshold for different binning time, the other about the peak duration. The different threshold values on the SNR for different binning time were calculated to keep the number of expected statistical fluctuations being classified as genuine peaks approximately constant: the shorter is the binning time and the correspondingly larger number of bins to be screened that span a given time interval. Regarding the peak duration, the duration of the peak must be greater than the size of the bin.

Results

We confirm that, on average, S-GRBs have significantly shorter MVT than L-GRBs. The MVT distribution of SEE-GRBs, such as 060614 and 211211A, is mostly compatible with that of S-GRBs. Moreover, the MVT distribution of SN-GRBs is not compatible with that of GRBs associated with KNe. This is interesting because it provides a new clue on the progenitor’s nature (see Fig. 3.1). Also the recent observation of GRB 230307A supports this idea: it has a long duration, a short MVT and a merger origin is assumed for this GRB, as suggested by the possible evidence for kilonova emission reported by Levan et al., 2023.

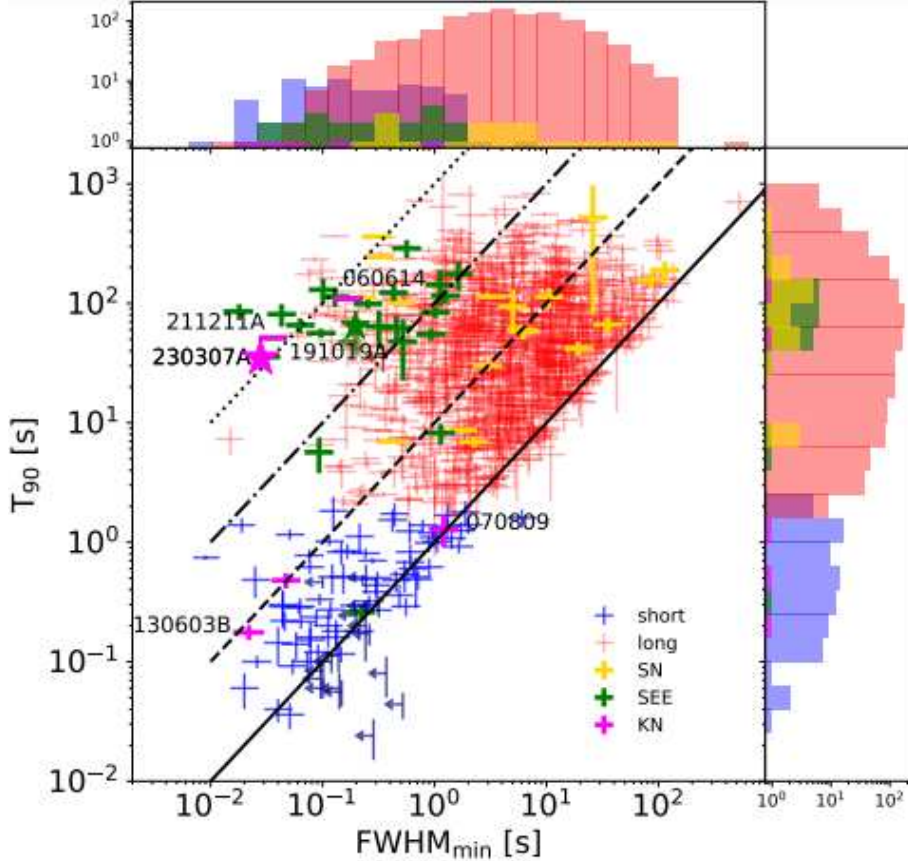


Figure 3.1: Scatter plot of FWHM_{min} and T_{90} for the Swift/BAT sample along with the corresponding marginal distributions for distinct populations of S-GRBs (blue), L-GRBs (red), SEE-GRBs (green). Gold points are L-GRBs with an associated SN, pink points are events that show evidence for kilonova emission, as reported in Section 1.13.3

Concerning the subsample of L-GRBs with measured redshift, upon a careful evaluation of the selection effects that impact the MVT measure in the MVT-peak rate plane, we confirm the existence of anti-correlations between MVT and peak luminosity L_p , and between MVT and initial Lorentz factor of the ejecta. We could establish that MVT anti-correlates also with the number of peaks and correlates with the jet opening angle. Globally, we find that GRBs with short MVT on average have narrower jets and/or smaller observer angles, higher Lorentz factors, high peak luminosities and exhibit several pulses. An interpretation is that we are observing a

structured and possibly wobbling jet: GRBs with short MVT would be seen within the jet core, resulting in higher L_p and Lorentz factor, shorter and more numerous peaks; GRBs viewed across the boundary between the jet core and the jet-cocoon interface, would appear as less luminous, with lower Lorentz factors and longer MVT, due to a smaller Doppler boosting and longer arrival time delays. The possibility that such a jet could wobble randomly within angles comparable if not greater than the jet core itself, further suggests that the different number of peaks observed in different GRBs could indicate how often the jet core points to the observer.

Finally, calling R the distance at which the dissipation of energy into gamma-rays is supposed to take place, we found that almost all GRBs lie in the $10^{15} \leq R/\text{cm} \leq 10^{17}$ range.

Chapter 4

Kilonovae detection

The study of a KN rapid evolution can improve our understanding of the role of compact object mergers in the origin of the heavy elements (see Section 1.13).

In this Chapter I describe a strategy to optimize the observation for the optical follow-up of KNe to constrain the model and the viewing angle once this has been identified and localized, both using light curves and polarization. In order to simulate KN light curves and polarization curves, I used the POSSIS code (Bulla, 2019, Section 4.2).

This is important as their rare and rapidly fading nature (see Eq. (1.12) and Eq. (1.13)) means that such a strategy should be planned in advance rather than being devised in an “ad-hoc” manner in the aftermath of the discovery. In addition, such pre-planned observing strategies lead to the optimal use of robotic telescopes in this kind of followup activities.

For the purposes of this work, we chose to study a specific case that could be generalized to most small-medium class facilities. The case chosen was to understand the optimum exposure sequence using instruments similar to the MOPTOP (Multi-colour OPTimised Optical Polarimeter, Shrestha et al., 2020) and IO:O (Smith and Steele, 2017) optical imaging cameras, which are currently deployed at the 2-m fully robotic Liverpool Telescope (LT; Steele et al., 2004). We assume that a network of similar telescopes and instruments (e.g. Tsapras et al., 2009) is located over a range of longitudes such that 24 hour coverage is available. Given the interest in such sources, this assumption is reasonable in that most world-wide telescopes are likely to be involved in the followup of such rare events (e.g. Brown et al. 2013).

4.1 Liverpool Telescope

The LT is a fully robotic telescope located at the Observatorio del Roque de los Muchachos on the island of La Palma, in the Canary Islands, Spain. It is operated by the Astrophysics Research Institute (ARI) at Liverpool John Moores University (LJMU). LT has a primary mirror with a diameter of 2.0 meters. It is a Ritchey-Chrétien telescope design, a type of reflecting telescope with high image quality over a wide field of view.

LT is primarily used for time-domain astronomy, which involves studying transient or rapidly changing celestial events: to this aim, it is fully robotic, so it can operate autonomously without the need for constant human supervision; this automation allows it to respond rapidly to transient events such as supernovae, GRBs

(Guidorzi et al., 2006), and other sudden cosmic occurrences. The telescope is equipped with 7 instruments that enable both imaging and spectroscopic observations. All LT instruments are mounted at the Cassegrain focus and the time overhead for instrument changes is 60 seconds (Copperwheat et al., 2016). In the next sections we briefly describe the instruments IO:O camera and MOPTOP; in particular, the latter plays a central role in our work.

In addition to scientific research, the LT is involved in educational activities and public outreach, offering opportunities to students and to the public to engage with astronomy and space science.

4.1.1 IO:O

IO:O is the optical imaging component of the IO (Infrared-Optical) suite of instruments. The detector is a 4096×4112 pixel covering a $10' \times 10'$ field of view. IO:O uses a single, 12 position filter wheel. By default this wheel contains the Sloan $u'g'r'i'z'$ set, Bessell B and V, and a selection of H α filters (Copperwheat et al., 2016, Smith and Steele, 2017).

4.1.2 MOPTOP

MOPTOP is a fully optimized polarimeter for time-domain astrophysics. The incoming white light beam from the telescope (see Fig. 4.1) is initially collimated (1); a continuously rotating half wave plate modulates the polarization angle of the incoming beam (2); light is then split in two polarization states, one is transmitted and the other reflected by the beam splitter (3). Each polarization state is then simultaneously recorded by two low-noise fast readout cameras synchronized to the wave plate angle (4). With the half wave plate in its initial position, the difference between the two images equals the Stokes Q parameter. The difference images at the subsequent half wave plate position (22.5°) equals the Stokes U parameter. The third wave plate position difference yields -Q and the fourth -U. The sum of all the images equals the Stokes I parameter (Shrestha et al., 2020, Jermak et al., 2016). MOPTOP comes with a set of filters: B, V, R, I, L .

4.2 POSSIS

POSSIS (Polarization Spectral Synthesis In Supernovae) is a 3-D Monte Carlo Radiative Transfer code that predicts photometric and polarimetric viewing-angle dependent signatures of supernovae and KNe (Bulla, 2019), working in three dimensions. The code considers a two-component (lanthanide rich and lanthanide poor) kilonova and incorporates wavelength- and time-dependent opacities; it predict LCs and polarimetric curve studying the interactions of photon packets with the medium. A number of Monte Carlo quanta are created at any time-step. Each of these quanta is assigned a location, an initial direction, energy, frequency and normalized Stokes vector. Each packet is propagated throughout the ejecta until it interacts with matter.

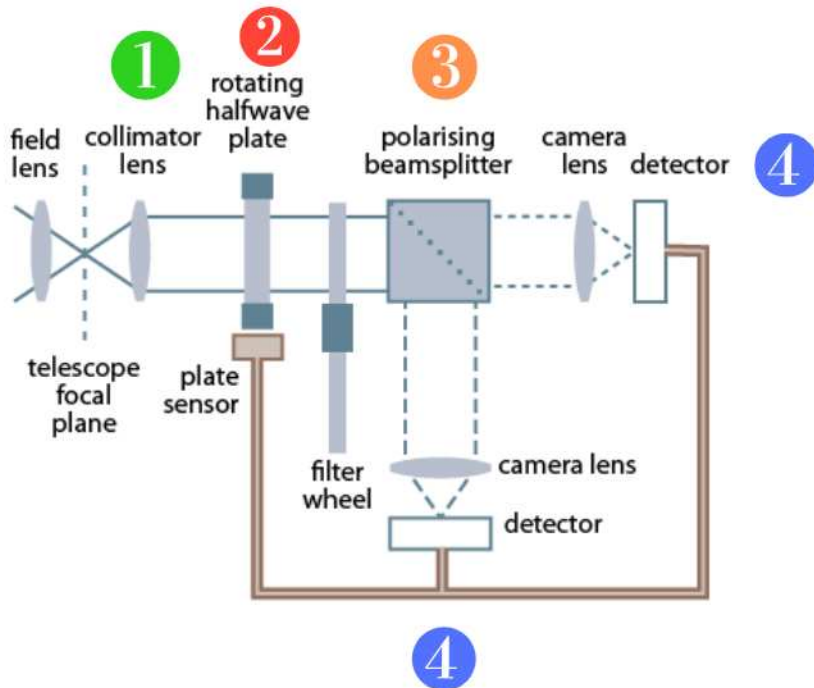


Figure 4.1: MOPTOP schematic view. Figure from Jermak et al., 2016.

4.3 Our simulations and results

Our aim was optimizing the observing strategy for the optical follow-up of identified and localized KNe to constrain the model and the viewing angle. Hereafter, a short summary follows. For an exhaustive description regarding light curves analysis, we refer the reader to Appendix C, where the full paper is reported: "Optimizing the observation of optical kilonovae with medium-size telescopes"; about polarization analysis, the paper is still in production, you can find preliminary results in Section 4.3.2.

4.3.1 Light curve analysis

Methods

We considered three different KN models obtained with POSSIS: one presents only a neutrino-driven wind component, the others also have jets with two different values of luminosity (see Fig. 4.2).

For each of the three models, we extracted KN LCs for 11 different inclination angles. We chose to evaluate our results considering observations in the Sloan filters i' , r' , and u' ; the source distance range is 20–350 Mpc (Fig. 4.3).

In order to find a reasonable time exposure sequence necessary to discriminate between different KN models characterized by different viewing angles, we followed three main steps:

- a. we considered four different time exposure sequences lasting 8 hours each;

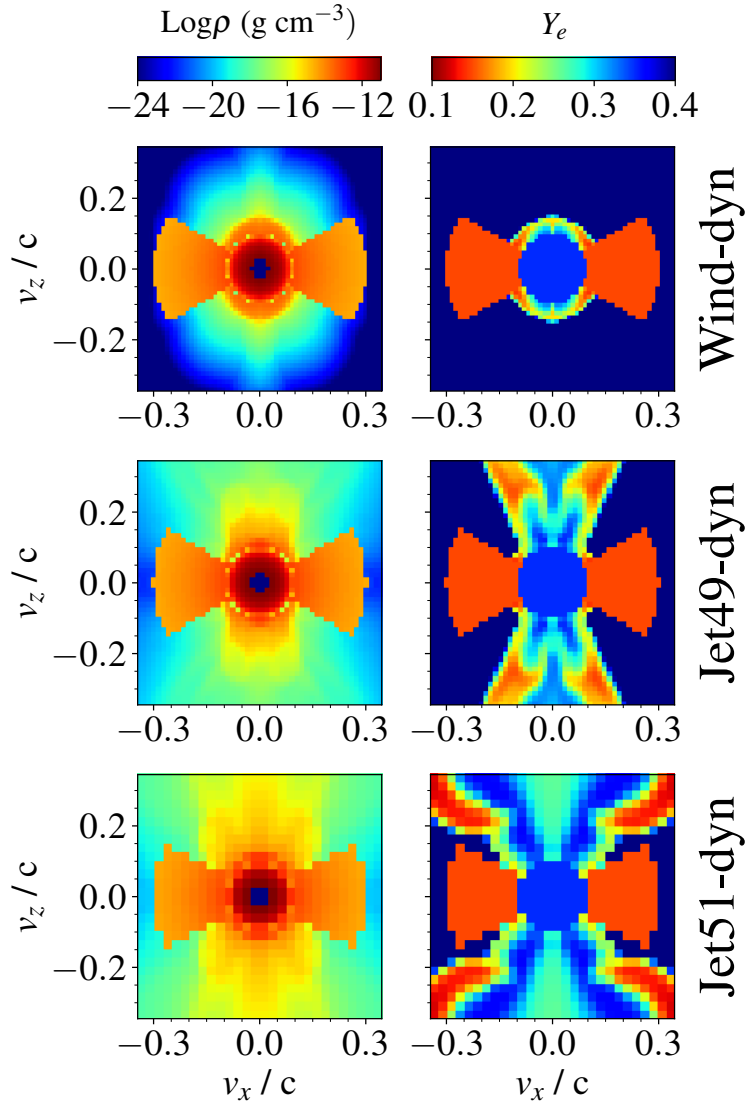


Figure 4.2: Density (left) and Y_e (right) distribution in the x - z plane for the three models used in this study (Wind-dyn, Jet49-dyn and Jet51-dyn from top to bottom). The modelled ejecta are taken from Nativi et al. 2021, where a neutrino-driven wind as described in Perego et al. 2014 was evolved assuming that either no jet (Wind), or a jet with a luminosity of $L_j = 10^{49}$ erg s^{-1} (Jet49), or a jet with $L_j = 10^{51}$ erg s^{-1} (Jet51) is launched. The wind mass is dominated by a secular component ejected 1s after the merger with $0.072 M_\odot$. We include an additional component to model dynamical ejecta: we adopt an idealised geometry for this component, with a lanthanide-rich dynamical-ejecta component ($Y_e = 0.15$ and velocities from 0.08 to 0.3c) from the grid in Dietrich et al. 2020 and selecting the best-fit model to the KN of GW170817 (mass $0.005 M_\odot$ and half-opening angle of 30°).

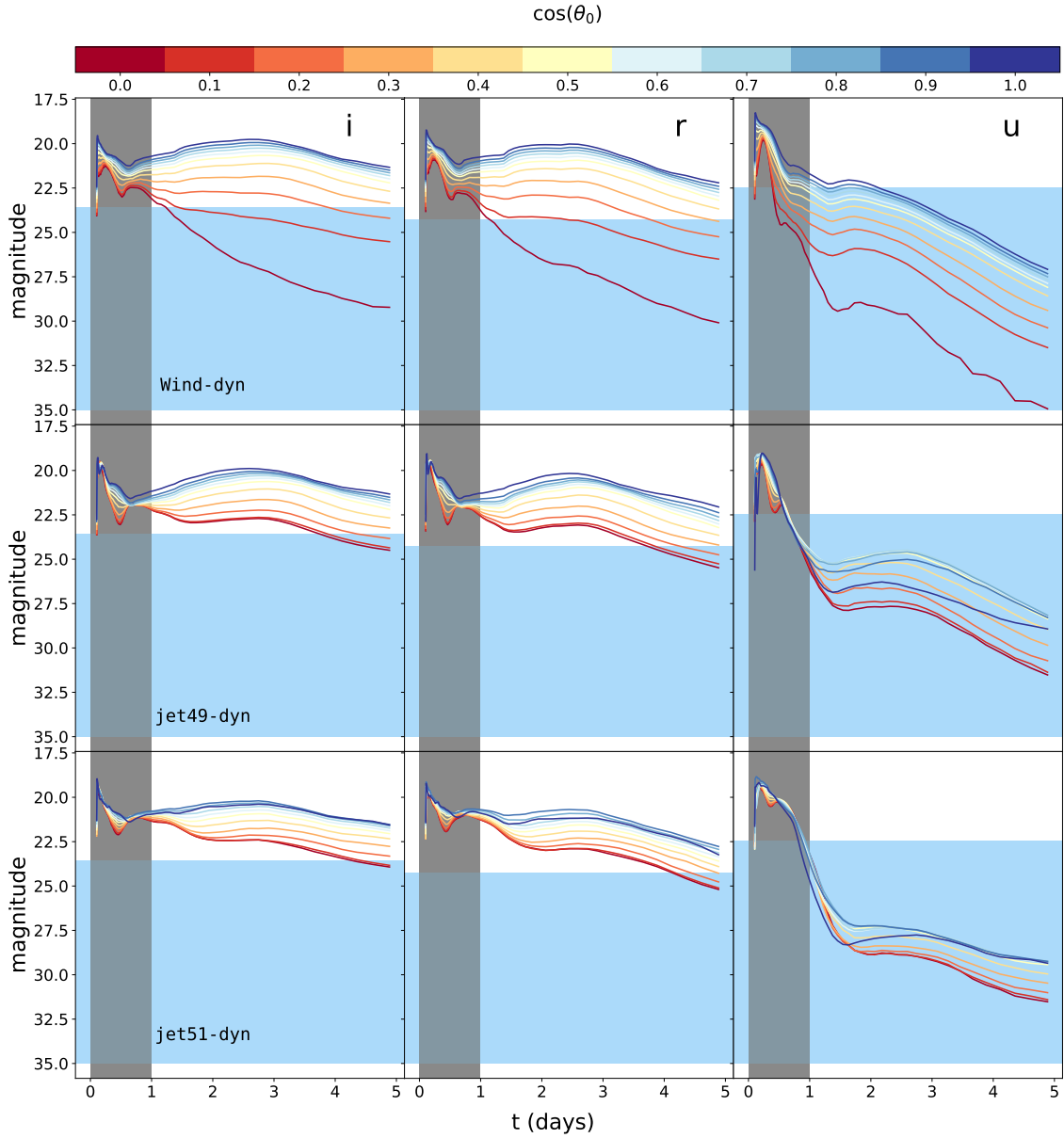


Figure 4.3: LCs for different models and viewing angles; first column refers to *i* filter, second one to filter *r*, third to filter *u*; the source has a distance of 160 Mpc. Grey area corresponds to the first day after the merger: LCs are not considered due to the inaccuracy in estimating the opacity. The blue area corresponds to the values in magnitude higher than the limiting magnitude of each filter, obtained with a time exposure of 1 hour.

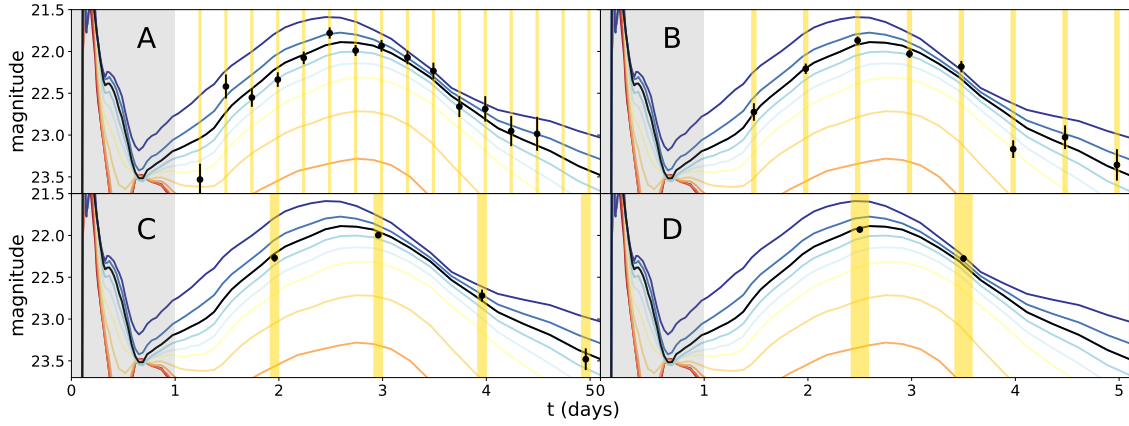


Figure 4.4: Each panel refer to a different time window sequence. In yellow, the 4 different time windows; in each plot, LCs referring to `jet49-dyn` model, $d=350$ Mpc, `i` filter. Black lines are LCs with $\cos\theta_0 = 0.8$, black points refer to the corresponding LCNs.

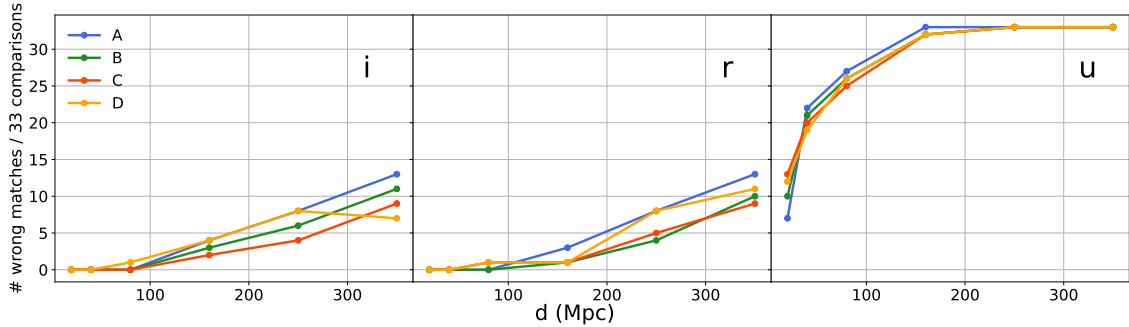


Figure 4.5: Number of wrong matches as a function of distance for different filters and different time exposure sequences (A, B, C, and D, with respectively 16, 8, 4, 2 observation windows). Since we have three models and 11 viewing angles, for each distance and filter we have 33 comparisons.

- b. for a fixed distance and filter, we added the appropriate photon counting noise to the LC (see Fig. 4.4); in this way we created LC with noise (LCN);
- c. we compared LCN with the LCs without noise and we analyzed how often we were able to identify the correct LC; in this comparison we also considered the cases in which there was an error on distance (either 1 or 2%), and the case in which the distance is unknown.

A similar procedure was used to compare color curves with color curves with noise.

Results

The use of the u' filter should be avoided, due to the high number of mismatches with all the time window sequences considered in this work (see Fig. 4.5). Also, a procedure with color curve is not as convenient. Alternative time window sequences sharing the same total net exposure (8 h) and with at least four observations and a maximum cadence of 1 d are essentially equivalent, as long as the error on distance is $\leq 2\%$ (see Fig. 4.5). Consequently, we suggest to use 1-d-cadence sequence, because

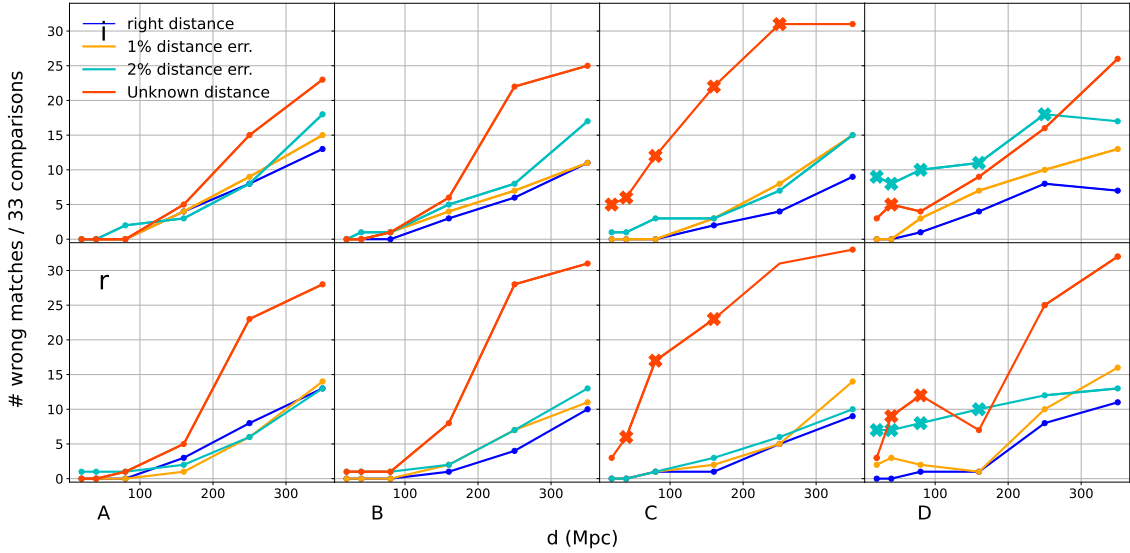


Figure 4.6: The number of wrong matches that occurs in 33 comparisons with A, B, C, and D time exposure sequences with a known distance (blue line), with an error of 1% on distance (yellow line), 2 % (cyan line) and without any information about the distance and the time of the merger (orange line). Points marked with "x" refer to values that are significantly different from the best value obtained with other time sequences.

it can be easily realized. If the distance of the source is unknown, short-cadence (≤ 0.5 d) sequences are to be preferred.

4.3.2 Polarization analysis

Methods

Similarly to what was done for the simulations of light curves, we used three different KN models and we obtained their polarization curves with POSSIS. For each of the three models, we extracted polarization curves for 11 different inclination angles θ . We chose to evaluate our results considering observations in filters I , R , and B ; the source distance range is 5–160 Mpc, the polarization angles φ in the range -90° - $+90^\circ$, with a step of 10° . Aiming to find a reasonable time exposure sequence necessary to discriminate between different KN models, viewing angles, and polarization angle, we followed the following steps:

- a. We explored four different time exposure sequences. Three of them have a total observation time of 12 hours, while the fourth intentionally offers an extensive observation time of 48 hours over three days.
- b. Using POSSIS, we generated polarization curves, which hereafter will be referred to as "PCs", for each model, viewing angles respect to KN, distances, filters, and angle between a fixed reference system and KN merging plane.
- c. For each time exposure sequence, we calculated the expected number of photons/s that would reach the MOPTOP polarimeter from two perpendicular

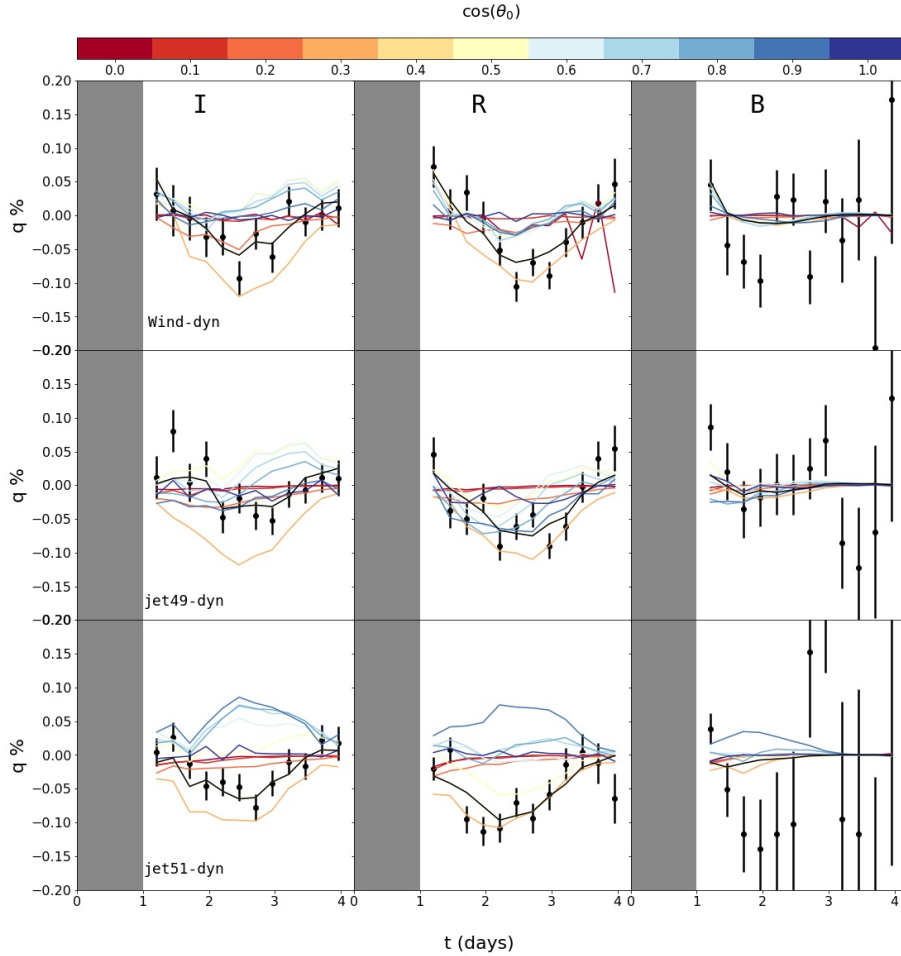


Figure 4.7: $q\%$ curves as a function of time for different models (rows), different filters (columns), different viewing angles (colors). Black curves refer to $\cos \theta=0.5$ (we covered the yellow curve to make it easier to recognize); black points with uncertainties are realizations of the back curves with added noise. The first day (gray area) was ignored, due to the inaccuracy in estimating the KN opacity. The source distance is 10 Mpc.

directions; we call the expected number of photons/s in the 2 different directions F_0 and F_{90} . In this calculation we also considered the instrumental polarization zeropoint (see the "MOPTOP technical specifications for details).

- d. Subsequently, we added appropriate photon counting noise to F_0 and F_{90} , obtaining $F_{0 \text{ noise}}$ and $F_{90 \text{ noise}}$. These noisy data are then used to obtain polarization curves with noise (PCN), simulating what the telescope would observe. This step was applied to all 33 PCs (3 models, 11 viewing angles). One may find an example of the application of this procedure in Fig. 4.7.
- e. We then compared the PCN to the noise-free PCs and analyzed how frequently we were able to correctly identify the original PC. This comparative analysis was carried out for each combination of distance and filter, and the process was repeated for all 33 PCNs, compared with 1188 PCs (3 models, 11 viewing angle, 36 polarization angles). We consider a KN undetectable if its $\text{SNR} < 5$.

Preliminary results

We present the results obtained using 48 hours of observation within three days (2 hours each 0.125 days); we considered both the cases of a polarization angle of 0° and 30° . We found that, even with this unrealistic time exposure sequence, we can have good results only with I filter and a KN with a distance less than 10 Mpc (see Fig. 4.8). Most of the mismatches are due to undetectable KNe; when the KN can be detected, most of mismatches regard the polarization angle. We will extend in the future our analysis considering a bigger collecting area, a possible error on distance measurements, both light and polarization curves information, observations that go beyond 4 days from the beginning of the emission, and determine the range of values of $q\%$ required to constrain the KN properties.

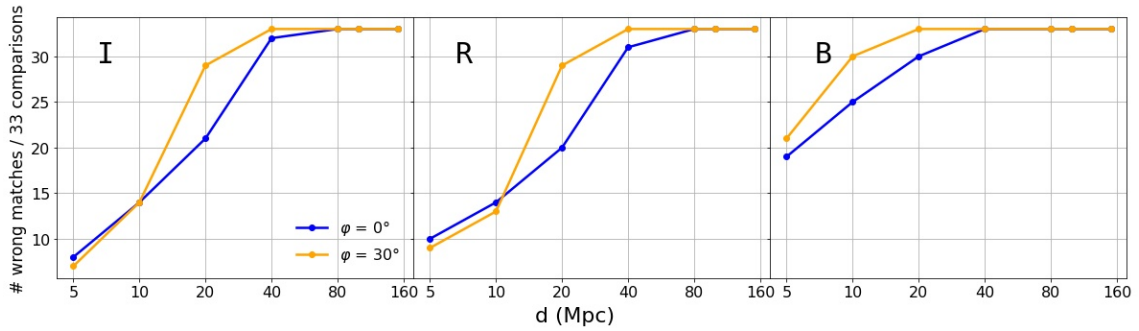


Figure 4.8: Number of wrong matches over 33 comparisons as a function of distance for different filters and different polarization angles.

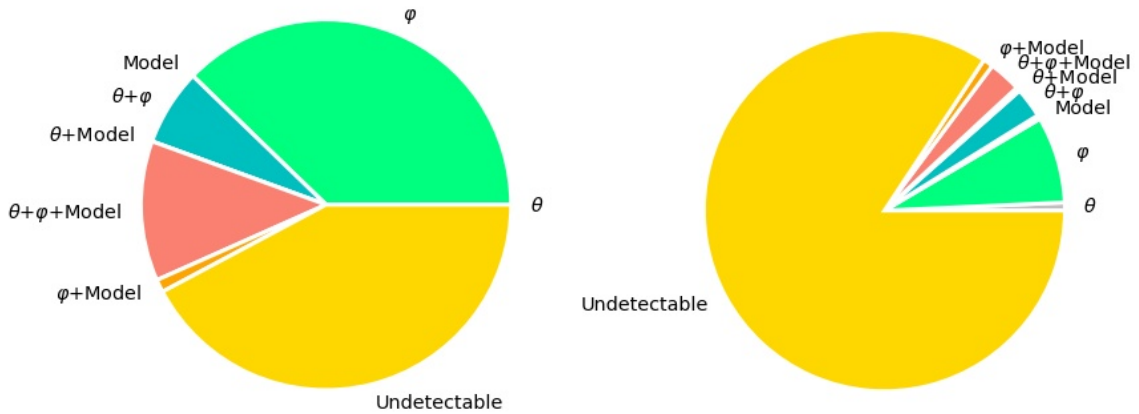


Figure 4.9: Left pie: different kind of wrong matches (viewing angle θ , polarization angle φ , mismatch due to a wrong model; we can also have that a mismatch can be due to 2 or all of the previous reason, or KN can't be detected); KN distance in ≤ 10 Mpc. Right pie: the same as the previous pie, with KN distance in ≤ 150 Mpc.

Conclusions

In this thesis I explored and highlighted the power of time evolution in the study of GRBs and KNe: it is fascinating to see how much information is hidden into a time series.

Through the simulation of GRB single-peak light curves I investigated and characterized the THESEUS/XGIS detection capabilities. In particular, I found that, for all the values of the peak energy E_p considered in our work and for all directions, detection both with SDD and scintillators, the detection efficiency of the joint combination of SDD and scintillators, which is one of the key properties of the XGIS instrument, is comparable/better than Fermi's Gamma-ray Burst Monitor one, also with a single XGIS unit (the peak flux necessary to have a detection efficiency equal or higher than 90 % with one XGIS camera for an energy peak in the range 10-1000 keV is $\leq 0.5 \text{ ph cm}^{-2} \text{ s}^{-1}$). We also found that the optimal performance of the considered detection algorithms is essentially unaffected by adding a sinusoidal variable background, as the one expected for a low-inclination orbit.

The analysis of GRB minimum variability timescale (MVT), using Swift-BAT and Insight-HXMT data, allowed us to provide a possible indicator of the nature of the possible progenitor (i.e., compact binary merger as opposed to collapsar) of GRBs and about GRBs geometry. In fact, we verified that, on average, S-GRBs exhibit considerably shorter MVT than L-GRBs (logarithmic mean of S-GRBs with Swift-BAT data is 0.2 s, L-GRBs one is 4 s; with HXMT data they are respectively 0.1 s and 1.3 s). Moreover, the MVT distribution of short-extended emission (SEE) GRBs is more compatible with that of S-GRBs rather than that of L-GRBs. Instead, the MVT distribution of SN-associated GRBs is significantly different from that of GRBs linked to kilonova (KN) events. This puts forward a link between a compact object merger and a short MVT. Observations of recent GRB 230307A further support this possibility: in fact, despite its long duration ($T_{90} = 34.56 \pm 0.6 \text{ s}$ from Fermi GBM team) this GRB displays a short MVT (28_{-7}^{+10} ms). Indeed, circumstantial evidence from the afterglow behavior as well its possible host galaxy support the merger scenario, as indicated by potential kilonova emission reported by Levan et al., 2023. Concerning the subsample of L-GRBs with measured redshift, we found that MVT correlates with the jet angle and anti-correlates with the Lorentz factor, the peak luminosity and the number of pulses. We can explain this if we think we might be observing a structured jet undergoing some wobbling: this is a possibility that is supported by state-of-the-art simulations Gottlieb et al., 2022. In this scenario, GRBs that show shorter MVT would likely be situated within the central part of the jet pointing toward us, resulting in higher peak luminosity and Lorentz

factor, leading to shorter and more frequent peaks. On the other hand, GRBs observed at the boundary between the jet core and the interface with the surrounding cocoon would appear less luminous, with lower Lorentz factors and longer MVT.

I finally used time-evolution models of magnitude and polarization of KNe to optimize the capability of medium-sized telescopes to constrain the properties of KNe. By using light curves observed with i' , r' , u' filters and 8-hour time windows starting from the end of the first day of observation, we found that there are better chances of constraining the kind of KN model and the viewing angle, provided that the i' and r' filters are used. Time window sequences that provide a total net exposure of 8 hours, including a minimum of four observations, and maintain a maximum observation frequency of 1 day, are essentially interchangeable, provided that the error in distance measurements remains below 2%. As a result, we recommend opting for a 1-day cadence sequence, given its ease of implementation. However, if the source distance is unknown, it is advisable to prioritize short-cadence sequences, which have observation intervals of 0.5 days or less. Regarding polarization curves, we found that we can constrain KN properties only with I filter and KNe with a distance less than 10 Mpc.

The current results open up interesting future prospects: on the one hand, new simulations of GRB prompt emission could be developed, considering events with more than one peak and envisioning observations with two XGIS cameras aboard the THESEUS mission concept; the relationship between MVT and the nature of the GRB progenitor (compact object merger or the collapse of a massive star) can be further analyzed, for instance, by searching for evidence of KNe in the early afterglow of those events displaying a short MVT or evidence for a SN when to rule out the merger scenario. Regarding KNe polarization, we plan to extend our analysis by incorporating a larger telescope diameter, accounting for potential errors in distance measurements, incorporating information from both light and polarization curves, and determining the $q\%$ value that can effectively constrain the properties of KNe. Finally, I developed a proposal to collaborate with the National School Observatory of Liverpool to create an educational program aimed at teachers and students in English high schools, involving the use of Python to simulate GRB light curves.

Bibliography

R. Abbasi, M. Ackermann, J. Adams, J. A. Aguilar, M. Ahlers, M. Ahrens, J. M. Alameddine, A. A. Alves, N. M. Amin, K. Andeen, T. Anderson, G. Anton, C. Argüelles, Y. Ashida, S. Athanasiadou, S. Axani, X. Bai, A. V. Balagopal, S. W. Barwick, V. Basu, S. Baur, R. Bay, J. J. Beatty, K. H. Becker, J. Becker Tjus, J. Beise, C. Bellenghi, S. Benda, S. BenZvi, D. Berley, E. Bernardini, D. Z. Besson, G. Binder, D. Bindig, E. Blaufuss, S. Blot, M. Boddenberg, F. Bontempo, J. Y. Book, J. Borowka, S. Böser, O. Botner, J. Böttcher, E. Bourbeau, F. Bradascio, J. Braun, B. Brinson, S. Bron, J. Brostean-Kaiser, R. T. Burley, R. S. Busse, M. A. Campana, E. G. Carnie-Bronca, C. Chen, Z. Chen, D. Chirkin, K. Choi, B. A. Clark, K. Clark, L. Classen, A. Coleman, G. H. Collin, A. Connolly, J. M. Conrad, P. Coppin, P. Correa, D. F. Cowen, R. Cross, C. Dappen, P. Dave, C. D. Clercq, J. J. DeLaunay, D. D. López, H. Dembinski, K. Deoskar, A. Desai, P. Desiati, K. D. de Vries, G. de Wasseige, T. DeYoung, A. Diaz, J. C. Díaz-Vélez, M. Dittmer, H. Dujmovic, M. A. DuVernois, T. Ehrhardt, P. Eller, R. Engel, H. Erpenbeck, J. Evans, P. A. Evenson, K. L. Fan, A. R. Fazely, A. Fedynitch, N. Feigl, S. Fiedlschuster, A. T. Fienberg, C. Finley, L. Fischer, D. Fox, A. Franckowiak, E. Friedman, A. Fritz, P. Fürst, T. K. Gaisser, J. Gallagher, E. Ganster, A. Garcia, S. Garrappa, L. Gerhardt, A. Ghadimi, C. Glaser, T. Glauch, T. Glüsenkamp, N. Goehlke, J. G. Gonzalez, S. Goswami, D. Grant, T. Grégoire, S. Griswold, C. Günther, P. Gutjahr, C. Haack, A. Hallgren, R. Hallday, L. Halve, F. Halzen, M. Ha Minh, K. Hanson, J. Hardin, A. A. Harnisch, A. Haungs, K. Helbing, F. Henningsen, E. C. Hettlinger, S. Hickford, J. Hignight, C. Hill, G. C. Hill, K. D. Hoffman, K. Hoshina, W. Hou, M. Huber, T. Huber, K. Hultqvist, M. Hünnefeld, R. Hussain, K. Hyman, S. In, N. Iovine, A. Ishihara, M. Jansson, G. S. Japaridze, M. Jeong, M. Jin, B. J. P. Jones, D. Kang, W. Kang, X. Kang, A. Kappes, D. Kappesser, L. Kardum, T. Karg, M. Karl, A. Karle, U. Katz, M. Kauer, M. Kellermann, J. L. Kelley, A. Kheirandish, K. Kin, J. Kiryluk, S. R. Klein, A. Kochocki, R. Koirala, H. Kolanoski, T. Kontrimas, L. Köpke, C. Kopper, S. Kopper, D. J. Koskinen, P. Koundal, M. Kovacevich, M. Kowalski, T. Kozynets, E. Krupczak, E. Kun, N. Kurahashi, N. Lad, C. Lagunas Gualda, M. J. Larson, F. Lauber, J. P. Lazar, J. W. Lee, K. Leonard, A. Leszczyńska, Y. Li, M. Lincetto, Q. R. Liu, M. Liubarska, E. Lohfink, C. J. L. Mariscal, L. Lu, F. Lucarelli, A. Ludwig, W. Luszczak, Y. Lyu, W. Y. Ma, J. Madsen, K. B. M. Mahn, Y. Makino, S. Mancina, I. C. Mariş, I. Martinez-Soler, R. Maruyama, S. McCarthy, T. McElroy, F. McNally, J. V. Mead, K. Meagher, S. Mechbal, A. Medina, M. Meier, S. Meighen-Berger, Y. Merckx, J. Micallef, D. Mockler, T. Montaruli, R. W. Moore, R. Morse, M. Moulai, T. Mukherjee, R. Naab, R. Nagai, U. Naumann, J. Necker, L. V. Nguyn, H. Niederhausen, M. U. Nisa, S. C. Nowicki, A. Obertacke Pollmann, M. Oehler, B. Oeyen, A. Olivas, E. O'Sullivan,

- H. Pandya, D. V. Pankova, N. Park, G. K. Parker, E. N. Paudel, L. Paul, C. Pérez de los Heros, L. Peters, J. Peterson, S. Philippen, S. Pieper, A. Pizzuto, M. Plum, Y. Popovych, A. Porcelli, M. Prado Rodriguez, B. Pries, G. T. Przybylski, C. Raab, J. Rack-Helleis, A. Raissi, M. Rameez, K. Rawlins, I. C. Rea, Z. Rechav, A. Rehman, P. Reichherzer, R. Reimann, G. Renzi, E. Resconi, S. Reusch, W. Rhode, M. Richman, B. Riedel, E. J. Roberts, S. Robertson, G. Roellinghoff, M. Rongen, C. Rott, T. Ruhe, D. Ryckbosch, D. Rysewyk Cantu, I. Safa, J. Saffer, D. Salazar-Gallegos, P. Sampathkumar, S. E. Sanchez Herrera, A. Sandrock, M. Santander, S. Sarkar, S. Sarkar, K. Satalecka, M. Schaufel, H. Schieler, S. Schindler, T. Schmidt, A. Schneider, J. Schneider, F. G. Schröder, L. Schumacher, G. Schwefer, S. Sclafani, D. Seckel, S. Seunarine, A. Sharma, S. Shefali, N. Shimizu, M. Silva, B. Skrzypek, B. Smithers, R. Snihur, J. Soedingrekso, A. Sogaard, D. Soldin, C. Spannfellner, G. M. Spiczak, C. Spiering, M. Stamatikos, T. Stanev, R. Stein, J. Stettner, T. Stezelberger, T. Stürwald, T. Stuttard, G. W. Sullivan, I. Taboada, S. Ter-Antonyan, J. Thwaites, S. Tilav, F. Tischbein, K. Tollefson, C. Tönnis, S. Toscano, D. Tosi, A. Trettin, M. Tselengidou, C. F. Tung, A. Turcati, R. Turcotte, J. P. Twagirayezu, B. Ty, M. A. Unland Elorrieta, N. Valtonen-Mattila, J. Vandenbroucke, N. van Eijndhoven, D. Vanerom, J. van Santen, J. Veitch-Michaelis, S. Verpoest, C. Walck, W. Wang, T. B. Watson, C. Weaver, P. Weigel, A. Weindl, J. Weldert, C. Wendt, J. Werthebach, M. Weyrauch, N. Whitehorn, C. H. Wiebusch, N. Willey, D. R. Williams, M. Wolf, G. Wrede, J. Wulff, X. W. Xu, J. P. Yanez, E. Yildizci, S. Yoshida, S. Yu, T. Yuan, Z. Zhang, P. Zhelnin, A. Goldstein, J. Wood, and Fermi Gamma-ray Burst Monitor. Searches for Neutrinos from Gamma-Ray Bursts Using the IceCube Neutrino Observatory. , 939(2):116, Nov. 2022. doi: 10.3847/1538-4357/ac9785.
- B. P. Abbott, R. Abbott, T. D. Abbott, F. Acernese, K. Ackley, C. Adams, T. Adams, P. Addesso, R. X. Adhikari, V. B. Adya, and et al. Multi-messenger Observations of a Binary Neutron Star Merger. , 848:L12, Oct. 2017. doi: 10.3847/2041-8213/aa91c9.
- L. Amati. To be short or long is not the question. *Nature Astronomy*, 5:877–878, July 2021. doi: 10.1038/s41550-021-01401-4.
- L. Amati, P. T. O’Brien, D. Götz, E. Bozzo, A. Santangelo, N. Tanvir, F. Frontera, S. Mereghetti, J. P. Osborne, A. Blain, S. Basa, M. Branchesi, L. Burderi, M. Caballero-García, A. J. Castro-Tirado, L. Christensen, R. Ciolfi, A. De Rosa, V. Doroshenko, A. Ferrara, G. Ghirlanda, L. Hanlon, P. Heddermann, I. Hutchinson, C. Labanti, E. Le Floch, H. Lerman, S. Paltani, V. Reglero, L. Rezzolla, P. Rosati, R. Salvaterra, G. Stratta, C. Tenzer, and Theseus Consortium. The THESEUS space mission: science goals, requirements and mission concept. *Experimental Astronomy*, 52(3):183–218, Dec. 2021. doi: 10.1007/s10686-021-09807-8.
- L. Amati, C. Labanti, S. Mereghetti, F. Frontera, R. Campana, N. Auricchio, G. Baldazzi, P. Bellutti, G. Bertuccio, M. Branchesi, R. C. Butler, M. D. Caballero-Garcia, A. E. Camisasca, A. J. Castro-Tirado, L. Cavazzini, R. Ciolfi, A. De Rosa, F. Evangelisti, R. Farinelli, L. Ferro, F. Ficorella, M. Fiorini, F. Fuschino, J. L. Gasent-Blesa, G. Ghirlanda, M. Grassi, C. Guidorzi, P. Hedderman, I. Kuvvetli,

- G. La Rosa, P. Lorenzi, P. Malcovati, E. Marchesini, M. Marisaldi, M. Melchiorri, F. Mele, M. Mikhalska, M. Orlandini, P. Orleanski, S. M. Pedersen, R. Piazzolla, A. Rachevski, I. Rashevskaya, P. Rosati, V. Reglero, S. Ronchini, A. Santangelo, R. Salvaterra, P. Sarra, F. Sortino, G. Sottile, G. Stratta, S. Squerzanti, J. B. Stephen, C. Tenzer, L. Terenzi, A. Trois, A. Vacchi, E. Virgilli, A. Volpe, M. Winkler, G. Zampa, N. Zampa, and A. Zdziarski. The X/Gamma-ray Imaging Spectrometer (XGIS) for THESEUS and other mission opportunities. In J.-W. A. den Herder, S. Nikzad, and K. Nakazawa, editors, *Space Telescopes and Instrumentation 2022: Ultraviolet to Gamma Ray*, volume 12181 of *Society of Photo-Optical Instrumentation Engineers (SPIE) Conference Series*, page 1218126, Aug. 2022. doi: 10.1117/12.2630178.
- Z.-H. An, S. Antier, X.-Z. Bi, Q.-C. Bu, C. Cai, X.-L. Cao, A.-E. Camisasca, Z. Chang, G. Chen, L. Chen, T.-X. Chen, W. Chen, Y.-B. Chen, Y. Chen, Y.-P. Chen, M. W. Coughlin, W.-W. Cui, Z.-G. Dai, T. Hussenot-Desenonges, Y.-Q. Du, Y.-Y. Du, Y.-F. Du, C.-C. Fan, F. Frontera, H. Gao, M. Gao, M.-Y. Ge, K. Gong, Y.-D. Gu, J. Guan, D.-Y. Guo, Z.-W. Guo, C. Guidorzi, D.-W. Han, J.-J. He, J.-W. He, D.-J. Hou, Y. Huang, J. Huo, Z. Ji, S.-M. Jia, W.-C. Jiang, D. A. Kann, A. Klotz, L.-D. Kong, L. Lan, A. Li, B. Li, C.-Y. Li, C.-K. Li, G. Li, M.-S. Li, T.-P. Li, W. Li, X.-B. Li, X.-Q. Li, X.-F. Li, Y.-G. Li, Z.-W. Li, J. Liang, X.-H. Liang, J.-Y. Liao, L. Lin, C.-Z. Liu, H.-X. Liu, H.-W. Liu, J.-C. Liu, X.-J. Liu, Y.-Q. Liu, Y.-R. Liu, F.-J. Lu, H. Lu, X.-F. Lu, Q. Luo, T. Luo, B.-Y. Ma, F.-L. Ma, R.-C. Ma, X. Ma, R. Maccary, J.-R. Mao, B. Meng, J.-Y. Nie, M. Orlandini, G. Ou, J.-Q. Peng, W.-X. Peng, R. Qiao, J.-L. Qu, X.-Q. Ren, J.-Y. Shi, Q. Shi, L.-M. Song, X.-Y. Song, J. Su, G.-X. Sun, L. Sun, X.-L. Sun, W.-J. Tan, Y. Tan, L. Tao, Y.-L. Tuo, D. Turpin, J.-Z. Wang, C. Wang, C.-W. Wang, H.-J. Wang, H. Wang, J. Wang, L.-J. Wang, P.-J. Wang, P. Wang, W.-S. Wang, X.-Y. Wang, X.-L. Wang, Y.-S. Wang, Y. Wang, X.-Y. Wen, B.-B. Wu, B.-Y. Wu, H. Wu, S.-H. Xiao, S. Xiao, Y.-X. Xiao, S.-L. Xie, S.-L. Xiong, S.-L. Xiong, D. Xu, H. Xu, Y.-J. Xu, Y.-B. Xu, Y.-C. Xu, Y.-P. Xu, W.-C. Xue, S. Yang, Y.-J. Yang, Z.-X. Yang, W.-T. Ye, Q.-B. Yi, S.-X. Yi, Q.-Q. Yin, Y. You, Y.-W. Yu, W. Yu, W.-H. Yu, M. Zeng, B. Zhang, B.-B. Zhang, D.-L. Zhang, F. Zhang, H.-M. Zhang, J. Zhang, L. Zhang, P. Zhang, P. Zhang, S. Zhang, S.-N. Zhang, W.-C. Zhang, X.-F. Zhang, X.-L. Zhang, Y.-Q. Zhang, Y.-T. Zhang, Y.-F. Zhang, Y.-H. Zhang, Z. Zhang, G.-Y. Zhao, H.-S. Zhao, H.-Y. Zhao, Q.-X. Zhao, S.-J. Zhao, X.-Y. Zhao, X.-F. Zhao, Y. Zhao, C. Zheng, S.-J. Zheng, D.-K. Zhou, X. Zhou, and X.-C. Zhu. Insight-HXMT and GECAM-C observations of the brightest-of-all-time GRB 221009A. *arXiv e-prints*, art. arXiv:2303.01203, Mar. 2023. doi: 10.48550/arXiv.2303.01203.
- I. Arcavi, G. Hosseinzadeh, D. A. Howell, C. McCully, D. Poznanski, D. Kasen, J. Barnes, M. Zaltzman, S. Vasylyev, D. Maoz, and S. Valenti. Optical emission from a kilonova following a gravitational-wave-detected neutron-star merger. , 551(7678):64–66, Nov. 2017. doi: 10.1038/nature24291.
- Z. Arzoumanian, D. F. Chernoff, and J. M. Cordes. The Velocity Distribution of Isolated Radio Pulsars. , 568(1):289–301, Mar. 2002. doi: 10.1086/338805.
- A. Baldeschi and C. Guidorzi. Gamma-ray burst engines may have no memory. *A&A*, 573:L7, Jan. 2015. doi: 10.1051/0004-6361/201425264.

- J. Barnes and D. Kasen. Effect of a High Opacity on the Light Curves of Radioactively Powered Transients from Compact Object Mergers. , 775(1):18, Sept. 2013. doi: 10.1088/0004-637X/775/1/18.
- S. D. Barthelmy, L. M. Barbier, J. R. Cummings, E. E. Fenimore, N. Gehrels, D. Hullinger, H. A. Krimm, C. B. Markwardt, D. M. Palmer, A. Parsons, G. Sato, M. Suzuki, T. Takahashi, M. Tashiro, and J. Tueller. The Burst Alert Telescope (BAT) on the SWIFT Midex Mission. *Space Sci. Rev.*, 120:143–164, Oct. 2005. doi: 10.1007/s11214-005-5096-3.
- E. Berger, W. Fong, and R. Chornock. An r-process Kilonova Associated with the Short-hard GRB 130603B. , 774(2):L23, Sept. 2013. doi: 10.1088/2041-8205/774/2/L23.
- R. Birkel, M. A. Aloy, H. T. Janka, and E. Müller. Neutrino pair annihilation near accreting, stellar-mass black holes. , 463(1):51–67, Feb. 2007. doi: 10.1051/0004-6361:20066293.
- R. D. Blandford and R. L. Znajek. Electromagnetic extraction of energy from Kerr black holes. , 179:433–456, May 1977. doi: 10.1093/mnras/179.3.433.
- J. S. Bloom. *What are Gamma-Ray Bursts?* Princeton University Press, Princeton and Oxford, 2011.
- J. S. Bloom, S. G. Djorgovski, and S. R. Kulkarni. The Redshift and the Ordinary Host Galaxy of GRB 970228. , 554(2):678–683, June 2001. doi: 10.1086/321398.
- J. S. Bloom, J. X. Prochaska, D. Pooley, C. H. Blake, R. J. Foley, S. Jha, E. Ramirez-Ruiz, J. Granot, A. V. Filippenko, S. Sigurdsson, A. J. Barth, H. W. Chen, M. C. Cooper, E. E. Falco, R. R. Gal, B. F. Gerke, M. D. Gladders, J. E. Greene, J. Hennanwi, L. C. Ho, K. Hurley, B. P. Koester, W. Li, L. Lubin, J. Newman, D. A. Perley, G. K. Squires, and W. M. Wood-Vasey. Closing in on a Short-Hard Burst Progenitor: Constraints from Early-Time Optical Imaging and Spectroscopy of a Possible Host Galaxy of GRB 050509b. , 638(1):354–368, Feb. 2006. doi: 10.1086/498107.
- G. Boella, R. C. Butler, G. C. Perola, L. Piro, L. Scarsi, and J. A. M. Bleeker. BeppoSAX, the wide band mission for X-ray astronomy. , 122:299–307, Apr 1997. doi: 10.1051/aas:1997136.
- Ž. Bošnjak, D. Götz, L. Bouchet, S. Schanne, and B. Cordier. The spectral catalogue of INTEGRAL gamma-ray bursts. results of the joint IBIS/SPI spectral analysis. *A&A*, 561:A25, Jan. 2014. doi: 10.1051/0004-6361/201322256.
- M. S. Briggs, W. S. Paciesas, G. N. Pendleton, C. A. Meegan, G. J. Fishman, J. M. Horack, M. N. Brock, C. Kouveliotou, D. H. Hartmann, and J. Hakkila. BATSE Observations of the Large-Scale Isotropy of Gamma-Ray Bursts. *ApJ*, 459:40, Mar. 1996. doi: 10.1086/176867.
- O. Bromberg, E. Nakar, T. Piran, and R. Sari. Short versus Long and Collapsars versus Non-collapsars: A Quantitative Classification of Gamma-Ray Bursts. *ApJ*, 764:179, Feb. 2013. doi: 10.1088/0004-637X/764/2/179.

- T. M. Brown, N. Baliber, F. B. Bianco, M. Bowman, B. Burleson, P. Conway, M. Crellin, É. Depagne, J. De Vera, B. Dilday, D. Dragomir, M. Dubberley, J. D. Eastman, M. Elphick, M. Falarski, S. Foale, M. Ford, B. J. Fulton, J. Garza, E. L. Gomez, M. Graham, R. Greene, B. Haldeman, E. Hawkins, B. Haworth, R. Haynes, M. Hidas, A. E. Hjelmstrom, D. A. Howell, J. Hygelund, T. A. Lister, R. Lobdill, J. Martinez, D. S. Mullins, M. Norbury, J. Parrent, R. Paulson, D. L. Petry, A. Pickles, V. Posner, W. E. Rosing, R. Ross, D. J. Sand, E. S. Saunders, J. Shobbrook, A. Shporer, R. A. Street, D. Thomas, Y. Tsapras, J. R. Tufts, S. Valenti, K. Vander Horst, Z. Walker, G. White, and M. Willis. Las Cumbres Observatory Global Telescope Network. , 125:1031–1055, Sept. 2013. doi: 10.1086/673168.
- M. Bulla. POSSIS: predicting spectra, light curves, and polarization for multidimensional models of supernovae and kilonovae. , 489(4):5037–5045, Nov. 2019. doi: 10.1093/mnras/stz2495.
- M. Bulla, S. Covino, K. Kyutoku, M. Tanaka, J. R. Maund, F. Patat, K. Toma, K. Wiersema, J. Bruten, Z. P. Jin, and V. Testa. The origin of polarization in kilonovae and the case of the gravitational-wave counterpart AT 2017gfo. Nature Astronomy, 3:99–106, Mar. 2019. doi: 10.1038/s41550-018-0593-y.
- M. Bulla, A. E. Camisasca, C. Guidorzi, L. Amati, A. Rossi, G. Stratta, and P. Singh. GRB 230307A: good match with kilonova models. GRB Coordinates Network, 33578:1, Apr. 2023.
- E. M. Burbidge, G. R. Burbidge, W. A. Fowler, and F. Hoyle. Synthesis of the Elements in Stars. Reviews of Modern Physics, 29(4):547–650, Jan. 1957. doi: 10.1103/RevModPhys.29.547.
- E. Burns, A. Goldstein, S. Lesage, S. Dalessi, and Fermi-GBM Team. GRB 230307A: possibly the second highest GRB energy fluence ever identified. GRB Coordinates Network, 33414:1, Mar. 2023.
- D. N. Burrows, J. A. Kennea, A. F. Abbey, A. Beardmore, S. Campana, M. Capalbi, G. Chincarini, G. Cusumano, P. A. Evans, J. E. Hill, P. Giommi, M. Goad, O. Godet, A. Moretti, D. C. Morris, J. P. Osborne, C. Pagani, K. L. Page, M. Perri, J. Racusin, P. Romano, R. L. C. Starling, G. Tagliaferri, F. Tamburelli, L. G. Tyler, and R. Willingale. The Swift X-Ray Telescope: Status and Performance. arXiv e-prints, art. arXiv:0803.1844, Mar. 2008. doi: 10.48550/arXiv.0803.1844.
- A. G. W. Cameron. On the origin of the heavy elements. , 62:9–10, Feb. 1957. doi: 10.1086/107435.
- A. E. Camisasca, C. Guidorzi, M. Bulla, L. Amati, A. Rossi, G. Stratta, and P. Singh. GRB 230307A: short minimum variability timescale compatible with a merger origin. GRB Coordinates Network, 33577:1, Apr. 2023.
- Z. Cano, L. Izzo, A. de Ugarte Postigo, C. C. Thöne, T. Krühler, K. E. Heintz, D. Malesani, S. Geier, C. Fuentes, T.-W. Chen, S. Covino, V. D’Elia, J. P. U. Fynbo, P. Goldoni, A. Gomboc, J. Hjorth, P. Jakobsson, D. A. Kann, B. Milvang-Jensen, G. Pugliese, R. Sánchez-Ramírez, S. Schulze, J. Sollerman, N. R. Tanvir,

- and K. Wiersema. GRB 161219B/SN 2016jca: A low-redshift gamma-ray burst supernova powered by radioactive heating. *A&A*, 605:A107, Sept. 2017. doi: 10.1051/0004-6361/201731005.
- R. Chornock, E. Berger, D. Kasen, P. S. Cowperthwaite, M. Nicholl, V. A. Villar, K. D. Alexander, P. K. Blanchard, T. Eftekhari, W. Fong, R. Margutti, P. K. G. Williams, J. Annis, D. Brout, D. A. Brown, H. Y. Chen, M. R. Drout, B. Farr, R. J. Foley, J. A. Frieman, C. L. Fryer, K. Herner, D. E. Holz, R. Kessler, T. Matheson, B. D. Metzger, E. Quataert, A. Rest, M. Sako, D. M. Scolnic, N. Smith, and M. Soares-Santos. The Electromagnetic Counterpart of the Binary Neutron Star Merger LIGO/Virgo GW170817. IV. Detection of Near-infrared Signatures of r-process Nucleosynthesis with Gemini-South. , 848(2):L19, Oct. 2017. doi: 10.3847/2041-8213/aa905c.
- C. M. Copperwheat, I. A. Steele, R. M. Barnsley, S. D. Bates, N. R. Clay, H. Jermak, J. M. Marchant, C. J. Mottram, A. Piascik, and R. J. Smith. Liverpool Telescope and Liverpool Telescope 2. In *Revista Mexicana de Astronomia y Astrofisica Conference Series*, volume 48 of *Revista Mexicana de Astronomia y Astrofisica Conference Series*, pages 48–53, Dec. 2016.
- J. M. Cordes. Space velocities of radio pulsars from interstellar scintillations. , 311: 183–196, Dec. 1986. doi: 10.1086/164764.
- E. Costa, F. Frontera, J. Heise, M. Feroci, J. in’t Zand, F. Fiore, M. N. Cinti, D. Dal Fiume, L. Nicastro, M. Orlandini, E. Palazzi, M. Rapisarda, G. Zavattini, R. Jager, A. Parmar, A. Owens, S. Molendi, G. Cusumano, M. C. Maccarone, S. Giarrusso, A. Coletta, L. A. Antonelli, P. Giommi, J. M. Muller, L. Piro, and R. C. Butler. Discovery of an X-ray afterglow associated with the γ -ray burst of 28 February 1997. *Nature*, 387:783–785, June 1997. doi: 10.1038/42885.
- D. A. Coulter, R. J. Foley, C. D. Kilpatrick, M. R. Drout, A. L. Piro, B. J. Shappee, M. R. Siebert, J. D. Simon, N. Ulloa, D. Kasen, B. F. Madore, A. Murguía-Berthier, Y.-C. Pan, J. X. Prochaska, E. Ramirez-Ruiz, A. Rest, and C. Rojas-Bravo. Swope supernova survey 2017a (SSS17a), the optical counterpart to a gravitational wave source. *Science*, 358(6370):1556–1558, dec 2017. doi: 10.1126/science.aap9811.
- P. S. Cowperthwaite, E. Berger, V. A. Villar, B. D. Metzger, M. Nicholl, R. Chornock, P. K. Blanchard, W. Fong, R. Margutti, M. Soares-Santos, K. D. Alexander, S. Allam, J. Annis, D. Brout, D. A. Brown, R. E. Butler, H. Y. Chen, H. T. Diehl, Z. Doctor, M. R. Drout, T. Eftekhari, B. Farr, D. A. Finley, R. J. Foley, J. A. Frieman, C. L. Fryer, J. García-Bellido, M. S. S. Gill, J. Guillochon, K. Herner, D. E. Holz, D. Kasen, R. Kessler, J. Marriner, T. Matheson, J. Neilsen, E. H., E. Quataert, A. Palmese, A. Rest, M. Sako, D. M. Scolnic, N. Smith, D. L. Tucker, P. K. G. Williams, E. Balbinot, J. L. Carlin, E. R. Cook, F. Durret, T. S. Li, P. A. A. Lopes, A. C. C. Lourenço, J. L. Marshall, G. E. Medina, J. Muir, R. R. Muñoz, M. Sauseda, D. J. Schlegel, L. F. Secco, A. K. Vivas, W. Wester, A. Zenteno, Y. Zhang, T. M. C. Abbott, M. Banerji, K. Bechtol, A. Benoit-Lévy, E. Bertin, E. Buckley-Geer, D. L. Burke, D. Capozzi, A. Carnero Rosell, M. Carrasco Kind, F. J. Castander, M. Croce, C. E. Cunha, C. B. D’Andrea, L. N.

- da Costa, C. Davis, D. L. DePoy, S. Desai, J. P. Dietrich, A. Drlica-Wagner, T. F. Eifler, A. E. Evrard, E. Fernandez, B. Flaugher, P. Fosalba, E. Gaztanaga, D. W. Gerdes, T. Giannantonio, D. A. Goldstein, D. Gruen, R. A. Gruendl, G. Gutierrez, K. Honscheid, B. Jain, D. J. James, T. Jeltema, M. W. G. Johnson, M. D. Johnson, S. Kent, E. Krause, R. Kron, K. Kuehn, N. Nuropatkin, O. Lahav, M. Lima, H. Lin, M. A. G. Maia, M. March, P. Martini, R. G. McMahon, F. Menanteau, C. J. Miller, R. Miquel, J. J. Mohr, E. Neilsen, R. C. Nichol, R. L. C. Ogando, A. A. Plazas, N. Roe, A. K. Romer, A. Roodman, E. S. Rykoff, E. Sanchez, V. Scarpine, R. Schindler, M. Schubnell, I. Sevilla-Noarbe, M. Smith, R. C. Smith, F. Sobreira, E. Suchyta, M. E. C. Swanson, G. Tarle, D. Thomas, R. C. Thomas, M. A. Troxel, V. Vikram, A. R. Walker, R. H. Wechsler, J. Weller, B. Yanny, and J. Zuntz. The Electromagnetic Counterpart of the Binary Neutron Star Merger LIGO/Virgo GW170817. II. UV, Optical, and Near-infrared Light Curves and Comparison to Kilonova Models. , 848(2):L17, Oct. 2017. doi: 10.3847/2041-8213/aa8fc7.
- S. Dalessi, O. J. Roberts, C. Meegan, and Fermi GBM Team. GRB 230307A: Fermi GBM Observation of a very bright burst. GRB Coordinates Network, 33411:1, Mar. 2023.
- S. Dall’Osso, G. Stratta, R. Perna, G. De Cesare, and L. Stella. Magnetar Central Engines in Gamma-Ray Bursts Follow the Universal Relation of Accreting Magnetic Stars. , 949(2):L32, June 2023. doi: 10.3847/2041-8213/accecc.
- P. D’Avanzo. Short gamma-ray bursts: A review. Journal of High Energy Astrophysics, 7:73–80, Sept. 2015. doi: 10.1016/j.jheap.2015.07.002.
- A. de Ugarte Postigo, J. Gorosabel, D. Xu, D. Malesani, G. Leloudas, P. Jakobsson, T. Kruehler, A. A. Djupvik, E. Gafton, and T. Libbrecht. GRB 140512A: Redshift from NOT. GRB Coordinates Network, 16310:1, Jan. 2014.
- M. Della Valle, G. Chincarini, N. Panagia, G. Tagliaferri, D. Malesani, V. Testa, D. Fugazza, S. Campana, S. Covino, V. Mangano, L. A. Antonelli, P. D’Avanzo, K. Hurley, I. F. Mirabel, L. J. Pellizza, S. Piranomonte, and L. Stella. An enigmatic long-lasting γ -ray burst not accompanied by a bright supernova. Nature, 444:1050–1052, Dec. 2006. doi: 10.1038/nature05374.
- S. Dichiara, D. Tsang, E. Troja, D. Neill, J. P. Norris, and Y. H. Yang. A Luminous Precursor in the Extremely Bright GRB 230307A. , 954(1):L29, Sept. 2023. doi: 10.3847/2041-8213/acf21d.
- T. Dietrich, M. W. Coughlin, P. T. H. Pang, M. Bulla, J. Heinzl, L. Issa, I. Tews, and S. Antier. Multimessenger constraints on the neutron-star equation of state and the Hubble constant. Science, 370(6523):1450–1453, Dec. 2020. doi: 10.1126/science.abb4317.
- N. Domoto, M. Tanaka, S. Wanajo, and K. Kawaguchi. Signatures of r-process Elements in Kilonova Spectra. , 913(1):26, May 2021. doi: 10.3847/1538-4357/abf358.

- R. C. Duncan and C. Thompson. Formation of Very Strongly Magnetized Neutron Stars: Implications for Gamma-Ray Bursts. , 392:L9, June 1992. doi: 10.1086/186413.
- E. E. Fenimore, J. J. M. in 't Zand, J. P. Norris, J. T. Bonnell, and R. J. Nemiroff. Gamma-Ray Burst Peak Duration as a Function of Energy. *ApJ*, 448:L101, Aug. 1995. doi: 10.1086/309603.
- W. Fong, E. Berger, and D. B. Fox. Hubble Space Telescope Observations of Short Gamma-Ray Burst Host Galaxies: Morphologies, Offsets, and Local Environments. , 708(1):9–25, Jan 2010. doi: 10.1088/0004-637X/708/1/9.
- W. Fong, E. Berger, R. Chornock, R. Margutti, A. J. Levan, N. R. Tanvir, R. L. Tunnicliffe, I. Czekala, D. B. Fox, D. A. Perley, S. B. Cenko, B. A. Zauderer, T. Laskar, S. E. Persson, A. J. Monson, D. D. Kelson, C. Birk, D. Murphy, M. Servillat, and G. Anglada. Demographics of the Galaxies Hosting Short-duration Gamma-Ray Bursts. , 769(1):56, May 2013. doi: 10.1088/0004-637X/769/1/56.
- W. Fong, E. Berger, R. Margutti, and B. A. Zauderer. A Decade of Short-duration Gamma-Ray Burst Broadband Afterglows: Energetics, Circumburst Densities, and Jet Opening Angles. , 815(2):102, Dec 2015. doi: 10.1088/0004-637X/815/2/102.
- W.-f. Fong, A. E. Nugent, Y. Dong, E. Berger, K. Paterson, R. Chornock, A. Levan, P. Blanchard, K. D. Alexander, J. Andrews, B. E. Cobb, A. Cucchiara, D. Fox, C. L. Fryer, A. C. Gordon, C. D. Kilpatrick, R. Lunnan, R. Margutti, A. Miller, P. Milne, M. Nicholl, D. Perley, J. Rastinejad, A. Rouco Escorial, G. Schroeder, N. Smith, N. Tanvir, and G. Terreran. Short GRB Host Galaxies I: Photometric and Spectroscopic Catalogs, Host Associations, and Galactocentric Offsets. , 940(1):56, Nov. 2022. doi: 10.3847/1538-4357/ac91d0.
- D. B. Fox, D. A. Frail, P. A. Price, S. R. Kulkarni, E. Berger, T. Piran, A. M. Soderberg, S. B. Cenko, P. B. Cameron, A. Gal-Yam, M. M. Kasliwal, D. S. Moon, F. A. Harrison, E. Nakar, B. P. Schmidt, B. Penprase, R. A. Chevalier, P. Kumar, K. Roth, D. Watson, B. L. Lee, S. Sheckman, M. M. Phillips, M. Roth, P. J. McCarthy, M. Rauch, L. Cowie, B. A. Peterson, J. Rich, N. Kawai, K. Aoki, G. Kosugi, T. Totani, H. S. Park, A. MacFadyen, and K. C. Hurley. The afterglow of GRB 050709 and the nature of the short-hard γ -ray bursts. , 437(7060):845–850, Oct 2005. doi: 10.1038/nature04189.
- D. A. Frail, S. R. Kulkarni, R. Sari, S. G. Djorgovski, J. S. Bloom, T. J. Galama, D. E. Reichart, E. Berger, F. A. Harrison, P. A. Price, S. A. Yost, A. Diercks, R. W. Goodrich, and F. Chaffee. Beaming in Gamma-Ray Bursts: Evidence for a Standard Energy Reservoir. , 562(1):L55–L58, Nov 2001. doi: 10.1086/338119.
- F. Frontera. The key role of BeppoSAX in the GRB history. *Rendiconti Lincei. Scienze Fisiche e Naturali*, 30:171–184, Dec. 2019. doi: 10.1007/s12210-019-00766-z.

- A. S. Fruchter, A. J. Levan, L. Strolger, P. M. Vreeswijk, S. E. Thorsett, D. Bersier, I. Burud, J. M. Castro Cerón, A. J. Castro-Tirado, C. Conselice, T. Dahlen, H. C. Ferguson, J. P. U. Fynbo, P. M. Garnavich, R. A. Gibbons, J. Gorosabel, T. R. Gull, J. Hjorth, S. T. Holland, C. Kouveliotou, Z. Levay, M. Livio, M. R. Metzger, P. E. Nugent, L. Petro, E. Pian, J. E. Rhoads, A. G. Riess, K. C. Sahu, A. Smette, N. R. Tanvir, R. A. M. J. Wijers, and S. E. Woosley. Long γ -ray bursts and core-collapse supernovae have different environments. , 441(7092):463–468, May 2006. doi: 10.1038/nature04787.
- J. P. U. Fynbo, D. Watson, C. C. Thöne, J. Sollerman, J. S. Bloom, T. M. Davis, J. Hjorth, P. Jakobsson, U. G. Jørgensen, J. F. Graham, A. S. Fruchter, D. Bersier, L. Kewley, A. Cassan, J. M. Castro Cerón, S. Foley, J. Gorosabel, T. C. Hinse, K. D. Horne, B. L. Jensen, S. Klose, D. Kocevski, J.-B. Marquette, D. Perley, E. Ramirez-Ruiz, M. D. Stritzinger, P. M. Vreeswijk, R. A. M. Wijers, K. G. Woller, D. Xu, and M. Zub. No supernovae associated with two long-duration γ -ray bursts. *Nature*, 444:1047–1049, Dec. 2006. doi: 10.1038/nature05375.
- A. Gal-Yam, E. O. Ofek, D. Poznanski, A. Levinson, E. Waxman, D. A. Frail, A. M. Soderberg, E. Nakar, W. Li, and A. V. Filippenko. Radio and Optical Follow-up Observations of a Uniform Radio Transient Search: Implications for Gamma-Ray Bursts and Supernovae. , 639:331–339, Mar. 2006. doi: 10.1086/499157.
- T. J. Galama, P. M. Vreeswijk, J. van Paradijs, C. Kouveliotou, T. Augusteijn, H. Bönhardt, J. P. Brewer, V. Doublier, J.-F. Gonzalez, B. Leibundgut, C. Lidman, O. R. Hainaut, F. Patat, J. Heise, J. in’t Zand, K. Hurley, P. J. Groot, R. G. Strom, P. A. Mazzali, K. Iwamoto, K. Nomoto, H. Umeda, T. Nakamura, T. R. Young, T. Suzuki, T. Shigeyama, T. Koshut, M. Kippen, C. Robinson, P. de Wildt, R. A. M. J. Wijers, N. Tanvir, J. Greiner, E. Pian, E. Palazzi, F. Frontera, N. Masetti, L. Nicastro, M. Feroci, E. Costa, L. Piro, B. A. Peterson, C. Tinney, B. Boyle, R. Cannon, R. Stathakis, E. Sadler, M. C. Begam, and P. Ianna. An unusual supernova in the error box of the γ -ray burst of 25 April 1998. , 395: 670–672, Oct. 1998. doi: 10.1038/27150.
- N. Gehrels, G. Chincarini, P. Giommi, K. O. Mason, J. A. Nousek, A. A. Wells, N. E. White, S. D. Barthelmy, D. N. Burrows, L. R. Cominsky, K. C. Hurley, F. E. Marshall, P. Mészáros, P. W. A. Roming, L. Angelini, L. M. Barbier, T. Belloni, S. Campana, P. A. Caraveo, M. M. Chester, O. Citterio, T. L. Cline, M. S. Cropper, J. R. Cummings, A. J. Dean, E. D. Feigelson, E. E. Fenimore, D. A. Frail, A. S. Fruchter, G. P. Garmire, K. Gendreau, G. Ghisellini, J. Greiner, J. E. Hill, S. D. Hunsberger, H. A. Krimm, S. R. Kulkarni, P. Kumar, F. Lebrun, N. M. Lloyd-Ronning, C. B. Markwardt, B. J. Mattson, R. F. Mushotzky, J. P. Norris, J. Osborne, B. Paczynski, D. M. Palmer, H.-S. Park, A. M. Parsons, J. Paul, M. J. Rees, C. S. Reynolds, J. E. Rhoads, T. P. Sasseen, B. E. Schaefer, A. T. Short, A. P. Smale, I. A. Smith, L. Stella, G. Tagliaferri, T. Takahashi, M. Tashiro, L. K. Townsley, J. Tueller, M. J. L. Turner, M. Vietri, W. Voges, M. J. Ward, R. Willingale, F. M. Zerbi, and W. W. Zhang. The Swift Gamma-Ray Burst Mission. *ApJ*, 611:1005–1020, Aug. 2004. doi: 10.1086/422091.
- N. Gehrels, C. L. Sarazin, P. T. O’Brien, B. Zhang, L. Barbier, S. D. Barthelmy, A. Blustin, D. N. Burrows, J. Cannizzo, J. R. Cummings, M. Goad, S. T. Hol-

- land, C. P. Hurkett, J. A. Kennea, A. Levan, C. B. Markwardt, K. O. Mason, P. Meszaros, M. Page, D. M. Palmer, E. Rol, T. Sakamoto, R. Willingale, L. Angelini, A. Beardmore, P. T. Boyd, A. Breeveld, S. Campana, M. M. Chester, G. Chincarini, L. R. Cominsky, G. Cusumano, M. de Pasquale, E. E. Fenimore, P. Giommi, C. Gronwall, D. Grupe, J. E. Hill, D. Hinshaw, J. Hjorth, D. Hullinger, K. C. Hurley, S. Kloze, S. Kobayashi, C. Kouveliotou, H. A. Krimm, V. Mangano, F. E. Marshall, K. McGowan, A. Moretti, R. F. Mushotzky, K. Nakazawa, J. P. Norris, J. A. Nousek, J. P. Osborne, K. Page, A. M. Parsons, S. Patel, M. Perri, T. Poole, P. Romano, P. W. A. Roming, S. Rosen, G. Sato, P. Schady, A. P. Smale, J. Sollerman, R. Starling, M. Still, M. Suzuki, G. Tagliaferri, T. Takahashi, M. Tashiro, J. Tueller, A. A. Wells, N. E. White, and R. A. M. J. Wijers. A short γ -ray burst apparently associated with an elliptical galaxy at redshift $z = 0.225$. , 437(7060):851–854, Oct 2005. doi: 10.1038/nature04142.
- N. Gehrels, J. P. Norris, S. D. Barthelmy, J. Granot, Y. Kaneko, C. Kouveliotou, C. B. Markwardt, P. Mészáros, E. Nakar, J. A. Nousek, P. T. O’Brien, M. Page, D. M. Palmer, A. M. Parsons, P. W. A. Roming, T. Sakamoto, C. L. Sarazin, P. Schady, M. Stamatikos, and S. E. Woosley. A new γ -ray burst classification scheme from GRB060614. *Nature*, 444:1044–1046, Dec. 2006. doi: 10.1038/nature05376.
- G. Ghisellini. Gamma ray bursts: some facts and ideas. *arXiv e-prints*, art. astro-ph/0111584, Nov. 2001. doi: 10.48550/arXiv.astro-ph/0111584.
- J. H. Gillanders, E. Troja, C. L. Fryer, M. Ristic, B. O’Connor, C. J. Fontes, Y.-H. Yang, N. Domoto, S. Rahmouni, M. Tanaka, O. D. Fox, and S. Dichiara. Heavy element nucleosynthesis associated with a gamma-ray burst. *arXiv e-prints*, art. arXiv:2308.00633, Aug. 2023. doi: 10.48550/arXiv.2308.00633.
- A. Goldstein, P. Veres, E. Burns, M. S. Briggs, R. Hamburg, D. Kocevski, C. A. Wilson-Hodge, R. D. Preece, S. Poolakkil, O. J. Roberts, C. M. Hui, V. Connaughton, J. Racusin, A. von Kienlin, T. Dal Canton, N. Christensen, T. Littenberg, K. Siellez, L. Blackburn, J. Broida, E. Bissaldi, W. H. Cleveland, M. H. Gibby, M. M. Giles, R. M. Kippen, S. McBreen, J. McEnery, C. A. Meegan, W. S. Paciesas, and M. Stanbro. An Ordinary Short Gamma-Ray Burst with Extraordinary Implications: Fermi-GBM Detection of GRB 170817A. , 848(2):L14, Oct 2017. doi: 10.3847/2041-8213/aa8f41.
- V. Z. Golkhou, N. R. Butler, and O. M. Littlejohns. The Energy Dependence of GRB Minimum Variability Timescales. *ApJ*, 811:93, Oct. 2015. doi: 10.1088/0004-637X/811/2/93.
- J. Goodman. Are gamma-ray bursts optically thick? , 308:L47, Sep 1986. doi: 10.1086/184741.
- O. Gottlieb, A. Levinson, and E. Nakar. High efficiency photospheric emission entailed by formation of a collimation shock in gamma-ray bursts. , 488(1):1416–1426, Sept. 2019. doi: 10.1093/mnras/stz1828.
- O. Gottlieb, O. Bromberg, C. B. Singh, and E. Nakar. The structure of weakly magnetized γ -ray burst jets. , 498(3):3320–3333, Nov. 2020a. doi: 10.1093/mnras/staa2567.

- O. Gottlieb, A. Levinson, and E. Nakar. Intermittent hydrodynamic jets in collapsars do not produce GRBs. , 495(1):570–577, June 2020b. doi: 10.1093/mnras/staa1216.
- O. Gottlieb, O. Bromberg, A. Levinson, and E. Nakar. Intermittent mildly magnetized jets as the source of GRBs. , 504(3):3947–3955, July 2021a. doi: 10.1093/mnras/stab1068.
- O. Gottlieb, E. Nakar, and O. Bromberg. The structure of hydrodynamic γ -ray burst jets. , 500(3):3511–3526, Jan. 2021b. doi: 10.1093/mnras/staa3501.
- O. Gottlieb, M. Liska, A. Tchekhovskoy, O. Bromberg, A. Lalakos, D. Giannios, and P. Mösta. Black Hole to Photosphere: 3D GRMHD Simulations of Collapsars Reveal Wobbling and Hybrid Composition Jets. , 933(1):L9, July 2022. doi: 10.3847/2041-8213/ac7530.
- C. Guidorzi. MEPSA: a flexible peak search algorithm designed for uniformly spaced time series. *Astronomy and Computing*, 10:54–60, Apr. 2015. ISSN 2213-1337. doi: 10.1016/j.ascom.2015.01.001. URL <http://www.sciencedirect.com/science/article/pii/S2213133715000025>.
- C. Guidorzi, A. Monfardini, A. Gomboc, C. J. Mottram, C. G. Mundell, I. A. Steele, D. Carter, M. F. Bode, R. J. Smith, S. N. Fraser, M. J. Burgdorf, and A. M. Newsam. The Automatic Real-Time Gamma-Ray Burst Pipeline of the 2 m Liverpool Telescope. *PASP*, 118:288–296, Feb. 2006. doi: 10.1086/499289.
- C. Guidorzi, S. Dichiara, F. Frontera, R. Margutti, A. Baldeschi, and L. Amati. A Common Stochastic Process Rules Gamma-Ray Burst Prompt Emission and X-Ray Flares. *ApJ*, 801:57, Mar. 2015. doi: 10.1088/0004-637X/801/1/57.
- F. A. Harrison, J. S. Bloom, D. A. Frail, R. Sari, S. R. Kulkarni, S. G. Djorgovski, T. Axelrod, J. Mould, B. P. Schmidt, M. H. Wieringa, R. M. Wark, R. Subrahmanyam, D. McConnell, P. J. McCarthy, B. E. Schaefer, R. G. McMahon, R. O. Markze, E. Firth, P. Soffitta, and L. Amati. Optical and Radio Observations of the Afterglow from GRB 990510: Evidence for a Jet. , 523(2):L121–L124, Oct. 1999. doi: 10.1086/312282.
- J. Hjorth, J. Sollerman, J. Gorosabel, J. Granot, S. Klose, C. Kouveliotou, J. Melinder, E. Ramirez-Ruiz, R. Starling, B. Thomsen, M. I. Andersen, J. P. U. Fynbo, B. L. Jensen, P. M. Vreeswijk, J. M. Castro Cerón, P. Jakobsson, A. Levan, K. Pedersen, J. E. Rhoads, N. R. Tanvir, D. Watson, and R. A. M. J. Wijers. GRB 050509B: Constraints on Short Gamma-Ray Burst Models. , 630(2):L117–L120, Sept. 2005. doi: 10.1086/491733.
- I. Horváth, Z. Bagoly, L. G. Balázs, A. de Ugarte Postigo, P. Veres, and A. Mészáros. Detailed Classification of Swift ’s Gamma-ray Bursts. *ApJ*, 713:552–557, Apr. 2010. doi: 10.1088/0004-637X/713/1/552.
- A. Janiuk and B. Kaminski. Nucleosynthesis of elements in the outflows from gamma ray bursts. In J.-U. Ness, editor, *The X-ray Universe 2014*, page 261, July 2014.

- A. Janiuk and K. Sapountzis. Gamma Ray Bursts. Progenitors, accretion in the central engine, jet acceleration mechanisms. *arXiv e-prints*, art. arXiv:1803.07873, Mar. 2018. doi: 10.48550/arXiv.1803.07873.
- H. Jermak, I. A. Steele, and R. J. Smith. MOPTOP: a multi-colour optimised optical polarimeter. In C. J. Evans, L. Simard, and H. Takami, editors, *Ground-based and Airborne Instrumentation for Astronomy VI*, volume 9908 of *Society of Photo-Optical Instrumentation Engineers (SPIE) Conference Series*, page 99084I, Aug. 2016. doi: 10.1117/12.2232324.
- Z.-P. Jin, X. Li, Z. Cano, S. Covino, Y.-Z. Fan, and D.-M. Wei. The Light Curve of the Macronova Associated with the LongShort Burst GRB 060614. *ApJ*, 811:L22, Oct. 2015. doi: 10.1088/2041-8205/811/2/L22.
- Z.-P. Jin, S. Covino, N.-H. Liao, X. Li, P. D’Avanzo, Y.-Z. Fan, and D.-M. Wei. A kilonova associated with GRB 070809. *Nature Astronomy*, 4:77–82, Jan. 2020. doi: 10.1038/s41550-019-0892-y.
- D. Kasen, B. Metzger, J. Barnes, E. Quataert, and E. Ramirez-Ruiz. Origin of the heavy elements in binary neutron-star mergers from a gravitational-wave event. , 551(7678):80–84, Nov. 2017. doi: 10.1038/nature24453.
- M. M. Kasliwal, D. Kasen, R. M. Lau, D. A. Perley, S. Rosswog, E. O. Ofek, K. Hotokezaka, R.-R. Chary, J. Sollerman, A. Goobar, and D. L. Kaplan. Spitzer mid-infrared detections of neutron star merger GW170817 suggests synthesis of the heaviest elements. , 510(1):L7–L12, Feb. 2022. doi: 10.1093/mnrasl/slz007.
- C. D. Kilpatrick, R. J. Foley, D. Kasen, A. Murguia-Berthier, E. Ramirez-Ruiz, D. A. Coulter, M. R. Drout, A. L. Piro, B. J. Shappee, K. Boutsia, C. Contreras, F. Di Mille, B. F. Madore, N. Morrell, Y. C. Pan, J. X. Prochaska, A. Rest, C. Rojas-Bravo, M. R. Siebert, J. D. Simon, and N. Ulloa. Electromagnetic evidence that SSS17a is the result of a binary neutron star merger. *Science*, 358(6370):1583–1587, Dec. 2017. doi: 10.1126/science.aaq0073.
- R. W. Klebesadel, I. B. Strong, and R. A. Olson. Observations of Gamma-Ray Bursts of Cosmic Origin. , 182:L85, June 1973. doi: 10.1086/181225.
- S. Kobayashi, T. Piran, and R. Sari. Can Internal Shocks Produce the Variability in Gamma-Ray Bursts? *ApJ*, 490:92, Nov. 1997. doi: 10.1086/512791.
- D. Kocevski and V. Petrosian. On the Lack of Time Dilation Signatures in Gamma-Ray Burst Light Curves. , 765(2):116, Mar. 2013. doi: 10.1088/0004-637X/765/2/116.
- O. Korobkin, R. T. Wollaeger, C. L. Fryer, A. L. Hungerford, S. Rosswog, C. J. Fontes, M. R. Mumpower, E. A. Chase, W. P. Even, J. Miller, G. W. Misch, and J. Lippuner. Axisymmetric Radiative Transfer Models of Kilonovae. , 910(2):116, Apr. 2021. doi: 10.3847/1538-4357/abe1b5.
- C. Kouveliotou, C. A. Meegan, G. J. Fishman, N. P. Bhat, M. S. Briggs, T. M. Koshut, W. S. Paciesas, and G. N. Pendleton. Identification of two classes of gamma-ray bursts. *ApJ*, 413:L101–L104, Aug. 1993. doi: 10.1086/186969.

- C. Kouveliotou, J. Granot, J. L. Racusin, E. Bellm, G. Vianello, S. Oates, C. L. Fryer, S. E. Boggs, F. E. Christensen, W. W. Craig, C. D. Dermer, N. Gehrels, C. J. Hailey, F. A. Harrison, A. Melandri, J. E. McEnery, C. G. Mundell, D. K. Stern, G. Tagliaferri, and W. W. Zhang. NuSTAR Observations of GRB 130427A Establish a Single Component Synchrotron Afterglow Origin for the Late Optical to Multi-GeV Emission. *ApJ*, 779:L1, Dec. 2013. doi: 10.1088/2041-8205/779/1/L1.
- P. Kumar and J. Granot. The Evolution of a Structured Relativistic Jet and Gamma-Ray Burst Afterglow Light Curves. *ApJ*, 591:1075–1085, July 2003. doi: 10.1086/375186.
- G. P. Lamb, N. R. Tanvir, A. J. Levan, A. de Ugarte Postigo, K. Kawaguchi, A. Corsi, P. A. Evans, B. Gompertz, D. B. Malesani, K. L. Page, K. Wiersema, S. Rosswog, M. Shibata, M. Tanaka, A. J. van der Horst, Z. Cano, J. P. U. Fynbo, A. S. Fruchter, J. Greiner, K. E. Heintz, A. Higgins, J. Hjorth, L. Izzo, P. Jakobsson, D. A. Kann, P. T. O’Brien, D. A. Perley, E. Pian, G. Pugliese, R. L. C. Starling, C. C. Thöne, D. Watson, R. A. M. J. Wijers, and D. Xu. Short GRB 160821B: A Reverse Shock, a Refreshed Shock, and a Well-sampled Kilonova. , 883(1):48, Sept. 2019. doi: 10.3847/1538-4357/ab38bb.
- N. Langer, A. J. van Marle, and S. C. Yoon. Wolf-Rayet stars as gamma-ray burst progenitors. , 54(3-6):206–210, Mar. 2010. doi: 10.1016/j.newar.2010.09.012.
- J. Larsson, A. J. Levan, M. B. Davies, and A. S. Fruchter. A new constraint for gamma-ray burst progenitor mass. , 376(3):1285–1290, Apr. 2007. doi: 10.1111/j.1365-2966.2007.11523.x.
- D. Lazzati. Precursor activity in bright, long BATSE gamma-ray bursts. *MNRAS*, 357:722–731, Feb. 2005. doi: 10.1111/j.1365-2966.2005.08687.x.
- M. Leng and D. Giannios. Testing the neutrino annihilation model for launching GRB jets. , 445:L1–L5, Nov. 2014. doi: 10.1093/mnras/slu122.
- A. Levan, B. P. Gompertz, O. S. Salafia, M. Bulla, E. Burns, K. Hotokezaka, L. Izzo, G. P. Lamb, D. B. Malesani, S. R. Oates, M. E. Ravasio, A. Rouco Escorial, B. Schneider, N. Sarin, S. Schulze, N. R. Tanvir, K. Ackley, G. Anderson, G. B. Brammer, L. Christensen, V. S. Dhillon, P. A. Evans, M. Fausnaugh, W. F. Fong, A. S. Fruchter, C. Fryer, J. P. U. Fynbo, N. Gaspari, K. E. Heintz, J. Hjorth, J. A. Kennea, M. R. Kennedy, T. Laskar, G. Leloudas, I. Mandel, A. Martin-Carrillo, B. D. Metzger, M. Nicholl, A. Nugent, J. T. Palmerio, G. Pugliese, J. Rastinejad, L. Rhodes, A. Rossi, S. J. Smartt, H. F. Stevance, A. Tohuvavohu, A. van der Horst, S. D. Vergani, D. Watson, T. Barclay, K. Bhirimbhakdi, E. Breedt, A. A. Breeveld, A. J. Brown, S. Campana, A. A. Chrimes, P. D’Avanzo, V. D’Elia, M. De Pasquale, M. J. Dyer, D. K. Galloway, J. A. Garbutt, M. J. Green, D. H. Hartmann, P. Jakobsson, P. Kerry, D. Langeroodi, J. K. Leung, S. P. Littlefair, J. Munday, P. O’Brien, S. G. Parsons, I. Pelisoli, A. Saccardi, D. I. Sahman, R. Salvaterra, B. Sbarufatti, D. Steeghs, G. Tagliaferri, C. C. Thöne, A. de Ugarte Postigo, and D. A. Kann. JWST detection of heavy neutron capture elements in a compact object merger. *arXiv e-prints*, art. arXiv:2307.02098, July 2023. doi: 10.48550/arXiv.2307.02098.

- A. J. Levan. *Gamma-Ray Bursts*. 2018. doi: 10.1088/2514-3433/aae164.
- C. K. Li, L. Lin, S. L. Xiong, M. Y. Ge, X. B. Li, T. P. Li, F. J. Lu, S. N. Zhang, Y. L. Tuo, Y. Nang, B. Zhang, S. Xiao, Y. Chen, L. M. Song, Y. P. Xu, C. Z. Liu, S. M. Jia, X. L. Cao, J. L. Qu, S. Zhang, Y. D. Gu, J. Y. Liao, X. F. Zhao, Y. Tan, J. Y. Nie, H. S. Zhao, S. J. Zheng, Y. G. Zheng, Q. Luo, C. Cai, B. Li, W. C. Xue, Q. C. Bu, Z. Chang, G. Chen, L. Chen, T. X. Chen, Y. B. Chen, Y. P. Chen, W. Cui, W. W. Cui, J. K. Deng, Y. W. Dong, Y. Y. Du, M. X. Fu, G. H. Gao, H. Gao, M. Gao, Y. D. Gu, J. Guan, C. C. Guo, D. W. Han, Y. Huang, J. Huo, L. H. Jiang, W. C. Jiang, J. Jin, Y. J. Jin, L. D. Kong, G. Li, M. S. Li, W. Li, X. Li, X. F. Li, Y. G. Li, Z. W. Li, X. H. Liang, B. S. Liu, G. Q. Liu, H. W. Liu, X. J. Liu, Y. N. Liu, B. Lu, X. F. Lu, T. Luo, X. Ma, B. Meng, G. Ou, N. Sai, R. C. Shang, X. Y. Song, L. Sun, L. Tao, C. Wang, G. F. Wang, J. Wang, W. S. Wang, Y. S. Wang, X. Y. Wen, B. B. Wu, B. Y. Wu, M. Wu, G. C. Xiao, H. Xu, J. W. Yang, S. Yang, Y. J. Yang, Y. J. Yang, Q. B. Yi, Q. Q. Yin, Y. You, W. C. Zhang, W. Z. Zhang, Y. Zhang, Y. Zhang, Y. F. Zhang, Y. J. Zhang, Z. Zhang, Z. Zhang, Z. L. Zhang, D. K. Zhou, J. F. Zhou, Y. Zhu, Y. X. Zhu, and R. L. Zhuang. HXMT identification of a non-thermal X-ray burst from SGR J1935+2154 and with FRB 200428. *Nature Astronomy*, 5:378, Jan. 2021.
- D. R. Lorimer, M. Bailes, M. A. McLaughlin, D. J. Narkevic, and F. Crawford. A Bright Millisecond Radio Burst of Extragalactic Origin. *Science*, 318:777, Nov. 2007. doi: 10.1126/science.1147532.
- G. A. MacLachlan, A. Shenoy, E. Sonbas, K. S. Dhuga, B. E. Cobb, T. N. Ukwatta, D. C. Morris, A. Eskandarian, L. C. Maximon, and W. C. Parke. Minimum variability time-scales of long and short GRBs. , 432(2):857–865, June 2013. doi: 10.1093/mnras/stt241.
- I. Mandel. The Orbit of GW170817 Was Inclined by Less Than 28° to the Line of Sight. , 853(1):L12, Jan. 2018. doi: 10.3847/2041-8213/aaa6c1.
- I. Mandel and S. E. de Mink. Merging binary black holes formed through chemically homogeneous evolution in short-period stellar binaries. , 458(3):2634–2647, May 2016. doi: 10.1093/mnras/stw379.
- R. Margutti, E. Berger, W. Fong, C. Guidorzi, K. D. Alexander, B. D. Metzger, P. K. Blanchard, P. S. Cowperthwaite, R. Chornock, T. Eftekhari, M. Nicholl, V. A. Villar, P. K. G. Williams, J. Annis, D. A. Brown, H. Chen, Z. Doctor, J. A. Frieman, D. E. Holz, M. Sako, and M. Soares-Santos. The Electromagnetic Counterpart of the Binary Neutron Star Merger LIGO/Virgo GW170817. V. Rising X-Ray Emission from an Off-axis Jet. , 848:L20, Oct. 2017. doi: 10.3847/2041-8213/aa9057.
- B. McBreen, K. J. Hurley, R. Long, and L. Metcalfe. Lognormal Distributions in Gamma-Ray Bursts and Cosmic Lightning. *MNRAS*, 271:662, Dec. 1994.
- S. Mereghetti, S. Balman, M. Caballero-Garcia, M. Del Santo, V. Doroshenko, M. H. Erkut, L. Hanlon, P. Hoefflich, A. Markowitz, J. P. Osborne, E. Pian, L. Rivera Sandoval, N. Webb, L. Amati, E. Ambrosi, A. P. Beardmore, A. Blain, E. Bozzo, L. Burderi, S. Campana, P. Casella, A. D’Aí, F. D’Ammando, F. De Colle,

- M. Della Valle, D. De Martino, T. Di Salvo, M. Doyle, P. Esposito, F. Frontera, P. Gandhi, G. Ghisellini, D. Gotz, V. Grinberg, C. Guidorzi, R. Hudec, R. Iaria, L. Izzo, G. K. Jaisawal, P. G. Jonker, A. K. H. Kong, M. Krumpe, P. Kumar, A. Manousakis, A. Marino, A. Martin-Carrillo, R. Mignani, G. Miniutti, C. G. Mundell, K. Mukai, A. A. Nucita, P. T. O'Brien, M. Orlandini, M. Orio, E. Palazzi, A. Papitto, F. Pintore, S. Piranomonte, D. Porquet, C. Ricci, A. Riggio, M. Rigoselli, J. Rodriguez, T. Saha, A. Sanna, A. Santangelo, R. Saxton, L. Sidoli, H. Stiele, G. Tagliaferri, F. Tavecchio, A. Tiengo, S. Tsygankov, S. Turiziani, R. Wijnands, S. Zane, and B. Zhang. Time domain astronomy with the THESEUS satellite. *Experimental Astronomy*, 52(3):309–406, Dec. 2021. doi: 10.1007/s10686-021-09809-6.
- P. Meszaros and M. J. Rees. Optical and Long-Wavelength Afterglow from Gamma-Ray Bursts. *ApJ*, 476:232, Feb. 1997. doi: 10.1086/303625.
- B. D. Metzger. Kilonovae. *Living Reviews in Relativity*, 23(1):1, Dec. 2019. doi: 10.1007/s41114-019-0024-0.
- B. D. Metzger, D. Giannios, T. A. Thompson, N. Bucciantini, and E. Quataert. The protomagnetar model for gamma-ray bursts. *MNRAS*, 413:2031–2056, May 2011. doi: 10.1111/j.1365-2966.2011.18280.x.
- B. D. Metzger, E. Berger, and B. Margalit. Millisecond Magnetar Birth Connects FRB 121102 to Superluminous Supernovae and Long-duration Gamma-Ray Bursts. , 841:14, May 2017. doi: 10.3847/1538-4357/aa633d.
- B. J. Morsony, D. Lazzati, and M. C. Begelman. Temporal and Angular Properties of Gamma-Ray Burst Jets Emerging from Massive Stars. *ApJ*, 665:569–598, Aug. 2007. doi: 10.1086/519483.
- E. Nakar, T. Piran, and J. Granot. The Detectability of Orphan Afterglows. , 579(2):699–705, Nov 2002. doi: 10.1086/342791.
- R. Narayan and P. Kumar. A turbulent model of gamma-ray burst variability. *MNRAS*, 394:L117–L120, Mar. 2009. doi: 10.1111/j.1745-3933.2009.00624.x.
- R. Narayan, B. Paczynski, and T. Piran. Gamma-ray bursts as the death throes of massive binary stars. *ApJ*, 395:L83–L86, Aug. 1992. doi: 10.1086/186493.
- L. Nativi, M. Bulla, S. Rosswog, C. Lundman, G. Kowal, D. Gizzi, G. P. Lamb, and A. Perego. Can jets make the radioactively powered emission from neutron star mergers bluer? , 500(2):1772–1783, Jan. 2021. doi: 10.1093/mnras/staa3337.
- L. Nava, L. Sironi, G. Ghisellini, A. Celotti, and G. Ghirlanda. Afterglow emission in gamma-ray bursts - I. Pair-enriched ambient medium and radiative blast waves. , 433(3):2107–2121, Aug. 2013. doi: 10.1093/mnras/stt872.
- J. P. Norris and J. T. Bonnell. Short Gamma-Ray Bursts with Extended Emission. *ApJ*, 643:266–275, May 2006. doi: 10.1086/502796.
- J. P. Norris, R. J. Nemiroff, J. T. Bonnell, J. D. Scargle, C. Kouveliotou, W. S. Paciesas, C. A. Meegan, and G. J. Fishman. Attributes of Pulses in Long Bright Gamma-Ray Bursts. *ApJ*, 459:393, Mar. 1996. doi: 10.1086/176902.

- J. P. Norris, J. T. Bonnell, D. Kazanas, J. D. Scargle, J. Hakkila, and T. W. Giblin. Long-Lag, Wide-Pulse Gamma-Ray Bursts. *ApJ*, 627:324–345, July 2005. doi: 10.1086/430294.
- B. O’Connor, E. Troja, G. Ryan, P. Beniamini, H. van Eerten, J. Granot, S. Dichiara, R. Ricci, V. Lipunov, J. H. Gillanders, R. Gill, M. Moss, S. Anand, I. Andreoni, R. L. Becerra, D. A. H. Buckley, N. R. Butler, S. B. Cenko, A. Chasovnikov, J. Durbak, C. Francile, E. Hammerstein, A. J. van der Horst, M. Kasliwal, C. Kouveliotou, A. S. Kutyrev, W. H. Lee, G. Srinivasaragavan, V. Topolev, A. M. Watson, Y. H. Yang, and K. Zhirkov. A structured jet explains the extreme GRB 221009A. *arXiv e-prints*, art. arXiv:2302.07906, Feb. 2023. doi: 10.48550/arXiv.2302.07906.
- A. Perego, S. Rosswog, R. M. Cabezón, O. Korobkin, R. Käppeli, A. Arcones, and M. Liebendörfer. Neutrino-driven winds from neutron star merger remnants. , 443(4):3134–3156, Oct. 2014. doi: 10.1093/mnras/stu1352.
- R. Perna and K. Belczynski. Short Gamma-Ray Bursts and Mergers of Compact Objects: Observational Constraints. , 570(1):252–263, May 2002. doi: 10.1086/339571.
- M. Petropoulou, P. Beniamini, G. Vasilopoulos, D. Giannios, and R. Barniol Duran. Deciphering the properties of the central engine in GRB collapsars. , 496(3): 2910–2921, June 2020. doi: 10.1093/mnras/staa1695.
- E. Pian, P. D’Avanzo, S. Benetti, M. Branchesi, E. Brocato, S. Campana, E. Cappellaro, S. Covino, V. D’Elia, J. P. U. Fynbo, F. Getman, G. Ghirlanda, G. Ghisellini, A. Grado, G. Greco, J. Hjorth, C. Kouveliotou, A. Levan, L. Limatola, D. Malesani, P. A. Mazzali, A. Melandri, P. Møller, L. Nicastro, E. Palazzi, S. Piranomonte, A. Rossi, O. S. Salafia, J. Selsing, G. Stratta, M. Tanaka, N. R. Tanvir, L. Tomasella, D. Watson, S. Yang, L. Amati, L. A. Antonelli, S. Ascenzi, M. G. Bernardini, M. Boër, F. Bufano, A. Bulgarelli, M. Capaccioli, P. Casella, A. J. Castro-Tirado, E. Chassande-Mottin, R. Ciolfi, C. M. Copperwheat, M. Dadina, G. De Cesare, A. di Paola, Y. Z. Fan, B. Gendre, G. Giuffrida, A. Giunta, L. K. Hunt, G. L. Israel, Z. P. Jin, M. M. Kasliwal, S. Klose, M. Lisi, F. Longo, E. Maiorano, M. Mapelli, N. Masetti, L. Nava, B. Patricelli, D. Perley, A. Pescalli, T. Piran, A. Possenti, L. Pulone, M. Razzano, R. Salvaterra, P. Schipani, M. Spera, A. Stamerra, L. Stella, G. Tagliaferri, V. Testa, E. Troja, M. Turatto, S. D. Vergani, and D. Vergani. Spectroscopic identification of r-process nucleosynthesis in a double neutron-star merger. , 551(7678):67–70, Nov. 2017. doi: 10.1038/nature24298.
- T. Piran. The physics of gamma-ray bursts. *Reviews of Modern Physics*, 76:1143–1210, Oct. 2004. doi: 10.1103/RevModPhys.76.1143.
- R. Popham, S. E. Woosley, and C. Fryer. Hyperaccreting Black Holes and Gamma-Ray Bursts. *ApJ*, 518:356–374, June 1999. doi: 10.1086/307259.
- R. D. Preece, M. S. Briggs, R. S. Mallozzi, G. N. Pendleton, W. S. Paciesas, and D. L. Band. The BATSE Gamma-Ray Burst Spectral Catalog. I. High Time Resolution Spectroscopy of Bright Bursts Using High Energy Resolution Data. *ApJS*, 126:19–36, Jan. 2000. doi: 10.1086/313289.

- J. L. Racusin, S. V. Karpov, M. Sokolowski, J. Granot, X. F. Wu, V. Pal'Shin, S. Covino, A. J. van der Horst, S. R. Oates, P. Schady, R. J. Smith, J. Cummings, R. L. C. Starling, L. W. Piotrowski, B. Zhang, P. A. Evans, S. T. Holland, K. Malek, M. T. Page, L. Vetere, R. Margutti, C. Guidorzi, A. P. Kamble, P. A. Curran, A. Beardmore, C. Kouveliotou, L. Mankiewicz, A. Melandri, P. T. O'Brien, K. L. Page, T. Piran, N. R. Tanvir, G. Wrochna, R. L. Aptekar, S. Barthelmy, C. Bartolini, G. M. Beskin, S. Bondar, M. Bremer, S. Campana, A. Castro-Tirado, A. Cucchiara, M. Cwiok, P. D'Avanzo, V. D'Elia, M. Della Valle, A. de Ugarte Postigo, W. Dominik, A. Falcone, F. Fiore, D. B. Fox, D. D. Frederiks, A. S. Fruchter, D. Fugazza, M. A. Garrett, N. Gehrels, S. Golenetskii, A. Gomboc, J. Gorosabel, G. Greco, A. Guarnieri, S. Immler, M. Jelinek, G. Kasprowicz, V. La Parola, A. J. Levan, V. Mangano, E. P. Mazets, E. Molinari, A. Moretti, K. Nawrocki, P. P. Oleynik, J. P. Osborne, C. Paganì, S. B. Pandey, Z. Paragi, M. Perri, A. Piccioni, E. Ramirez-Ruiz, P. W. A. Roming, I. A. Steele, R. G. Strom, V. Testa, G. Tosti, M. V. Ulanov, K. Wiersema, R. A. M. J. Wijers, J. M. Winters, A. F. Zarnecki, F. Zerbi, P. Mészáros, G. Chincarini, and D. N. Burrows. Broadband observations of the naked-eye γ -ray burst GRB080319B. *Nature*, 455:183–188, Sept. 2008. doi: 10.1038/nature07270.
- J. C. Rastinejad, B. P. Gompertz, A. J. Levan, W.-f. Fong, M. Nicholl, G. P. Lamb, D. B. Malesani, A. E. Nugent, S. R. Oates, N. R. Tanvir, A. de Ugarte Postigo, C. D. Kilpatrick, C. J. Moore, B. D. Metzger, M. E. Ravasio, A. Rossi, G. Schroeder, J. Jencson, D. J. Sand, N. Smith, J. F. Agüí Fernández, E. Berger, P. K. Blanchard, R. Chornock, B. E. Cobb, M. De Pasquale, J. P. U. Fynbo, L. Izzo, D. A. Kann, T. Laskar, E. Marini, K. Paterson, A. R. Escorial, H. M. Sears, and C. C. Thöne. A kilonova following a long-duration gamma-ray burst at 350 Mpc. , 612(7939):223–227, Dec. 2022. doi: 10.1038/s41586-022-05390-w.
- M. J. Rees and P. Meszaros. Unsteady outflow models for cosmological gamma-ray bursts. *ApJ*, 430:L93–L96, Aug. 1994. doi: 10.1086/187446.
- E. Rossi, D. Lazzati, and M. J. Rees. Afterglow light curves, viewing angle and the jet structure of γ -ray bursts. *MNRAS*, 332:945–950, June 2002. doi: 10.1046/j.1365-8711.2002.05363.x.
- M. Ruffert and H. T. Janka. Gamma-ray bursts from accreting black holes in neutron star mergers. , 344:573–606, Apr. 1999. doi: 10.48550/arXiv.astro-ph/9809280.
- O. S. Salafia, G. Ghisellini, A. Pescalli, G. Ghirlanda, and F. Nappo. Light curves and spectra from off-axis gamma-ray bursts. , 461(4):3607–3619, Oct 2016. doi: 10.1093/mnras/stw1549.
- Y. Sato, K. Murase, Y. Ohira, and R. Yamazaki. Two-component jet model for multiwavelength afterglow emission of the extremely energetic burst GRB 221009A. , 522(1):L56–L60, June 2023. doi: 10.1093/mnrasl/slad038.
- V. Savchenko, C. Ferrigno, E. Kuulkers, A. Bazzano, E. Bozzo, S. Brandt, J. Chenevez, T. J. L. Courvoisier, R. Diehl, A. Domingo, L. Hanlon, E. Jourdain, A. von Kienlin, P. Laurent, F. Lebrun, A. Lutovinov, A. Martin-Carrillo, S. Mereghetti,

- L. Natalucci, J. Rodi, J. P. Roques, R. Sunyaev, and P. Ubertini. INTEGRAL Detection of the First Prompt Gamma-Ray Signal Coincident with the Gravitational-wave Event GW170817. , 848(2):L15, Oct. 2017. doi: 10.3847/2041-8213/aa8f94.
- B. Schneider, E. Le Floch, M. Arabsalmani, S. D. Vergani, and J. T. Palmerio. Are the host galaxies of long gamma-ray bursts more compact than star-forming galaxies of the field? , 666:A14, Oct. 2022. doi: 10.1051/0004-6361/202243367.
- V. Sharma, S. Iyyani, and D. Bhattacharya. Identifying Black Hole Central Engines in Gamma-Ray Bursts. , 908(1):L2, Feb. 2021. doi: 10.3847/2041-8213/abd53f.
- M. Shibata and K. Hotokezaka. Merger and Mass Ejection of Neutron Star Binaries. *Annual Review of Nuclear and Particle Science*, 69:41–64, Oct. 2019. doi: 10.1146/annurev-nucl-101918-023625.
- M. Shrestha, I. A. Steele, A. S. Piascik, H. Jermak, R. J. Smith, and C. M. Copperwheat. Characterization of a dual-beam, dual-camera optical imaging polarimeter. , 494(4):4676–4686, June 2020. doi: 10.1093/mnras/staa1049.
- M. Shrestha, M. Bulla, L. Nativi, I. Markin, S. Rosswog, and T. Dietrich. Impact of jets on kilonova photometric and polarimetric emission from binary neutron star mergers. , 523(2):2990–3000, Aug. 2023. doi: 10.1093/mnras/stad1583.
- S. J. Smartt, T. W. Chen, A. Jerkstrand, M. Coughlin, E. Kankare, S. A. Sim, M. Fraser, C. Inserra, K. Maguire, K. C. Chambers, M. E. Huber, T. Krühler, G. Leloudas, M. Magee, L. J. Shingles, K. W. Smith, D. R. Young, J. Tonry, R. Kotak, A. Gal-Yam, J. D. Lyman, D. S. Homan, C. Agliozzo, J. P. Anderson, C. R. Angus, C. Ashall, C. Barbarino, F. E. Bauer, M. Berton, M. T. Botticella, M. Bulla, J. Bulger, G. Cannizzaro, Z. Cano, R. Cartier, A. Cikota, P. Clark, A. De Cia, M. Della Valle, L. Denneau, M. Dennefeld, L. Dessart, G. Dimitriadis, N. Elias-Rosa, R. E. Firth, H. Flewelling, A. Flörs, A. Franckowiak, C. Frohmaier, L. Galbany, S. González-Gaitán, J. Greiner, M. Gromadzki, A. N. Guelbenzu, C. P. Gutiérrez, A. Hamanowicz, L. Hanlon, J. Harmanen, K. E. Heintz, A. Heinze, M. S. Hernandez, S. T. Hodgkin, I. M. Hook, L. Izzo, P. A. James, P. G. Jonker, W. E. Kerzendorf, S. Klose, Z. Kostrzewa-Rutkowska, M. Kowalski, M. Kromer, H. Kuncarayakti, A. Lawrence, T. B. Lowe, E. A. Magnier, I. Manulis, A. Martin-Carrillo, S. Mattila, O. McBrien, A. Müller, J. Nordin, D. O’Neill, F. Onori, J. T. Palmerio, A. Pastorello, F. Patat, G. Pignata, P. Podsiadlowski, M. L. Pumo, S. J. Prentice, A. Rau, A. Razza, A. Rest, T. Reynolds, R. Roy, A. J. Ruiter, K. A. Rybicki, L. Salmon, P. Schady, A. S. B. Schultz, T. Schweyer, I. R. Seitenzahl, M. Smith, J. Sollerman, B. Stalder, C. W. Stubbs, M. Sullivan, H. Szegedi, F. Taddia, S. Taubenberger, G. Terreran, B. van Soelen, J. Vos, R. J. Wainscoat, N. A. Walton, C. Waters, H. Weiland, M. Willman, P. Wiseman, D. E. Wright, L. Wyrzykowski, and O. Yaron. A kilonova as the electromagnetic counterpart to a gravitational-wave source. , 551(7678):75–79, Nov 2017. doi: 10.1038/nature24303.
- R. Smith and I. A. Steele. Liverpool Telescope Technical Note 1: Telescope and IO:O Throughput. Technical report, Feb. 2017.

- E. Sonbas, G. A. MacLachlan, K. S. Dhuga, P. Veres, A. Shenoy, and T. N. Ukwatta. Gamma-ray Bursts: Temporal Scales and the Bulk Lorentz Factor. , 805(2):86, June 2015. doi: 10.1088/0004-637X/805/2/86.
- I. A. Steele, R. J. Smith, P. C. Rees, I. P. Baker, S. D. Bates, M. F. Bode, M. K. Bowman, D. Carter, J. Etherton, M. J. Ford, S. N. Fraser, A. Gomboc, R. D. J. Lett, A. G. Mansfield, J. M. Marchant, G. A. Medrano-Cerda, C. J. Mottram, D. Raback, A. B. Scott, M. D. Tomlinson, and R. Zamanov. The Liverpool Telescope: performance and first results. In J. Oschmann, Jacobus M., editor, Ground-based Telescopes, volume 5489 of Society of Photo-Optical Instrumentation Engineers (SPIE) Conference Series, pages 679–692, Oct. 2004. doi: 10.1117/12.551456.
- M. Tanaka. Kilonova/Macronova Emission from Compact Binary Mergers. Advances in Astronomy, 2016:634197, Jan. 2016. doi: 10.1155/2016/6341974.
- M. Tanaka, D. Kato, G. Gaigalas, and K. Kawaguchi. Systematic opacity calculations for kilonovae. , 496(2):1369–1392, Aug. 2020. doi: 10.1093/mnras/staa1576.
- N. R. Tanvir, K. Wiersema, D. Xu, and J. P. U. Fynbo. GRB 130612A: VLT/X-shooter redshift. GRB Coordinates Network, 14882:1, Jan. 2013.
- G. B. Taylor, D. A. Frail, E. Berger, and S. R. Kulkarni. The Angular Size and Proper Motion of the Afterglow of GRB 030329. , 609(1):L1–L4, Jul 2004. doi: 10.1086/422554.
- C. Thompson. A Model of Gamma-Ray Bursts. MNRAS, 270:480, Oct. 1994.
- D. Thornton, B. Stappers, M. Bailes, B. Barsdell, S. Bates, N. D. R. Bhat, M. Burgay, S. Burke-Spolaor, D. J. Champion, P. Coster, N. D’Amico, A. Jameson, S. Johnston, M. Keith, M. Kramer, L. Levin, S. Milia, C. Ng, A. Possenti, and W. van Straten. A Population of Fast Radio Bursts at Cosmological Distances. Science, 341:53–56, July 2013. doi: 10.1126/science.1236789.
- E. Troja, V. M. Lipunov, C. G. Mundell, N. R. Butler, A. M. Watson, S. Kobayashi, S. B. Cenko, F. E. Marshall, R. Ricci, A. Fruchter, M. H. Wieringa, E. S. Gorbovskoy, V. Kornilov, A. Kutyrev, W. H. Lee, V. Toy, N. V. Tyurina, N. M. Budnev, D. A. H. Buckley, J. González, O. Gress, A. Horesh, M. I. Panasyuk, J. X. Prochaska, E. Ramirez-Ruiz, R. Rebolo Lopez, M. G. Richer, C. Roman-Zuniga, M. Serra-Ricart, V. Yurkov, and N. Gehrels. Significant and variable linear polarization during the prompt optical flash of GRB 160625B. Nature, 547: 425–427, July 2017. doi: 10.1038/nature23289.
- E. Troja, C. L. Fryer, B. O’Connor, G. Ryan, S. Dichiara, A. Kumar, N. Ito, R. Gupta, R. Wollaeger, J. P. Norris, N. Kawai, N. Butler, A. Aryan, K. Misra, R. Hosokawa, K. L. Murata, M. Niwano, S. B. Pandey, A. Kutyrev, H. J. van Eerten, E. A. Chase, Y. D. Hu, M. D. Caballero-Garcia, and A. J. Castro-Tirado. A long gamma-ray burst from a merger of compact objects. Nature, 612:228–231, Dec. 2022. doi: 10.1038/s41586-022-05327-3.

- Y. Tsapras, R. Street, K. Horne, C. Snodgrass, M. Dominik, A. Allan, I. Steele, D. M. Bramich, E. S. Saunders, N. Rattenbury, C. Mottram, S. Fraser, N. Clay, M. Burgdorf, M. Bode, T. A. Lister, E. Hawkins, J. P. Beaulieu, P. Fouqué, M. Albrow, J. Menzies, A. Cassan, and D. Dominis-Prester. RoboNet-II: Follow-up observations of microlensing events with a robotic network of telescopes. *Astronomische Nachrichten*, 330(1):4, Jan. 2009. doi: 10.1002/asna.200811130.
- V. V. Usov. Millisecond pulsars with extremely strong magnetic fields as a cosmological source of gamma-ray bursts. *Nature*, 357:472–474, June 1992. doi: 10.1038/357472a0.
- J. van Paradijs, P. J. Groot, T. Galama, C. Kouveliotou, R. G. Strom, J. Telting, R. G. M. Rutten, G. J. Fishman, C. A. Meegan, M. Pettini, N. Tanvir, J. Bloom, H. Pedersen, H. U. Nørdgaard-Nielsen, M. Linden-Vørnle, J. Melnick, G. Van der Steene, M. Bremer, R. Naber, J. Heise, J. in’t Zand, E. Costa, M. Feroci, L. Piro, F. Frontera, G. Zavattini, L. Nicastro, E. Palazzi, K. Bennett, L. Hanlon, and A. Parmar. Transient optical emission from the error box of the γ -ray burst of 28 February 1997. , 386:686–689, Apr. 1997. doi: 10.1038/386686a0.
- V. A. Villar, J. Guillochon, E. Berger, B. D. Metzger, P. S. Cowperthwaite, M. Nicholl, K. D. Alexander, P. K. Blanchard, R. Chornock, T. Eftekhari, W. Fong, R. Margutti, and P. K. G. Williams. The Combined Ultraviolet, Optical, and Near-infrared Light Curves of the Kilonova Associated with the Binary Neutron Star Merger GW170817: Unified Data Set, Analytic Models, and Physical Implications. , 851(1):L21, Dec. 2017. doi: 10.3847/2041-8213/aa9c84.
- A. von Kienlin, C. A. Meegan, W. S. Paciesas, P. N. Bhat, E. Bissaldi, M. S. Briggs, J. M. Burgess, D. Byrne, V. Chaplin, W. Cleveland, V. Connaughton, A. C. Collazzi, G. Fitzpatrick, S. Foley, M. Gibby, M. Giles, A. Goldstein, J. Greiner, D. Gruber, S. Guiriec, A. J. van der Horst, C. Kouveliotou, E. Layden, S. McBreen, S. McGlynn, V. Pelassa, R. D. Preece, A. Rau, D. Tierney, C. A. Wilson-Hodge, S. Xiong, G. Younes, and H.-F. Yu. The Second Fermi GBM Gamma-Ray Burst Catalog: The First Four Years. *ApJS*, 211:13, Mar. 2014. doi: 10.1088/0067-0049/211/1/13.
- A. von Kienlin, C. A. Meegan, W. S. Paciesas, P. N. Bhat, E. Bissaldi, M. S. Briggs, E. Burns, W. H. Cleveland, M. H. Gibby, M. M. Giles, A. Goldstein, R. Hamburg, C. M. Hui, D. Kocevski, B. Mailyan, C. Malacaria, S. Poolakkil, R. D. Preece, O. J. Roberts, P. Veres, and C. A. Wilson-Hodge. The Fourth Fermi-GBM Gamma-Ray Burst Catalog: A Decade of Data. , 893(1):46, Apr. 2020. doi: 10.3847/1538-4357/ab7a18.
- D. Watson, C. J. Hansen, J. Selsing, A. Koch, D. B. Malesani, A. C. Andersen, J. P. U. Fynbo, A. Arcones, A. Bauswein, S. Covino, A. Grado, K. E. Heintz, L. Hunt, C. Kouveliotou, G. Leloudas, A. J. Levan, P. Mazzali, and E. Pian. Identification of strontium in the merger of two neutron stars. , 574(7779):497–500, Oct. 2019. doi: 10.1038/s41586-019-1676-3.
- S. E. Woosley. Gamma-ray bursts from stellar mass accretion disks around black holes. *ApJ*, 405:273–277, Mar. 1993. doi: 10.1086/172359.

- Q. Wu, B. Zhang, W.-H. Lei, Y.-C. Zou, E.-W. Liang, and X. Cao. The extension of variability properties in gamma-ray bursts to blazars. *MNRAS*, 455:L1–L5, Jan. 2016. doi: 10.1093/mnrasl/slv136.
- W. Xie, W.-H. Lei, and D.-X. Wang. What Can We Learn about GRB from the Variability Timescale Related Correlations? , 838(2):143, Apr. 2017. doi: 10.3847/1538-4357/aa6718.
- B. Yang, Z.-P. Jin, X. Li, S. Covino, X.-Z. Zheng, K. Hotokezaka, Y.-Z. Fan, T. Piran, and D.-M. Wei. A possible macronova in the late afterglow of the long-short burst GRB 060614. *NatCo*, 6:7323, Apr. 2015. doi: 10.1038/ncomms8323.
- J. Yang, S. Ai, B. B. Zhang, B. K. Zhang, Z. K. Liu, X. I. Wang, Y. H. Yang, Y. H. Yin, Y. Li, and H. J. Lü. A long-duration gamma-ray burst with a peculiar origin. *Nature*, 612:232–235, Dec. 2022. doi: 10.1038/s41586-022-05403-8.
- B. Zhang. Open questions in GRB physics. *Comptes Rendus Physique*, 12:206–225, Apr. 2011. doi: 10.1016/j.crhy.2011.03.004.
- B. Zhang, X. Dai, N. M. Lloyd-Ronning, and P. Mészáros. Quasi-universal Gaussian Jets: A Unified Picture for Gamma-Ray Bursts and X-Ray Flashes. *ApJ*, 601: L119–L122, Feb. 2004. doi: 10.1086/382132.
- S.-Q. Zhong, L. Li, and Z.-G. Dai. GRB 211211A: A Neutron Star-White Dwarf Merger? , 947(2):L21, Apr. 2023. doi: 10.3847/2041-8213/acca83.
- J.-P. Zhu, X. I. Wang, H. Sun, Y.-P. Yang, Z. Li, R.-C. Hu, Y. Qin, and S. Wu. Long-duration Gamma-Ray Burst and Associated Kilonova Emission from Fast-spinning Black Hole-Neutron Star Mergers. , 936(1):L10, Sept. 2022. doi: 10.3847/2041-8213/ac85ad.
- L. Zou, Z.-M. Zhou, L. Xie, L.-L. Zhang, H.-J. Lü, S.-Q. Zhong, Z.-J. Wang, and E.-W. Liang. Magnetar as Central Engine of Gamma-Ray Bursts: Central Engine-Jet Connection, Wind-Jet Energy Partition, and Origin of Some Ultra-long Bursts. , 877(2):153, June 2019. doi: 10.3847/1538-4357/ab17dc.

Appendix A



Technical Note

**LC trigger algorithms
applied to XGIS synthetic GRB profiles**

Reference name	THS-UNIFE-XGIS-TN-0002_MEPSA_rate_trigger
Version	1.1
Date	2021-06-04

Prepared by	A. E. Camisasca, C. Guidorzi
Checked by	
Approved by	

Technical notes	THS-UNIFE-XGIS-TN-0002_MEPSA_rate_trigger	2/26
Contact		

Technical notes	THS-UNIFE-XGIS-TN-0002_MEPSA_rate_trigger	3/26
-----------------	---	------

Document Change Record		
Date	Version	Changes
2021-06-04	1.1	Cristiano Guidorzi

Technical notes	THS-UNIFE-XGIS-TN-0002_MEPSA_rate_trigger	4/26
-----------------	---	------

Applicable documents		
Reference	Reference name	Title
[AD1]		

Reference documents		
Reference	Reference name	Title
[RD1]		

Technical notes	THS-UNIFE-XGIS-TN-0002_MEPSA_rate_trigger	6/26

Contents

1. Introduction.....	8
2. Characteristics of simulated GRBs.....	8
3. Short description of MEPSA algorithm.....	11
4. MEPSA detection efficiency with constant background	11
4.1 Efficiency with different peak energies, for different fluences.....	12
4.2 Best results among the different bands.....	13
4.3 Efficiency for different configurations.....	13
4.4 Efficiency as a function of peak flux for different peak energies.....	15
4.5 False positive rate.....	18
4.6 Signal to noise ratio (SNR).....	20
5. Variable background analysis.....	21
6. Further development	25
6.1. Pattern selection	25
6.2. Analysis with different characteristics of simulated GRBs	26
6.3. Analysis using individual bands	26

1. Introduction

We aim to test the efficiency of different algorithms in detecting GRB events; in particular we test light curves trigger algorithms applied to XGIS synthetic GRB profiles as seen in a single unit.

2. Characteristics of simulated GRBs

We start our analysis by simulating single GRB light curve profiles affected by Gaussian uncorrelated noise. The assumed temporal profile is that of a single FRED pulse. This was done following three different steps:

- a. assume a given GRB spectrum;
 - b. determine background counts;
 - c. simulate light curve profiles in different energy bands as well as in the total passband.
- a. Our single-GRB spectrum models are described by the empirical Band function with $\alpha = -1$, $\beta = -2.3$; peak energy varies in the range 2 - 1000 keV.

The photon fluence varies from 1 to 955 ph cm⁻² in the energy band 2-2000 keV, corresponding to the energy fluence range 10⁻⁸ to 10⁻⁵ erg cm⁻².

We consider 3 different GRB directions: on axis (0 deg), off axis (15deg, 30 deg), based on the available XGIS response functions.

Using pyspec and XGIS response and ancillary files, version 7, we determine the predicted counts for 8 contiguous energy bands reported below along with the corresponding name adopted hereafter in the present note.

Band number	Energy range (keV)	Band name	Bands group name	
1	2-5	X1	X	XS
2	5-10	X2		
3	10-30	X3		
4	20-50	S1	S	
5	50-100	S2		
6	100-200	S3		
7	200-400	S4		
8	400-2000	S5		

Table 1 The energy bands and their names as adopted in the present note

- b.** Background counts are determined separately for the energy bands previously defined, always using pyspec and XGIS response and ancillary files. This was done by setting a negligible value to the normalisation of the GRB spectrum (10^{-10}).
We first considered the case of a constant background. Next, we will assume a variable background, as expected from the planned THESEUS orbit.
- c.** We create GRB light curves assuming a Fast Rise and Exponential Decay (FRED) profile, whose time profile is described by the following equation:

$$F(t) = \begin{cases} A \exp\left[-\left(\frac{|t-t_0|}{\tau_r}\right)^p\right] & (t < t_0) \\ A \exp\left[-\left(\frac{|t-t_0|}{\tau_d}\right)^p\right] & (t \geq t_0) \end{cases}$$

Hereafter, we consider $t_0=0$, and a typical value for the peakedness, $p = 1.3$, for all energy bands (e.g., Norris et al. 1996). For the hardest energy channel we used the rise and decay times $\tau_r=0.5$ s, $\tau_d= 1.6$ s; for the other energy bands, the corresponding rise and decay times, τ_r and τ_d , are calculated based on the temporal width $w(E)$, whose scaling with energy is modelled following Fenimore et al. 1995:

$$w(E) \propto E^{-0.4}$$

where, E is the geometric mean of the boundary energies for a given band, given the typical power-law piecewise shape of GRB spectra. The normalisation parameter A is determined based on the desired counts obtained in step a.

Light curves start at -30 s and end at 80 s with an original bin time of 1 ms, and then are rebinned to 64 ms.

As an example, we consider counts obtained with a GRB model with peak energy = 300 keV, fluence = 10 ph cm⁻² on axis (0 deg). We obtained the following counts and light curves:

band number	GRB counts	background counts/s
1	678.190	1500.000
2	736.826	888.670
3	624.924	519.240
4	971.742	652.360

5	655.500	639.240
6	709.039	647.340
7	520.449	586.160
8	223.328	485.300

Table 2 Counts obtained with a GRB model with $E_{peak} = 300 \text{ keV}$, fluence = 10 ph cm^{-2} , on axis.

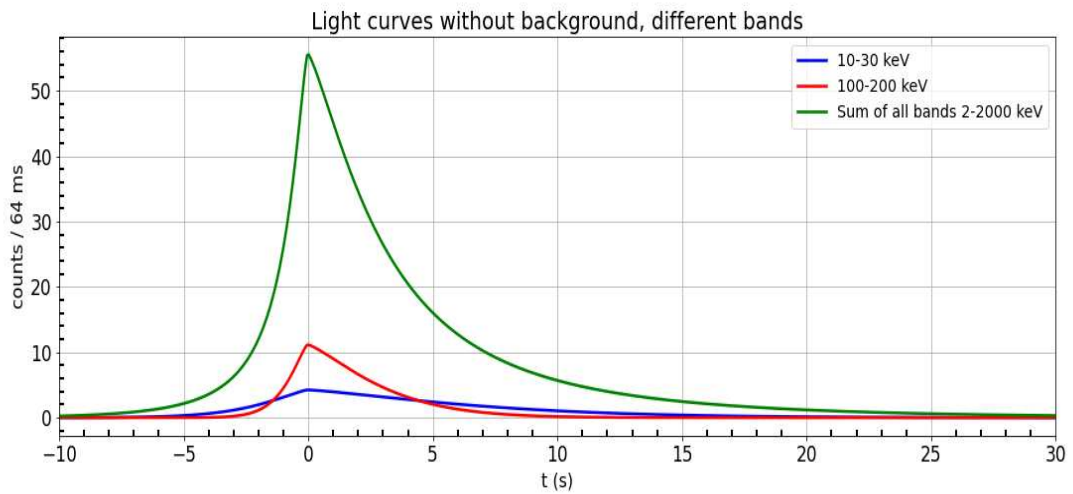


Figure 1 Light curves obtained with a GRB model with $E_{peak} = 300 \text{ keV}$, fluence = 10 ph cm^{-2} , on axis

It is possible to notice different light curve widths for different energy bands. Simulations are carried out in the time interval from -30 to +80 s. Figure 1 shows a close in in the time interval from -10 to 30 s to better illustrate the different time profiles of the GRB.

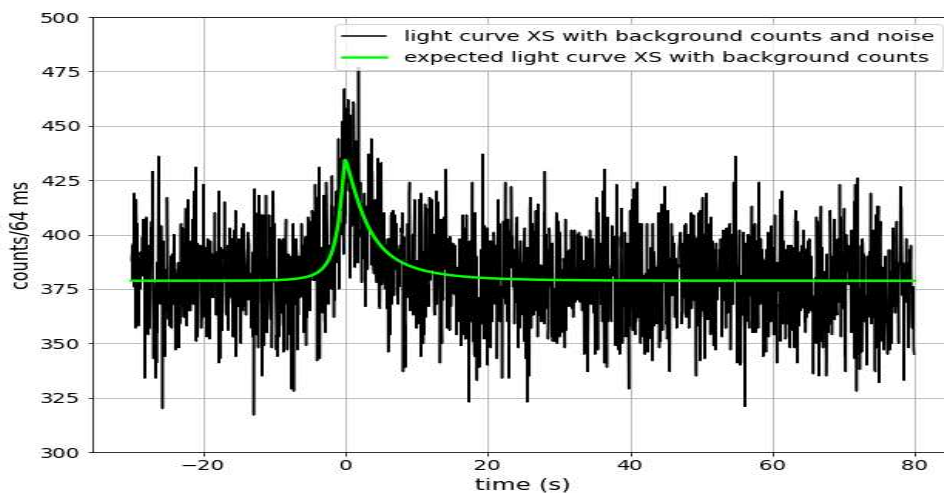


Figure 2 Total light curve XS with background counts; the same light curve affected by poissonian uncorrelated noise

Once we obtain the GRB light curve profiles, we add the background counts, to which the corresponding Poisson noise is added. The results are shown in Figure 2. The final step of background subtraction is required by MEPSA, which assumes uncorrelated Gaussian noise. This assumption holds true as long as the number of counts per bin is large enough to ensure the Gaussian limit.

3. Short description of MEPSA algorithm

“MEPSA” algorithm (multiple excess peak search algorithm; Guidorzi 2015) aims at identifying peaks within a uniformly sampled time series affected by uncorrelated Gaussian noise.

It scans the time series at different timescales by comparing a given peak candidate with a variable number of adjacent bins. In particular, MEPSA searches the input light curves for peaks by applying simultaneously a multi-pattern set of excesses, i.e. a set of $N=39$ patterns. The series must be either background-subtracted, or removed of possible trends, so that changes in the expected value should only be due to signal and not to background.

For each bin of the light curve, let r_i the rate in the i th bin. A given pattern P_k ($k=1, \dots, N$) consists of a fixed number of adjacent bins around the given i th bin: around i there are a given $n_{k,l}$ leftward bins (which temporally precede the i th bin) and $n_{k,r}$ rightward bins (which temporally follow the i th bin). The pattern assigns each of its bins, except for the i th bin, a threshold $v_{k,j}$ ($j=1, \dots, n_{k,l}+n_{k,r}$) in terms of number of σ 's (where σ is the statistical noise corresponding to that bin).

Pattern P_k is then said to be fulfilled by bin i when the following conditions are simultaneously fulfilled:

$$\begin{cases} r_i - r_j \geq v_{k,(j-i+n_{k,l}+1)} \sigma_{ij'} & (j = i - n_{k,l}, \dots, i - 1) \\ r_i - r_j \geq v_{k,(j-i+n_{k,r})} \sigma_{ij'} & (j = i + 1, \dots, i + n_{k,r}) \end{cases}$$

where $\sigma_{ij'} = (\sigma_i^2 + \sigma_j^2)^{1/2}$. Each pattern has different numbers of leftward and rightward bins; these numbers vary from 1 to 5. Each pattern has also different threshold values; they vary in a range from 0 to 5.

For each bin i the search is performed by applying simultaneously a set of 39 different patterns ($k=1, \dots, 39$) and the i -bin is promoted to peak candidate if at least one pattern is fulfilled. The complete set of threshold values $v_{k,j}$ currently adopted is reported in Guidorzi (2015).

When the entire light curve has been screened, the whole procedure is repeated to rebinned versions of the same curve, each time increasing the rebinning factor by one up to a maximum value established by the user.

4. MEPSA detection efficiency with constant background

We test MEPSA efficiency using light curves with different energies peaks, different GRB directions, different fluences.

We consider that a peak is detected by MEPSA when the estimated peak time (t_p) lies in time window $[-\tau_r, \tau_d]$ of the third energy band.

Since $\tau_r=0.5$ s, $\tau_d= 1.6$ s for the hardest band and $t_0=0$, considering that the temporal width $w(E)$ is proportional to $E^{-0.4}$, the requirement above translates into the following: -2.4 s $< t_p < 7.75$ s.

Every simulated light curve lasts 110 s and we made 100 simulations for every kind of configuration characterised by a given set of values for the three defining properties (fluence, energy peak, direction).

4.1 Efficiency with different peak energies, for different fluences

We analyse MEPSA efficiency as a function of peak energy for 5 different fluences: 1, 5, 10, 50, 100 photons cm^{-2} .

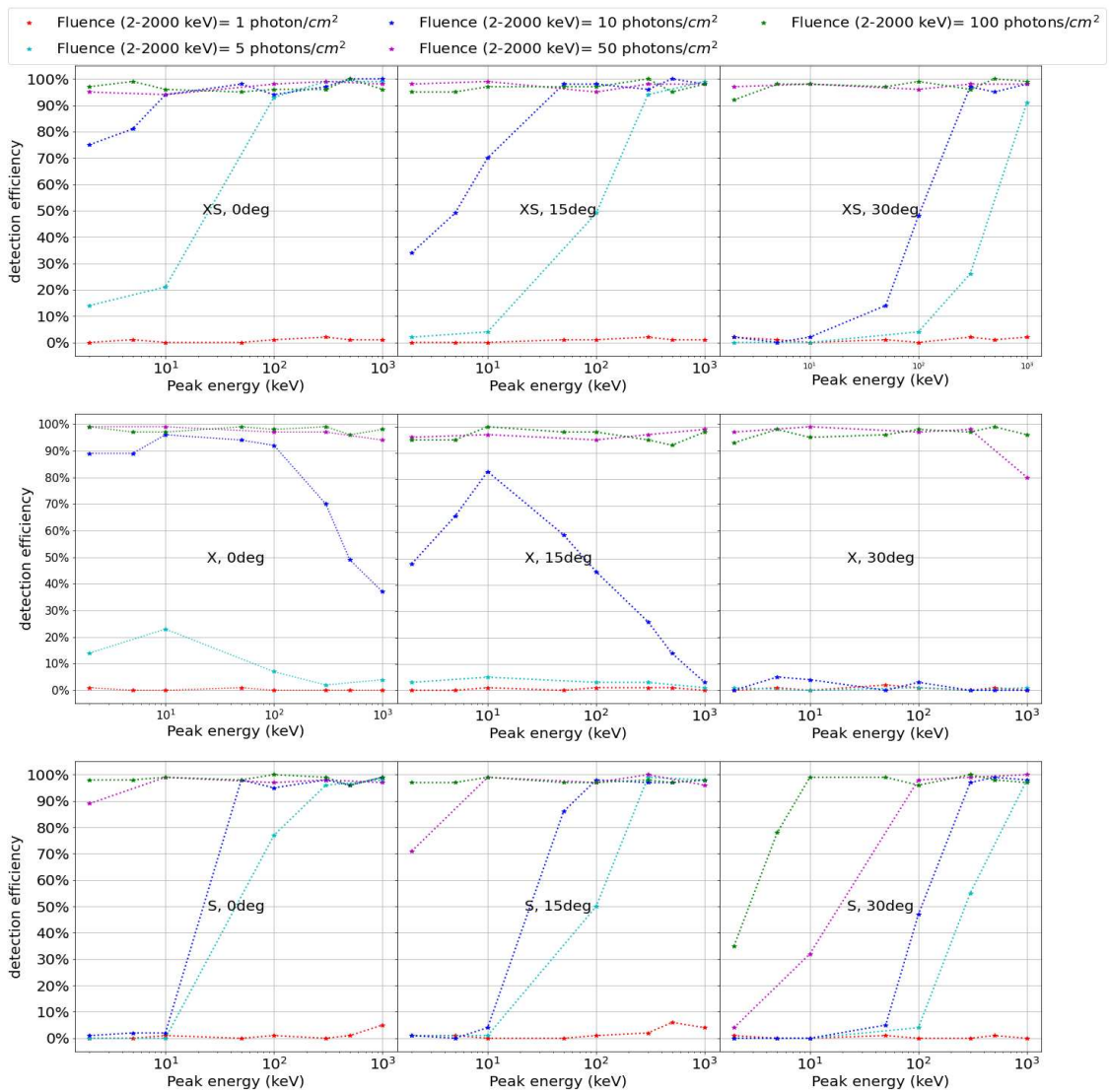


Figure 3 MEPSA efficiency as a function of peak energy for 5 different fluences at different directions, with detection in different bands

4.2 Best results among the different bands

We determined, for different energy peak values, the best result achieved among the different bands. As an example, we present the results obtained with a fluence of 10 ph cm^{-2} .

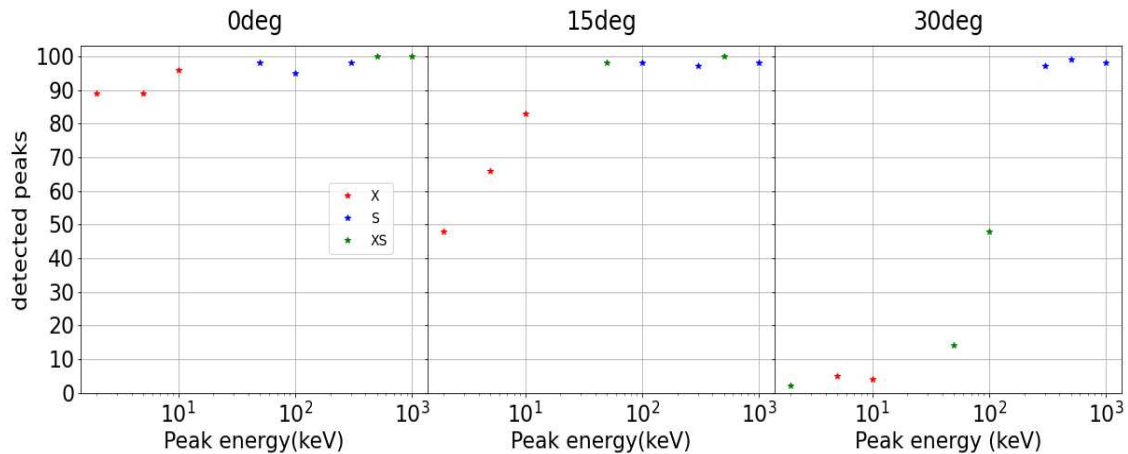


Figure 4 The best results among bands, with a fluence = 10 ph cm^{-2}

First of all, it is no wonder that, at low peak energies, the use of X bands alone performs better than using all bands. Analogously, at high peak energies the S bands alone work better than using all the bands. From Figure 4 it is also possible to see how the detection efficiency as a function of peak energy depends on the direction.

4.3 Efficiency for different configurations

We study the MEPSA efficiency as a function of the photon fluence for four different values of the peak energy. The photon fluence, in ph cm^{-2} , is reported in both 2-2000 keV and 50-300 keV energy bands, to allow for a more straightforward comparison with the analogous sensitivity curves of other past and current experiments.

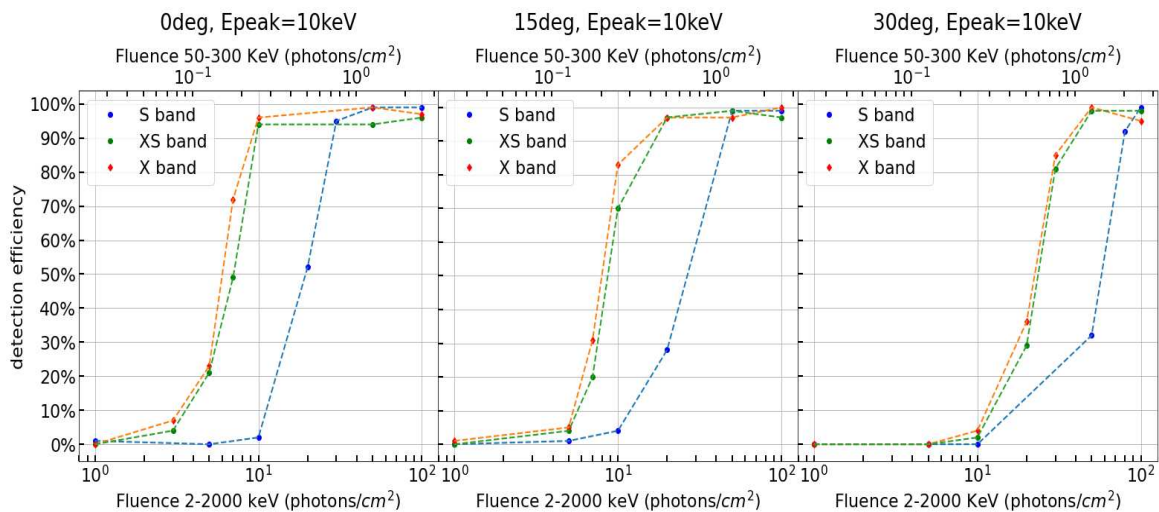


Figure 5 MEPSA efficiency as a function of the photon fluence, Epeak=10 keV

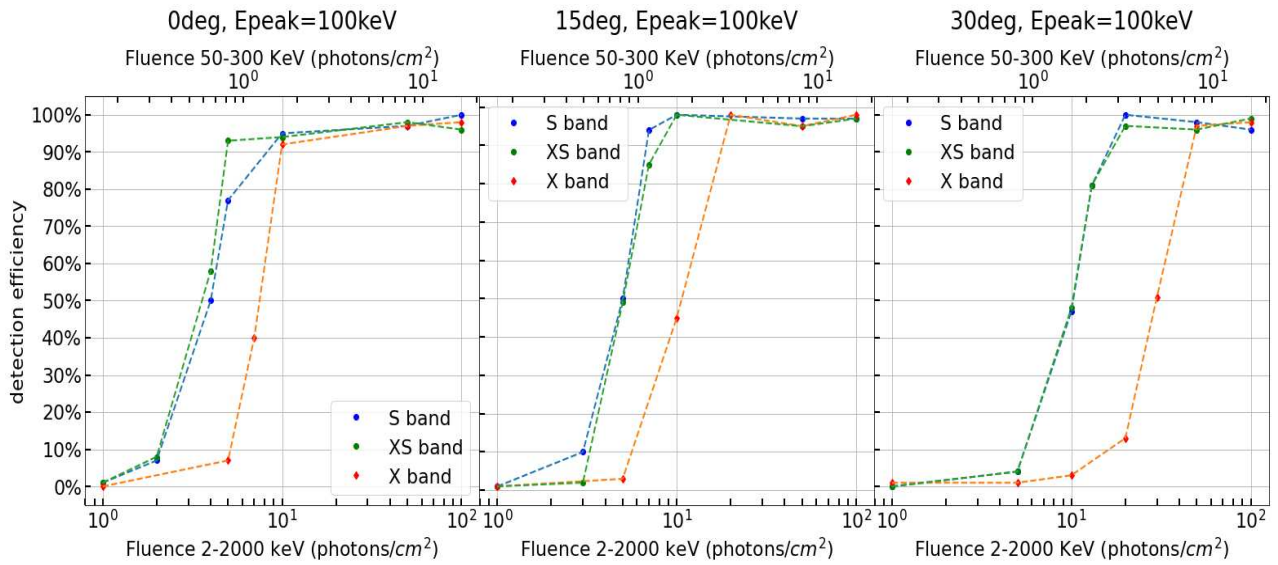


Figure 6 MEPSA efficiency as a function of the photon fluence, $E_{peak}=100\text{ keV}$

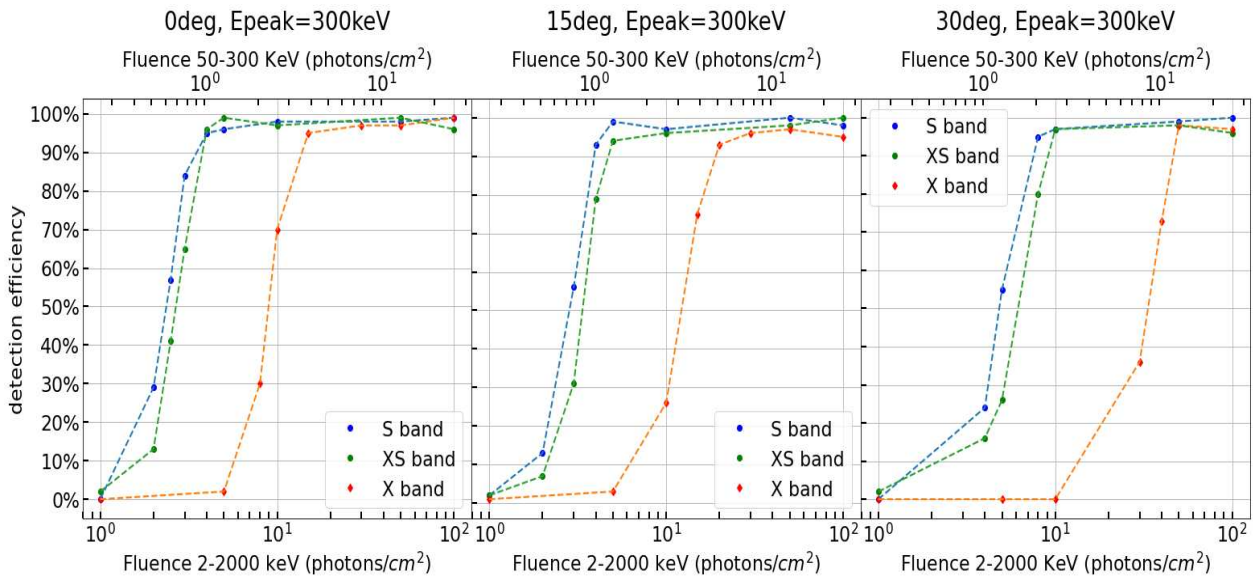


Figure 7 MEPSA efficiency as a function of the photon fluence, $E_{peak}=300\text{ keV}$

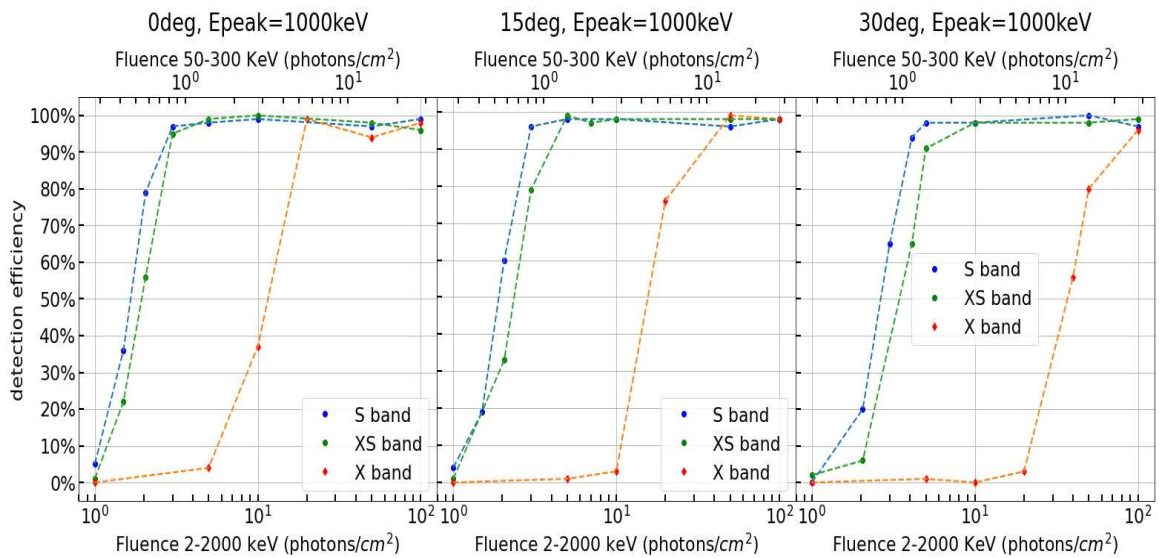


Figure 8 MEPSA efficiency as a function of the photon fluence, Epeak=1000 keV

4.4 Efficiency as a function of peak flux for different peak energies

We express the results as a function of peak fluxes.

To convert fluence into peak flux, for a particular fluence and energy peak, we consider the total light curve and we determine the 1 s interval that maximises the number of counts; then renormalise the fluence 2-2000 keV based on the ratio between the peak counts in the 1-s interval and the total counts.

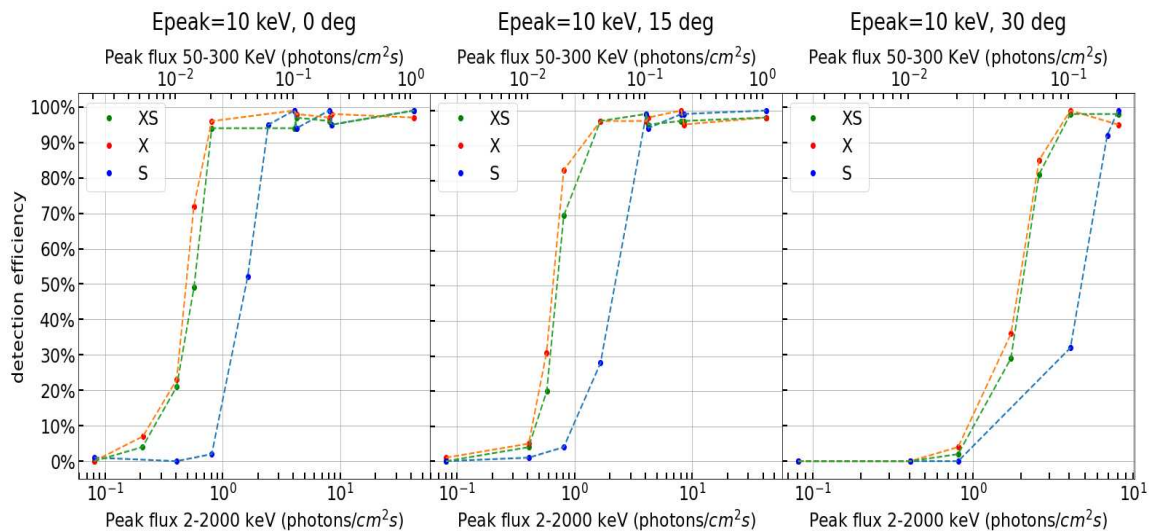


Figure 9 MEPSA efficiency as a function of the peak photon flux, Epeak=10 keV

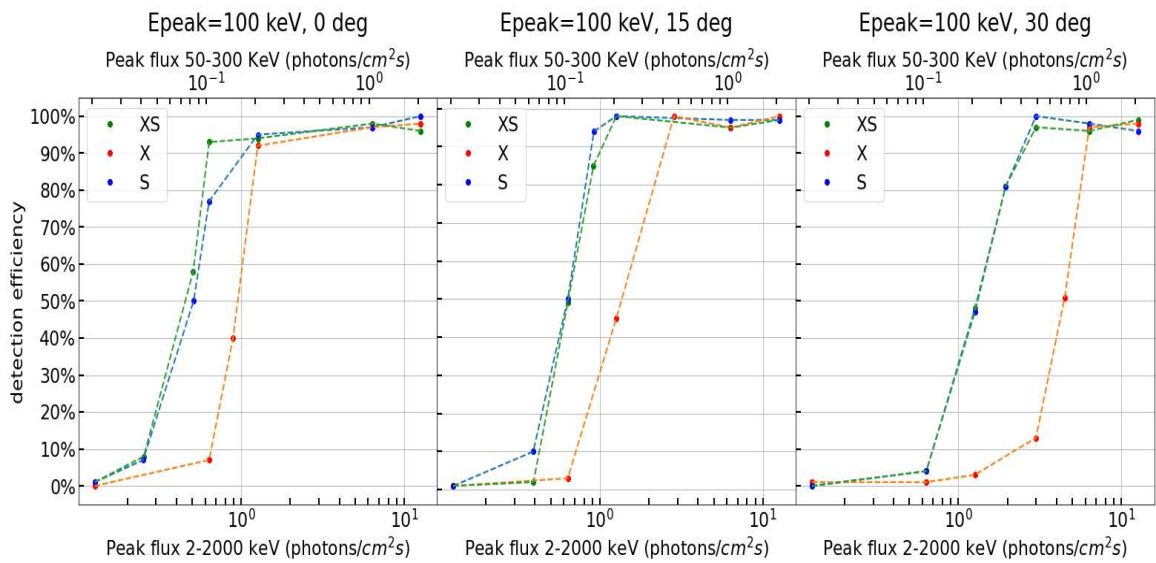


Figure 10 MEPSA efficiency as a function of the peak photon flux, $E_{peak}=100$ keV

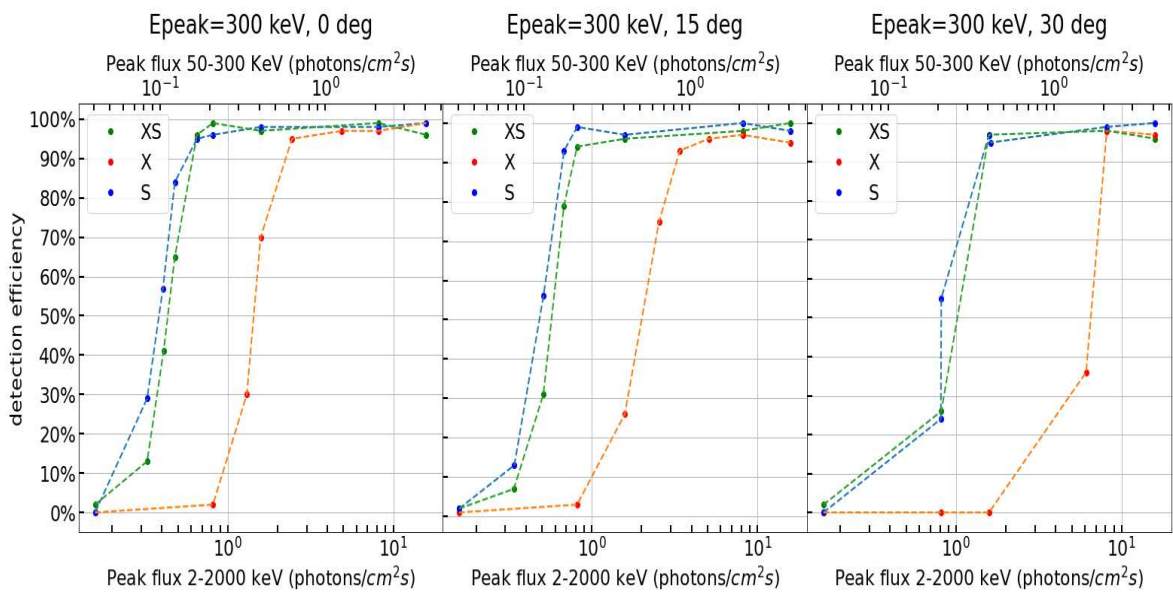


Figure 11 MEPSA efficiency as a function of the peak photon flux, $E_{peak}=300$ keV

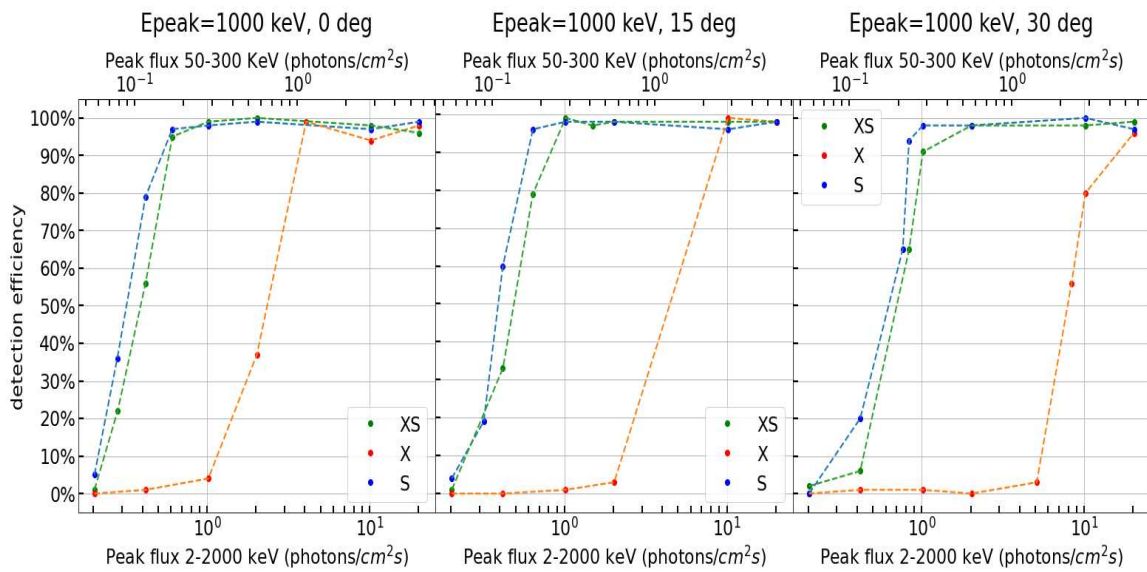


Figure 12 MEPSA efficiency as a function of the peak photon flux, $E_{peak}=1000$ keV

4.5 False positive rate

Figure 13 shows on the x axis the peak energy, on y axes the number of false positive (#FP) rate that were found in a particular configuration. We consider a peak a false positive when detected at the wrong time (out of the range $-2.4 \text{ s} < t_p < 7.75 \text{ s}$, as explained in Section 4) or if we have 2 or more wrong peaks in a simulation. For each configuration, we make 100 simulations of 110 s each, rebinned to 64 ms, so we have 171875 bins for each configuration.

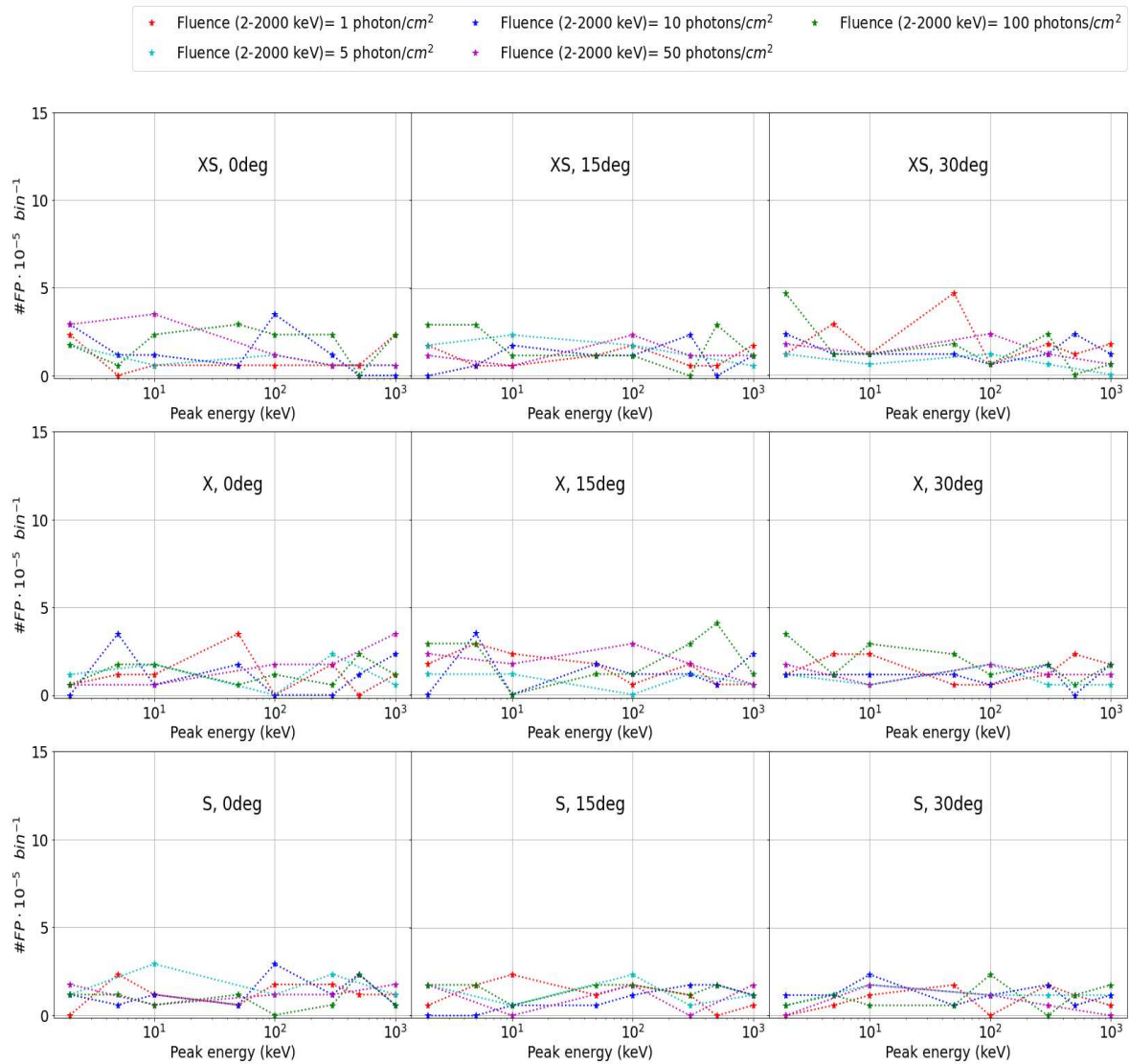


Figure 13 The number of false positives (#FP) as a function of the peak energy, for different fluences, different bands, different directions

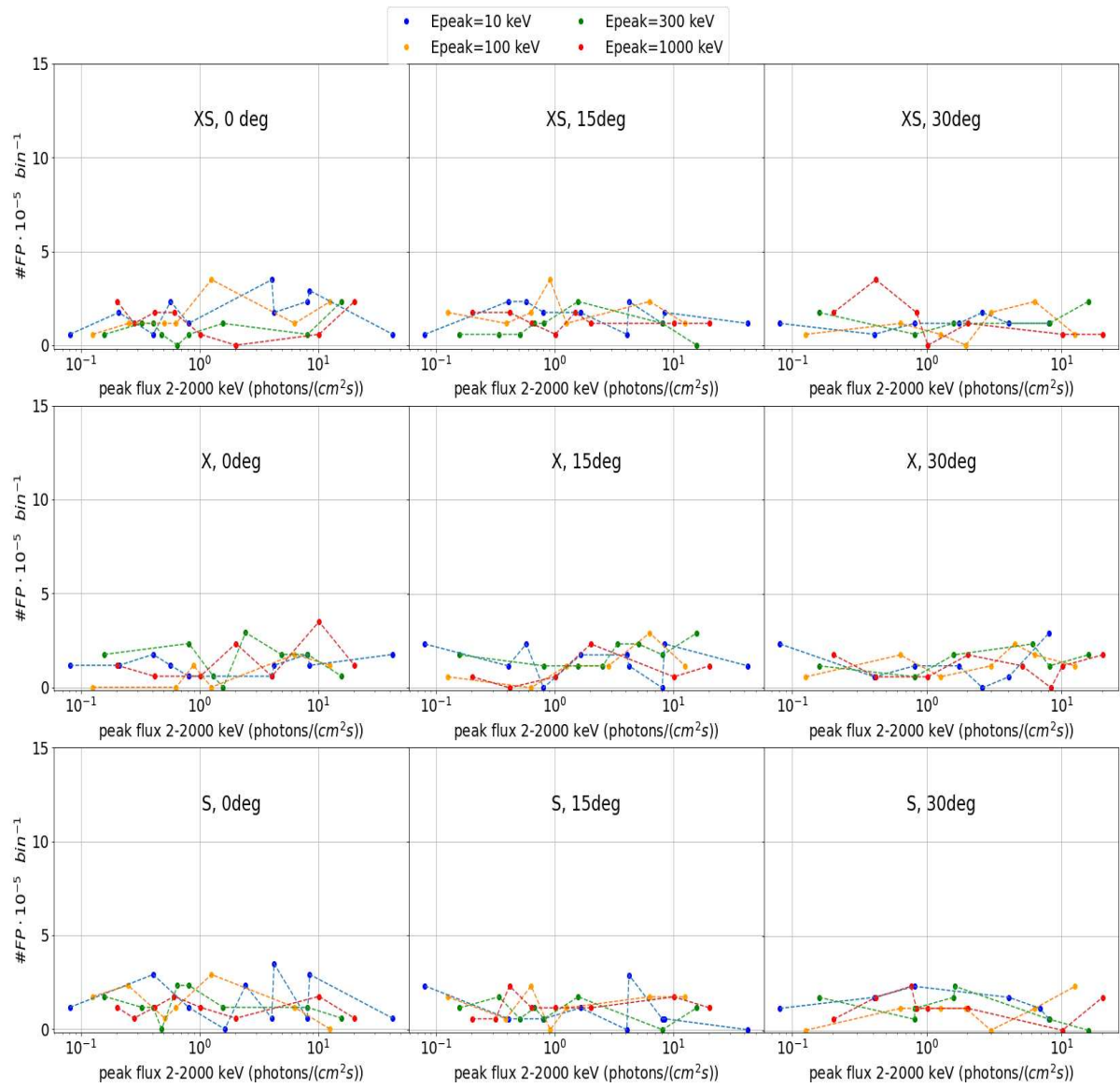


Figure 14 The number of false positives (#FP) as a function of the peak flux, for different peak energies, different bands, different directions

4.6 Signal to noise ratio (SNR)

We consider $E_{peak} = 300 \text{ keV}$; we compare MEPSA results with the results we obtain when we adopt an alternative and simple algorithm based on a threshold above background equivalent to $SNR > 7$. In particular:

- we consider the Norris pulse associated with each simulation, and we summed all the counts in FWHM;
- we generate a poissonian distribution which has the counts in FWHM as expected value, another with the respective background as expected value;
- we take into account 100 simulations, so we obtained 100 different SNR and we consider that the pulse is detected if $SNR > 7$.

From the comparison we can see to which extent MEPSA perform better than a discriminator on $SNR > 7$.

We obtain the following results:

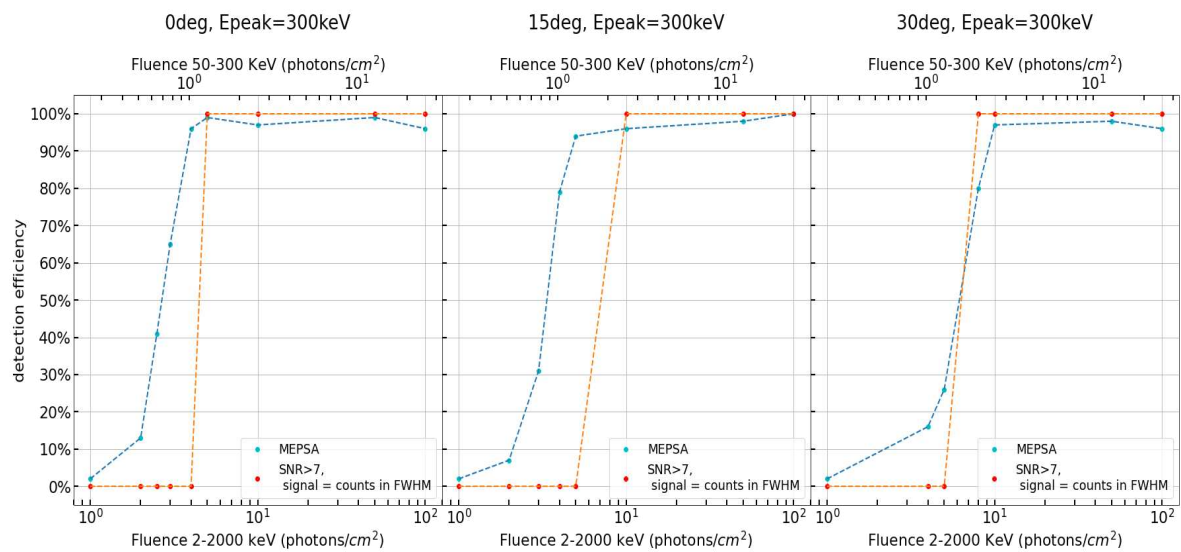


Figure 15 MEPSA detection efficiency compared with that obtained considering a peak detected if $SNR > 7$; peak energy = 300 keV, XS bands

5. Variable background analysis

In order to refine our analysis and make our simulations more realistic, we are going to consider a variable background. In particular we simulate a background modulation along the orbit assuming a simple sinusoidal shape with 0.1 fractional amplitude, an orbital period of 6000 s, and random phase (Campana, private communication), as expected for a low-inclination orbit.

Once we obtained the GRB light curve with Norris profiles (paragraph 2.c), we added the background sinusoidal counts; then we added uncorrelated Poisson noise.

Since MEPSA works with background-subtracted curves, we preliminarily interpolated the background. To this aim, we model the light curves affected by statistical noise with a second degree polynomial and iteratively remove the counts in excess of the interpolated background by > 2 sigma, until no more bins are rejected.

As an example, we use a GRB model with peak energy = 300 keV, count fluence = 4.17 ph cm^{-2} in the range 2-2000 keV, corresponding to $5.26 \times 10^{-7} \text{ erg cm}^{-2}$ in 2-2000 keV and to $5 \times 10^{-7} \text{ erg cm}^{-2}$ in 20-2000 keV, 15 deg direction.

Figure 15 shows the resulting light curves from top to bottom in the total, S, #6, and X band, respectively, with 64-ms bin time. Figure 16 shows the same light curves with a bin time of 1.024 s.

By running MEPSA on the consequent background-subtracted light curve, it detected the peak in all of the above light curves, except for the X one alone.

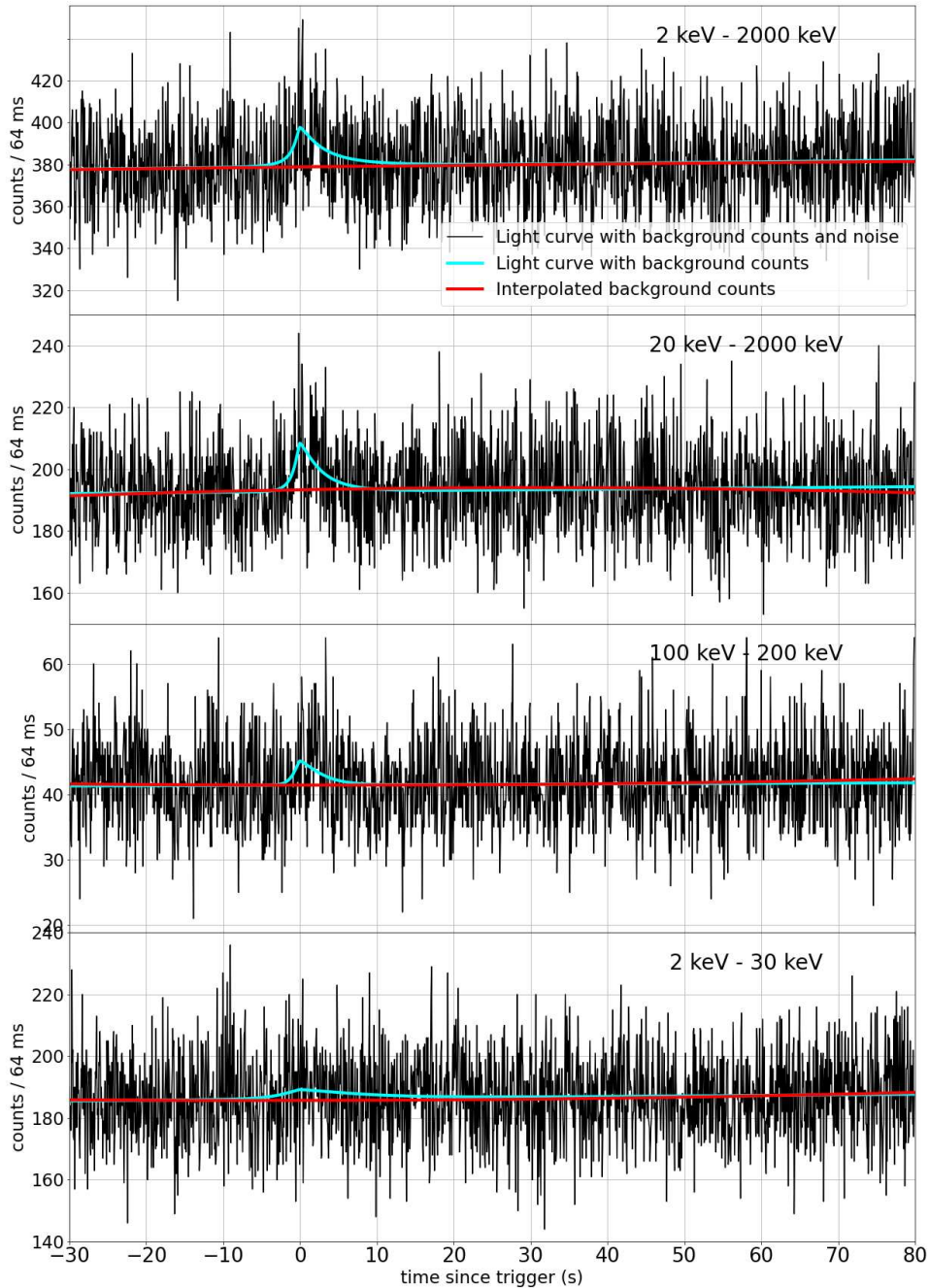


Figure 16 Light curves obtained with a GRB model with peak energy = 300 keV, photon fluence = 4.17 ph cm^{-2} in the range 2-2000 keV, 15 deg direction; from top to bottom in the total light curve, S bands, #6 band, X band, respectively, with 64-ms bin time.

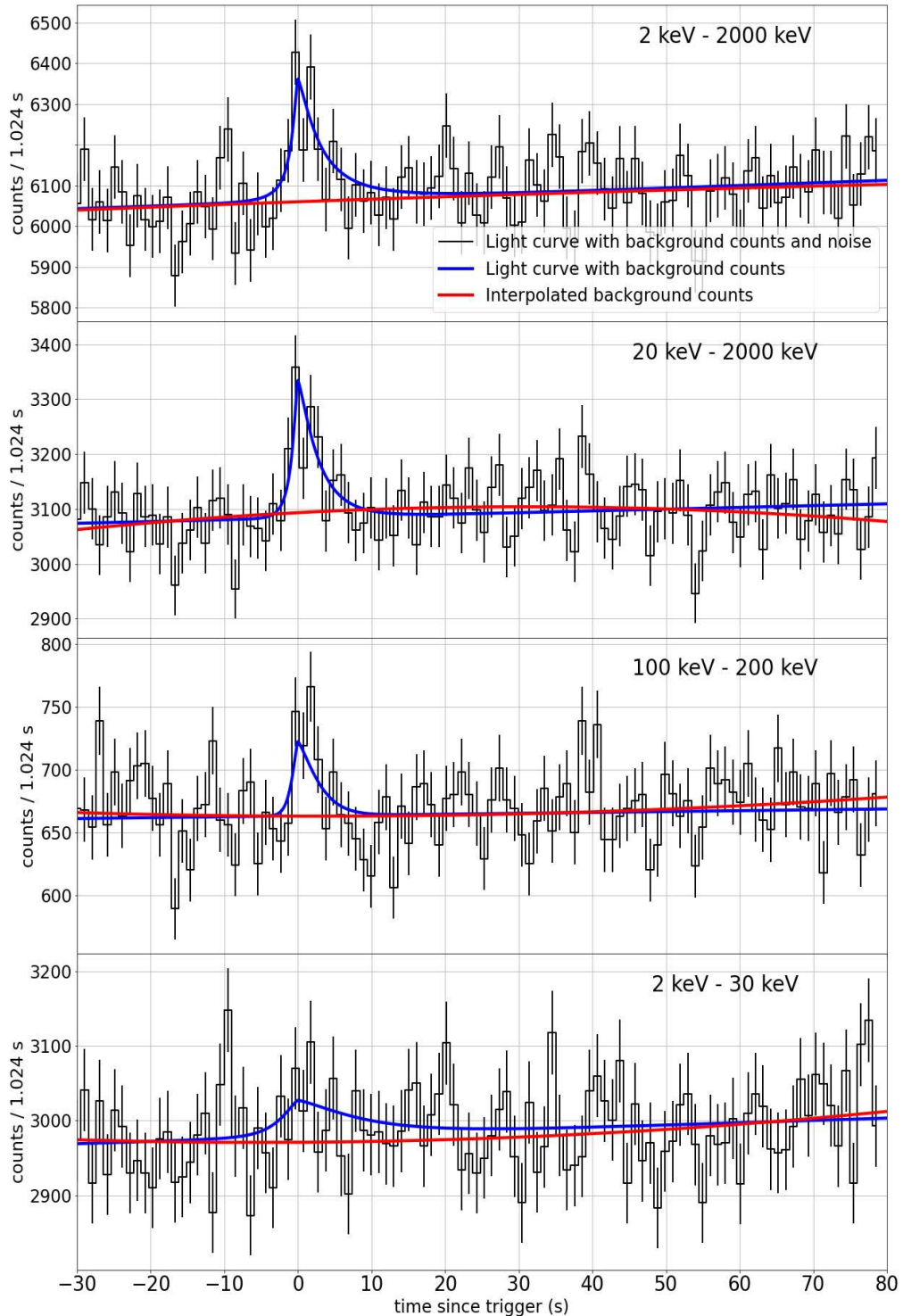


Figure 17 Light curves obtained with a GRB model with peak energy = 300 keV, photon fluence = 4.17 ph cm⁻² in the range 2-2000 keV, 15 deg direction; from top to bottom in the total light curve, S bands, #6 band, X band, respectively, with 1.024 s bin time.

We make a comparison between the results obtained with variable and constant background, analysing the case of $E_{peak} = 300$ keV. It is immediate to notice that we have the same detection efficiency with a variable and constant background.

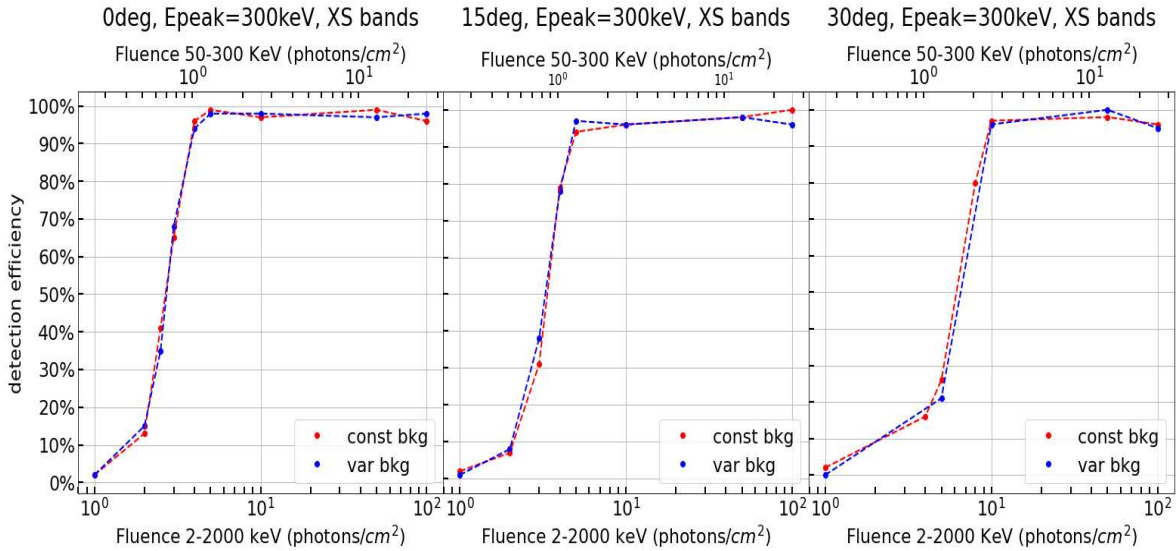


Figure 18 A comparison between detection efficiency obtained with simulations with a constant background and with a variable background modulation assuming a simple sinusoidal shape with 0.1 fractional amplitude, an orbital period of 6000 s, and random phase. We consider $E_{peak} = 300$ keV, XS bands, different directions

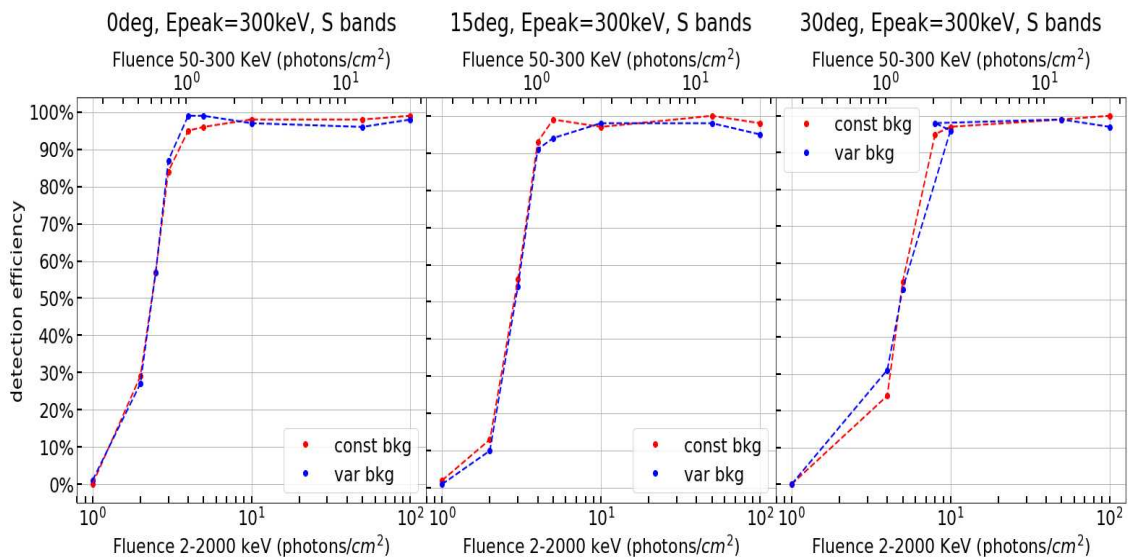


Figure 19 A comparison between detection efficiency obtained with simulations with a constant background and with a variable background modulation assuming a simple sinusoidal shape with 0.1 fractional amplitude, an orbital period of 6000 s, and random phase. We consider $E_{peak} = 300$ keV, S bands, different directions

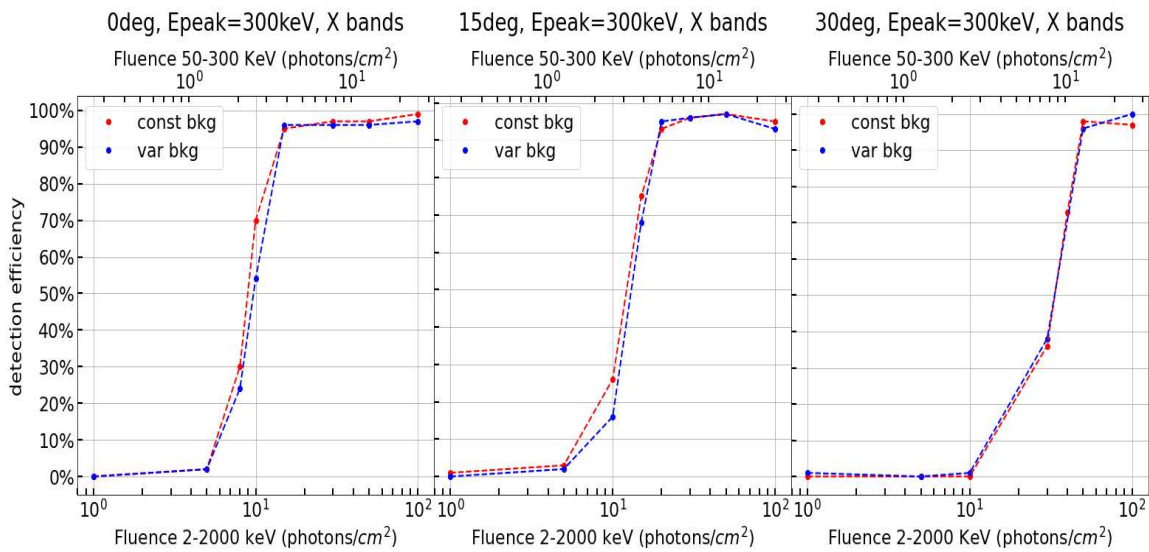


Figure 2016 A comparison between detection efficiency obtained with simulations with a constant background and with a variable background modulation assuming a simple sinusoidal shape with 0.1 fractional amplitude, an orbital period of 6000 s, and random phase. We consider $E_{peak} = 300$ keV, X bands, different directions.

6. Further development

Here we discuss possible further improvements and developments that can be addressed in future investigations.

6.1. Pattern selection

We analysed the different patterns used by MEPSA to detect peaks and we make a comparison between patterns used to detect true and false peaks, as you can see in Figure 21.

Noticeably, pattern #26 detects a relatively small number of true peaks at the high cost of many more false ones than the other criteria do, so one might consider the possibility of disabling it.

The line of reasoning can be applied to patterns #27, #34, #36, #37, #38.

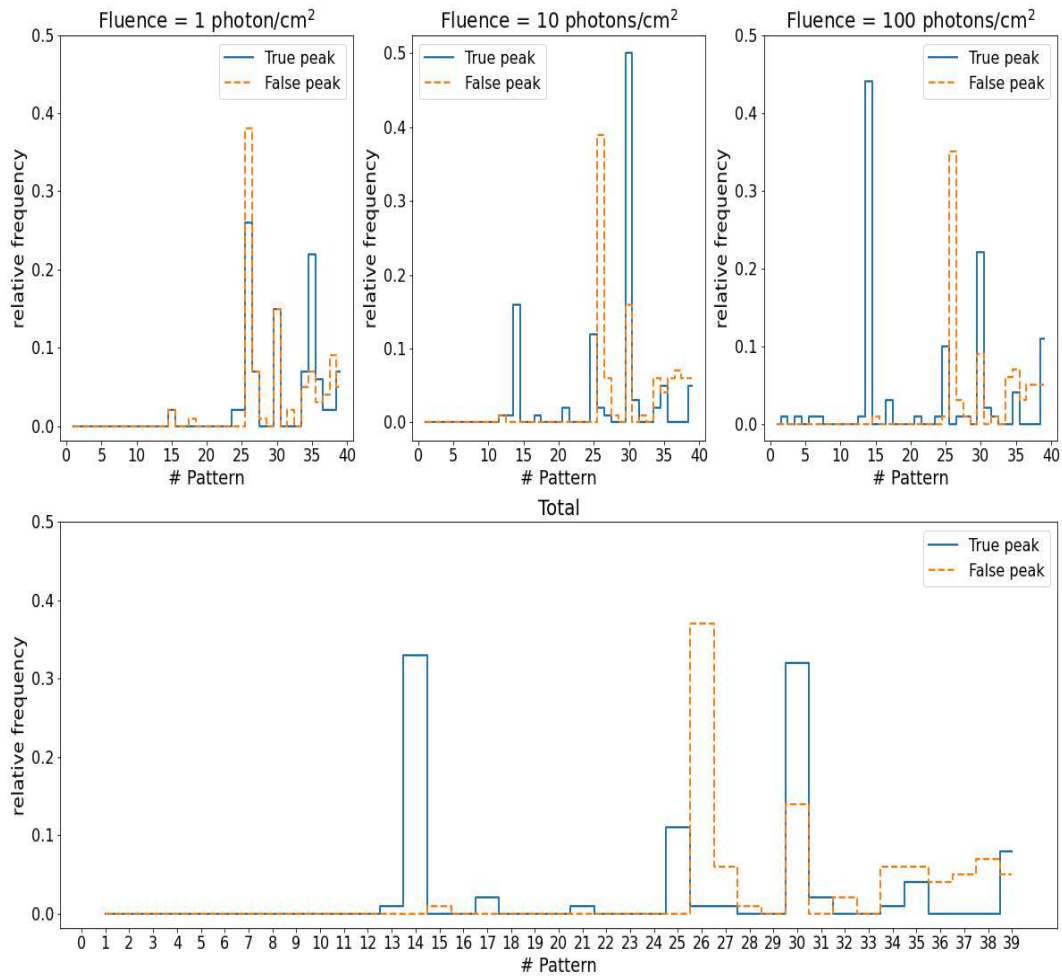


Figure 21 A comparison between patterns used to detect true and false peaks. At the top of the panel, different results for different fluences; for fluence=1 ph cm⁻² one can see a not so different result with true and false peak patterns. For higher fluences, one can see that pattern #26 detects many false peaks without detecting a big quantity of true ones.

6.2. Analysis with different characteristics of simulated GRBs









We plan on extending our analysis by changing the characteristics of the simulated GRBs: e.g., (i) by modifying the rise and the decay times, (ii) by considering light curves with more than one peak.

6.3. Analysis using individual bands

Another aspect worth a deeper investigation is the analysis of MEPSA detection efficiency using single bands, rather than using S, X, XS bands.

Appendix B

GRB minimum variability timescale with Insight-HXMT and *Swift* Implications for progenitor models, dissipation physics, and GRB classifications[★]

A. E. Camisasca¹ , C. Guidorzi^{1,2,3} , L. Amati³, F. Frontera^{1,3} , X. Y. Song⁴, S. Xiao^{4,5}, S. L. Xiong⁴, S. N. Zhang^{4,5}, R. Margutti^{6,7} , S. Kobayashi⁸, C. G. Mundell⁹ , M. Y. Ge⁴, A. Gomboc¹⁰, S. M. Jia⁴, N. Jordana-Mitjans⁹ , C. K. Li⁴, X. B. Li⁴, R. Maccary¹ , M. Shrestha¹¹ , W. C. Xue⁴, and S. Zhang⁴

¹ Department of Physics and Earth Science, University of Ferrara, Via Saragat 1, 44122 Ferrara, Italy
 e-mail: annaelisa.camisasca@unife.it

² INFN – Sezione di Ferrara, Via Saragat 1, 44122 Ferrara, Italy

³ INAF – Osservatorio di Astrofisica e Scienza dello Spazio di Bologna, Via Piero Gobetti 101, 40129 Bologna, Italy

⁴ Key Laboratory of Particle Astrophysics, Institute of High Energy Physics, Chinese Academy of Sciences, 19B Yuquan Road, Beijing 100049, PR China

⁵ University of Chinese Academy of Sciences, Chinese Academy of Sciences, Beijing 100049, PR China

⁶ Department of Astronomy, University of California, 501 Campbell Hall, Berkeley, CA 94720, USA

⁷ Department of Physics, University of California, 366 Physics North MC 7300, Berkeley, CA 94720, USA

⁸ Astrophysics Research Institute, Liverpool John Moores University, IC2, Liverpool Science Park, 146 Brownlow Hill, Liverpool L3 5RF, UK

⁹ Department of Physics, University of Bath, Claverton Down, Bath BA2 7AY, UK

¹⁰ Center for Astrophysics and Cosmology, University of Nova Gorica, Vipavska 13, 5000 Nova Gorica, Slovenia

¹¹ Steward Observatory, University of Arizona, 933 North Cherry Avenue, Tucson, AZ 85721-0065, USA

Received 9 December 2022 / Accepted 2 January 2023

ABSTRACT

Context. There has been significant technological and scientific progress in our ability to detect, monitor, and model the physics of γ -ray bursts (GRBs) over the 50 years since their first discovery. However, the dissipation process thought to be responsible for their defining prompt emission is still unknown. Recent efforts have focused on investigating how the ultrarelativistic jet of the GRB propagates through the progenitor’s stellar envelope for different initial composition shapes, jet structures, magnetisation, and, consequently, possible energy dissipation processes. Study of the temporal variability – in particular the shortest duration of an independent emission episode within a GRB – may provide a unique way to distinguish the imprint of the inner engine activity from geometry and propagation related effects. The advent of new high-energy detectors with exquisite time resolution now makes this possible.

Aims. We aim to characterise the minimum variability timescale (MVT) defined as the shortest duration of individual pulses that shape a light curve for a sample of GRBs in the keV–MeV energy range and test correlations with other key observables such as the peak luminosity, the Lorentz factor, and the jet opening angle. We compare these correlations with predictions from recent numerical simulations for a relativistic structured – possibly wobbling – jet and assess the value of temporal variability studies as probes of prompt-emission dissipation physics.

Methods. We used the peak detection algorithm MEPSA to identify the shortest pulse within a GRB time history and preliminarily calibrated MEPSA to estimate the full width at half maximum duration. We then applied this framework to two sets of GRBs: *Swift* GRBs (from 2005 to July 2022) and Insight Hard Modulation X-ray Telescope (Insight-HXMT) GRBs (from June 2017 to July 2021, including the exceptional 221009A). We then selected 401 GRBs with measured redshift to test for correlations.

Results. We confirm that, on average, short GRBs have significantly shorter MVTs than long GRBs. The MVT distribution of short GRBs with extended emission such as 060614 and 211211A is compatible only with that of short GRBs. This is important because it provides a new clue concerning the progenitor’s nature. The MVT for long GRBs with measured redshift anti-correlates with peak luminosity; our analysis includes careful evaluation of selection effects. We confirm the anti-correlation with the Lorentz factor and find a correlation with the jet opening angle as estimated from the afterglow light curve, along with an inverse correlation with the number of pulses.

Conclusions. The MVT can identify the emerging putative new class of long GRBs that are suggested to be produced by compact binary mergers. For otherwise typical long GRBs, the different correlations between MVT and peak luminosity, Lorentz factor, jet opening angle, and number of pulses can be explained within the context of structured, possibly wobbling, weakly magnetised relativistic jets.

Key words. radiation mechanisms: non-thermal – relativistic processes – gamma-ray burst: general – stars: jets

[★] Full Tables 1, 2, and 5 are only available at the CDS via anonymous ftp to cdsarc.cds.unistra.fr (130.79.128.5) or via <https://cdsarc.cds.unistra.fr/viz-bin/cat/J/A+A/671/A112>

1. Introduction

The prompt emission of γ -ray bursts (GRBs) is the first energetic and short-lived electromagnetic messenger produced by a relativistic jet that forms in at least two classes of progenitors: (i) binary compact object mergers, where at least one of the two components is thought to be a neutron star (NS; Eichler et al. 1989; Paczynski 1991; Narayan et al. 1992); and (ii) collapsars, massive stars whose core collapses into a compact object, which powers a relativistic jet that breaks out of the stellar envelope (Woosley 1993; Paczyński 1998; MacFadyen & Woosley 1999). Most GRBs of the former (latter) class have a typical duration of a few 0.1 s (> several seconds) and are therefore referred to as ‘short’ (‘long’), hereafter SGRBs (LGRBs). The discovery of so-called soft extended emission short GRBs (hereafter SEE-SGRBs; Norris & Bonnell 2006), that is, GRBs whose duration is formally long ($T_{90} > 2$ s, usually taken as the boundary), but whose profile includes an initial hard subsecond spike followed by a several-second-long-lived soft tail, and for which evidence points to class (i), emphasised that duration alone can occasionally be misleading (e.g. Amati 2021). The occurrence of baffling SEE-SGRBs, such as 060614 (Gehrels et al. 2006; Della Valle et al. 2006; Fynbo et al. 2006; Jin et al. 2015) and the recent 211211A (Rastinejad et al. 2022; Gompertz et al. 2023; Yang et al. 2022; Troja et al. 2022; Xiao et al. 2022), shows that events of class (i) may exhibit time profiles that further challenge and elude this picture. Opposite cases of apparent SGRBs that instead belong to class (ii) have also been identified (Ahumada et al. 2021; Zhang et al. 2021; Rossi et al. 2022), so in hindsight the emerging picture raises the issue of a contamination between the two classes that is potentially more widespread than believed so far, purely based on time profiles. Consequently, to avoid confusion and adopting previous suggestions (Zhang 2006; Zhang et al. 2007; Kann et al. 2011; Tsvetkova et al. 2017), when talking about the progenitor case, hereafter we refer to (i) and (ii) candidates as Type-I and Type-II, respectively.

Many open and intertwined issues still enshroud the GRB prompt emission, including the question of which source of energy turns into γ -rays between bulk kinetic or magnetic. One may also seek to determine by which dissipation process they are ruled, the composition of the relativistic jet, and at what distance from the inner progenitor the dissipation takes place.

Among the distinctive properties are the variety and complexity of GRB light curves (LCs), which manifest as a wide range of variability over several timescales. While this complexity likely retains a wealth of information, a full understanding has yet to be found. This variability can be the result of several different contributions: (a) inner engine activity both in terms of short timescales and number of peaks (Kobayashi et al. 1997); (b) propagation of the relativistic flow through the stellar envelope, which in turn also depends on (c) the jet composition (Gottlieb et al. 2019, 2020a,b, 2021a,b); (d) geometry: structure of the jet and angle of the observer, θ_{obs} , with respect to the opening angle of the jet core, θ_j (e.g. Salafia et al. 2016); and (e) a possible precessing or wobbling jet (Portegies Zwart et al. 1999; Portegies Zwart & Totani 2001; Fargion 2001; Reynoso et al. 2006; Lei et al. 2007; Budai et al. 2020), as suggested by state-of-the-art, 3D, general-relativity-magnetohydrodynamic (GRMHD) simulations (Gottlieb et al. 2022a).

Numerous definitions of GRB variability have been put forward in the literature, aimed at quantifying the net variance of the GRB signal once the contribution of the noise due

to counting statistics (hereafter statistical noise) is removed. This was done either by summing the contributions of all timescales after excluding some kind of trend (e.g. Reichart et al. 2001; Fenimore & Ramirez-Ruiz 2000) or decomposing the signal variance over a timescale base. In the latter case, the decomposition can be done either in time (Li 2001; Margutti 2009; Margutti et al. 2011) or frequency domain, based on either Fourier analysis (Guidorzi et al. 2016; Dichiara et al. 2016) or wavelets (Golkhou & Butler 2014, hereafter GB14; Golkhou et al. 2015; Vianello et al. 2018). In spite of the scatter, variability was found to correlate with peak luminosity for LGRBs (Fenimore & Ramirez-Ruiz 2000; Reichart et al. 2001; Guidorzi et al. 2005), although the slope can vary remarkably depending on the definition of variability and other aspects (Guidorzi et al. 2006).

A related way to characterise the variability is the identification of the minimum variability timescale (MVT)¹, which is the shortest timescale on which uncorrelated power is found to be in significant excess of the statistical noise as well as of the correlated signal due to the overall temporal shape of the GRB LC. In principle this quantity helps to constrain the emitting region size and the activity of the inner engine and could help identify the different contributions (a)–(e) listed above, especially when it is studied in conjunction with other key properties.

The two classes of SGRBs and LGRBs have partially overlapping, but different, MVT distributions, with median rest-frame values of 10 and 45 ms, respectively, and very few (<10%) with ms MVT (Golkhou et al. 2015; see also MacLachlan et al. 2013). The MVT of LGRBs was found to correlate with the bulk Lorentz factor Γ_0 (Sonbas et al. 2015) estimated from the early afterglow peak, whenever this is due to the deceleration of the relativistic jet in the thin shell regime (Sari & Piran 1999; Molinari et al. 2007).

A drawback of most definitions lies in the meaning itself and how this is to be interpreted: while connections are sometimes found with simple properties, such as the individual pulse rise time (MacLachlan et al. 2012), the interpretation is not straightforward. This is partly due to the complexity of the GRB signal, which is short-lived, highly non-stationary, and occasionally has an evolving power density spectrum (e.g. Margutti et al. 2008). A common feature of most definitions of MVT is that the identification of one or more temporal structures associated with MVT relies on their relative weight in the total net variance of the GRB LC. As a consequence, a given spike could be identified or not, depending on its impact on the time-averaged power density spectrum.

In this paper, we adopted an alternative approach that builds on a simple definition of MVT as the full width at half maximum (FWHM) of the shortest (statistically significant) peak (hereafter FWHM_{min}). The identification of statistically significant peaks is done using the sensitive and well-calibrated algorithm MEPSA (Guidorzi 2015). A similar idea, based on the identification of individual pulses within a GRB, was already proposed in the past (Bhat et al. 2012; Bhat 2013), but it was not explored any further. This approach has three main advantages: (1) the interpretation is straightforward; (2) it is related directly to a specific temporal structure within the overall GRB time profile and, as such, the probability of it being identified does not depend on its relative weight within the total variance of the GRB; and (3) a careful evaluation of how the measure of MVT is affected by the signal-to-noise ratio (S/N) is feasible and, consequently, of the impact on the correlations involving MVT. To this aim, we

¹ Shortened to “MTS” in some papers.

Table 1. First 10 GRBs of *Swift* sample.

GRB name	FWHM _{min} (s)	T_{90} (s)	z	N_{peaks}	Type
050117	$0.810^{+0.280}_{-0.208}$	166.648 ± 2.423	–	15	L
050124	$1.009^{+0.349}_{-0.259}$	3.936 ± 2.012	–	2	L
050126	$9.063^{+3.134}_{-2.329}$	48.000 ± 22.627	1.290	1	L
050128	$0.296^{+0.102}_{-0.076}$	28.000 ± 9.055	–	7	L
050202	$\leq 0.103^{+0.036}_{-0.026}$	0.112 ± 0.031	–	1	S
050215A	$6.238^{+2.158}_{-1.603}$	66.412 ± 5.307	–	1	L
050215B	$4.384^{+1.516}_{-1.127}$	11.044 ± 3.931	–	1	L
050219A	$7.432^{+2.570}_{-1.910}$	23.812 ± 2.258	0.211	1	L
050219B	$0.770^{+0.266}_{-0.198}$	28.720 ± 7.120	–	4	L
050223	$23.518^{+8.134}_{-6.044}$	22.680 ± 4.481	0.592	1	L

Notes. This table is available in its entirety in machine-readable form at the CDS.

carried out our analysis using two GRB catalogues with complementary energy passbands: the first GRB catalogue (Song et al. 2022) of the Insight Hard X-ray Modulation Telescope (Insight-HXMT; Li 2007; Zhang et al. 2020) and that of the Burst Alert Telescope (BAT, 15–150 keV; Barthelmy et al. 2005) aboard the *Neil Gehrels Swift* Observatory (Gehrels et al. 2004).

The HXMT, named ‘Insight’ after launch on June 15, 2017, is the first Chinese X-ray astronomy satellite. Its scientific payload consists of three main instruments: the Low Energy X-ray telescope (LE; 1–15 keV; Chen et al. 2020), the Medium Energy X-ray telescope (ME; 5–30 keV; Cao et al. 2020), and the High Energy X-ray telescope (HE; Liu et al. 2020). The HE consists of 18 NaI/CsI detectors which cover the 20–250 keV energy band for pointing observations. In addition, it can be used as an open sky GRB monitor in the 0.2–3 MeV energy range. The unique combination of a large geometric area ($\sim 5100 \text{ cm}^2$) and of continuous event tagging with timing accuracy $< 10 \mu\text{s}$, makes HXMT/HE an ideal instrument to study MVTs with GRBs. In this work, we investigated this possibility by carrying out a systematic analysis of the data acquired with HE, which was used as an open sky γ -ray monitor.

Section 2 describes the GRB samples; the data analysis is reported in Sect. 3, whereas results are in Sect. 4. We discuss the implications in Sect. 5 and conclude in Sect. 6. Hereafter, we assume the latest *Planck* cosmological parameters: $H_0 = 67.74 \text{ km s}^{-1} \text{ Mpc}^{-1}$, $\Omega_m = 0.315$, $\Omega_\Lambda = 0.685$ (Planck Collaboration VI 2020).

2. Data set

2.1. *Swift*/BAT sample

We considered all GRBs detected by *Swift*/BAT in burst mode from January 2005 to July 2022. We extracted the mask-weighted LCs in the 15–150 keV energy band following the standard procedure recommended by the BAT team² with a set of different uniform bin times: 1, 4, 64, and 1000 ms. We excluded all the GRBs whose LCs were not entirely covered in burst mode. We then systematically applied MEPSA to each of the

² https://swift.gsfc.nasa.gov/analysis/threads/bat_threads.html

LCs. For each GRB, the FWHM_{min} was determined through the procedure described in Sect. 3. Finally, we ignored the GRBs for which either the FWHM_{min} or T_{90} is not significant. The final sample of GRBs includes 1291 GRBs (*Swift* sample hereafter). For 21 GRBs only an upper limit on the FWHM_{min} was derived. We also considered the duration of each GRB (expressed in terms of T_{90}) using the values by Lien et al. (2016), which cover up to October 2015. For the remaining GRBs we adopted the values reported by the BAT team through dedicated BAT refined Gamma-ray Coordinates Network (GCN) circulars³. For about one third of the sample (401/1291) the redshift is known.

Although a lower threshold was suggested for *Swift* (Bromberg et al. 2013), we take the value of 2 s as an approximate boundary between S- and LGRBs, in line with the traditional division (Kouveliotou et al. 1993) and with the choice of *Swift* team members (D’Avanzo et al. 2014). In this way, we obtained 78 SGRBs. In addition, the sample includes 24 SEE-GRBs⁴. The overall sample consists of 102 Type-I GRBs, that is 8% of the whole sample. Table 1 reports the data.

2.2. *Insight-HXMT/HE* sample

We considered all GRBs detected by Insight-HXMT/HE from June 2017 to June 2021, as catalogued by the Insight-HXMT team (Song et al. 2022). Since HE continuously acquires data in event mode, it has no trigger logic on board. For each GRB, whenever the GRB was detected in common by other experiments, such as *Swift*/BAT or *Fermi*/GBM, we took the trigger time provided by them as the GRB start. Differently, we determined the start time by visual inspection of the HE LC.

For each GRB, we extracted the event files and auxiliary files including time-resolved information about the detectors’ dead time, spacecraft’s attitude, and the position, within a time window from -300 to 300 s around the GRB time. Using the HE

³ https://gcn.gsfc.nasa.gov/gcn3_archive.html

⁴ They are: 050724, 051227, 060614, 061006, 061210, 070714B, 071227, 080503, 090510, 090531B, 090715A, 090916, 110402A, 111121A, 150424A, 160410A, 161129A, 170728B, 180618A, 180805B, 181123B, 200219A, 211211A, 211227A.

units as an open-sky monitor, for each of the 18 HE detectors, we extracted a set of LCs with the same bin times as for the *Swift* sample (i.e. 1, 4, 64, and 1000 ms) selecting only the CsI events, as was done in [Song et al. \(2022\)](#). The LCs include dead-time corrected counts within the total energy passband from all 18 HE detectors summed together. The total energy passband depends on the HE operation mode:

- normal mode: 80–800 keV;
- GRB mode (low gain): 200–3000 keV.

We analysed 21 GRBs⁵ separately; due to their very intense peak count rates, the onboard electronics of at least one physical data acquisition unit (PDAU; see [Liu et al. 2020](#) for details) were temporarily unable to keep up with the exceptional rate of events to be recorded (see [Xiao et al. 2020](#); [Song et al. 2022](#) for details). We restricted our analysis to the time windows where no PDAU was saturated. For these GRBs, we consequently ended up with upper limits on the FWHM_{\min} . In the following, we consider the LCs summed over the 18 detectors.

The background was estimated in two independent ways: (i) through interpolation with a maximum of a third-degree polynomial within two time windows, preceding and following the GRB, respectively (the size of each time window varies for different GRBs and had to be determined by visual inspection); and (ii) by iterative interpolation of a unique time interval that includes both time windows used in (i) as well as the GRB interval. At every iteration, all the time bins whose counts exceeded the interpolated signal (where σ is the corresponding Poisson uncertainty) by $\geq 2\sigma$ are rejected. Iterations stop when no further bins are rejected. This iterative procedure was applied to the 1-s LC, and the resulting background model was then properly renormalised to the LCs with different bin times. To determine which of the two outcomes is to be used for each GRB, we calculated the null hypothesis probability (NHP) associated with a two-tail χ^2 test applied to the residuals of each LC with respect to each background model and chose the more probable one, provided that NHP was $\geq 1\%$.

With the exception of the saturated GRBs, we used the T_{90} values reported for the GRBs belonging to golden and silver samples of the HXMT GRB catalogue ([Song et al. 2022](#)). For the saturated sample, we used the T_{90} as reported on Konus-Wind, *Fermi*-GBM, and Insight-HXMT GCN circulars. If different estimates of T_{90} were provided by different experiments for a given GRB, we conservatively used a mean and an error that include all the values.

We decided to include the recent, exceptionally bright 221009A ([Dichiara et al. 2022](#)). Since it repeatedly saturated the electronics of Insight-HXMT/HE ([Ge et al. 2022](#)), we provided an upper limit on the FWHM_{\min} as for the other saturated GRBs. We estimated T_{90} using the data of BepiColombo-MGNS in the 280–460 keV passband, which has one of the few unsaturated and publicly available time profiles ([Kozyrev et al. 2022](#)). The 2-s time resolution is too coarse to constrain the MVT, but it is enough for the T_{90} , given the very long duration. The background was interpolated linearly using the intervals $-900 \text{ s} \leq t \leq 100 \text{ s}$ and $670 \text{ s} \leq t \leq 1600 \text{ s}$, with t measured since 13:15:26.90 UTC.

⁵ They are 171011B, 180113B, 180113C, 180218A, 180720B, 180914B, 181222B, 190103A, 190114C, 190305A, 190411A, 190415A, 190530A, 190606A, 190706C, 190928A, 191025B, 191227B, 201016A, 201227A, and 221009A. 200415A saturated the electronics too, but it was not considered as it is probably an extragalactic magnetar giant flare; ([Yang et al. 2020](#); [Fermi-LAT Collaboration 2021](#); [Roberts et al. 2021](#); [Svinkin et al. 2021](#)).

Finally, we systematically ran MEPSA on all the LCs and applied the procedure described in Sect. 3 to determine the FWHM_{\min} of each GRB as we did for the *Swift* sample (Sect. 2.1). Unlike for the BAT LCs, for which the Gaussian-noise regime is ensured by the fact that the rates are linear combinations of several thousands of independent detectors, in the case of the 1-ms LCs summed over all the 18 HE detectors the mean counts per bin amount to $\lesssim 10$. Hence, the Gaussian-noise assumption is only approximately matched. To partially account for this deviation and use a more conservative estimate of the variance of a Poisson variate for small numbers, we corrected the uncertainties following the prescriptions by [Gehrels \(1986\)](#).

We ignored the GRBs with non-significant values for either FWHM_{\min} or T_{90} , as we did with the *Swift* sample. The final sample of Insight-HXMT/HE includes 212 GRBs, 25 of which were detected in GRB mode, while the remaining ones in normal mode. Hereafter we will refer to them as the HXMT sample. For 14 GRBs, only an upper limit on the FWHM_{\min} was obtained. Taking the value of 2 s as an approximate boundary between SGRBs and LGRBs, we find that 24 are SGRBs, while two are SEE-GRBs. Thus, 26 are Type-I GRBs, which corresponds to 12% of the total. This result shows that Insight-HXMT is more effective in detecting short hard GRBs than *Swift* (7%; Sect. 2.1).

For six GRBs, the redshift is known. There are 44 GRBs that were detected by *Swift*/BAT and Insight-HXMT and for which a comparative analysis of our results is feasible and done in Sect. 4.2. Data are reported in Table 2.

3. Data analysis

We applied MEPSA to the dataset described in Sect. 2 in order to obtain the FWHM_{\min} . In particular, for each GRB, we started from the 64-ms LC. A detected peak is considered a candidate when it satisfies the following two conditions: (i) $S/N > S/N_{\min}^{(\Delta t)}$, where the threshold depends on the LC bin time Δt ; (ii) $\Delta t_{\text{det}} > \Delta t_{\text{det},\min}^{(\Delta t)}$, where Δt_{det} is the so-called detection timescale, a MEPSA parameter which defines the bin timescale that optimises the peak identification ([Guidorzi 2015](#)). Both sets of thresholds are reported in Table 3. Requirement (ii) is to ensure that the bin time is short enough to resolve the temporal structure: the duration of the peak must be greater than the size of the bin. This is the reason for setting the threshold to twice the corresponding bin time: $\Delta t_{\text{det},\min}^{(\Delta t)} = 2\Delta t$. The different threshold values on the S/N for different Δt were calculated to keep the number of expected statistical fluctuations being classified as genuine peaks approximately constant: the shorter Δt and the correspondingly larger number of bins to be screened that span a given time interval.

We decided to start with $\Delta t = 64 \text{ ms}$ and systematically avoided research with finer resolutions because preliminary attempts showed that the number of peak candidates was higher than expected, especially in the HXMT data. The reason behind this behaviour is the presence of sub-millisecond spikes caused by the electronics repeatedly counting the large signal deposited by energetic cosmic rays ([Wu et al. 2022](#)). Whenever only (i) is fulfilled, we move to a finer time resolution (i.e. 4 ms and then 1 ms if necessary) and look for the same peak until both (i) and (ii) are satisfied; if (i) and (ii) are never satisfied, an upper limit on the FWHM_{\min} is taken from the finest timescale for which (i) is satisfied. When no peak is found at 64 ms that fulfils both (i) and (ii), we move to the $\Delta t = 1 \text{ s}$. If no qualified peak is found, the GRB is discarded because of poor S/N. Figure 1 shows a schematic description of the procedure. The

Table 2. First 10 GRBs of Insight-HXMT sample.

GRB name	FWHM _{min} (s)	T_{90} (s)	z	N_{peaks}	Type
170626A	$0.097^{+0.033}_{-0.025}$	12.690 ± 0.081	–	4	L
170626B	$1.969^{+0.681}_{-0.506}$	6.511 ± 1.120	–	2	L
170705A	$0.784^{+0.271}_{-0.201}$	18.460 ± 6.340	2.010	1	L
170708A	$0.041^{+0.014}_{-0.011}$	0.200 ± 0.022	–	1	S
170712A	$1.188^{+0.411}_{-0.305}$	8.511 ± 1.119	–	1	L
170718A	$6.802^{+2.353}_{-1.748}$	24.160 ± 3.322	–	1	L
170726A	$0.149^{+0.051}_{-0.038}$	22.871 ± 0.901	–	8	L
170728B	$\leq 0.275^{+0.095}_{-0.071}$	16.860 ± 2.371	–	2	L
170801A	$0.021^{+0.007}_{-0.005}$	0.460 ± 0.750	–	1	S
170802A	$0.033^{+0.012}_{-0.009}$	0.820 ± 0.014	–	2	S

Notes. This table is available in its entirety in machine-readable form at the CDS.

Table 3. Thresholds on S/N and on Δt_{det} corresponding to the different bin times that were adopted to determine the FWHM_{min}.

Bin time Δt (ms)	$S/N_{\text{min}}^{(\Delta t)}$	$\Delta t_{\text{det,min}}^{(\Delta t)}$ (ms)
1	7.0	2
4	6.8	8
64	6.4	128
1000	6.0	2000

FWHM of each peak is estimated through the calibrated relation based on the combination of S/N and Δt_{det} (see Appendix A for details).

4. Results

4.1. Comparison between FWHM_{min} and other minimum variability timescale metrics

Our choice of adopting the FWHM_{min} as an indicator of the MVT of a given GRB LC in principle represents a different definition than other ones that appeared in the literature. In particular, the most distinctive feature of FWHM_{min} is that the duration of a possible, statistically significant, narrow pulse can be enough to qualify it as the MVT, irrespective of its impact on the overall variance of the GRB profile and for its physical impact. Nevertheless, it is worth exploring how the FWHM_{min} correlates with other metrics. To this aim, we selected a common sample of 467 BAT GRBs, for which GB14 estimated the MVT. Both GB14's and our estimates are derived from the same BAT data. Figure 2 shows the comparison between the FWHM_{min} and the corresponding MVT estimated by GB14, with equality shown by a solid line. The two metrics evidently correlate over four decades, with some scatter around equality: this result proves that, although strongly correlated, the two metrics are not completely interchangeable, with a sizeable fraction of cases for which they differ by up to one decade.

4.2. FWHM_{min} as a function of energy

Figure 3 shows the comparison of the FWHM_{min} as measured with both Insight-HXMT and *Swift*/BAT using the common sample of 44 GRBs, three of which only have an upper limit on the FWHM_{min} available. The distribution of the logarithm of the ratio between the two measures is approximately normal, with the mean value and standard deviation corresponding to a multiplicative factor of 2 and 3, respectively. Hence, the FWHM_{min} as measured with *Swift* is on average twice as long as that measured with Insight-HXMT. This is similar to the result obtained by Golkhou et al. (2015) from the comparison between *Fermi*/GBM and *Swift*/BAT, as one should expect due to the narrowing of pulses with energy.

Additionally, we can constrain the power-law index α of the relation $\text{FWHM}(E) \propto E^{-\alpha}$, where E is the geometric mean of the boundaries of the energy passband. To this aim, for each GRB in the common sample we did not restrict to the shortest pulse of each GRB, instead we calculated α considering the FWHM of the different peaks as detected with MEPSA in both HXMT and BAT data. The identification of the same peak, as seen in the two LCs, is assessed through the temporal coincidence within uncertainties. We identified 93 peaks, four of which were in SGRBs. For the energy values, we used the geometric mean of the boundaries of the corresponding energy bands (15–150 keV for BAT, 80–800 keV for HXMT normal mode, 200–3000 keV for HXMT GRB or low-gain mode; HXMT energy bands refer to the deposited energies of incident photons). We find $\alpha_{\text{mean}} = 0.45 \pm 0.08$, $\alpha_{\text{median}} = 0.54 \pm 0.07$, $\sigma = 0.77$; this result is consistent with the values derived modelling the auto-correlation function width (Fenimore et al. 1995): $\alpha = 0.37$ to 0.43 (see also Borgonovo et al. 2007, who found median values in the range from 0.21 to 0.29). Figure 4 displays the α distribution for all GRBs (black histogram), SGRBs (blue histogram), and LGRBs (red histogram).

4.3. FWHM_{min} versus T_{90}

Figure 5 shows the scatter plots of the FWHM_{min} and T_{90} for *Swift*/BAT and Insight-HXMT samples along with the corresponding marginal distributions. FWHM_{min} spans the range

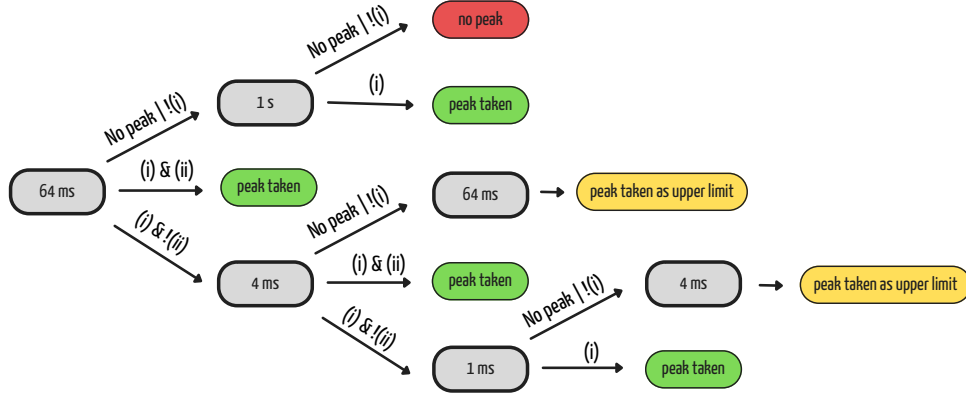


Fig. 1. A schematic description of the procedure adopted to determine the FWHM_{\min} of each GRB (see Sect. 3).

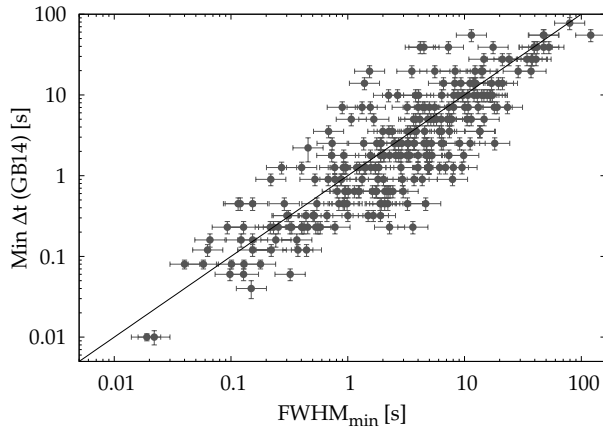


Fig. 2. Comparison between shortest FWHM as estimated with MEPSA (this work) and MVT estimated by GB14 for a common sample of *Swift*/BAT GRBs. Black line corresponds to equality.

from 10^{-2} to 10^2 s, whereas T_{90} spans from 10^{-2} to 10^3 s (10^2 s for Insight-HXMT). The bimodal nature of the marginal distribution of T_{90} seems to be slightly more evident in the Insight-HXMT sample, in spite of the lower number of GRBs. Equality is shown with a solid line. In addition, to guide the eye, we show lines that mark constant values for the ratio $r = T_{90}/\text{FWHM}_{\min}$: 10 (dashed), 100 (dash-dotted), and 1000 (dotted). Clearly, r increases with an increasing number of pulses within a GRB and/or with the presence of quiescent times. Most single-pulse GRBs lie in the region of $1 \lesssim r < 10$. Unsurprisingly, almost all SGRBs lie within this region. LGRBs instead span the $1 \lesssim r \lesssim 10^3$ range.

The marginal FWHM_{\min} distributions of SGRBs and of LGRBs are evidently different: for the *Swift* sample, a Kolmogorov–Smirnov (KS) test⁶ yields a 10^{-37} probability of being drawn from the same population; the logarithmic means of SGRBs and of LGRBs are, respectively, 0.2 and 4 s with a comparable scatter of 0.6 dex. Also in the Insight-HXMT sample, the two classes of S- and LGRBs have significantly different FWHM_{\min} distributions, with a 3×10^{-12} probability of being drawn from a common population. The logarithmic mean values are 0.1 and 1.3 s for the S- and LGRBs with the same scatter

⁶ The two-sample KS test was done using `scipy.stats.ks_2samp`.

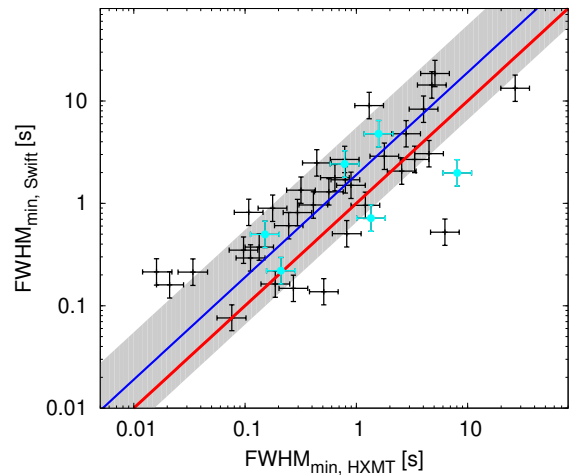


Fig. 3. FWHM as determined from Insight-HXMT/HE and *Swift*/BAT data for a sample of 44 GRBs in common. The red solid line shows the equality, while the blue line and the shaded area show the best proportionality relation and $1\text{-}\sigma$ region, corresponding to a factor of 2 and a relative scatter of a factor of 3, respectively. Cyan points are GRBs with spectroscopically measured redshift.

of ~ 0.6 dex, respectively, that is shorter than the corresponding quantities obtained in the softer energy band of the *Swift* sample, in line with the results of Sect. 4.2.

In the *Swift* sample we highlight the population of SEE-GRBs (green), with emphasis on two peculiar events whose LC and duration look like a typical LGRB one, but for which robust evidence for a compact binary merger progenitor rather than a collapsar was found: 060614 (Gehrels et al. 2006; Della Valle et al. 2006; Fynbo et al. 2006; Jin et al. 2015) and 211211A (Rastinejad et al. 2022; Gompertz et al. 2023; Yang et al. 2022; Troja et al. 2022). In spite of being just 24, their FWHM_{\min} values are more similar to those of SGRBs than of LGRBs. While both KS and Anderson-Darling (AD)⁷ tests between the FWHM_{\min} of SGRBs and SEE-GRBs do not reject the common population null hypothesis, the comparison between LGRBs and SEE-GRBs does so with a 3.4×10^{-14} KS-

⁷ The two-sample AD test was done using `scipy.stats.anderson_ksamp`.

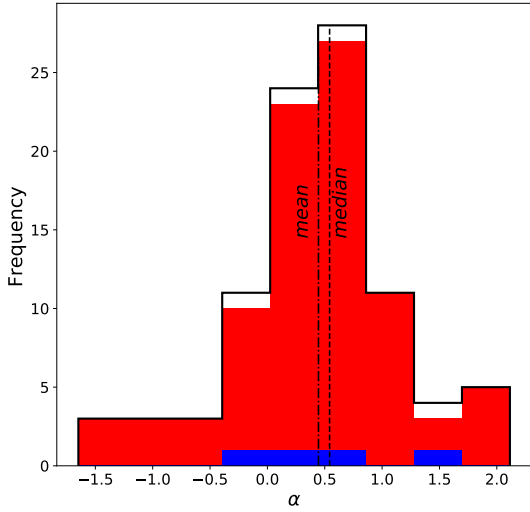


Fig. 4. Distribution of power-law index α ($FWHM \propto E^{-\alpha}$) for all the peaks that were identified in the GRB data of both *Swift* and HXMT (black histogram): SGRBs (filled blue histogram) and LGRBs (filled red histogram). Dash-dotted and dashed lines represent the mean (0.45 ± 0.08) and the median (0.54 ± 0.07) values, respectively.

probability (AD probability $< 10^{-3}$). Therefore, the $FWHM_{\min}$ is a promising metric to identify SEE-GRBs, even when the LC does not look like a single spike followed by a long, soft, and smooth tail, but rather shows multiple peaks extending over several seconds, as was the case of 060614 and 211211A. This suggests that the contamination of long GRBs with a $FWHM_{\min} \lesssim 0.1$ s that are currently misclassified as Type-II GRBs could be higher than expected, as was recently put forward from the observations of events like 211211A.

As a further check, we also show 18 LGRBs for which the collapsar origin is not disputable, thanks to the identification of an associated SN (gold points)⁸. Although a few of them have a $FWHM_{\min}$ that is comparable with that of SEE-GRBs, the bulk of SN-associated GRBs have longer MVTs, more representatively of the entire population of Type-II GRBs. Furthermore, the comparison between LGRBs associated with SN and SEE-GRBs done with KS and AD tests rejects the common population null hypothesis with a probability of 1.2×10^{-5} ($< 10^{-3}$) for KS (AD).

To the Insight-HXMT plot (see Fig. 5, right panel), we added the saturated GRBs (cyan), highlighting the cases of 190114C and 221009A; for 5⁹ of the 21 saturated GRBs it was not possible to find any eligible peak. These GRBs are SGRBs, and the time windows that are not saturated are too short for estimating $FWHM_{\min}$.

4.4. Dependence of $FWHM_{\min}$ and T_{90} on redshift

For the BAT sample with measured redshift, we studied whether the T_{90} and $FWHM_{\min}$ distributions show evidence for cosmological time dilation. We calculated the geometric mean of groups of GRBs: 30 (6) GRBs each for LGRBs (SGRBs) and

⁸ They are: 060729, 090618, 091127, 100316D, 101219B, 111228A, 120422A, 120714B, 120729A, 130215A, 130427A, 130831A, 140506A, 161219B, 171205A, 180728A, 190114C, and 190829A.

⁹ They are: 181222B, 190606A, 191025B, 191227B, and 201227A.

then fitted the geometric mean values as a function of $(1+z)^\alpha$, with the power-law index α free to vary. Figure 6 shows the results, which suggest that there is no evidence of a dependence on redshift (α being compatible with zero), at least as far LGRBs are concerned. The reason is that the different effects at play combine in such a way that the cosmological dilation is not dominant, as also found by previous investigations (Kocevski & Petrosian 2013; GB14; Golkhou et al. 2015; Littlejohns & Butler 2014). In particular, there are two main effects that contribute to mask the impact of cosmic dilation: (a) for a given observer energy passband, further GRBs are observed in a rest-frame harder band, which implies narrower temporal structures, according to the narrowing of pulses with energy (Norris et al. 1996; Fenimore et al. 1995); (b) the S/N of a LC decreases with increasing z so that only the brightest portion of the LC can be detected (Kocevski & Petrosian 2013).

For SGRBs the results seem to indicate values of both $FWHM_{\min}$ and T_{90} increasing with redshift. The reason for this apparently different behaviour from LGRBs is not obvious; in particular, it is not clear why the same effects mentioned above for LGRBs do not appear to affect SGRBs in a comparable way. It is nonetheless worth noting that each SGRB group includes just six events, a choice forced by the small number of SGRBs with known z , so our accuracy in estimating the standard deviation of $FWHM_{\min}$ and T_{90} for SGRB groups is lower than for LGRBs. In any case, the redshift range is shorter than that of LGRBs, so in principle the cosmic dilation correction does not have the same impact as it should for LGRBs, notwithstanding that there are counteracting effects at play. Moreover, should we correct the $FWHM_{\min}$ values for the SGRB sample, the result of statistically different distributions of $FWHM_{\min}$ for LGRBs and SGRBs would be reinforced. For this reason, we conservatively avoided correcting the observer-frame value for $FWHM_{\min}$ for cosmological time dilation.

4.5. Peak rate versus $FWHM_{\min}$

The peak rate PR_{\max} is defined as the peak rate of the most intense pulse of a given GRB. To explore the relation between isotropic-equivalent peak luminosity (L_p) and $FWHM_{\min}$, we first need to understand the relation between PR_{\max} and $FWHM_{\min}$ focusing on the selection effects that inevitably come into play. We did not consider the cosmological time dilation in its simplest formulation, which is $FWHM_{\min}/(1+z)$, given the interplay of different effects already discussed in Sect. 4.4. PR_{\max} appears to be anti-correlated with $FWHM_{\min}$ (Fig. 7). However, the selection effect at play here is to be evaluated carefully: for a very short pulse to be detected, its peak rate must be high enough to ensure the required minimum S/N. To this aim, we simulated a number of fast rise exponential decay (FRED) pulses covering the PR_{\max} versus $FWHM_{\min}$ space of interest and counted the fraction of pulses that were identified by our procedure. As a result, we modelled the detection efficiency, ϵ_{\det} , defined as the fraction of simulated pulses that are correctly identified, as a function of both PR_{\max} and $FWHM_{\min}$: $\epsilon_{\det}(PR_{\max}, FWHM_{\min})$. We found that the dependence is approximately linear in the logarithms for both *Swift* and HXMT data sets:

$$\epsilon_{\det} = a \log_{10} \left(\frac{FWHM_{\min}}{s} \right) + b \log_{10} \left(\frac{PR_{\max}}{\text{rate unit}} \right) + c, \quad (1)$$

where the rate units are either counts $s^{-1} \text{det}^{-1}$ (*Swift*/BAT) or counts s^{-1} (HXMT/HE). For BAT, the best-fit parameters are

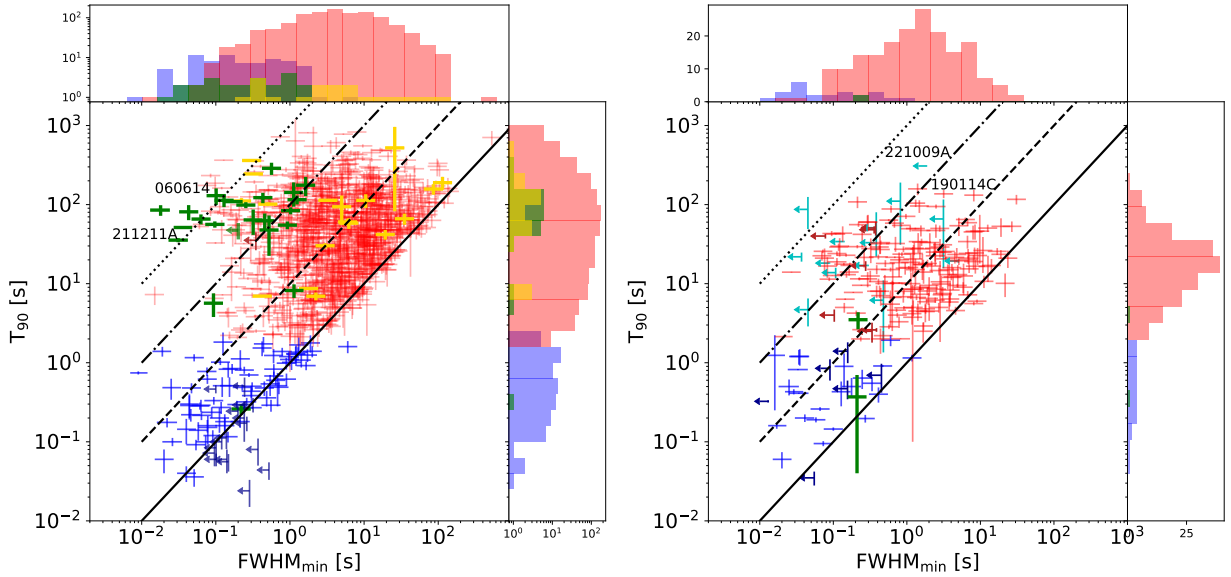


Fig. 5. Scatter plot of FWHM_{\min} and T_{90} for the *Swift*/BAT sample (left panel) and for the Insight-HXMT sample (right panel) along with the corresponding marginal distributions for three distinct populations of SGRBs (blue), LGRBs (red), and SEE-GRBs (green). Gold points are LGRBs with an associated SN. We highlight two SEE-GRBs, 060614 and 211211A, for which there is strong evidence of a binary merger rather than a collapsar origin. Cyan points refer to the Insight-HXMT saturated GRBs. We highlight 190114C and 221009A because of their high extreme energy (MAGIC Collaboration 2019; Frederiks et al. 2022). We do not consider *Swift* data where $T_{90} < \sigma_{T_{90}}$. Solid, dashed, dash-dotted, and dotted lines represent the equality, 10^1 , 10^2 , and 10^3 factor, respectively.

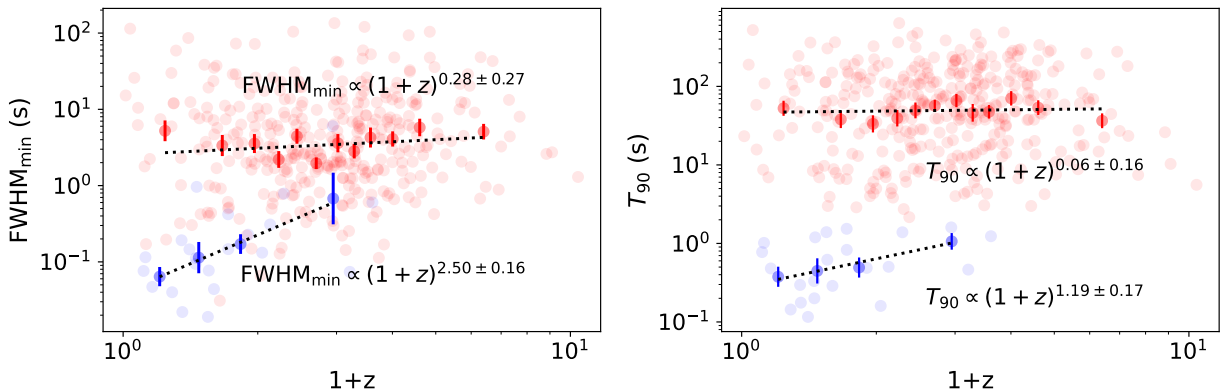


Fig. 6. FWHM_{\min} versus $(1+z)$ (left panel) and T_{90} versus $(1+z)$ (right panel) for the *Swift* sample as seen in the observer frame. Red (blue) dots correspond to LGRBs (SGRBs). Lighter dots refer to individual GRBs; darker ones refer to T_{90} geometrical mean of groups of 30 (6) LGRBs (SGRBs), sorted with increasing z .

$a = 0.78$, $b = 1.42$, and $c = 1.64$, and it is clipped either to 0 for negative values, or to 1 for values exceeding it. One can conveniently invert Eq. (1) to express the minimum value for PR_{\max} required for a pulse with a given FWHM_{\min} to be detected, which in the case of *Swift*/BAT becomes

$$\text{PR}_{\max}^{(\text{BAT})} \geq 0.35 \text{ cts s}^{-1} \text{ det}^{-1} \left(\frac{\text{FWHM}_{\min}}{s} \right)^{-0.55} 10^{0.7(\epsilon-1)}. \quad (2)$$

Figure 7 shows the results for both data sets; *Swift*/BAT (left panel) and HXMT (right panel) are shown as a colour-coded shaded area with detection efficiency being split into ten different ranges, from 0 to 1. This selection effect clearly affects the observed correlation between the two quantities for both classes of SGRBs and LGRBs.

Replicating similar simulations and analysis for the HXMT sample, we obtained a similar result, which is described by Eq. (1) with the following parameters: $a = 1.78$, $b = 3.05$, and $c = -8.40$. The analogous condition of Eq. (2) for HXMT is therefore

$$\text{PR}_{\max}^{(\text{HXMT})} \geq 1200 \text{ cts s}^{-1} \left(\frac{\text{FWHM}_{\min}}{s} \right)^{-0.58} 10^{0.33(\epsilon-1)}. \quad (3)$$

4.6. Peak luminosity versus FWHM_{\min}

When we move from the observer to the GRB rest frame by replacing PR_{\max} with the intrinsic quantity L_p , the problem of accounting for this bias becomes more complicated, due to the wide range in luminosity distance D_L spanned by the subsample

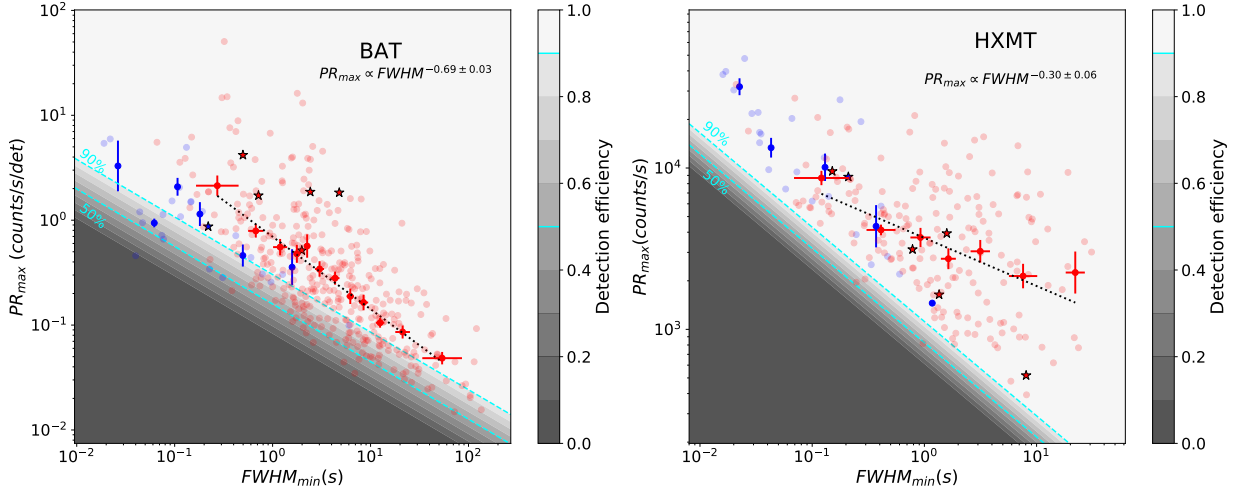


Fig. 7. Peak rate versus FWHM_{\min} for the *Swift* (left) and HXMT (right) samples. Blue dots correspond to Type-I GRBs (i.e. SGRBs and SEE-GRBs), and red ones correspond to Type-II GRBs. Lighter dots refer to single GRB data, darker ones refer to geometrical mean of data of groups of GRBs sorted with increasing z . For Type-I, each group is composed 6 of GRBs; for Type-II, each group is composed of 30 GRBs. Stars refer to the six GRBs in common between the *Swift* sample and HXMT sample. Dotted lines indicate the best fit of Type-II GRBs. The shaded areas show ten different regions with detection efficiency spanning the 0–1 range. Cyan dashed lines show the 50% and 90% detection efficiency contours.

with measured redshift. In fact, a given peak rate corresponds to a range in luminosities which is dominated by the range spanned by D_L^2 .

Given the paucity of GRBs with measured redshift in the HXMT sample, we only analysed L_p as a function of FWHM_{\min} for the *Swift* sample with known z . We estimated L_p for this sample by renormalising the peak count rate by the ratio between total counts and the fluence (in units of erg cm^{-2} in the 15–150 keV energy band), as published by the BAT team¹⁰. This procedure assumes a time-averaged spectrum, which is equivalent to neglecting any spectral evolution. However, for our purposes, the impact of an error on L_p up to a factor of a few is negligible overall.

We split the sample into nine subsets, with luminosity distance evenly spaced logarithmically, and considered the impact of detection efficiency in the L_p – FWHM_{\min} plane independently of each other. The results are shown in Fig. 8; the selection effect clearly affects the final correlation. In particular, two properties are evident: (i) the absence of relatively low luminosity GRBs with short FWHM_{\min} (bottom left corner of each panel) is clearly an observational bias; (ii) the absence of luminous GRBs with a long FWHM_{\min} (top right corner of each panel) is an intrinsic propriety of GRBs and suggests the possible existence of a maximum radiated energy within a single pulse (e.g. Dado & Dar 2022). To better appreciate this possibility, in each panel we show a grid with constant isotropic-equivalent released energy values of a single pulse, roughly estimated as $E_{\text{iso}}^{(\text{pulse})} \approx L_p \text{FWHM}_{\min}$.

Taken at face value, for the sample of BAT Type-I GRBs with measured z there is no evidence of correlation between L_p and FWHM_{\min} , possibly due to the relatively few GRBs. On the contrary, in the case of Type-II GRBs the two observables do correlate: null-hypothesis probabilities given by Pearson’s linear-rank- (calculated on logarithmic values) and Spearman’s and Kendall’s rank-correlation tests are 1.5×10^{-21} , 2.6×10^{-23} , and 9.8×10^{-22} , respectively. However, the key aspect is

understanding the extent by which this correlation is driven by the selection bias.

To this aim, we carried out a suite of simulations under the assumption that L_p is distributed independently of FWHM_{\min} and hence no intrinsic correlation exists. For each of the nine subsets with different redshift bins we randomly generated as many points in the FWHM_{\min} – L_p plane as those in the true subset, taking the very same values of L_p and assuming, for the FWHM_{\min} , a Gaussian kernel density estimation¹¹ of the observed FWHM_{\min} distribution of the entire LGRB sample with measured z as the probability density distribution. For each point to be accepted, we also set two conditions: (1) we randomly ran a Bernoulli trial assuming a probability given by the detection efficiency calculated at that point according to Eq. (1), and only the points with an outcome of 1 were taken; (2) $L_p \text{FWHM}_{\min} \leq E_{\text{iso,max}}^{(\text{pulse})}$, i.e. we required that the isotropic-equivalent pulse energy did not overcome the highest value observed in the corresponding real subsample. Each subset trial continued until the number of accepted simulated points was equal to the real ones. The rationale behind point (1) is mimicking the effect of the selection bias, whereas the purpose of (2) is to account for the absence of a very luminous and long FWHM_{\min} that is observed in the real sample. Every such round ended up with a simulated sample that shared the same number of Type-II GRBs as the real one and was affected by the same selection bias, with no intrinsic correlation between L_p and FWHM_{\min} . We simulated 10^4 such samples and derived a density map in the FWHM_{\min} – L_p plane to be compared with the real sample. Figure 9 shows the result. While the synthetic population does exhibit a correlation, as expected, it also appears more clustered than the real set.

To quantitatively assess how compatible the real and all the simulated samples are, we adopted the following approach: for each of them, we calculated the three correlation coefficients as we did for the real sample and obtained the corresponding distributions. Figure 10 shows the p -value distributions of the

¹⁰ https://swift.gsfc.nasa.gov/archive/grb_table/

¹¹ We used the `scipy.stats.kde.gaussian_kde()` function.

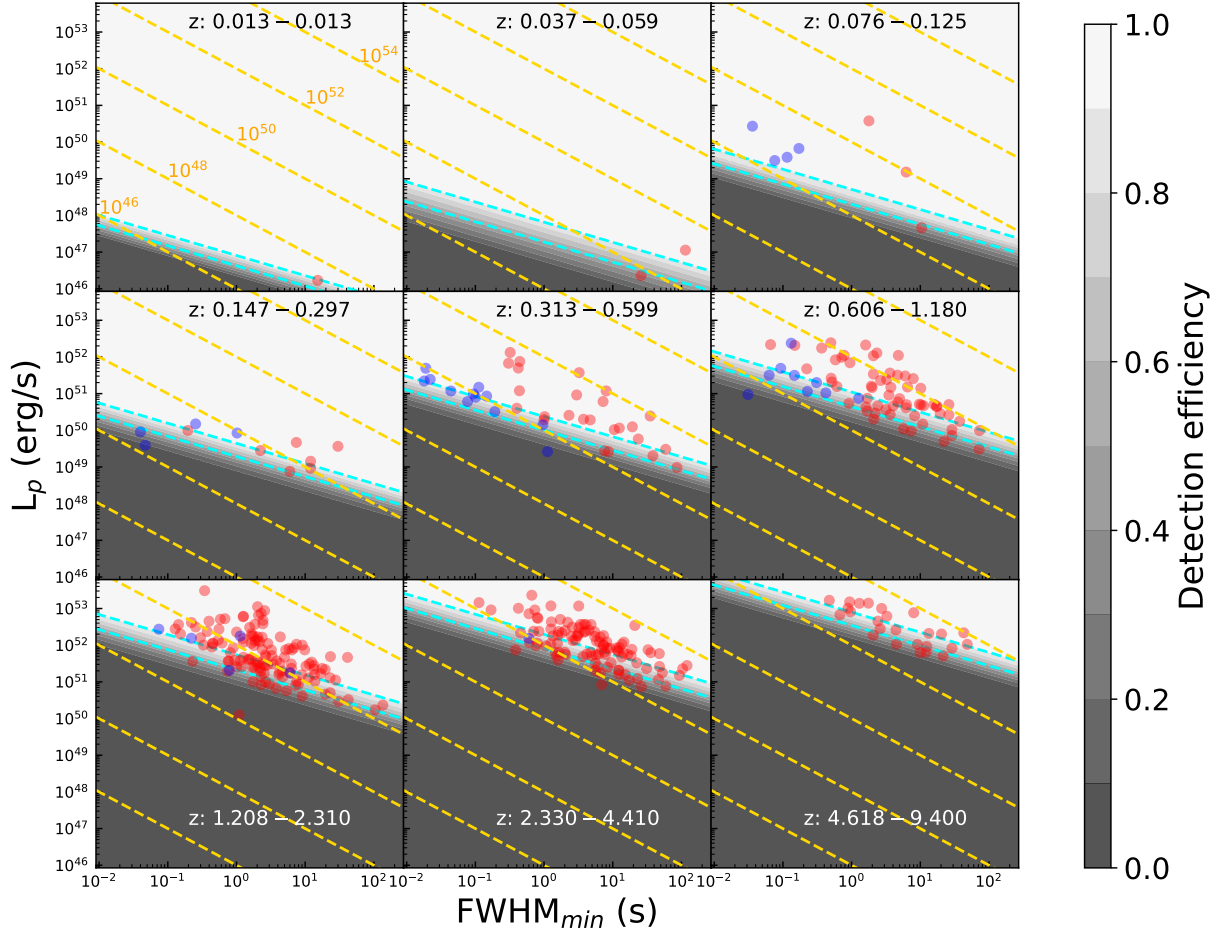


Fig. 8. Peak luminosity versus FWHM_{\min} for the *Swift*/BAT sample split into nine redshift bins with constant logarithmic space in luminosity distance; blue dots correspond to Type-I GRBs, and red ones correspond to Type-II GRBs. Dashed cyan lines correspond to 90% and 50% detection efficiency (vertical bar). Gold dashed lines represent loci of constant isotropic-equivalent released energy (in erg) of each individual peak, approximately calculated as $E_{\text{iso}} = L_p \text{FWHM}_{\min}$.

simulated samples, compared with the analogous quantities obtained for the real sample. The real sample exhibits a more significant correlation than simulated samples do: for each of the three correlation tests, only ≤ 20 synthetic samples out of 10^4 exhibited lower p values than the real sample.

We further explored how tightly this result depends on the assumed distribution of FWHM_{\min} : in fact, the observed one is inevitably the result of the same selection bias, whose impact we aim to study. We then repeated the same suite of simulations by assuming broader FWHM_{\min} distributions, in particular extending towards small values. As a result, the comparison between the simulated and the real correlation coefficients essentially did not change, so the conclusion that the observed correlation cannot be entirely ascribed to the selection bias still holds.

4.7. Number of peaks versus FWHM_{\min}

We investigated the role of the number of peaks within a GRB, as determined with MEPSA, in the FWHM_{\min} - L_p correlation. We therefore split the Type-II GRB sample with measured z into four groups with comparable size, depending on the number of peaks

that was previously established with MEPSA: $N_{\text{peaks}} = 1, 2, 3$ or $4, \geq 5$. The left panel of Fig. 11 shows the result. GRBs with the largest number of pulses evidently cluster in the most luminous and narrow FWHM_{\min} region. To understand whether this is mainly due to a S/N effect, we selected the 1/3 with the narrowest pulse with the highest S/N (threshold of $S/N > 12.26$). The result is shown in the right panel of Fig. 11 and clearly proves that the conclusion remains unaffected. To further characterise the link between number of peaks and FWHM_{\min} , in Fig. 12 we show both observables in a scatter plot, where both colour and symbol size show the S/N. Notably, the FWHM_{\min} significantly shifts towards lower values for GRBs with increasing numbers of pulses.

In principle, if the probability density function of the FWHM_{\min} of a peak is the same for all GRBs, regardless of the number of peaks, a GRB with more peaks is more likely to have a small FWHM_{\min} , since more peaks means more trials. However, Fig. 12 (top panel) clearly rules this case out; in fact, this putative distribution should result from sampling the $N_{\text{peaks}} = 1$ observation, which is clearly incompatible with the FWHM_{\min} distribution of GRBs with several peaks. We confirmed this through

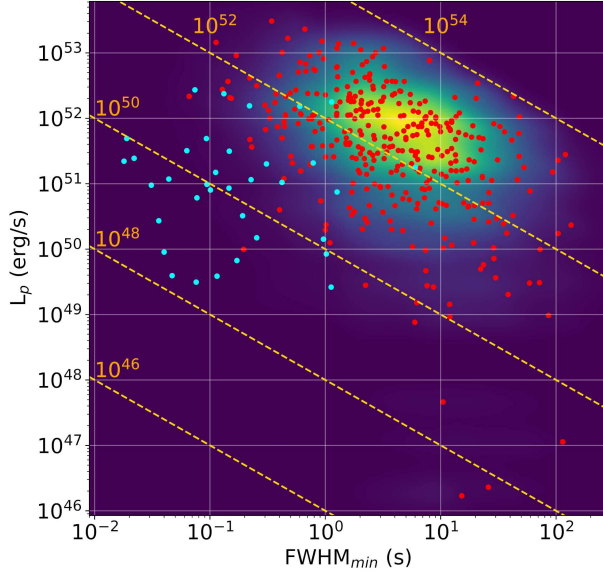


Fig. 9. Peak Luminosity L_p versus FWHM_{\min} for the *Swift*/BAT Type-II GRB sample (red circles). The colour-coded density map is the result of a simulated sample of Type-II GRBs that accounts for the selection effects shown in Fig. 8 under the assumption of no correlation between L_p and FWHM_{\min} . For comparison, we also show SGRBs (cyan circles). Gold dashed lines represent loci with constant isotropic-equivalent released energy of each individual peak, approximately calculated as $E_{\text{iso}} = L_p \text{FWHM}_{\min}$.

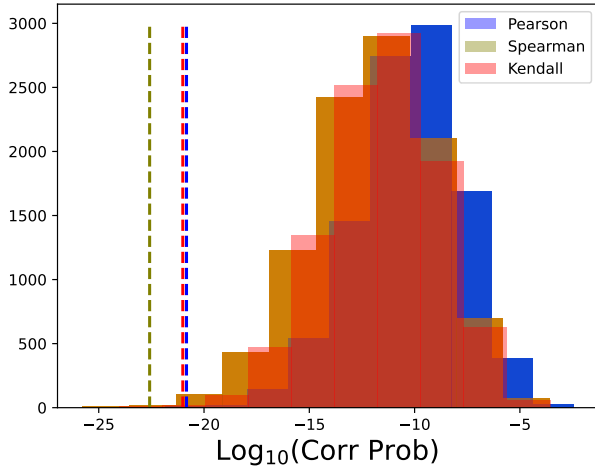


Fig. 10. FWHM_{\min} - L_p correlation probability distributions of the simulated samples of Type-II GRBs, compared with the corresponding values obtained for the real sample of Type-II GRBs with measured z (vertical lines).

the following test: we considered all the *Swift* Type-II GRBs (regardless of the knowledge of z) with $N_{\text{peaks}} \geq 10$ (hereafter Obs10 sample). We then generated a population of fake GRBs (hereafter Sim10) with the same distribution of number of peaks as Obs10 (but with 100 times as many GRBs as Obs10), where each peak was chosen randomly from the distribution of GRBs with $N_{\text{peaks}} = 1$ (hereafter Obs1). We determined the FWHM_{\min} distribution of Sim10 and compared with that of Obs10 through

two-population KS and AD tests. The probability that the two distributions of FWHM_{\min} are drawn from the same parent populations is 3×10^{-9} ($< 10^{-3}$) with KS (AD) test. Using the same procedure with the HXMT sample, so including GRBs with unknown z (bottom panel of Fig. 12), we obtain a probability of 5×10^{-4} ($< 10^{-3}$) according to the KS (AD) test.

4.8. Lorentz factor versus FWHM_{\min}

To study the relation between MVT and Lorentz factor of the ejecta, we selected a subsample of Type-II GRBs for which an estimate of the latter was available in the literature. To this aim, we considered the following references: Lü et al. (2012), Yi et al. (2017), Xue et al. (2019), and Ghirlanda et al. (2018), along with a couple of additional references relative to individual GRBs: 111228A (Xin et al. 2016) and 150910A (Xie et al. 2020). All of these estimates, except for the GRBs of Xue et al. (2019), who obtained pseudo estimates based on the $E_{p,i} - L_{\text{iso}} - \Gamma_0$ relation (Liang et al. 2015), are based on the peak time of the early afterglow, interpreted as the deceleration of the fireball in the thin shell regime. Because of this, we assumed the Γ_0 values obtained from the deceleration peak for the GRBs in common. In any case, we graphically distinguish the different sources, to spot any possible difference. Our final sample consists of 131 GRBs, 39 of which have Γ_0 from the deceleration peak from Lü et al. (2012), Yi et al. (2017), Xin et al. (2016), and Xie et al. (2020), and 92 are pseudo values from Xue et al. (2019).

We treated the sample of Ghirlanda et al. (2018) separately, given that this is a rich collection that resulted from a homogeneous selection and treatment, and which also provides a set of lower limits on Γ_0 for many GRBs. Specifically, we calculated Γ_0 using their Eq. (11), taken from Nava et al. (2013). The estimated values were obtained for 50 GRBs that our sample shares with their golden and silver samples, while for the remaining 74 common GRBs we calculated the corresponding lower limits. We checked the mutual consistency of the estimated values taken from Ghirlanda et al. (2018) and the other references for a sample of common GRBs (41 values and 50 lower limits), and we found only a few incompatible estimates, whereas most estimates differ by $\lesssim 20\%$, and a dozen or so lower limits are incompatible with the estimates provided by the other works.

Figure 13 shows the results. The left panel shows the GRBs with colour-coded references for the Γ_0 estimates, whereas the right panel uses the sample in common with Ghirlanda et al. (2018). The anti-correlation is evident for both data sets, although significantly scattered.

It is not straightforward to understand the impact of the selection bias affecting the sample of FWHM_{\min} discussed in Sect. 4.6. Consequently, the apparent power-law slope of this correlation should be taken with care. Yet, interestingly, both data sets show an overall consistency with $\text{FWHM}_{\min} \propto \Gamma_0^{-2}$, as shown by the dashed lines that correspond to constant values of $R = 2c\Gamma_0^2 \text{FWHM}_{\min}$, which is the typical distance at which the dissipation of energy into γ -rays is supposed to take place. Almost all GRBs lie in the $10^{15} \leq R/\text{cm} \leq 10^{17}$ range.

This range appears to be larger than $10^{13} - 10^{14}$ cm, which is usually estimated in the case of internal shocks (e.g. Zhang & Mészáros 2004). However, there are several cases for which the estimates are consistent with our results: for a number of *Swift* GRBs for which the early X-ray afterglow steep decay could be interpreted as high-latitude emission, the onset time of this decay enabled to obtain $R \geq 10^{15} - 10^{16}$ cm (Lyutikov 2006; Kumar et al. 2007; Lazzati & Begelman 2006;

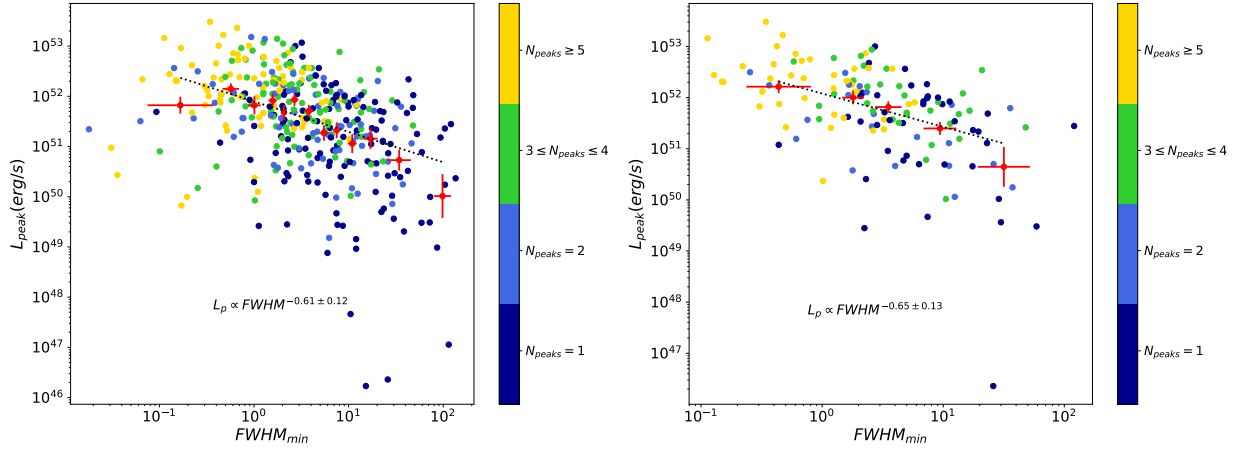


Fig. 11. Peak Luminosity versus FWHM_{\min} for the *Swift* sample of Type-II GRBs for different number of peaks N_{peaks} (left panel); L_p versus FWHM_{\min} for the *Swift* sample of Type-II GRBs, $S/N > 12.26$ (right panel), for different number of peaks N_{peaks} . Red dots refer to geometrical mean of groups of GRBs, with each group including 30 GRBs, independently of N_{peaks} .

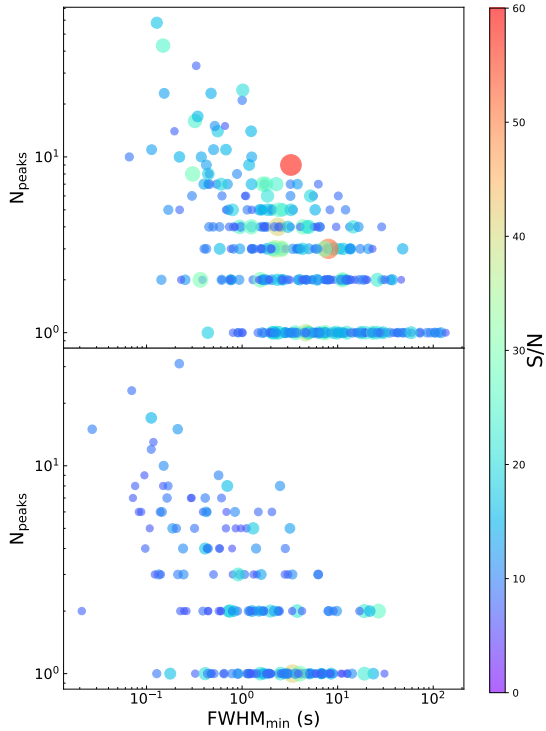


Fig. 12. Number of peaks versus FWHM_{\min} , Type-II GRBs for the *Swift* sample (top panel; here only GRBs with known z are shown for the sake of clarity) and HXMT sample (bottom panel). Symbol size and colour scale with S/N .

Hascoët et al. 2012). Also, for the naked-eye burst 080319B, $R \gtrsim 10^{16}$ cm was found, due to its bright prompt optical emission, which requires a synchrotron self-absorption frequency that is not too far above the optical band (Racusin et al. 2008; Kumar & Panaitescu 2008).

Different models can accommodate these values for R ; for a Poynting flux-dominated outflow, a typical value of 3×10^{16} cm

is predicted (Lyutikov & Blandford 2003). Alternatively, hybrid models such as the Internal Collision-induced MAGnetic Reconnection and Turbulence (ICMART; Zhang & Yan 2011) based on internal shocks, in which the dissipation mechanism is magnetic reconnection, also predict $R \sim 10^{15} - 10^{16}$ cm. Also, classical multi-zone internal shocks with reasonable Lorentz factor distributions for the wind of shells can predict dissipation radii in the range $10^{15} - 10^{16}$ cm, whereas the possible associated high-energy (HE) neutrinos and ultra-high-energy cosmic rays (UHECRs) are mostly expected to be accelerated at distances $\sim 10 - 100$ times closer to the engine (Bustamante et al. 2015, 2017). Our results may suggest that, if most GRB internal shocks take place above $\sim 10^{15}$ cm, that would explain why bright GRB prompt emission is not accompanied by HE neutrinos, at least as long as low-luminosity GRBs are ignored. This is in agreement with the upper limit of 1% on the contribution due to cosmological GRBs to the observed HE neutrino diffuse flux (Abbasi et al. 2022).

For each GRB we also compared the dissipation radius with the deceleration one, R_{dec} , at which the ejecta decelerates, which corresponds to the time at which the afterglow LC peaks. In particular, we took the Γ_0 and afterglow peak times of the sample by Ghirlanda et al. (2018) and verified that it was $R < R_{\text{dec}}$ for all GRBs.

4.9. Jet opening angle versus FWHM_{\min}

We explored the relation between the MVT and jet opening angle, θ_j , as measured from the afterglow modelling for the GRBs for which evidence of an achromatic jet break was found. To this aim, we took the values reported in Zhao et al. (2020) in the two cases of ISM and wind environments. The resulting subset with measured θ_j includes 57 of our Type-II GRB sample with a measured FWHM_{\min} and the number of peaks. Figure 14 shows the results for ISM (left panel) and wind (right panel); the information on the number of pulses is colour-coded.

Despite the apparent scattering, there is evidence of a correlation between jet opening angle and MVT with significance values of a few times 10^{-3} (Table 4). Motivated by the result in Fig. 14, we further tested the apparent clustering of GRBs with numerous peaks in the narrow jet–short MVT through a 2D,

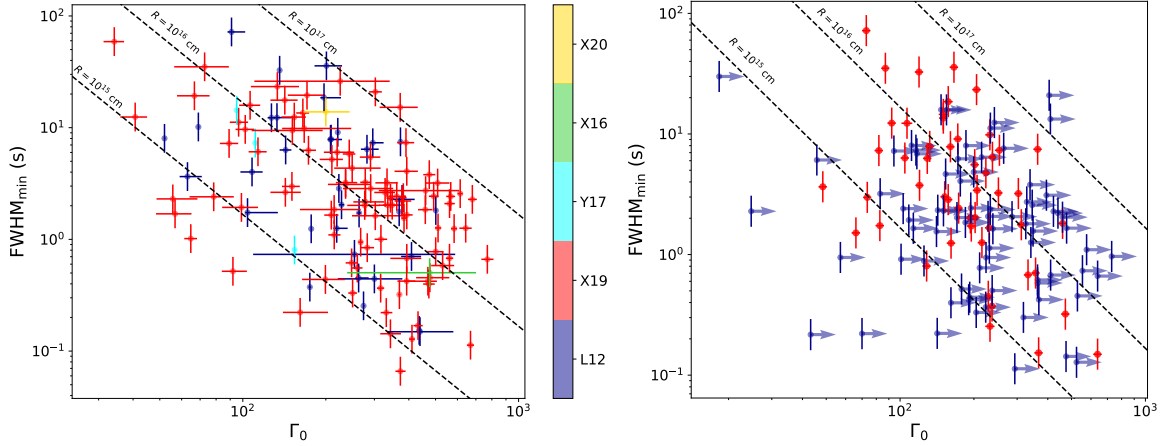


Fig. 13. FWHM_{\min} versus the initial Lorentz factor Γ_0 for a number of Type-II GRBs. *Left*: the values for the latter were taken from different data sets, which are colour-coded: L12 (Lü et al. 2012), X19 (Xue et al. 2019), Y17 (Yi et al. 2017), X16 (Xin et al. 2016), and X20 (Xie et al. 2020). Dashed lines correspond to the typical distance $R = 2 c \Gamma_0^2 \text{FWHM}_{\min}$ at which the dissipation process responsible for the prompt emission could take place. *Right*: same as left, except that we calculated Γ_0 from the data set by Ghirlanda et al. (2018). Red points are the GRBs belonging to their golden and silver samples, while blue points are lower limits on Γ_0 .

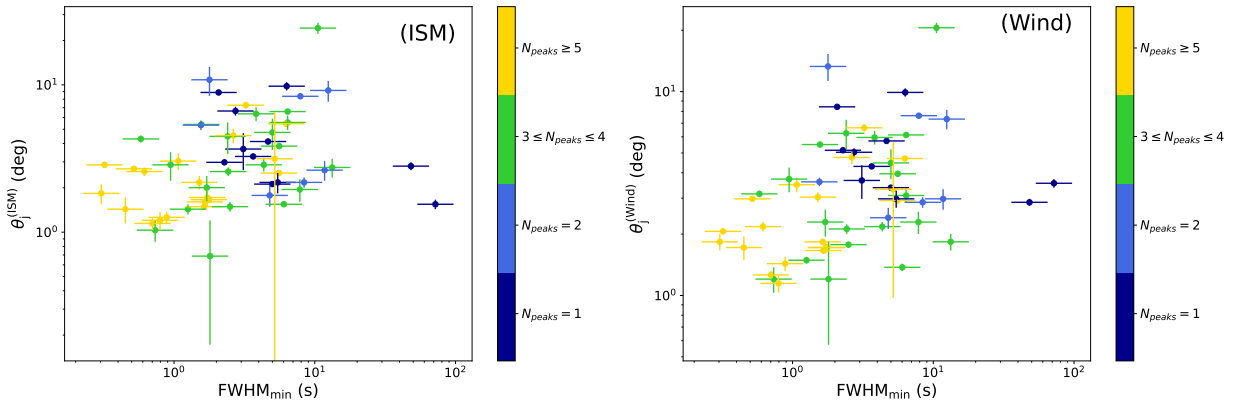


Fig. 14. Jet opening angles versus FWHM_{\min} for a set of Type-II GRBs for which both quantities could be estimated, assuming two different circumburst environments: ISM (*left*) and wind (*right*). Colours indicate the number of pulses.

Table 4. P -values of tests of correlation between MVT and jet opening angle for a sample of 57 Type-II GRBs displayed in Fig. 14.

Environment	Test	p -value
ISM	Pearson	2.4×10^{-2}
ISM	Spearman	5.6×10^{-3}
ISM	Kendall	5.2×10^{-3}
Wind	Pearson	4.6×10^{-3}
Wind	Spearman	2.0×10^{-3}
Wind	Kendall	4.4×10^{-3}

two-population KS test (Press et al. 1992) after dividing the sample into two groups, one including 18 GRBs with $N_{\text{peaks}} \leq 2$ and another including 39 GRBs with $N_{\text{peaks}} > 2$. Using the ISM (wind) values of θ_j , the probability that the number of peaks is uncorrelated with the position in the FWHM_{\min} - θ_j plane is 4.1×10^{-3} (1.5×10^{-3}), equivalent to 2.9σ (3.2σ).

5. Discussion

Our results show that the observation of millisecond-long individual pulses is very rare in either class of GRBs. At one end, even if they exist, their identification is limited by instrumental sensitivity, given the strong dependence of the detection threshold on the FWHM_{\min} (Fig. 7). At the other end, we do observe rare GRBs with a peak rate high enough to ensure the possibility of detecting ms-long pulses, but in practice this rarely seems to be the case. The short end of the MVT distributions of both Type-I and Type-II GRBs extends to ~ 10 ms within a factor of a few, depending on the energy passband. The two classes have overlapping MVT distributions, although the populations are statistically different. In this respect, SEE-GRBs, that is Type-I GRBs with an ambiguous time profile, exhibit an average MVT that is shorter than that of Type-II GRBs, making our MVT estimate a useful indicator of the progenitor class. In SEE-GRBs, whose environmental properties are indistinguishable from those of SGRBs (Fong et al. 2022; Nugent et al. 2022), the presence of a prolonged γ -ray activity characterised by a longer MVT that follows an initial spike could hint to

Table 5. First ten GRBs of *Swift* sample.

GRB name	L_p (10^{50} erg s $^{-1}$)	Γ_0	Ref.	$\Gamma_0^{(G)}$	θ_j^{ISM} (rad)	θ_j^{Wind} (rad)
050126	4.13 ± 0.66	–	–	–	–	–
050219A	0.47 ± 0.04	–	–	–	–	–
050223	0.58 ± 0.08	–	–	–	–	–
050315	37.4 ± 3.0	–	–	–	0.111 ± 0.012	0.104 ± 0.008
050318	38 ± 4	–	–	57 ± 2	–	–
050319	95 ± 15	–	–	–	0.053 ± 0.007	0.061 ± 0.005
050401	912 ± 76	254^{+335}_{-145}	L12	554 ± 25	0.018 ± 0.003	0.021 ± 0.003
050416A	5.44 ± 0.85	–	–	101 ± 6	–	–
050505	311 ± 40	–	–	–	–	–
050525A	69.4 ± 1.5	268 ± 5	X19	224 ± 10	0.050 ± 0.011	0.065 ± 0.009

Notes. $\Gamma_0^{(G)}$ is the Lorentz factor from Ghirlanda et al. (2018) using Eq. (11) therein from Nava et al. (2013). This table is available in its entirety in machine-readable form at the CDS.

a long-lived, downward-spinning protomagnetar (Metzger et al. 2008; Bucciantini et al. 2012), a scenario that can also account for the complex broadband evolution exhibited by GRBs such as 180618A (Jordana-Mitjans et al. 2022). There are alternative interpretations, such as the one proposed to explain 211211A, in which the SEE would be produced by the prolonged accretion-powered activity of a newly formed black hole (BH), ruled by the strong magnetic field of one of the merging NSs (Gao et al. 2022). Regardless of the possible presence of the SEE and of its interpretation, the shorter MVT of Type-I GRBs appears to be a distinctive property with respect to the bulk of Type-II events. Although the nature of the inner engines that power the two classes could be similar (e.g. either a supramassive magnetar or an hyperaccreting newly formed BH), the longer MVT in Type-II GRBs might be due to the engine variability being smeared out by the interaction with the massive envelope, whereas in Type-I the central engine variability imprint in the jet is retained throughout the propagation in less massive merger ejecta (e.g. see Gottlieb et al. 2022b). The other major difference between the two classes is the apparent absence of correlation between MVT and peak luminosity for Type-I GRBs, as shown in Fig. 9.

Concerning the properties of Type-II GRBs with measured redshifts, upon a careful evaluation of the involved selection effects on both luminosity and FWHM_{min} , we confirm that L_p and MVT do correlate, although a mathematical description that is corrected for the selection effects requires more extensive simulations that go beyond the scope of the present investigation. Additional information comes from the other correlations that we report here, and it involves MVT: in particular, (Type-II) GRBs that display many (>2) pulses have short MVTs on average (typically in the range of 0.01–1 s), are more luminous, have a higher bulk Lorentz factor, and, whenever the information is available, tend to have narrower jets or a smaller off-axis angle (see Table 5).

The jet opening angle θ_j is usually estimated from afterglow modelling and, in particular, from the observation of an achromatic break in the afterglow light curves that would correspond to the time at which the Lorentz factor Γ of the forward shock is such that $1/\Gamma \sim \theta_j$. While this is true for an on-axis observer, for $\theta_{\text{obs}} \neq 0$ but $\theta_{\text{obs}} < \theta_j$, the jet break time is actually set by the furthest edge from the observer, i.e. when the relativistic beaming decreases to the point at which $1/\Gamma \sim \theta_j + \theta_{\text{obs}}$ (van Eerten et al. 2010). In practice, when one also includes other factors, such as jet spreading, angular structure of a jet (as opposed to the sim-

plistic case of a top-hat jet), radial fluid structure, and arrival time effects, deviations of the afterglow LC from simple power laws hinder an accurate measure of both jet and observer angles (van Eerten & MacFadyen 2012). Besides this, for increasing observer angles, but still $\theta_{\text{obs}} < \theta_j$, the jet break time may occur correspondingly later by a factor of 3–5 (De Colle et al. 2012). Consequently, the variable that we found to correlate with the MVT is likely more indicative of $(\theta_j + \theta_{\text{obs}})$ or, at least, of a combination of both θ_j and θ_{obs} rather than θ_j alone for an on-axis view ($\theta_{\text{obs}} \simeq 0$).

A simple interpretation of these correlations invokes a structured jet viewed through a range of different observer angles for different GRBs. Simulations suggest that the angular structure of a GRB jet consists of a flat core with an opening angle θ_j , followed by a power-law decline ($E_{\text{iso}} \propto \theta^{-\delta}$ for $\theta_j < \theta < \theta_c$) that models the so-called jet-cocoon interface (JCI). This is an interface layer between the jet core and the cocoon which extends to θ_c (Gottlieb et al. 2021a). The power-law index δ depends on the jet magnetisation: $\delta \sim 3$ for a weakly magnetised jet and $\delta \sim 1-2$ for a purely hydrodynamic jet. This difference arises from the different degree of mixing between jet and cocoon at the JCI, which in turn affects the baryon loading of jet: a magnetised jet, whose existence is also supported by early-time optical polarisation measurements (e.g. Gomboc et al. 2008; Mundell et al. 2013; Japelj et al. 2014; Steele et al. 2017), would suffer from a reduced mixing, with less energy transferred to the JCI and a consequent steeper energy angular profile (Gottlieb et al. 2020b).

Assuming similar values for θ_j for different GRBs as could be plausible in a quasi-universal jet structure (e.g. see Salafia et al. 2020 and references therein), or at least assuming that the spread of values of θ_{obs} is greater than that of θ_j for the observed population, the variety of values measured from the afterglow LC for the jet opening angle, which is actually more revealing of $(\theta_j + \theta_{\text{obs}})$, mostly reflects the range of θ_{obs} . For a relatively on-axis view, observed high Lorentz factor, high isotropic-equivalent peak luminosity are naturally accounted for. A short MVT and the abundance of pulses would suggest that we are looking through the jet core at the inner engine activity, unaffected by smoothing and blending that instead would characterise a more off-axis view, but still close to the JCI boundary ($\theta_{\text{obs}} \sim \theta_j$) because of lower Doppler boosting and longer arrival time delays (e.g. see Salafia et al. 2016). In addition, the LC blending could hinder the identification of distinct adjacent pulses, thus explaining why these GRBs show fewer pulses

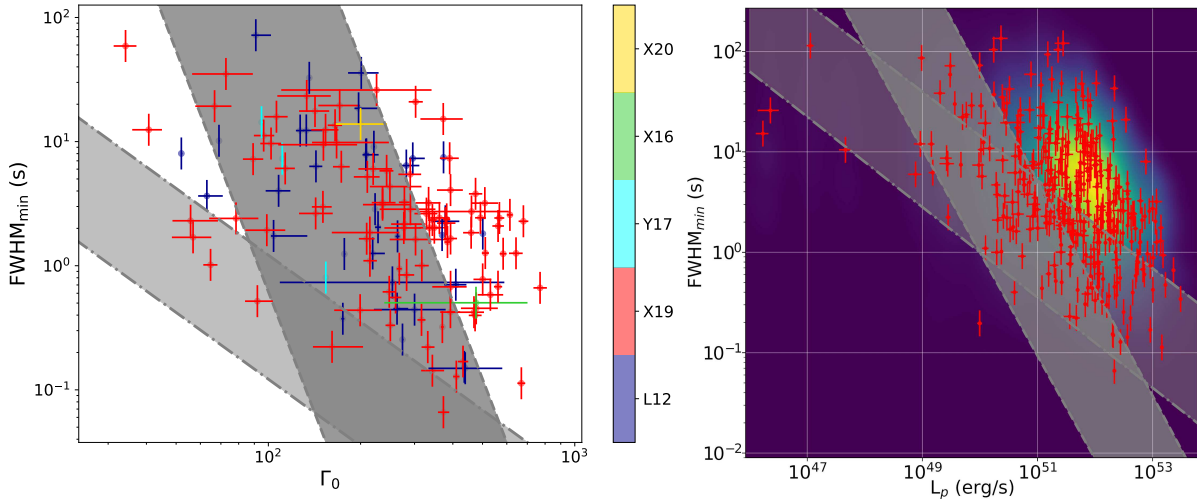


Fig. 15. FWHM_{\min} versus the initial Lorentz factor Γ_0 for a number of Type-II GRBs, with the predictions discussed by Xie et al. (2017), highlighted by the light shaded region between dash-dotted lines ($\nu\bar{\nu}$ annihilation mechanism) and by the dark shaded region between dashed lines (BZ mechanism). *Left:* same as Fig. 13. *Right:* same as Fig. 9, except that the two axes are swapped for ease of comparison with the expectations discussed by Xie et al. (2017).

on average. Concerning more off-axis GRBs, i.e. those with $\theta_j < \theta_{\text{obs}} < \theta_c$, they would appear as low-luminosity GRBs, which are mostly missing from present GRB catalogues.

A possible additional key property is suggested by recent 3D GRMHD simulations of the temporal evolution of a jet that results from a collapsar: some shocked gas would free-fall towards the newly formed BH and would be then deflected by the jet towards the accretion disc, which would consequently make the jet tilt randomly with respect to the BH rotational axis (Gottlieb et al. 2022c). The resulting jet would break out of the photosphere with a typical opening angle of $\theta_j \sim 6^\circ$ and would wobble around with an angle of $\theta_i \sim 12^\circ$ and a hybrid composition of magnetic and thermal energy due to the variable mixing. In this picture, the short MVT (0.01–0.1 s) would reflect the inner engine activity, possibly due to random fluctuations in the accretion process and launching mechanism, whereas long (1–10 s) interpulse times would occur whenever the jet points away from the observer (Gottlieb et al. 2022a). While the possibility of precessing jets in GRB sources is not new (Portegies Zwart et al. 1999; Portegies Zwart & Totani 2001; Fargion 2001; Reynoso et al. 2006; Lei et al. 2007), the stochastic nature of this wobbling, supported by state-of-the-art simulations, suggests that a multi-pulsed, luminous GRB with a short MVT and high Lorentz factor could be due to a jet wobbling around the line of sight, thus giving rising to more short pulses and, on average, exposing the variability of the inner engine during the frequent on-axis alignments. Less luminous GRBs, with fewer pulses and longer MVTs would harbour wobbling jets that are on average more misaligned with respect to the line of sight; these GRBs would correspond to the cases in which the angle between the time-average pointing direction of the jet and the line of sight is similar to the jet opening angle, $\langle \theta_{\text{obs}} \rangle \sim \theta_j$. This would turn into fewer pulses, given that the jet would spend more time with the line of sight off the jet core. The scatter of the observed correlations could be explained as being due to the fact that, even for such a GRB, the probability of a temporary fortuitous on-axis view, thus giving a narrow pulse, is not negligible, although less likely. This interpretation is sup-

ported by some Monte Carlo simulations of randomly wobbling structured jets: using a different definition of variability related to the number of pulses, a connection is predicted between variability and the jet opening angle as measured from the afterglow light curves (Budai et al. 2020), which agrees with our result.

A similar correlation between θ_j (or $\theta_j + \theta_{\text{obs}}$, as explained above) and a former definition of variability was already established by Kobayashi et al. (2002) for a few GRBs with measured quantities available at the time. According to their interpretation, GRBs with constant energy may result in different jet masses, so a smaller mass loading would be associated with a narrower jet, higher Lorentz factor, and isotropic-equivalent luminosity, as supported by simulations.

The scaling between the MVT versus Lorentz factor Γ_0 and the MVT versus luminosity may help constrain the mechanism used by the inner engine to power the relativistic jet. In this respect, Xie et al. (2017) considered two alternative scenarios that invoke a BH: (i) extraction of the BH rotational energy through the magnetic field sustained by the accretion disc according to the Blandford & Znajek mechanism (BZ; Blandford & Znajek 1977); (ii) a neutrino-dominated accretion flow (NDAF; Popham et al. 1999), whose neutrinos and anti-neutrinos annihilate and power the jet. In the BZ mechanism there is also an NDAF that supports and influences the magnetic field, which in turn suppresses the baryon loading from the neutrino-driven wind. In either case the MVT is determined by the viscous instability of the NDAF. In Fig. 15 we show our results on the correlations between the MVT and Γ_0 (left panel) and between the MVT and peak luminosity (right panel), along with the regions expected in each of the two scenarios: the light shaded region between dash-dotted lines refers to the $\nu\bar{\nu}$ annihilation mechanism, whereas the dark shaded region between dashed lines refers to the BZ one. The values of each set of model parameters are the same as the ones that are considered in Xie et al. (2017): as a consequence, while both regions can be shifted parallelly, their slopes are more of a distinctive property of each and, as such, should be considered. While the slopes of the MVT- Γ_0 predicted relations seem to be overall compatible with

the data set, which is significantly scattered, the same comparison in the $MVT-L_p$ plane seems to favour the BZ mechanism, as also argued by Xie et al. (2017). The $\nu\bar{\nu}$ annihilation model looks significantly shallower ($\text{FWHM}_{\min} \propto (L_p^{(\nu\bar{\nu})})^{-1/2}$) than the data, whereas the BZ slope is $\text{FWHM}_{\min} \propto (L_p^{(\text{BZ})})^{-1}$.

The relations found for a common sample of GRBs and blazars by Wu et al. (2016), $MVT \propto \Gamma_0^{-4.7 \pm 0.3}$ and $MVT \propto L_p^{-1.0 \pm 0.1}$ are both compatible with our samples, although the large scatter observed in our $MVT-\Gamma_0$ sample makes it noncritical.

A hyperaccreting Kerr BH with a magnetised torus is expected to power, via BZ, a magnetically dominated jet. MHD simulations identify the BH spin as the main driver of the GRB variability along with the magnetic field strength, although other factors should be considered that contribute to the conversion efficiency of the dissipation of energy into γ -rays (e.g. Granot et al. 2015). The MVT, in terms of minimum duration of pulses, would reflect the timescale of the fastest growing mode of magneto-rotational instabilities in the accretion disc (Janiuk et al. 2021). In this scenario, a higher BH spin would launch a jet with a correspondingly higher Lorentz factor and shorter MVT, thus accounting for the observed correlation. On average, for small values of θ_{obs} , a higher Γ_0 is also expected, although the relation does not always appear to be monotonic for different values of BH spin parameter and magnetic field strength.

6. Conclusions

We proposed a simple definition of MVT of GRB prompt emission as the FWHM of the shortest pulse that is identified through MEPSA, a thoroughly tested GRB peak search algorithm. We applied this method to two independent and complementary GRB data sets: *Swift*/BAT and *Insight-HXMT*/HE, both of which were split into two groups: Type-I and Type-II GRBs, the former including SEE-GRBs. Firstly, ms-long MVT is very rarely observed, the shortest values being around 10 ms. However, this could be partly due to a S/N-related selection effect. Although the two groups have overlapping MVT distributions, MVT of Type-I GRBs is in the range 10 ms–1 s and is on average significantly shorter than that of Type-II GRBs, which encompasses the range of ~ 0.1 –100 s. Remarkably, SEE-GRBs with $T_{90} > 2$ s, characterised by deceptively long and structured time profiles such as 060614 and 211211A, also display a short MVT that is more typical of Type-I GRBs, thus propelling this definition of MVT as a useful indicator of the progenitor class, especially in the presence of ambiguous γ -ray time profiles. The origin of this difference could stem from the different ejecta masses that the relativistic jets of either class have to pierce.

Concerning the subsample of Type-II GRBs with measured redshift, upon careful evaluation of the selection effects that impact the MVT measure in the MVT-peak rate plane, we confirm the existence of anti-correlations between MVT and peak luminosity, L_p , and between MVT and initial Lorentz factor of the ejecta Γ_0 . Moreover, we were able to establish that MVT also correlates with the number of peaks and the jet opening angle (measured from the achromatic break in the afterglow light curves), although the latter is probably more of a sum of jet and observer angles. Taken together, we find that GRBs with short MVTs (0.1–1 s) on average have narrower jets and/or smaller observer angles ($\lesssim 2$ – 4°), higher Lorentz factors ($\Gamma_0 \gtrsim 100$), high peak luminosities ($L_p \gtrsim 10^{51}$ erg s $^{-1}$), and exhibit several pulses. A possible interpretation that builds on 3D GRMHD

state-of-the-art simulations of a jet propagating through stellar envelopes involves a structured jet with a flat core ($0 \leq \theta < \theta_j$) and a power-law profile that models the jet-cocoon interface ($\theta_j < \theta < \theta_c$). GRBs with short MVTs would be seen within the jet core, resulting in higher L_p and Γ_0 , shorter and more numerous peaks, and revealing the true variability imprinted by the inner engine, such as a hyperaccreting BH possibly powered via the Blandford-Znajek mechanism. Conversely, GRBs viewed across the boundary between the jet core and the jet-cocoon interface would appear as less luminous, with lower Lorentz factors and longer MVT due to a smaller Doppler boosting and longer arrival time delays. The possibility that such a jet could wobble randomly within angles comparable to, if not greater than, the jet core itself, further suggests that the different number of peaks observed in different GRBs could indicate how often the jet core points to the observer, thus revealing to what extent the line of sight is off-axis with respect to the average jet direction.

Acknowledgements. We are grateful to the Referee for their useful comments which helped us to improve the paper. A.E.C. and C.G. acknowledge financial support from FIRD 2022 of UNIFE Dept. Physics and Earth Science under the project “Caratterizzazione e simulazioni di curve di luce di Gamma-Ray Burst come processi stocastici e validazione attraverso tecniche di machine learning” (PI: CG). C.G.M. and N.J.M. acknowledge support from Hiroko and Jim Sherwin. This work is supported by the National Program on Key Research and Development Project (2021YFA0718500) and the National Natural Science Foundation of China under grants 11733009, U1838201 and U1838202. This work made use of data from the *Insight-HXMT* mission, a project funded by China National Space Administration (CNSA) and the Chinese Academy of Sciences (CAS).

References

- Abbasi, R., Ackermann, M., Adams, J., et al. 2022, *ApJ*, 939, 116
 Ahumada, T., Singer, L. P., Anand, S., et al. 2021, *Nat. Astron.*, 5, 917
 Amati, L. 2021, *Nat. Astron.*, 5, 877
 Barthelmy, S. D., Barbier, L. M., Cummings, J. R., et al. 2005, *Space Sci. Rev.*, 120, 143
 Bhat, P. N. 2013, ArXiv e-prints [arXiv:1307.7618]
 Bhat, P. N., Briggs, M. S., Connaughton, V., et al. 2012, *ApJ*, 744, 141
 Bishop, C. M. 2006, *Pattern Recognition and Machine Learning (Information Science and Statistics)* (Berlin, Heidelberg: Springer-Verlag)
 Blandford, R. D., & Znajek, R. L. 1977, *MNRAS*, 179, 433
 Borgonovo, L., Frontera, F., Guidorzi, C., et al. 2007, *A&A*, 465, 765
 Bromberg, O., Nakar, E., Piran, T., & Sari, R. 2013, *ApJ*, 764, 179
 Bucciantini, N., Metzger, B. D., Thompson, T. A., & Quataert, E. 2012, *MNRAS*, 419, 1537
 Budai, A., Raffai, P., Borgulya, B., et al. 2020, *MNRAS*, 491, 1391
 Bustamante, M., Baerwald, P., Murase, K., & Winter, W. 2015, *Nat. Commun.*, 6, 6783
 Bustamante, M., Heinze, J., Murase, K., & Winter, W. 2017, *ApJ*, 837, 33
 Cao, X., Jiang, W., Meng, B., et al. 2020, *Sci. China-Phys. Mech. Astron.*, 63, 249504
 Chen, Y., Cui, W., Li, W., et al. 2020, *Sci. China-Phys. Mech. Astron.*, 63, 249505
 Dado, S., & Dar, A. 2022, *ApJ*, 940, L4
 D’Avanzo, P., Salvaterra, R., Bernardini, M. G., et al. 2014, *MNRAS*, 442, 2342
 De Colle, F., Ramirez-Ruiz, E., Granot, J., & Lopez-Camara, D. 2012, *ApJ*, 751, 57
 Della Valle, M., Chincarini, G., Panagia, N., et al. 2006, *Nature*, 444, 1050
 Dichiaro, S., Guidorzi, C., Amati, L., Frontera, F., & Margutti, R. 2016, *A&A*, 589, A97
 Dichiaro, S., Gropp, J. D., Kennea, J. A., et al. 2022, *ATel*, 15650, 1
 Eichler, D., Livio, M., Piran, T., & Schramm, D. N. 1989, *Nature*, 340, 126
 Fargion, D. 2001, ArXiv e-prints [arXiv:astro-ph/0104446]
 Fenimore, E. E., & Ramirez-Ruiz, E. 2000, ArXiv e-prints [arXiv:astro-ph/0004176]
 Fenimore, E. E., in ‘t Zand, J. J. M., Norris, J. P., Bonnell, J. T., & Nemiroff, R. J. 1995, *ApJ*, 448, L101
 Fermi-LAT Collaboration 2021, *Nat. Astron.*, 5, 385
 Fong, W.-F., Nugent, A. E., Dong, Y., et al. 2022, *ApJ*, 940, 28
 Frederiks, D., Lysenko, A., Ridnaia, A., et al. 2022, *GRB Coordinates Network*, 32668, 1

Camisasca, A. E., et al.: A&A 671, A112 (2023)

- Fynbo, J. P. U., Watson, D., Thöne, C. C., et al. 2006, *Nature*, 444, 1047
- Gao, H., Lei, W.-H., & Zhu, Z.-P. 2022, *ApJ*, 934, L12
- Ge, M. Y., Chen, Y. P., Liao, J. Y., et al. 2022, *ATel*, 15703, 1
- Gehrels, N. 1986, *ApJ*, 303, 336
- Gehrels, N., Chincarini, G., Giommi, P., et al. 2004, *ApJ*, 611, 1005
- Gehrels, N., Norris, J. P., Barthelmy, S. D., et al. 2006, *Nature*, 444, 1044
- Ghirlanda, G., Nappo, F., Ghisellini, G., et al. 2018, *A&A*, 609, A112
- Golkhou, V. Z., & Butler, N. R. 2014, *ApJ*, 787, 90
- Golkhou, V. Z., Butler, N. R., & Littlejohns, O. M. 2015, *ApJ*, 811, 93
- Gomboc, A., Kobayashi, S., Guidorzi, C., et al. 2008, *ApJ*, 687, 443
- Gompertz, B. P., Ravasio, M. E., Nicholl, M., et al. 2023, *Nat. Astron.*, 7, 67
- Gottlieb, O., Levinson, A., & Nakar, E. 2019, *MNRAS*, 488, L416
- Gottlieb, O., Levinson, A., & Nakar, E. 2020a, *MNRAS*, 495, 570
- Gottlieb, O., Bromberg, O., Singh, C. B., & Nakar, E. 2020b, *MNRAS*, 498, 3320
- Gottlieb, O., Nakar, E., & Bromberg, O. 2021a, *MNRAS*, 500, 3511
- Gottlieb, O., Bromberg, O., Levinson, A., & Nakar, E. 2021b, *MNRAS*, 504, 3947
- Gottlieb, O., Liska, M., Tchekhovskoy, A., et al. 2022a, *ApJ*, 933, L9
- Gottlieb, O., Moseley, S., Ramirez-Aguilar, T., et al. 2022b, *ApJ*, 933, L2
- Gottlieb, O., Lalakos, A., Bromberg, O., Liska, M., & Tchekhovskoy, A. 2022c, *MNRAS*, 510, 4962
- Granot, J., Piran, T., Bromberg, O., Racusin, J. L., & Daigne, F. 2015, *Space Sci. Rev.*, 191, 471
- Guidorzi, C. 2015, *Astron. Comput.*, 10, 54
- Guidorzi, C., Frontera, F., Montanari, E., et al. 2005, *MNRAS*, 363, 315
- Guidorzi, C., Frontera, F., Montanari, E., et al. 2006, *MNRAS*, 371, 843
- Guidorzi, C., Dichiaro, S., & Amati, L. 2016, *A&A*, 589, A98
- Hascoët, R., Daigne, F., Mochkovitch, R., & Vennin, V. 2012, *MNRAS*, 421, 525
- Janiuk, A., James, B., & Palit, I. 2021, *ApJ*, 917, 102
- Japelj, J., Kopač, D., Kobayashi, S., et al. 2014, *ApJ*, 785, 84
- Jin, Z.-P., Li, X., Cano, Z., et al. 2015, *ApJ*, 811, L22
- Jordana-Mitjans, N., Mundell, C. G., Guidorzi, C., et al. 2022, *ApJ*, 939, 106
- Kann, D. A., Klose, S., Zhang, B., et al. 2011, *ApJ*, 734, 96
- Kobayashi, S., Piran, T., & Sari, R. 1997, *ApJ*, 490, 92
- Kobayashi, S., Ryde, F., & MacFadyen, A. 2002, *ApJ*, 577, 302
- Kocevski, D., & Petrosian, V. 2013, *ApJ*, 765, 116
- Kouveliotou, C., Meegan, C. A., Fishman, G. J., et al. 1993, *ApJ*, 413, L101
- Kozyrev, A. S., Golovin, D. V., Litvak, M. L., et al. 2022, *GRB Coordinates Network*, 32805, 1
- Kumar, P., & Panaitescu, A. 2008, *MNRAS*, 391, L19
- Kumar, P., McMahon, E., Panaitescu, A., et al. 2007, *MNRAS*, 376, L57
- Lazzati, D., & Begelman, M. C. 2006, *ApJ*, 641, 972
- Lei, W. H., Wang, D. X., Gong, B. P., & Huang, C. Y. 2007, *A&A*, 468, 563
- Li, T.-P. 2001, *Chin. J. Astron. Astrophys.*, 1, 313
- Li, T.-P. 2007, *Nucl. Phys. B Proc. Suppl.*, 166, 131
- Liang, E.-W., Lin, T.-T., Lü, J., et al. 2015, *ApJ*, 813, 116
- Lien, A., Sakamoto, T., Barthelmy, S. D., et al. 2016, *ApJ*, 829, 7
- Littlejohns, O. M., & Butler, N. R. 2014, *MNRAS*, 444, 3948
- Liu, C. Z., Zhang, Y. F., Li, X. F., et al. 2020, *Sci. China-Phys. Mech. Astron.*, 63, 249503
- Lü, J., Zou, Y.-C., Lei, W.-H., et al. 2012, *ApJ*, 751, 49
- Lytikov, M. 2006, *MNRAS*, 369, L5
- Lytikov, M., & Blandford, R. 2003, *ArXiv e-prints* [arXiv:astro-ph/0312347]
- MacFadyen, A. I., & Woosley, S. E. 1999, *ApJ*, 524, 262
- MacLachlan, G. A., Shenoy, A., Sonbas, E., et al. 2012, *MNRAS*, 425, L32
- MacLachlan, G. A., Shenoy, A., Sonbas, E., et al. 2013, *MNRAS*, 432, 857
- MAGIC Collaboration (Acciari, V. A., et al.) 2019, *Nature*, 575, 455
- Margutti, R. 2009, *Toward New Insights on the Gamma-ray Burst Physics: From X-ray Spectroscopy to the Identification of Characteristic Time Scales* (Milan: Università degli Studi Milano-Bicocca)
- Margutti, R., Guidorzi, C., Chincarini, G., et al. 2008, in 2008 Nanjing Gamma-ray Burst Conference, eds. Y. F. Huang, Z. G. Dai, & B. Zhang, *AIP Conf. Ser.*, 1065, 259
- Margutti, R., Guidorzi, C., & Chincarini, G. 2011, *Int. J. Mod. Phys. D*, 20, 1969
- Metzger, B. D., Quataert, E., & Thompson, T. A. 2008, *MNRAS*, 385, 1455
- Molinari, E., Vergani, S. D., Malesani, D., et al. 2007, *A&A*, 469, L13
- Mundell, C. G., Kopac, D., Arnold, D. M., et al. 2013, *Nature*, 504, 119
- Narayan, R., Paczynski, B., & Piran, T. 1992, *ApJ*, 395, L83
- Nava, L., Sironi, L., Ghisellini, G., Celotti, A., & Ghirlanda, G. 2013, *MNRAS*, 433, 2107
- Norris, J. P., & Bonnell, J. T. 2006, *ApJ*, 643, 266
- Norris, J. P., Nemiroff, R. J., Bonnell, J. T., et al. 1996, *ApJ*, 459, 393
- Nugent, A. E., Fong, W.-F., Dong, Y., et al. 2022, *ApJ*, 940, 23
- Paczynski, B. 1991, *Acta Astron.*, 41, 257
- Paczynski, B. 1998, *ApJ*, 494, L45
- Planck Collaboration VI. 2020, *A&A*, 641, A6
- Popham, R., Woosley, S. E., & Fryer, C. 1999, *ApJ*, 518, 356
- Portegies Zwart, S. F., & Totani, T. 2001, *MNRAS*, 328, 951
- Portegies Zwart, S. F., Lee, C.-H., & Lee, H. K. 1999, *ApJ*, 520, 666
- Press, W. H., Teukolsky, S. A., Vetterling, W. T., & Flannery, B. P. 1992, *Numerical Recipes in C: The Art of Scientific Computing* (Cambridge: Cambridge University Press)
- Racusin, J. L., Karpov, S. V., Sokolowski, M., et al. 2008, *Nature*, 455, 183
- Rastinejad, J. C., Gompertz, B. P., Levan, A. J., et al. 2022, *Nature*, 612, 223
- Reichart, D. E., Lamb, D. Q., Fenimore, E. E., et al. 2001, *ApJ*, 552, 57
- Reynoso, M. M., Romero, G. E., & Sampayo, O. A. 2006, *A&A*, 454, 11
- Roberts, O. J., Veres, P., Baring, M. G., et al. 2021, *Nature*, 589, 207
- Rossi, A., Rothberg, B., Palazzi, E., et al. 2022, *ApJ*, 932, 1
- Salafia, O. S., Ghisellini, G., Pescalli, A., Ghirlanda, G., & Nappo, F. 2016, *MNRAS*, 461, 3607
- Salafia, O. S., Barbieri, C., Ascenzi, S., & Toffano, M. 2020, *A&A*, 636, A105
- Sari, R., & Piran, T. 1999, *ApJ*, 520, 641
- Sonbas, E., MacLachlan, G. A., Dhuga, K. S., et al. 2015, *ApJ*, 805, 86
- Song, X.-Y., Xiong, S.-L., Zhang, S.-N., et al. 2022, *ApJS*, 259, 46
- Steele, I. A., Kopač, D., Arnold, D. M., et al. 2017, *ApJ*, 843, 143
- Svinkin, D., Frederiks, D., Hurley, K., et al. 2021, *Nature*, 589, 211
- Troja, E., Fryer, C. L., O'Connor, B., et al. 2022, *Nature*, 612, 228
- Tsvetkova, A., Frederiks, D., Golenetskii, S., et al. 2017, *ApJ*, 850, 161
- van Eerten, H. J., & MacFadyen, A. I. 2012, *ApJ*, 751, 155
- van Eerten, H., Zhang, W., & MacFadyen, A. 2010, *ApJ*, 722, 235
- Vianello, G., Gill, R., Granot, J., et al. 2018, *ApJ*, 864, 163
- Woosley, S. E. 1993, *ApJ*, 405, 273
- Wu, Q., Zhang, B., Lei, W.-H., et al. 2016, *MNRAS*, 455, L1
- Wu, B., Zhang, Y., Li, X., et al. 2022, *Exp. Astron.*, 53, 1037
- Xiao, S., Xiong, S. L., Liu, C. Z., et al. 2020, *J. High Energy Astrophys.*, 26, 58
- Xiao, S., Zhang, Y. Q., Zhu, Z. P., et al. 2022, *ArXiv e-prints* [arXiv:2205.02186]
- Xie, W., Lei, W.-H., & Wang, D.-X. 2017, *ApJ*, 838, 143
- Xie, L., Wang, X.-G., Zheng, W., et al. 2020, *ApJ*, 896, 4
- Xin, L.-P., Wang, Y.-Z., Lin, T.-T., et al. 2016, *ApJ*, 817, 152
- Xue, L., Zhang, F.-W., & Zhu, S.-Y. 2019, *ApJ*, 876, 77
- Yang, J., Chand, V., Zhang, B.-B., et al. 2020, *ApJ*, 899, 106
- Yang, J., Ai, S., Zhang, B. B., et al. 2022, *Nature*, 612, 232
- Yi, S.-X., Lei, W.-H., Zhang, B., et al. 2017, *J. High Energy Astrophys.*, 13, 1
- Zhang, B. 2006, *Nature*, 444, 1010
- Zhang, B., & Mészáros, P. 2004, *Int. J. Mod. Phys. A*, 19, 2385
- Zhang, B., & Yan, H. 2011, *ApJ*, 726, 90
- Zhang, B., Zhang, B.-B., Liang, E.-W., et al. 2007, *ApJ*, 655, L25
- Zhang, S.-N., Li, T., Lu, F., et al. 2020, *Sci. China Phys. Mech. Astron.*, 63, 249502
- Zhang, B. B., Liu, Z. K., Peng, Z. K., et al. 2021, *Nat. Astron.*, 5, 911
- Zhao, W., Zhang, J.-C., Zhang, Q.-X., et al. 2020, *ApJ*, 900, 112

Appendix A: Estimating the peak FWHM through MEPSA

The Multiple Excess Peak Search Algorithm (MEPSA) is an algorithm aimed at identifying peaks in LCs affected by uncorrelated Gaussian noise. MEPSA scans the time series at different timescales by comparing a peak candidate with a variable number of adjacent bins; the number of adjacent bins involved in the detection is called N_{adiac} .

When the entire LC has been screened, the process is re-run on the rebinned versions of the same curve; each time the rebinning factor is increased by one up to a maximum established by the user. At the end of the procedure, MEPSA provides the detection timescale Δt_{det} for each peak candidate; this is the product between the original time resolution of the time series and the rebinning factor. We refer the reader to [Guidorzi \(2015\)](#) for a more detailed description.

Since MEPSA does not provide direct information on the FWHM of a detected peak, we had to preliminarily calibrate it, starting from the rule of thumb declared in [Guidorzi \(2015\)](#). This establishes a set of different scalings between Δt_{det} and FWHM for different ranges of S/N. In order to determine a more precise calibration between the FWHM, Δt_{det} , and S/N, we simulated LCs with FWHM values taken from a given lognormal distribution. For our calibration, we used 1600 fast rise and exponential decay (FRED) profiles:

$$F(t) = \begin{cases} A \exp\left[-\left(\frac{t_0-t}{t_r}\right)^p\right], & \text{if } t < t_0 \\ A \exp\left[-\left(\frac{t-t_0}{t_d}\right)^p\right], & \text{if } t \geq t_0 \end{cases}, \quad (\text{A.1})$$

with $t_0 = 0$, $p = 1.5$; $t_d = 3t_r$; and $\text{FWHM} = 10^x$ s, where x is the random normal distributed with $\mu = \log 0.6$ and $\sigma = 0.5$, following the same prescriptions adopted in [Guidorzi \(2015\)](#). Simulated LCs at 1 ms were rebinned with rebinning factors = 1, 4, 64, and 1000. These profiles were affected by uncorrelated Gaussian noise.

We tried to include more parameters provided by MEPSA to see whether we could further reduce the scatter around the best fitting relation. To this aim, we assumed that the FWHM could be described by the following relation:

$$\text{FWHM} \propto \Delta t_{\text{det}} \left(\frac{S/N}{S/N_0} - 1\right)^\alpha P^\beta, \quad (\text{A.2})$$

where S/N_0 is a hard lower limit for S/N that had preliminarily been fixed to 4.7, P is a generic MEPSA parameter and α and β are power-law indices to be determined. After choosing P ,

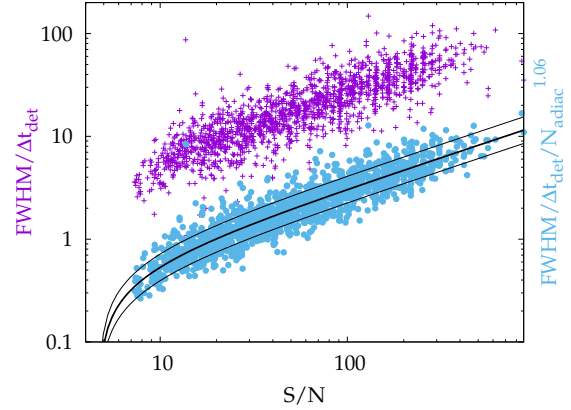


Fig. A.1. Ratio between true FWHM and MEPSA detection timescale Δt_{det} (red crosses; left-hand side vertical axis) versus S/N for a sample of simulated GRB-like pulses. The right vertical axis displays the same ratio further divided by MEPSA parameter $N_{\text{adiac}}^{1.06}$ for the same data set (blue circles). The latter quantity is found to minimise the scatter around the best fitting relation.

we considered the corresponding logarithmic quantities of the multiplicative terms in Eq. (A.2) and determined α and β by finding the maximum likelihood within a linear model regression approach (see Section 3.1.1 of [Bishop 2006](#)). As a result, we found a significant improvement by using N_{adiac} as the third parameter P . As shown in Figure A.1, the best fitting relation correlates FWHM with Δt_{det} , the S/N, and N_{adiac} :

$$\text{FWHM} = 10^{-0.31} \Delta t_{\text{det}} \left(\frac{S/N}{4.7} - 1\right)^{0.60} N_{\text{adiac}}^{1.06}. \quad (\text{A.3})$$

$$\sigma_{\text{FWHM}} = \text{FWHM} (10^{\pm 0.13} - 1)$$

The scatter around the best fitting relation, expressed by σ_{FWHM} , is calculated as the multiplicative coefficient that corresponds to the logarithmic standard deviation of the simulated points. To account for the asymmetric nature of the corresponding uncertainty on the FWHM, in Eq. (A.3) we distinguish between negative and positive uncertainties, but in practice the $1-\sigma$ uncertainty on the FWHM that affects the calibration of Eq. A.3 is about 35%. Consequently, all the FWHM values and relative uncertainties that were derived through MEPSA in this paper were calculated using Eq. (A.3).

Published Circular available at: <https://gcn.nasa.gov/circulars/33577>

TITLE: GCN CIRCULAR

NUMBER: 33577

SUBJECT: GRB 230307A: short minimum variability timescale compatible with a merger origin

DATE: 23/04/06 11:06:22 GMT

FROM: Cristiano Guidorzi at Ferrara U,Italy <guidorzi@fe.infn.it>

A.E. Camisasca, C. Guidorzi, M. Bulla (Ferrara U.), L. Amati, A. Rossi (INAF-OAS), G. Stratta, P. Singh (Goethe U. Frankfurt) on behalf of a larger collaboration report:

"We determined the minimum variability timescale (MVT) of GRB 230307A (Fermi GBM team, GCN 33405; Xiong et al., GCN 33406; Xiao & Krucker, GCN 33410; Cosentini et al., GCN 33412; Navaneeth et al., GCN 33415) from the Fermi/GBM light curve (NaI detectors 10 and 6) following the prescriptions of Camisasca et al. (2023), i.e. as the minimum full width half maximum (FWHM_{min}) of all statistically significant pulses, and found $\text{FWHM}_{\text{min}} = 28$ (-7, +10) ms. Combined with the $T_{90} = 34.56 \pm 0.6$ s (Fermi GBM team, GCN 33405), in the T_{90} - FWHM_{min} plot GRB 230307A (purple star in the Figure below) lies in the region populated by other long-lasting merger candidates, such as also GRB 191019A (green star in Figure; Levan et al. 2023; Lazzati et al. 2023). In particular, it lies very close to the merger GRB211211A (Gompertz et al. 2023; Mei et al. 2022; Rastinejad et al. 2022; Troja et al 2022; Yang et al 2022). Despite its long duration and complex light curve, its short MVT therefore supports the merger origin for GRB230307A, as suggested by the possible evidence for kilonova emission reported by Levan et al. (GCN 33569).

In addition, assuming a redshift $z=0.065$ (Gillanders et al. GCN 33485), a fluence of 3.6×10^{-3} erg cm^{-2} (Svinkin et al. GCN 33427) would correspond to $E_{\text{iso}} = 3.7 \times 10^{52}$ erg. Combined with $E_p \sim 1$ MeV (Svinkin et al.), the position of GRB 230307A in the E_p - E_{iso} plane seems to be more compatible with short rather than long GRBs.

http://www.fe.infn.it/u/guidorzi/T90_vs_FWHMmin_neu.pdf (Figure adapted from Camisasca et al. 2023)

References

- Camisasca et al., 2023, A&A, 671, A112, <https://doi.org/10.1051/0004-6361/202245657>
- Gompertz et al., 2023, Nature Astronomy, 7, 67
- Lazzati et al., 2023, arXiv:2303.12935
- Levan et al., 2023, arXiv:2303.12912
- Mei et al., 2022, Nature, 612, 236
- Rastinejad et al., 2022, Nature, 612, 223
- Troja et al., 2022, Nature, 612, 228
- Yang et al., 2022, Nature, 612, 232

Appendix C

Optimizing the observation of optical kilonovae with medium-size telescopes

A. E. Camisasca¹,^{*} I. A. Steele,² M. Bulla^{1,3,4}, C. Guidorzi^{1,3,5} and M. Shrestha^{2,6}

¹Department of Physics and Earth Science, University of Ferrara, via Saragat 1, I-44122 Ferrara, Italy

²Astrophysics Research Institute, Liverpool John Moores University, Liverpool Science Park IC2, 146 Brownlow Hill, Liverpool L3 5RF, UK

³INFN – Sezione di Ferrara, via Saragat 1, I-44122 Ferrara, Italy

⁴INAF – Osservatorio Astronomico d’Abruzzo, via Mentore Maggini snc, I-64100 Teramo, Italy

⁵INAF – Osservatorio di Astrofisica e Scienza dello Spazio di Bologna, via Piero Gobetti 101, I-40129 Bologna, Italy

⁶Steward Observatory, University of Arizona, 933 North Cherry Avenue, Tucson, AZ 85721-0065, USA

Accepted 2023 April 11. Received 2023 April 3; in original form 2022 November 18

ABSTRACT

We consider the optimization of the observing strategy (cadence, exposure time, and filter choice) using medium-size (2-m-class) optical telescopes in the follow-up of kilonovae localized with arcminute accuracy to be able to distinguish among various kilonova models and viewing angles. To develop an efficient observation plan, we made use of the synthetic light curves obtained with the Monte Carlo radiative transfer code POLarization Spectral Synthesis In Supernovae for different kilonova models and as a function of different viewing angles and distances. By adding the appropriate photon counting noise to the synthetic light curves, we analysed four alternative sequences having the same total time exposure of 8 h, with different time windows (0.5, 1, 2, and 4 h), each with *i*, *r*, and *u* filters, to determine the observing sequence that maximizes the chance of a correct identification of the model parameters. We suggest to avoid *u* filter and to avoid the use of colour curves. We also found that, if the error on distance is ≤ 2 per cent, 0.5, 1, and 2-h time window sequences are equivalent, so we suggest to use 2-h one, because it has 1-d cadence, so it can be easily realized. When the distance of the source is unknown, 0.5-h time window sequence is preferable.

Key words: telescopes – black hole – neutron star mergers – gamma-ray bursts – neutron star mergers.

1 INTRODUCTION

Coalescences of neutron star binaries and black hole–neutron star systems lead to the formation of neutron-rich material. Such material undergoes rapid neutron capture nucleosynthesis (*r*-process) as it decompresses in space, leading to the creation of rare heavy elements such as gold and platinum (Li & Paczyński 1998). The radioactive decay of these unstable nuclei fuels a thermal transient known as ‘kilonova’ (hereafter, KN; see Metzger 2019 for a review). On 2017 August 17, Advanced LIGO/Virgo made the first detection (Abbott et al. 2017b) of gravitational waves (GWs) from a binary neutron star merger, GW170817, simultaneously with the detection of short gamma-ray burst (GRB) by *Fermi* (Goldstein et al. 2017) and *INTEGRAL* (Savchenko et al. 2017): GRB 170817A. 11 h after the GW170817 trigger, an optical counterpart was discovered in the nearby ($d = 40$ Mpc) galaxy NGC 4993 (Coulter et al. 2017). The ultraviolet, optical, and near-infrared emissions were consistent with being powered by the radioactive decay of nuclei synthesized in the merger ejecta by the *r*-process (Villar et al. 2017; Watson et al. 2019; Domoto et al. 2021; Kasliwal et al. 2022). This was the first time one source was detected both in GWs and electromagnetic (EM) radiation, and the first time spectroscopic evidence of a KN was obtained (Chornock et al. 2017; Kasen et al. 2017; Pian et al. 2017; Smartt et al. 2017).

The study of a KN’s rapid evolution can improve our understanding of the role of neutron star mergers in the origin of heavy elements. In addition, KN spectra encode key information to constrain the outflows that produced their EM emission. There has been only one confirmed case of KN detection in the form AT2017gfo and few other possible candidates such as KNe associated to GRB 130603B (Tanvir et al. 2017) and GRB 211211A (Rastinejad et al. 2022). Hence, the whole community is working on various simulations to model the KN emission properties. There is a variety of predicted light-curve (LC) features (e.g. Wollaeger et al. 2018; Bulla 2019). Klion et al. (2021) and Nativi et al. (2021) showed how the presence of a jet impacts the KN LCs and makes them brighter and bluer when viewed pole on. Thus, it is important to come up with efficient observational strategies to get the best observational data to constrain the properties from computational models.

In this work, we aim to optimize the observing strategy for the optical follow-up of KNe to constrain the properties of the KN emission (viewing angle, mass of the different ejecta components, and their velocities), once this has been identified and localized with arcminute accuracy, which enables observations with narrow field facilities. Arcminute accuracy can be achieved with current high-energy instruments, such as the Burst Alert Telescope (Barthelmy et al. 2005) on board the *Neil Gehrels Swift Observatory* (Gehrels et al. 2004), or, in the near future, with *Space-based multi-band astronomical Variable Objects Monitor* (SVOM, Atteia, Cordier & Wei 2022), Einstein Probe (Yuan et al. 2022), and in the next decade possibly *Transient High-Energy Sky and Early Universe Surveyor*

* E-mail: annaelisa.camisasca@unife.it

(THESEUS, Amati et al. 2021). Also, the advent of third-generation GW observatories, such as the Einstein Telescope (Punturo et al. 2010) and Cosmic Explorer (Abbott et al. 2017a), will lead to an accuracy in localization better than 10 deg^2 at $z < 3$, which is enough to enable prompt and efficient multiwavelength search for EM counterparts (Ronchini et al. 2022). A GW detector capable of arcminute accuracy or better could be realized within the Voyage 2050 programme (Baker et al. 2021).

We made extensive use of simulated multifilter LCs of KNe obtained with the POLarization Spectral Synthesis In Supernovae (POSSIS; Bulla 2019) code. Similar works recently carried out (e.g. Scolnic et al. 2018; Setzer et al. 2019; Almualla et al. 2021; Andreoni et al. 2022; Chase et al. 2022; Colombo et al. 2022) focus on optimizing strategies of wide field and follow-up facilities to detect KNe. In this work, instead, we aim to determine the optimal combinations of time exposure sequence and filters that help to constrain the model parameters with follow-up instruments.

We chose to study the specific case of small–medium-class instruments; we considered two optical imaging cameras that are currently deployed at the 2-m fully robotic Liverpool Telescope (Steele et al. 2004): Multicolour OPTimised Optical Polarimeter (MOPTOP, Shrestha et al. 2020) and IO:O (Smith & Steele 2017). We assume that a network of similar telescopes and instruments (e.g. Tsapras et al. 2009) is located throughout a range of longitudes such that 24-h coverage is available. Given the interest in such sources, this assumption is reasonable in that most telescopes worldwide are likely to be involved in the follow-up of such rare events (e.g. Brown et al. 2013).

In Section 2, we describe the characteristics of KN models generated with POSSIS. In Sections 3 and 4, we describe, respectively, the preliminary procedure and results obtained under the hypothesis of known source distance. In Sections 5 and 6, we introduce the procedure and the results we adopted under the assumption of a distance uncertainty. We report our conclusions in Section 7.

2 MODEL PARAMETERS

We use KN models produced with POSSIS, a 3D Monte Carlo radiative transfer code that predicts photometric and polarimetric signatures of supernovae and KNe (Bulla 2019). The modelled ejecta are taken from Nativi et al. (2021), where a neutrino-driven wind as described in Perego et al. (2014) was evolved assuming that either no jet (Wind), or a jet with a luminosity of $L_j = 10^{49} \text{ erg s}^{-1}$ (Jet49), or a jet with $L_j = 10^{51} \text{ erg s}^{-1}$ (Jet51) is launched. The wind mass is dominated by a secular component ejected 1 s after the merger with $0.072 M_\odot$. Unlike in Nativi et al. (2021), here we include an additional component to model dynamical ejecta. Specifically, we adopt an idealized geometry for this component, with a lanthanide-rich dynamical ejecta component ($Y_e = 0.15$ and velocities from 0.08 to $0.3c$) from the grid in Dietrich et al. (2020) and selecting the best-fitting model to the KN of GW170817 (mass $0.005 M_\odot$ and half-opening angle of 30°). These models are referred to as Wind-dyn, Jet49-dyn, and Jet51-dyn to distinguish them from those in Nativi et al. (2021). Fig. 1 shows density and Y_e distributions for the three models.

Radiative transfer simulations are carried out for the three models using the latest version of POSSIS (Bulla 2023). Compared with the first version of the code (Bulla 2019, also used by Nativi et al. 2021), the improved version assumes heating rates (Rosswog & Korobkin 2022), thermalization efficiencies (Barnes et al. 2016; Wollaeger et al. 2018), and wavelength- and time-dependent opacities (Tanaka et al. 2020) that depend on the local properties of the ejecta such as density,

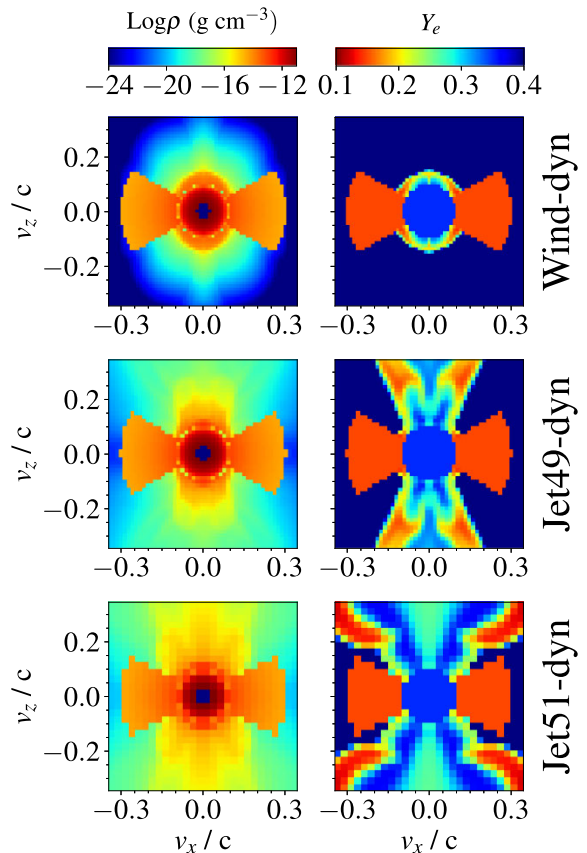


Figure 1. Density (left) and Y_e (right) distribution in the x – z plane for the three models used in this study (Wind-dyn, Jet49-dyn, and Jet51-dyn from top to bottom). Density maps are shown at 1 d after the merger.

temperature, and electron fraction. For each of the three models, we extract KN LCs for 11 different inclination angles for each model. Consequently, for a given distance and filter one has 33 different LCs. LCs are computed by POSSIS from 0.1 to 30 d after the merger, but for this work we focus on the time window from 1.0 to 5.0 d after the merger. We decided to ignore the code predictions earlier than 1 d after the merger because current opacity values assumed by POSSIS are likely affected by inaccuracies in the presence of highly ionized ejecta (Tanaka et al. 2020). We do not consider LCs after 5 d due to the low value of flux.

The viewing angle θ is defined as the angle between the direction perpendicular to the merging plane and the line of sight. We used 11 values for the viewing angle separated by a constant step in cosine of 0.1: $\cos \theta$ can assume the values 0, 0.1, 0.2, ..., 1, with $\cos \theta = 0$ corresponding to an observer in the merger plane (edge-on view) and $\cos \theta = 1$ to an observer along the jet axis (face-on view). We assumed the following range of values for distance: 20, 40, 80, 160, 250, and 350 Mpc.

We chose to evaluate our results considering observations in the Sloan filters i' , r' , and u' (hereafter referred to as i , r , and u). These wavebands were chosen as being commonly available at most telescopes. In particular, we were keen to understand what (if any) additional value was added by carrying out u -band observations, which are generally seen as more difficult than the r and i bands

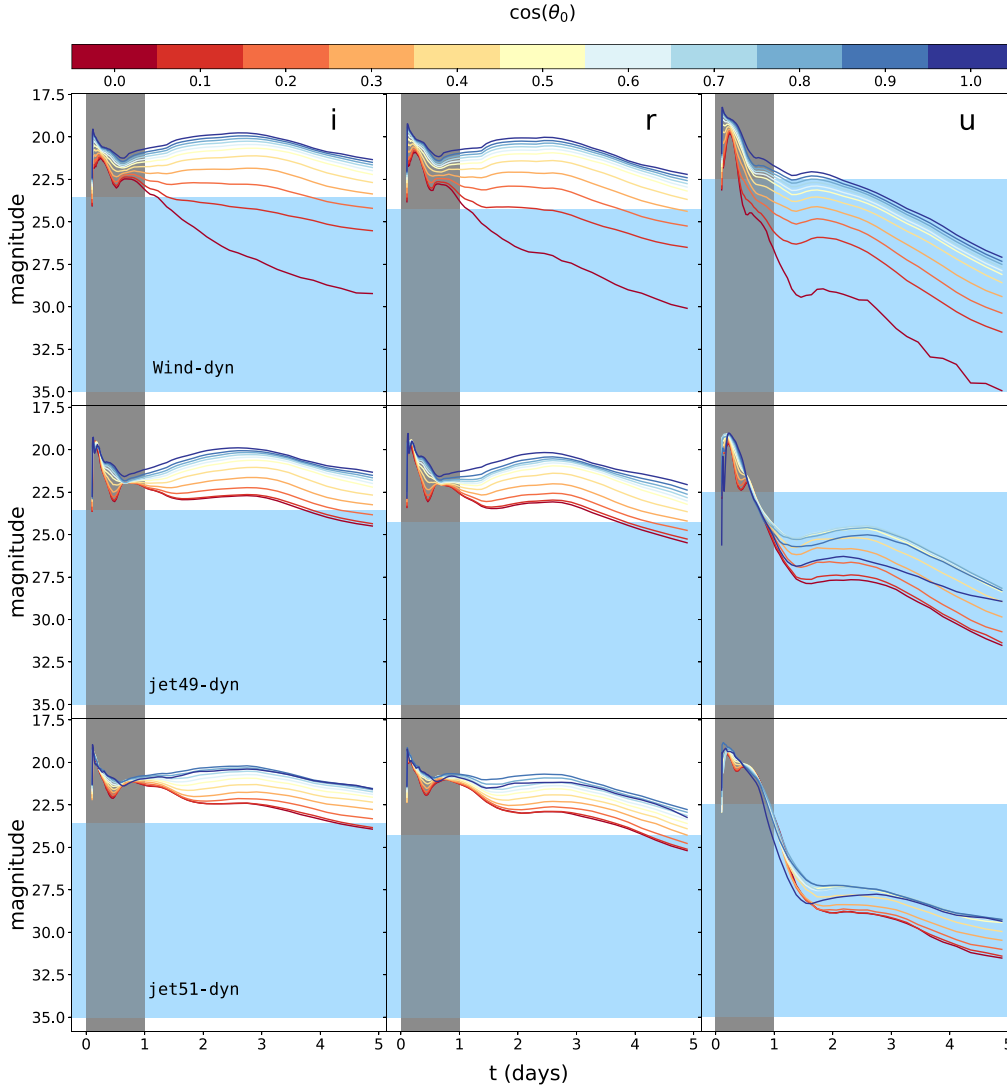


Figure 2. LCs for different models and viewing angles; first column refers to filter i , second one to filter r , and third to filter u ; the source has a distance of 160 Mpc. Grey area corresponds to the first day after the merger; LCs are not considered due to the inaccuracy in estimating the opacity. The blue area corresponds to the values in magnitude higher than the limiting magnitude of each filter, obtained with a time exposure of 1 h.

due to lower system throughputs and detector quantum efficiencies at near-ultraviolet wavelengths.

In Fig. 2, we show the LCs obtained with $d = 160$ Mpc for different filters, models, and viewing angles. The KN brightness decreases going from the jet axis ($\cos\theta = 1$) to the merger plane ($\cos\theta = 0$) for all the three models, an effect that is caused by the presence of lanthanide-rich dynamical ejecta material absorbing part of the escaping flux (‘lanthanide curtain’; Kasen, Fernández & Metzger 2015; Wollaeger et al. 2018). The area highlighted in light blue in Fig. 2 shows, for each filter, the magnitudes that are not detectable. Limiting magnitudes were obtained imposing a minimum signal-to-noise ratio (SNR) threshold of 5. See Appendix A for more details.

We point out that our study is restricted to a specific configuration in terms of ejecta properties (e.g. masses and compositions), since we do not aim to assess the ability of medium-size telescopes to

constrain these properties, but rather to select the correct model and correct viewing angle. Extending this analysis to a large grid of models with different ejecta properties is beyond the scope of this paper and could be done in the future.

3 PROCEDURE WITH KNOWN DISTANCES

In order to find a reasonable time exposure sequence necessary to distinguish between different KN models characterized by different viewing angles, we follow three main steps:

- (i) We considered four different time exposure sequences, see Section 3.1 for a detailed explanation.
- (ii) For a fixed distance and filter, we add the appropriate photon counting noise to the LC; the results depend on the time exposure

Table 1. Duration of time exposure windows and cadence for four different time exposure sequences.

Name	Duration Time exposure window (h)	Cadence (d)
A	0.5	0.25
B	1	0.5
C	2	1
D	4	See Section 3.1 for a description

sequence; we apply this step to all 33 LCs. Henceforward we will call the LC with noise ‘LCN’ (see Section 3.2).

(iii) We compare LCN with the LCs without noise and we analyse how often we are able to identify the correct LC. This is done for each combination of distance and filter. We repeat this for all the 33 different LCNs (see Section 3.3).

In the first part, the distance of the source is assumed to be known with negligible uncertainty, so we compare LCNs with LCs at the same distance.

3.1 Time exposure sequences

We considered four different time exposure sequences (hereafter, referred to as A, B, C, and D), each of them with a total net exposure of 8 h. Table 1 reports the time windows and cadence for A, B, and C sequences. Sequence D requires a separate description: it consists of two 4-h intervals 1 d apart. The exact times of the two observations are determined by maximizing the difference between the two expected magnitude values taking into account the corresponding uncertainties. To this aim, for each instant we find the median of

$$\frac{|m_{\text{model}_i} - \bar{m}|}{\sigma_{m_i}}, \quad (1)$$

where m_{model_i} is the magnitude of the i th LC at that instant, \bar{m} is the mean of all 33 LCs at that instant, and σ_{m_i} is

$$\sigma_{m_i} = \frac{1}{0.4 \sqrt{F_i t_{\text{exp}} \ln(10)}},$$

where F_i is the photoelectron count expected in 1 s for the i th model and $t_{\text{exp}} = 4$ h. We sum the median (equation 1) obtained with different filters and distances and we find the mean value of this quantity in 4-h intervals. We finally determine the maximum of the sum of the value obtained in two 4-h intervals 1 d apart. In this way, we obtain the intervals where the models are more different. Fig. 3 displays the resulting time windows.

3.2 Adding noise to light curves

We used A, B, C, and D time exposure sequences to simulate different LCNs for all combinations of filters, distances, viewing angles, and models. In more detail, at each time we calculated the expected photoelectron counts as $t_{\text{exp}}(F + F_{\text{sky}})$, where F_{sky} are the counts s^{-1} due to the sky (see Appendix A for more details). We then obtained the simulated counts C_P by adding the statistical noise assuming the Poisson distribution.

The noise-affected flux of the k th LC is calculated as follows:

$$F_{\text{noise},k} = \frac{C_{P,k}}{t_{\text{exp}}} - F_{\text{sky}}, \quad (2)$$

along with the corresponding magnitude

$$m_{\text{noise},k} = z_P - 2.5 \log_{10}(F_{\text{noise},k}). \quad (3)$$

Equation (3) gives a generic LCN. Fig. 3 shows the results of this step.

3.3 Comparison between LC with noise and models

We compare any given LCN with all of the 33 models and select the model that minimizes the following χ^2 :

$$\chi^2(k, i) = \sum_{j=0}^{N_i} \left(\frac{m_{\text{model}_i}(t_j) - m_{\text{noise}_k}(t_j)}{\sigma_{m_{\text{noise}_k}}(t_j)} \right)^2 \cdot \frac{1}{N_i}, \quad (4)$$

where we are summing over the N_i different data, i and k , respectively, identify LC and LCN, and $\sigma_{m_{\text{noise}_k}}$ is the uncertainty on m_{noise_k} , obtained by error propagating from $C_{P,k}$, using equations (2) and (3) and assuming $\sigma_{C_{P,k}} = \sqrt{C_{P,k}}$. It is given by

$$\sigma_{m_{\text{noise}_k}} = \frac{\sqrt{C_{P,k}}}{0.4 F_{\text{noise},k} \ln(10) t_{\text{exp}}}. \quad (5)$$

In this way, we obtain, for each model, viewing angle and distance (so, for each configuration), using four different time exposure sequences, the number of correct/incorrect matches.

4 RESULTS WITH KNOWN DISTANCES

Fig. 4 shows, for each distance and for each model, the number of incorrect matches out of 33 comparisons. Noticeably, it is better to avoid u filter. Hereafter, in our analysis, we will consider only i and r filters.

We take note of three different kinds of mismatching errors between the simulated data points and the model LC:

- (i) The most similar curve model corresponds to the simulated model, but the viewing angle is wrong.
- (ii) The most similar model turns out to be different from the original one.
- (iii) LCN is not detectable because the magnitude value is higher than the limiting value for each point of LCN.

We summarize the results about the most common mismatches (i.e. misidentifications) in the left-hand pie of Fig. 5. The outermost ring corresponds to the different number of mismatches obtained with the four exposure combinations (i and r filters); the innermost one refers to the different kinds of mismatches. Overall, most of the mismatches are of type (iii). The percentage of mismatches of type (ii) is higher than that of type (i). Type (ii) mismatches are shown in the central pie of Fig. 5 including both i and r filters; undetectable LCs are ignored. The number of mismatches is quite similar among all the kinds of models and with every sequence. If we consider i and r filters individually, the results are similar; if we include the not detectable LCs, the number of mismatches with `wind-dyn` model increases. Let θ_0 be the viewing angle of the LCN. We check if there is any particular value of θ_0 for which we have most of the mismatches and how significant the mismatch is for the different viewing angle θ_0 . As shown in the right-hand pie of Fig. 5, D time exposure sequence has a wider range of starting angle that can bring to mismatches; with A, B, and C most mismatches happen for $78^\circ \leq \theta_0 \leq 90^\circ$. Analysing the difference between $\cos \theta_0$ and the value of $\cos \theta$ of the most similar LC, we find that with C time exposure sequence we always have $|\Delta \cos \theta| \leq 0.1$; with A and B we have more than 80 per cent of mismatches with $|\Delta \cos \theta| \leq 0.2$, with D it is 62 per cent.

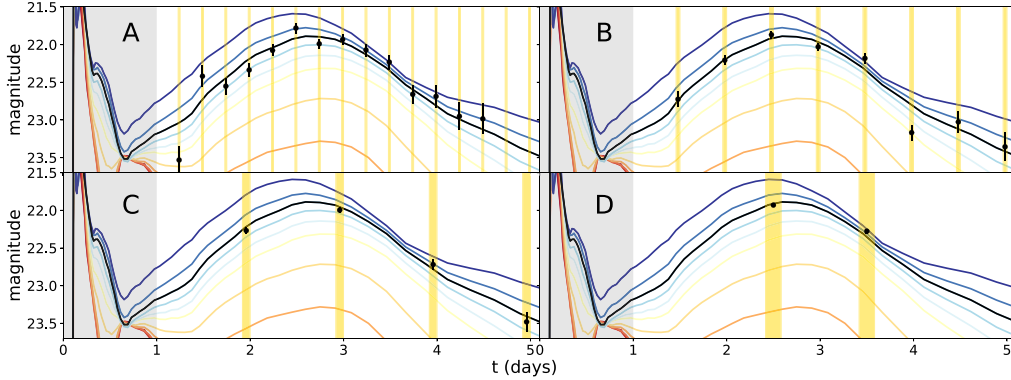
2520 *A. E. Camisasca et al.*


Figure 3. Each panel refers to a different time window sequence: A, B, C, and D. In yellow, A, B, C, and D time windows; in each plot, LCs referring to Jet49-dyn model, $d = 350$ Mpc, and i filter. Black lines are LCs with $\cos\theta_0 = 0.8$, black points refer to the corresponding LCNs.

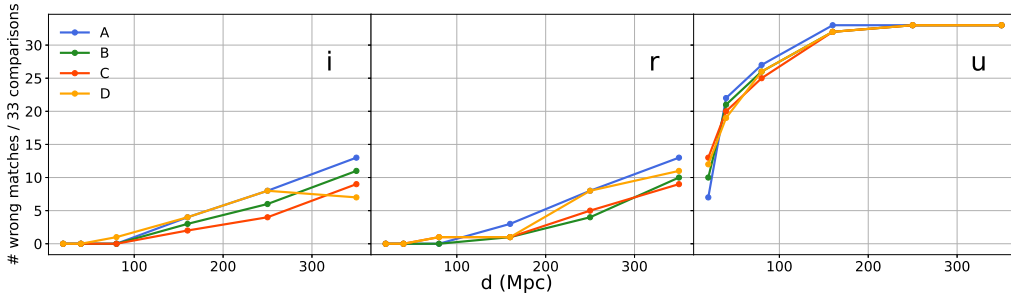


Figure 4. Number of wrong matches as a function of distance for different filters and different time exposure sequences.

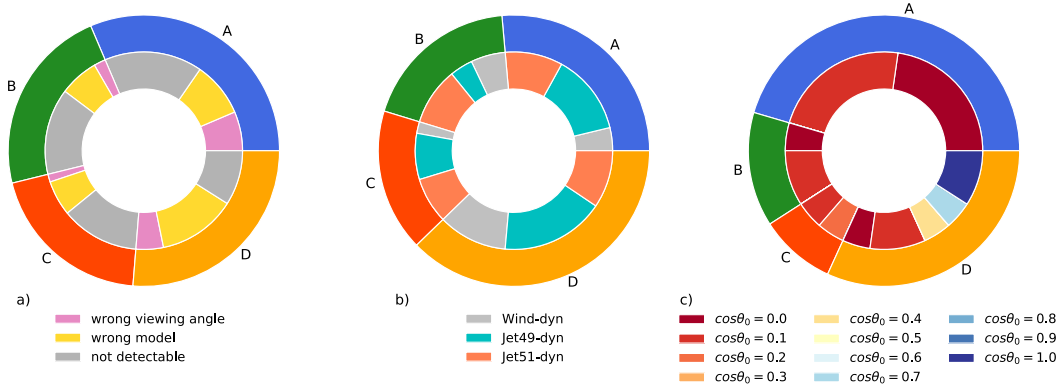


Figure 5. For every different time exposure sequence, we analyse the type of mismatch that occurs in comparing the simulated curve with the model ones. We considered both i and r filters. (a) In the outer ring, the number of wrong matches for each time exposure; in the inner ring, the kind of mismatch. (b) For every different time exposure sequence, we analyse which model is more difficult to detect. In the outer ring, the number of wrong matches for each time exposure; in the inner ring, the number of mismatch for each kind of model. (c) In the outer ring, the number of wrong matches for each time exposure; in the inner ring, $\cos\theta_0$.

The fact that the most of the mismatches refer to edge-on view and that i and r filters perform better than u can easily be understood looking at Fig. 2:

(i) Edge-on-view LCs are more significantly affected by statistical noise, since they have lower fluxes than face-on ones; also, they can

partially or totally fade below the limiting magnitude to the point that they become undetectable.

(ii) u -filter LCs have lower fluxes and their limiting magnitude value is lower than i and r ones; these characteristics lead to a low performance of the u filter.

5 PROCEDURE WITH DISTANCE UNCERTAINTY

We now examine the realistic situation of non-negligible uncertainty on distance, and, in addition, the possibility that there is no information on the distance of the source as well as on the time of the merger. We restrict our analysis to i and r filters, due to the low performance of u .

5.1 1 and 2 per cent error on distance

We analysed the consequences of an error on distance of 1 and 2 per cent. Such a level of accuracy in estimating the distance based on GW data alone appears to be feasible for a sizeable fraction of cases: third-generation GW detector network will measure distances with an accuracy of 0.1–3 per cent for sources within ≤ 300 Mpc (see fig. 9 from Gupta et al. 2019). To study this case, when we look for the matches between LCN and LCs, we shift the magnitude of the LC models due to the error on distance. We consider both a +1 per cent (+2 per cent) and –1 per cent (–2 per cent) error on distance.

5.2 Unknown distance, χ^2 -minimization technique

Let us assume that we have no information on distance as well as on the merger time. When we have to compare LCN with LCs, we start using the LCs model with the intermediate distance of 160 Mpc (LC-160) and we shift LC-160 both in time (Δt) and in magnitude (Δm), in order to find, among the 33 comparisons, Δt and Δm that minimize χ^2 (equation 4). Once we have Δm , we follow this procedure:

- (i) We use Δm to find an estimated distance (d_s) of the source.
- (ii) We create a set of LC models with which to compare LCN, with a step of 0.1 mag between one model and the following one.
- (iii) We choose the model with the nearest distance to d_s .
- (iv) We compare LCN with the model at the most similar distance with d_s , shifting LCs both in time and magnitude to find the best match.

5.3 Colour curves technique

We adopted colour curves to try to limit the possible effect of distance uncertainties. To create colour curve with noise (CCN), we add noise to LCs with different filters, then we subtract them. Since CCNs have a dependence on distance (even if small), when we compare CCNs with colour curve models (CCs), we compare them with CCs model at the intermediate distance of 160 Mpc (CC-160).

6 RESULTS WITH DISTANCE UNCERTAINTY

6.1 Single filter technique

In Fig. 6, we present the number of wrong matches that occur in 33 comparisons with A, B, C, and D time exposure sequences, using filters individually. We reported the results obtained without error on distance and we compare it with what we obtain with an error of 1 per cent, 2 per cent, and without information on distance and time of the merger. For 1 per cent (and 2 per cent) error on distance, we plot the highest number of mismatches between +1 and –1 per cent (+2 and –2 per cent).

For each filter, each distance, we compare the results obtained with A, B, C, and D checking if the number of mismatches within each

time exposure sequence is compatible with the best results obtained within the limits of Poisson statistics.¹ In Fig. 6, we marked with ‘x’ the cases that are significantly different from the best value obtained with other time sequences; if the error on distance is ≤ 2 per cent, no particular statistical differences emerge between sequences A, B, and C. When the distance is unknown, C and D time windows should be avoided. Hereafter, we restrict our analysis to A and C time exposure sequences, since C, with 1-d cadence, can easily be carried out with a single telescope, but should be avoided when no information on the source distance is available. The comparison between i and r shows that they are equivalent.

6.1.1 Error on distance ≤ 2 per cent

Focusing on time sequence C with error on distance ≤ 2 per cent, Fig. 7 shows that the number of mismatches of types (i), (ii), and (iii) is mostly the same. The number of mismatches concerning the models are equally distributed between `Wind-dyn`, `Jet49-dyn`, and `Jet51-dyn`, provided that the LC can be detected. If we consider also not detectable LCNs, `Wind-dyn` model mismatches increase (i.e. `Wind-dyn` model would be harder to be detected). With an error on distance of 1 per cent, the majority of the mismatches are in the interval $73^\circ \leq \theta_0 \leq 90^\circ$; this interval becomes wider for increasing errors on distance. When the error on distance is ≤ 2 per cent, both with i and r filters we have $|\Delta \cos \theta| \leq 0.2$ for all the mismatches.

6.1.2 Unknown distance

If we do not have information about the distance, in order to have the lowest number of mismatches, it is recommendable to use A time window sequence; with this sequence the number of mismatches of types (i), (ii), and (iii) is similar; also, the mismatches concerning the models are equally distributed among `Wind-dyn`, `Jet49-dyn`, and `Jet51-dyn`. Regarding viewing angle mismatches, they occur with the same frequency for every θ_0 ; furthermore, $|\Delta \cos \theta| \leq 0.2$ for 82 per cent of mismatches.

6.1.3 Focus on viewing angle estimation

For each combination of distance and of its error, we adopted the following procedure: for each viewing angle θ_0 , we determined the uncertainty on the estimated viewing angle θ_{est} , using either C or A time sequence, respectively, for error on distance ≤ 2 per cent and for unknown distance. Then, we took the largest uncertainty among all the values of θ_0 : in this way, we associated to any combination of distance and error on it with a conservative uncertainty in the estimated viewing angle, as the result of any possible value of θ_0 . Table 2 reports the results.

If the error on distance is ≤ 2 per cent, the error on θ_{est} is always $\leq 7^\circ$; these errors implicitly assume that the inaccuracies intrinsic to the POSS1 models and its assumptions are negligible. In practice,

¹When we compare the results of two observations N_1 and N_2 , we assume that the numbers of wrong matches are independently Poisson distributed. Consequently, $|N_2 - N_1|$ is the absolute value of a Skellam-distributed random variate. We calculate the probability of having $\geq |N_2 - N_1|$ assuming as expected value for the common Poisson distribution the mean value of N_1 and N_2 . When the probability is < 5 per cent, the two numbers are considered significantly different.

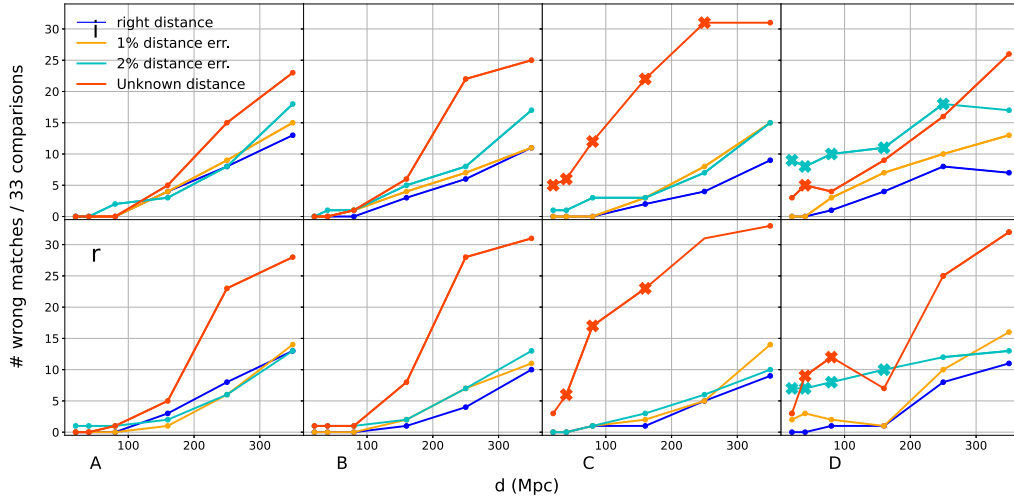
2522 *A. E. Camisasca et al.*


Figure 6. The number of wrong matches that occur in 33 comparisons with A, B, C, and D time exposure sequences with a known distance (blue line), with an error of 1 per cent on distance (yellow line), 2 per cent (cyan line), and without any information about the distance and the time of the merger (orange line). Points marked with ‘x’ refer to values that are significantly different from the best value obtained with other time sequences.

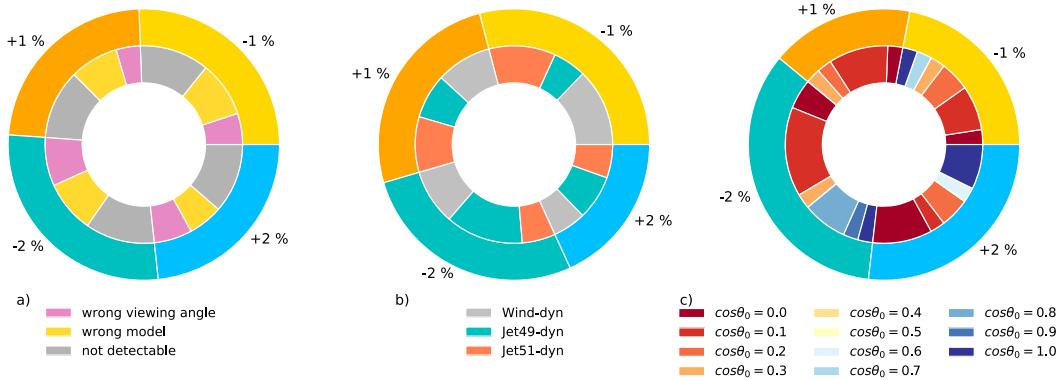


Figure 7. Using time sequence C, we consider the number of wrong matches we have when we make an error on distance of ± 1 and ± 2 per cent. (a) In the outer ring, the number of wrong matches for each error on distance; in the inner ring, the kind of mismatch. (b) For every different model of the simulated source, we analyse how many mismatches we have. (c) For every different observational direction, we analyse the number of mismatches.

Table 2. The higher standard deviation on θ_{est} for different distances.

d (Mpc)	1 per cent distance		Unknown distance
	err.	err.	
20	3°	4°	11°
40	2°	7°	7°
80	1°	4°	5°
160	3°	4°	12°
250	2°	4°	14°
350	7°	4°	25°

should this be no more the case; an independent estimate of the viewing angle, combined with the errors reported in Table 2, could help to constrain the POSSIS accuracy, thus providing useful feedback to tweak and refine the code itself.

MNRAS **522**, 2516–2524 (2023)

6.2 Colour curve technique

For each time windows sequence, we analysed the results obtained comparing CCN with CC-160 for $i-r$ CCs. As we can see in Fig. 8, this procedure gives a higher number of wrong matches than single filter techniques; this is due to the fact that the use of two LCs increases the possibility that, in a given instant, there is at least one undetectable LC. Moreover, uncertainties on both curves combine and lower the SNR; furthermore, LCs in i and r are really similar and there is really little viewing angle dependence in $i-r$ colour. We do not consider $i-u$ and $r-u$ CCs due to u -filter outcomes; using another filter combined with i and r might lead to better results. Finally, since there is a slight dependence of CCs on distance, we use in the comparison CC-160; this makes the match more difficult when the distance is highly different from 160 Mpc.

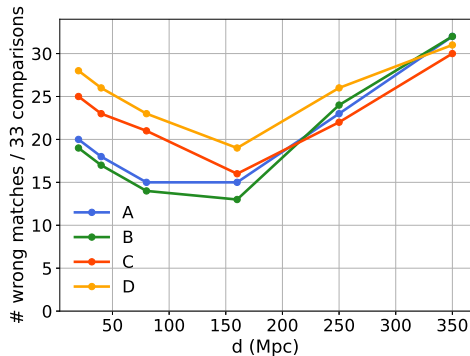


Figure 8. Number of wrong matches as a function of distance for different time exposure sequence using colour curves $i-r$.

7 CONCLUSIONS

The aim of the paper was finding the best strategy to characterize accurately localized KNe with follow-up small–medium-size optical telescopes. We found that the use of the u filter should be avoided, due to the high number of mismatches with all the time window sequences considered in this work (see Fig. 4). Even a procedure with $i-r$ colour curve is not as convenient as one might think: it gives a higher number of wrong matches than single filter technique, due to the fact that the use of two LCs increases the possibility that, in a moment, there is at least one undetectable LC. Alternative time window sequences sharing the same total net exposure and with at least four observations and a maximum cadence of 1 d are essentially equivalent, provided that the error on distance is ≤ 2 per cent. Consequently, we suggest to use 1-d-cadence sequence, because it can be easily realized. If the distance of the source is unknown, short-cadence (≤ 0.5 d) sequences are preferable.

Finally, we demonstrated that, for any distance considered in the present analysis (from 20 to 350 Mpc) and an error on distance ≤ 2 per cent, the viewing angle is estimated very accurately: the correct value is always compatible with the estimated one within uncertainties, with an error that is always $\leq 7^\circ$. This means that an independent measurement of the viewing angle could help to constrain the accuracy of POSSIS, providing useful information to refine the code itself. In addition, more stringent constraints on the viewing angle can better reduce the distance–inclination angle degeneracy in GW data, and, consequently, lead to a more accurate estimate of the distance and of the Hubble constant H_0 (e.g. Guidorzi et al. 2017; Dhawan et al. 2020; see Bulla et al. 2022 for a review).

ACKNOWLEDGEMENTS

We are grateful to the Referee for the careful reading and constructive comments, which helped us to improve the paper. AEC thanks IAS for the hospitality at the Astrophysics Research Institute of Liverpool JM University and the significant research opportunity and acknowledges the University of Ferrara for financial support under the programme ‘Call for mobility scholarship for periods at European and extra European Institutions’. The radiative transfer simulations with POSSIS were performed on resources provided by the Swedish National Infrastructure for Computing (SNIC) at Kebnekaise.

DATA AVAILABILITY

The uri LCs for the six models used in this study will be made available at https://github.com/mbulla/kilonova_models. The POSSIS code used to simulate the LCs is not publicly available.

REFERENCES

- Abbott B. P. et al., 2017a, *Class. Quantum Gravity*, 34, 044001
 Abbott B. P. et al., 2017b, *ApJ*, 848, L12
 Almualla M. et al., 2021, *MNRAS*, 504, 2822
 Amati L. et al., 2021, *Exp. Astron.*, 52, 183
 Andreoni I. et al., 2022, *ApJS*, 260, 18
 Atteia J. L., Cordier B., Wei J., 2022, *Int. J. Mod. Phys. D*, 31, 2230008
 Baker J. et al., 2021, *Exp. Astron.*, 51, 1441
 Barnes J., Kasen D., Wu M.-R., Martínez-Pinedo G., 2016, *ApJ*, 829, 110
 Barthelmy S. D. et al., 2005, *Space Sci. Rev.*, 120, 143
 Brown T. M. et al., 2013, *PASP*, 125, 1031
 Bulla M., 2019, *MNRAS*, 489, 5037
 Bulla M., 2023, *MNRAS*, 520, 2558
 Bulla M., Coughlin M. W., Dhawan S., Dietrich T., 2022, *Universe*, 8, 289
 Chase E. A. et al., 2022, *ApJ*, 927, 163
 Chornock R. et al., 2017, *ApJ*, 848, L19
 Colombo A., Salafia O. S., Gabrielli F., Ghirlanda G., Giacomazzo B., Perego A., Colpi M., 2022, *ApJ*, 937, 79
 Coulter D. A. et al., 2017, *Science*, 358, 1556
 Dhawan S., Bulla M., Goobar A., Sagués Carracedo A., Setzer C. N., 2020, *ApJ*, 888, 67
 Dietrich T., Coughlin M. W., Pang P. T. H., Bulla M., Heinzel J., Issa L., Tews I., Antier S., 2020, *Science*, 370, 1450
 Domoto N., Tanaka M., Wanajo S., Kawaguchi K., 2021, *ApJ*, 913, 26
 Gehrels N. et al., 2004, *ApJ*, 611, 1005
 Goldstein A. et al., 2017, *ApJ*, 848, L14
 Guidorzi C. et al., 2017, *ApJ*, 851, L36
 Gupta A., Fox D., Sathyaprakash B. S., Schutz B. F., 2019, *ApJ*, 886, 71
 Kasen D., Fernández R., Metzger B. D., 2015, *MNRAS*, 450, 1777
 Kasen D., Metzger B., Barnes J., Quataert E., Ramirez-Ruiz E., 2017, *Nature*, 551, 80
 Kasliwal M. M. et al., 2022, *MNRAS*, 510, L7
 Klion H., Duffell P. C., Kasen D., Quataert E., 2021, *MNRAS*, 502, 865
 Li L.-X., Paczyński B., 1998, *ApJ*, 507, L59
 Metzger B. D., 2019, *Living Rev. Relativ.*, 23, 1
 Nativi L., Bulla M., Rosswog S., Lundman C., Kowal G., Gizzi D., Lamb G. P., Perego A., 2021, *MNRAS*, 500, 1772
 Perego A., Rosswog S., Cabezón R. M., Korobkin O., Käppeli R., Arcones A., Liebendörfer M., 2014, *MNRAS*, 443, 3134
 Pian E. et al., 2017, *Nature*, 551, 67
 Punturo M. et al., 2010, *Class. Quantum Gravity*, 27, 194002
 Rastinejad J. C. et al., 2022, *Nature*, 612, 223
 Ronchini S. et al., 2022, *A&A*, 665, A97
 Rosswog S., Korobkin O., 2022, *Annalen der Physik, Heavy Elements and Electromagnetic Transients from Neutron Star Mergers*. Available at: <https://arxiv.org/abs/2203.11111>
 Savchenko V. et al., 2017, *ApJ*, 848, L15
 Scolnic D. et al., 2018, *ApJ*, 852, L3
 Setzer C. N., Biswas R., Peiris H. V., Rosswog S., Korobkin O., Wollaeger R. T., LSST Dark Energy Science Collaboration, 2019, *MNRAS*, 485, 4260
 Shrestha M., Steele I. A., Piascik A. S., Jermak H., Smith R. J., Copperwheat C. M., 2020, *MNRAS*, 494, 4676
 Smartt S. J. et al., 2017, *Nature*, 551, 75
 Smith R., Steele I. A., 2017, Technical Report, Liverpool Telescope Technical Note 1: Telescope and IO:O Throughput
 Steele I. A. et al., 2004, in Oschmann J. M. J. ed., Proc. SPIE Conf. Ser. Vol. 5489, Ground-based Telescopes. SPIE, Bellingham, p. 679
 Tanaka M., Kato D., Gaigalas G., Kawaguchi K., 2020, *MNRAS*, 496, 1369
 Tanvir N. R. et al., 2017, *ApJ*, 848, L27
 Tsapras Y. et al., 2009, *Astron. Nachr.*, 330, 4
 Villar V. A. et al., 2017, *ApJ*, 851, L21

2524 *A. E. Camisasca et al.*

Watson D. et al., 2019, *Nature*, 574, 497
 Wollaeger R. T. et al., 2018, *MNRAS*, 478, 3298
 Yuan W., Zhang C., Chen Y., Ling Z., 2022, in Bambi C., Santangelo A., eds,
 Handbook of X-ray and Gamma-ray Astrophysics. Springer, Singapore

APPENDIX: EXPOSURE TIME FORMULA FOR A SINGLE FILTER

We calculate F_{lim} , defined as the minimum photoelectron count collected in 1 s to have a detectable signal, assuming a limiting SNR, $\text{SNR}_{\text{lim}} = 5$, through the following equation:

$$\text{SNR}_{\text{lim}} = \frac{F_{\text{lim}} t_{\text{exp}}}{\sqrt{F_{\text{lim}} t_{\text{exp}} + F_{\text{sky}} t_{\text{exp}}}},$$

with

$$F_{\text{sky}} = 10^{0.4(z_p - m_{\text{sky}})} A,$$

where z_p is the instrument zero-point referred to a particular filter (the magnitude corresponding to one detected photoelectron per second), m_{sky} is the sky magnitude in 1 arcsec², and A is the area of the photometric aperture used. We used z_p and m_{sky} values as suggested

Table A1. z_p and m_{sky} values.

Filter	z_p	m_{sky} (mag arcsec ⁻²)
<i>i</i>	25.06	17.3
<i>r</i>	15.39	18.4
<i>u</i>	21.00	18.0

at the Liverpool Telescope website,² assuming m_{sky} as intermediate between a dark and a bright sky (Table A1). Since the typical La Palma seeing is 0.75 arcsec, we adopted an aperture diameter two times that value (i.e. 1.5 arcsec), which yields $A = 1.8$ arcsec².

²https://github.com/LivTel/ETC_calcs/blob/master/NRT_calc.html

This paper has been typeset from a $\text{\TeX}/\text{\LaTeX}$ file prepared by the author.